A Measurement of the Neutron Magnetic Form Factor G_M^n from Quasi-elastic ${}^2\vec{H}(\vec{e}, e')$ at low Q^2

by

Nikolas Meitanis

Submitted to the Department of Physics
in partial fulfillment of the requirements for the degree of

Doctor of Philosophy

at the

MASSACHUSETTS INSTITUTE OF TECHNOLOGY

[June 2006]
March 2006

Author ....
Department of Physics
March 7, 2006

Certified by ....
Richard Milner
Professor of Physics
Thesis Supervisor

Accepted by ....
Thomas J. Greytak
Chairman of Graduate Committee

A Measurement of the Neutron Magnetic Form Factor $\mathbf{G_M^n}$ from Quasi-elastic $^2\vec{\mathbf{H}}(\vec{\mathbf{e}}, \mathbf{e}')$ at low $\mathbf{Q^2}$

by

Nikolas Meitanis

Submitted to the Department of Physics
on March 7, 2006, in partial fulfillment of the
requirements for the degree of
Doctor of Philosophy

Abstract

The neutron magnetic form factor G_M^n has been measured using the inclusive electrodisintegration $^2\vec{H}(\vec{e}, e')$ of the deuteron for the first time. The longitudinally polarized electron beam of the MIT-Bates Linear Accelerator was used in conjunction with an isotopically pure, polarized deuterium internal gas target. The Bates Large Acceptance Spectrometer Toroid (BLAST) was used for the measurement. The form factor G_M^n was extracted from the ratio of the inclusive asymmetry α_{ed}^V in perpendicular over parallel kinematics and at $Q^2 = 0.135$, 0.189, 0.252, 0.316 (GeV/c)^2.

Thesis Supervisor: Richard Milner
Title: Professor of Physics

To my family.

Acknowledgments

It is customary for dissertations to carry a brief Acknowledgements section to recognize the human components of the experiment.

I would like to thank Professor Richard Milner for his guidance, kindness and understanding over the long years of the experiment. Professor Kevin McIlhany who spent countless hours teaching me fundamental physics while a post-doc at MIT. Chi Zhang who spent lots of time answering my questions regarding software as well as the physics of BLAST. Vitalyi Ziskin and Aaron Maschinot for all the help they gave me over the years with both software and analysis. Michael Kohl for his contributions on the analysis presented herein. Professors Bill Donnelly and Hartmuth Arenhövel for numerous explanations on the physics of the experiment. Hauke Kolster, Genya Tsentalovich and Ernie Ihloff for all the help regarding ABS physics and operation. Jim Kelsey for lots of long discussions. Doug Hasell, Karen Dow, Chris Crawford, Tim Smith, Bill Franklin, Tancredi Botto, Akihisa Shinozaki, Townsend Zwart, Manoucher Farkondeh, Taylan Akdogan, Renee Fatemi, Eugene Geis, Adrian Sindile, Peter Karpius, Yuan Xiao and Tavi Filoti for all their contributions to the experiment. Peter Binns, Brian O'Rourke, Rich Capodilupo, Steve Ciacera, Ignacio Diaz, Bob Abruzio, Chris Brown, Peter Goodwyn, Chris Vidal and Bill Nispel for many years of moral support and social interaction. Dick Heider and Dave Scoggins for the coffee, cream and sugar. Rich Coviello and Frank Casalli for allowing me to practice my English. Ernie Bisson for help with computer hardware and software. Jason Seely and Ben Classie for sharing an office with me the last few months as well as everyday discussions and games of chess. I apologize to anyone I unintentionally omitted due to memory deficiency.

Most importantly, I would like to thank my family for their support, without which I would not have reached this end.

Contents

List of Figures

List of Tables

Chapter 1

Theoretical Framework

In this chapter, the relevant theoretical background is presented in brief. The chapter consists of four major parts. The general properties of elastic electron-nucleon scattering, followed by a section on electron-deuteron scattering. The chapter concludes with a survey of existing experimental data as well as capsule-descriptions and references to theoretical models and calculations related to the experiments. When necessary, the sections are divided into subsections covering specific topics in order to maintain clarity of presentation.

1.1 Elastic Electron-Nucleon Scattering

1.1.1 Unpolarized Target

In this section, elastic electron-nucleon scattering is discussed. Following the notation of Donnelly [1], the spin-dependent differential cross section is expressed in terms of the four-vectors of the particles participating in the interaction. K and K$'$ denote the four-vectors of the incoming and outgoing electron, respectively, while P and P$'$ refer to the initial and final target state. The momentum transfer four-vector is then expressed in terms of the electron four-vectors as $Q = K - K'$. The masses of the electron and the target nucleon are denoted by m_e and m_N, respectively. In addition, ϵ and ϵ' are the initial and final electron energy, respectively, whereas E$'$

is the final target energy. The differential cross section can be written as

$$d\sigma^{Lab} = \frac{1}{\beta}\left(\frac{m_e}{\epsilon}\right)\overline{\sum_{if}}|M_{fi}|^2\left[\frac{m_e}{\epsilon'}\frac{d\vec{k}'}{(2\pi)^3}\right]\left[\frac{m_N}{E'}\frac{d\vec{p}'}{(2\pi)^3}\right](2\pi)^4\delta^4((K+P)-(K'+P')). \tag{1.1}$$

Here, $\beta = |\vec{k}|/\epsilon$, and the delta function and phase-space factors conserve energy and momentum for the reaction. The above expression is quite general[1] and from here the discussion can proceed in a number of different directions, in each case evaluating the matrix element $\overline{\sum_{if}}|M_{fi}|^2$ accordingly. This matrix element results from a contraction of the leptonic and hadronic currents and enters the cross section calculation as a sum over all final states and an average over all initial ones, as indicated by the summation. For the simple case of elastic electron-nucleon scattering (fig. 1-1), it is given by

$$M_{fi} = i\left(\frac{1}{Q^2}\right)j_\mu J^\mu, \tag{1.2}$$

where

$$\begin{aligned} j^\mu &= -e\bar{u}_e(\epsilon', \vec{k}')\gamma^\mu u_e(\epsilon, \vec{k}), \\ J^\mu &= +e\bar{u}_p(E', \vec{p}')\gamma^\mu u_p(E, \vec{p}) \end{aligned} \tag{1.3}$$

are the electromagnetic currents for the electron and the pointlike nucleon.

In the (heuristic) case of unpolarized and spinless electrons scattering off spinless, pointlike nucleons, the interaction is described by the simple form of the Rutherford cross section. However, for a relativistic, spin$-\frac{1}{2}$ electron, spin-effects modify the result to the *Mott cross section* as

$$\left(\frac{d\sigma}{d\Omega}\right)_{Mott} = \frac{\alpha^2\cos^2\left(\frac{\theta}{2}\right)}{4\epsilon^2\sin^4\left(\frac{\theta}{2}\right)\left(1 + 2(\epsilon/m_N)\sin^2\left(\frac{\theta}{2}\right)\right)}, \tag{1.4}$$

where θ is the angle of the scattered electron, m_N is the nucleon mass and α the fine structure constant. The Mott cross section is often written in terms of the recoil

---

[1] Quantum Field Theory textbooks provide advanced treatments of the topic [2, 3].

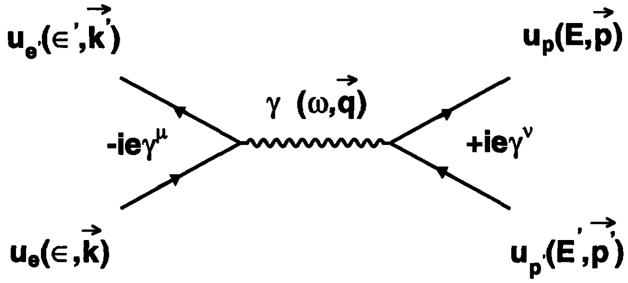

Figure 1-1: Electron-pointlike nucleon elastic scattering. Here, the incoming and scattered electrons are represented by their respective Dirac spinors u_e, $u_{e'}$, with ϵ, ϵ' the respective energies and $\vec{k}$, $\vec{k'}$ the respective three-momenta involved. On the hadronic side, the incoming and scattered nucleons are represented by u_p, $u_{p'}$, with E, E' and $\vec{p}$, $\vec{p'}$ the related energies and momenta. The virtual photon of energy ω and vector momentum $\vec{q}$ is denoted as $\gamma(\omega, \vec{q})$, whereas $-ie\gamma^\mu$, $+ie\gamma^\nu$ are the vertex factors using the appropriate Dirac matrices.

factor defined as

$$f_{rec} \equiv \left(1 + 2(\epsilon/m_N)\sin^2\left(\frac{\theta}{2}\right)\right). \tag{1.5}$$

The Mott cross section drops more rapidly at large scattering angles as compared to the Rutherford cross section. Furthermore, in the (still heuristic) case of unpolarized, spin$-\frac{1}{2}$ electrons scattering off spin-$\frac{1}{2}$ pointlike nucleons, the scattering is described by the *Dirac cross section.* Taking the spin of the target into account, gives rise to a magnetic interaction in addition to the Coulombic.

In order to account for the structure of the nucleon, the Dirac matrix used previously for the hadronic vertex is replaced by a generalized Γ^ν function. This function incorporates all relevant structure and must be constructed out of the 4-vector momenta $Q^\mu = p^\mu - p^{\mu'}$, p^μ, $p^{\mu'}$ and the Dirac matrices γ^μ. Lorentz invariance and current conservation have to be obeyed, thus resulting in

$$\Gamma^\mu = \gamma^\mu F_1(Q^2) + \frac{i}{2m}\sigma^{\mu\nu}Q_\nu F_2(Q^2), \tag{1.6}$$

where $\sigma^{\mu\nu} = \frac{1}{2i}[\gamma^\mu, \gamma^\nu]$ and F_1, F_2 are the *Dirac* and *Pauli* form factors, respectively. Using this expression for the nucleon electromagnetic current and working through the algebra[2], one arrives at the *Rosenbluth cross section* for elastic electron-nucleon scattering [6]

$$\left(\frac{d\sigma}{d\Omega}\right)_{Ros} = \left(\frac{d\sigma}{d\Omega}\right)_{Mott} \left[(F_1^2 + \tau\, F_2^2) \,+\, 2\tau\,(F_1 + F_2)^2 \,\tan^2(\tfrac{\theta}{2})\right], \tag{1.7}$$

where $\tau = Q^2/4M^2$ with M the mass of the target. Sachs and collaborators [7, 8] demonstrated that certain linear combinations of the Dirac and Pauli form factors allow further physical interpretation. They proposed expressing the electric and magnetic form factors[3] as

$$\begin{aligned} G_E(Q^2) &= F_1(Q^2) - \tau F_2(Q^2), \\ G_M(Q^2) &= F_1(Q^2) + F_2(Q^2). \end{aligned} \tag{1.8}$$

In a particular frame, known as the *Breit frame*, where $Q^2 = |\vec{q}|^2$ (which is equivalent to a zero energy transfer ($\omega = 0$) and is often referred to as the "brick-wall" frame because there is no target recoil), the electric and magnetic form factors can be interpreted as the Fourier transforms of the spatial charge and magnetization distributions

$$\begin{aligned} G_E(Q^2) &= \int \rho_{ch}(\vec{r})\, e^{-i\vec{q}\cdot\vec{r}} d^3\vec{r} \\ G_M(Q^2) &= \mu \int \rho_{magn}(\vec{r})\, e^{-i\vec{q}\cdot\vec{r}} d^3\vec{r}, \end{aligned} \tag{1.9}$$

where μ is the anomalous magnetic moment of the nucleon in units of the nuclear magneton μ_N. As a consequence of this physical interpretation of the form factors, the integrals in eq. (1.9) can be expressed in terms of the respective rms radii for the distributions, r_{el} and r_{mag}. By Taylor expansion around $Q^2 = 0$, the expectation value of the squared radii can be written as

$$< r_{el}^2 > = -6\left(\frac{dG_E(Q^2)}{dQ^2}\right)\Bigg|_{Q^2=0} \quad , \quad < r_{mag}^2 > = -6\,\frac{1}{\mu}\left(\frac{dG_M(Q^2)}{dQ^2}\right)\Bigg|_{Q^2=0}, \tag{1.10}$$

---

[2] The derivation can be found in any standard Field Theory textbook [2, 3].

[3] These are known as the *Sachs form factors.*

for the electric and magnetic distributions. The nucleon elastic form factors are described to first order by the dipole form[4]

$$G_D(Q^2) = \left(\frac{1}{1+\frac{Q^2}{0.71}}\right)^2, \tag{1.11}$$

and they are normalized by the magnetic moments where appropriate. The Sachs form factors are then expressed as

$$G_E^p(Q^2) = \frac{G_M^p(Q^2)}{\mu_p} = \frac{G_M^n(Q^2)}{\mu_n} = G_D(Q^2). \tag{1.12}$$

For the neutron electric form factor, the parametrization

$$\left(G_E^n(Q^2)\right)_{Galster} = -\frac{\mu_n \tau}{1+b\tau} G_D(Q^2), \tag{1.13}$$

known as the *Galster parametrization*[5], is frequently used. In terms of the Sachs form factors, the Rosenbluth cross section eq. (1.7) is given by

$$\left(\frac{d\sigma}{d\Omega}\right)_{Ros} = \left(\frac{d\sigma}{d\Omega}\right)_{Mott} \left(\frac{1}{1+\tau}\right) \left[G_E^2 + \frac{\tau}{\epsilon} G_M^2\right], \tag{1.14}$$

where ϵ is the transverse polarization of the virtual photon defined as

$$\epsilon \equiv \left(1 + 2(1+\tau)\tan^2\left(\frac{\theta}{2}\right)\right)^{-1}. \tag{1.15}$$

Finally, it is often useful to define the *reduced cross section* σ_R, by dividing out the Mott cross section and the factor $1/(1+\tau)$. This is given by

$$\sigma_R \equiv G_E^2 + \frac{\tau}{\epsilon} G_M^2. \tag{1.16}$$

---

[4] This ansatz is physically motivated: the dipole form is the Fourier transfrom of an exponentially decaying distribution.

[5] Galster et al. [9], extracted G_E^n from the structure function $A(Q^2)$ measured in unpolarized electron deuteron elastic scattering. The best fit was obtained with the Feshbach-Lomon potential and a value b = 5.3 for the fitting parameter.

1.1.2 Polarized Target

The case of a polarized target is more complex[6]. Considering the case in which the recoil electron polarization is not measured, the electron-nucleon elastic cross section can be expressed as [10]

$$\left(\frac{d\sigma}{d\Omega_e}\right) = c\Big(\rho_L f_L + \rho_T f_T + \rho_{LT} f_{LT} + \rho_{TT} f_{TT} + h\big(\rho'_{LT} f'_{LT} + \rho'_T f'_T\big)\Big). \quad (1.17)$$

Here, the $\rho^{(\prime)}_{ij}$ describe the density matrix of the virtual photon and depend only on the kinematics, while the $f^{(\prime)}_{ij}$ are the nucleon structure functions derived from the hadronic current operator and have simple forms in terms of the Sachs form factors:

$$\begin{cases} f_L = G_E^2 \quad , \quad f_T = 2\tau G_M^2 \\ f'_{LT} = -2\sqrt{2\tau}\, G_E G_M P_x \quad , \quad f'_T = -2\tau G_M^2 P_z \quad , \end{cases} \quad (1.18)$$

while f_{TT} and f_{LT} vanish. P_i denote the components of the target polarization. Equation (1.17) indicates that polarization effects in the cross section are a function of the coupling of beam and target polarization. In addition, reversing the x component of the target polarization produces an asymmetry in terms of the form factor ratio G_E/G_M.

The target polarization is often expressed in spherical coordinates by taking the $\hat{z}$-axis along $\vec{q}$, where the angles (θ^*, ϕ^*) determine the target-spin orientation with respect to the $\hat{z}$-axis. With these conventions, the beam-target asymmetry for electron-nucleon elastic scattering is given by

$$A_{\vec{e}\vec{N}} = -hP_t \frac{4\sqrt{2\tau}\,\rho'_{LT}\, G_E\, G_M\, sin\theta^*_d\, cos\phi^*_d + \rho'_T\, G_M^2\, cos\theta^*_d}{2\sqrt{2\tau}\,\rho_L\, G_E^2 + \rho_T\, G_M^2}. \quad (1.19)$$

The x and z components of the asymmetry are given by

$$A^x_{eN} = -\frac{4\sqrt{2\tau}\rho'_{LT}(\frac{G_E}{G_M})}{2\sqrt{2\tau}\rho_L(\frac{G_E}{G_M})^2 + \rho_T} \quad (1.20)$$

---

[6] The discussion in this section will focus on a summary of the main results. Extensive discussions can be found in [1, 5, 10].

and

$$A_{eN}^{z} = -\frac{\rho_T^{'}}{2\sqrt{2\tau}\rho_L(\frac{G_E}{G_M})^2 + \rho_T}, \tag{1.21}$$

where A_{eN}^{y} vanishes.

1.2 Electron Deuteron Scattering

1.2.1 Deuteron Properties

The importance of the deuteron properties for enhancing our understanding of fundamental nuclear physics cannot be overestimated. It is the simplest nuclear system, consisting of only a proton and a neutron, and thus provides a testing ground for any theory that seeks to understand nuclear structure and nucleon-nucleon interactions. In addition, its weak binding allows extraction of information on the structure of the nucleons themselves. This is especially significant in the case of the neutron, given the absence of stable, free neutrons in nature.

The non-relativistic deuteron wavefunction is a linear combination of the $^3S_1$ and $^3D_1$ components

$$\Psi = \frac{u(r)}{r} Y_{101}^{m}(\theta, \phi) + \frac{w(r)}{r} Y_{121}^{m}(\theta, \phi), \tag{1.22}$$

where $Y_{jls}^{m}(\theta, \phi)$ are spin-angular functions derived from the usual spherical harmonics[7]. The radial functions u(r) and w(r) correspond to the S and D state contributions with

$$P_S = \int_0^{\infty} u^2(r) dr \quad , \quad P_D = \int_0^{\infty} w^2(r) dr, \tag{1.24}$$

where P_S and P_D are the probabilities for S and D state, respectively.

This admixture of the S and D states results from a non-central term in the NN potential (tensor force) which has distinct implications for the deuteron structure. More

---

[7] The relation between the spin-angular $Y_{jls}^{m}(\theta, \phi)$ and the spherical harmonics is given by

$$Y_{jls}^{m}(\theta, \phi) = \sum_{m_l m_s} < j, m \,|\, l, m_l; s, m_s > Y_{lm}(\theta, \phi) \,|s, m_s > \tag{1.23}$$

where the spherical harmonics are the usual solutions of the angular part of the Laplacian.

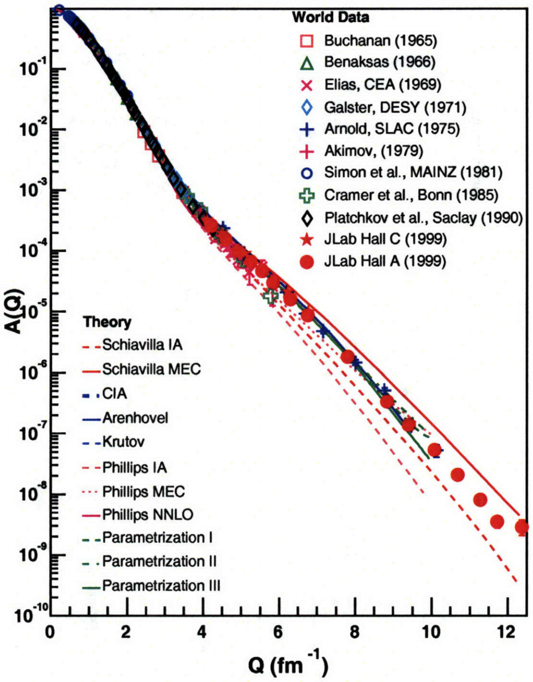

Figure 1-2: World data for the $A(Q^2)$ structure function from elastic electron deuteron scattering experiments along with parametrizations by Abbot [109] and various model predictions.

specifically, measurements of static properties such as the magnetic dipole and electric quadrupole moments establish stringent requirements for any model-theoretical approach to deuteron structure in particular and nuclear structure in general[8]. For example, the rms-radius is given by

$$r_{rms} = \sqrt{\frac{1}{4}\int_0^\infty \Big(u^2(r) + w^2(r)\Big) r^2 dr} \tag{1.25}$$

and depends entirely on the actual form of the radial wave functions while the quadrupole magnetic moment is expressed as

$$Q_d = \frac{1}{\sqrt{50}}\int_0^\infty w(r)\left(u(r) - \frac{w(r)}{\sqrt{8}}\right) r^2 dr. \tag{1.26}$$

Both have been measured experimentally with good precision. The rms-radius has

---

[8] A thorough review of current experimental and theoretical knowledge on the deuteron can be found in references [11, 12]

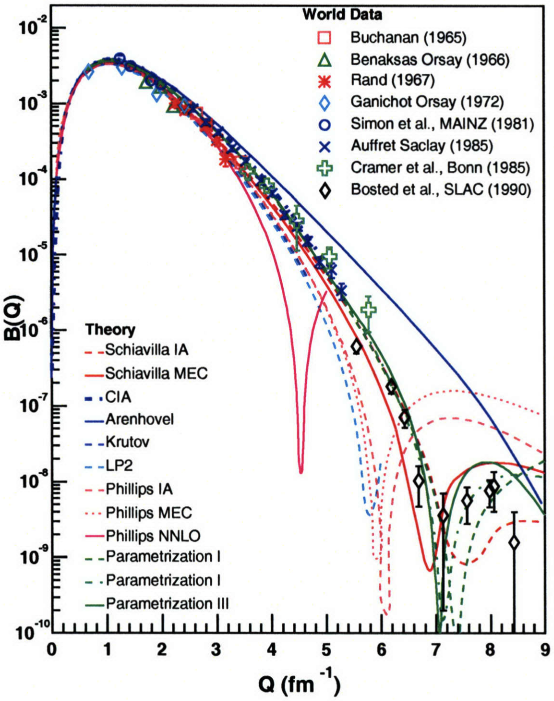

Figure 1-3: World data for the $B(Q^2)$ structure function from elastic electron deuteron scattering experiments along with parametrizations by Abbot [109] and various model predictions.

been measured to be $r_{rms} = 1.975\,fm$ and the quadrupole magnetic moment $Q_d = 0.2859\,fm^2$ [11].

1.2.2 Electron-Deuteron Elastic Scattering

The unpolarized differential cross section for electron-deuteron elastic scattering can be expressed as [13]

$$\left(\frac{d\sigma}{d\Omega}\right)_{Unpol} = \left(\frac{d\sigma}{d\Omega}\right)_{Mott} f_{rec}^{-1}\left[A(Q^2) + B(Q^2)\tan^2\left(\frac{\theta}{2}\right)\right], \qquad (1.27)$$

where the structure functions $A(Q^2)$ and $B(Q^2)$ are functions of the elastic electromagnetic form factors of the deuteron and are given by

$$A(Q^2) = G_C^2(Q^2) + \frac{8}{9}\tau^2 G_Q^2(Q^2) + \frac{2}{3}\tau G_M^2(Q^2)$$

$$B(Q^2) \;=\; \tau(1\,+\,\tau)\,G_M^2(Q^2). \tag{1.28}$$

The form factors are normalized to the charge, magnetic and quadrupole moments of the deuteron at $Q^2 = 0$ [12]:

$$G_C(0) \,=\, 1 \quad ,\; G_Q(0) \,=\, Q_d m_d^2 \quad ,\; G_M(0) \,=\mu_d 2m_d. \tag{1.29}$$

The available data on $A(Q^2)$ and $B(Q^2)$ are shown in figs. 1-2 and 1-3.

As evident in eq. (1.28), extraction of A and B from a Rosenbluth separation of unpolarized cross section measurements does not allow the separation of all three form factors. In fact, a polarization experiment is needed in order to separate $G_Q(Q^2)$ and $G_C(Q^2)$. Following the formalism of [11], the polarized cross section for elastic electron deuteron scattering with a longitudinally polarized beam[9]of helicity h and a polarized deuterium target can be expressed as

$$\begin{aligned}\frac{d\sigma}{d\Omega} \;=\; \left(\frac{d\sigma}{d\Omega}\right)_{Unpol} \Big[1 \,+\, \rho_{20}T_{20}(Q^2,\theta) \,+\, 2Re\rho_{21}T_{21}(Q^2,\theta) \,+ 2Re\rho_{22}T_{22}(Q^2,\theta) \\ + h\rho_{10}T_{10}^e(Q^2,\theta) \,+\, 2hRe\rho_{11}T_{11}^e(Q^2,\theta)\Big],\end{aligned} \tag{1.30}$$

where the ρ_{ij} are elements of a spherical tensor used to express the corresponding elements of the deuteron density matrix and the $T_{ij}^{(e)}$ are the tensor polarization observables. All tensor polarization observables can be expressed in terms of the electromagnetic form factors. The expression for T_{20} is given by

$$\begin{aligned}-\sqrt{2}\,f_{rec}\left[\left(\frac{d\sigma}{d\Omega}\right)_{Unpol}\Big/\left(\frac{d\sigma}{d\Omega}\right)_{Mott}\right] T_{20}(Q^2,\theta) \;=\; \Big(\frac{8}{3}\tau G_C(Q^2)G_Q(Q^2) \,+\, \frac{8}{9}\tau^2 G_Q^2(Q^2) \\ + \frac{1}{3}\tau\Big[1 \,+\, 2(1+\tau)\tan^2\left(\frac{\theta}{2}\right)\Big]G_M^2(Q^2)\Big) \quad .\end{aligned} \tag{1.31}$$

Both T_{22} and T_{11} are only functions of G_M and do not provide information on the other two form factors. Among the remaining observables, T_{21} and T_{10}^e are

---

[9] In this context, longitudinal and transverse refer to the direction of the electron spin with respect to its momentum direction.

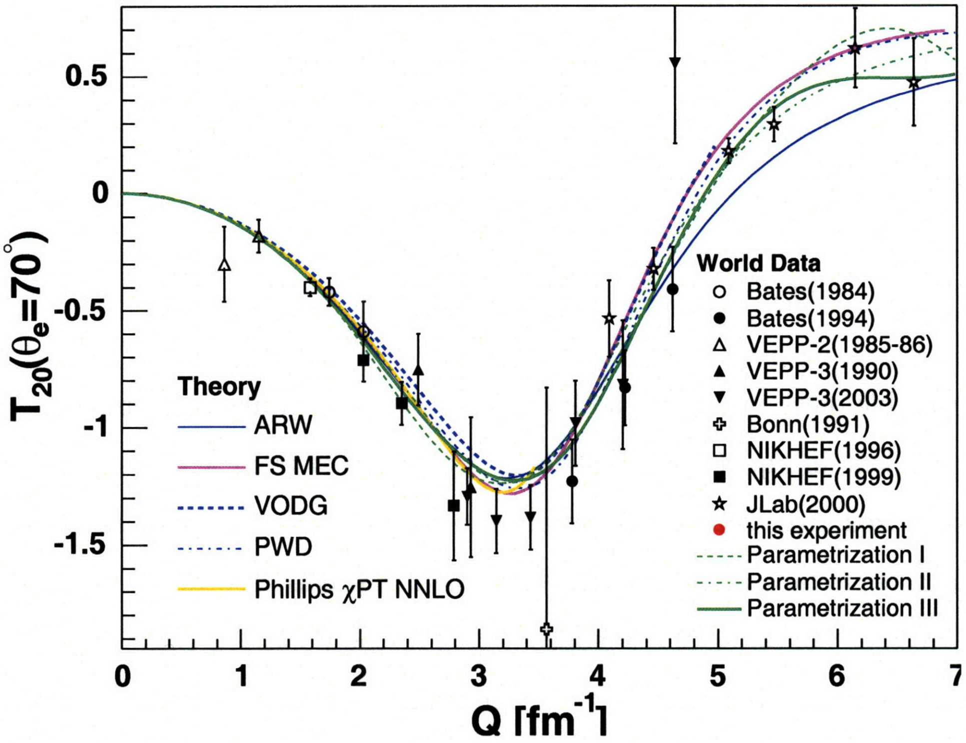

Figure 1-4: World data for the observable $T_{20}(Q^2, \theta)$ from elastic electron-deuteron scattering experiments.

proportional to G_M and therefore of smaller magnitude relative to T_{20}, which is the observable most frequently chosen. The world data on $A(Q^2)$ and $B(Q^2)$ are shown on figures 1-2 and 1-3, respectively. The data on $T_{20}(Q^2, \theta)$ are shown in figure 1-4.

1.2.3 Deuteron Electrodisintegration

While elastic scattering off the deuteron is kinematically constrained by the relation $Q^2 = 2\, M_d\, \omega$, where M_d is the mass of the deuteron, there is no such constraint in the electrodisintegration reaction. In the latter, the deuteron breaks into its constituent hadrons, a proton and a neutron. In general, the nucleons inside the deuteron have a non-zero momentum governed by Fermi motion. Denoting as E_d the energy of the detected nucleon and $\vec{p_d}$ its momentum, the corresponding energy and momentum of the undetected nucleon can be expressed as

$$\vec{p}_m = \vec{q} - \vec{p}_d \tag{1.32}$$

$$E_m = M_d + \omega - E_d, \tag{1.33}$$

where E_m and $\vec{p_m}$ are referred to as the missing energy and missing momentum.

A special case of the electrodisintegration reaction is *Quasi-elastic* scattering, which is defined as the reaction in which the exchanged virtual photon breaks up the nucleus without exciting any internal degrees of freedom. Within quasi-elastic kinematics, the *Plane Wave Impulse Approximation* (PWIA) refers to the case in which the virtual photon interacts with a single nucleon, while the remaining constituents of the nucleus essentially act as spectators. The struck nucleon separates from the rest of the nucleus and is emitted in the direction of the transferred momentum. The reaction is characterized by the relation $Q^2 = 2\,M_N\,\omega$, where M_N is the mass of the struck nucleon. The kinematics of the deuteron electrodisintegration reaction are shown in figure 1-5 whereas a schematic of the quasi-elastic reaction is shown in figure 1-6.

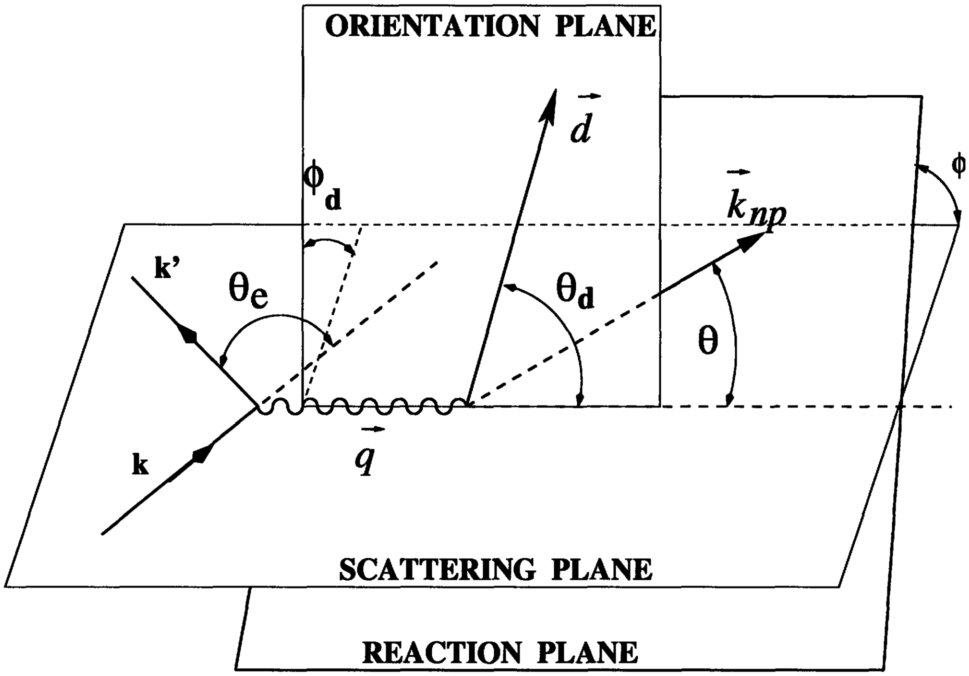

Figure 1-5: The geometry of the electrodisintegration reaction of the deuteron.

The differential cross section for the coincidence electrodisintegration reaction in the case of a longitudinally polarized beam of helicity h impacting a polarized deuterium target can be written as [10]

$$S = S_o\Big(1 + P_1^d A_d^V + P_2^d A_d^T + h\,(A_e + P_1^d A_{ed}^V + P_2^d A_{ed}^T)\Big), \tag{1.34}$$

where $P_1^d = \sqrt{\frac{3}{2}}P_z$ is the vector and $P_2^d = \sqrt{\frac{1}{2}}P_{zz}$ the tensor polarization. A_e is the beam analyzing power and A_d^V and A_d^T the vector and tensor target analyzing powers. Finally, A_{ed}^V and A_{ed}^T are both beam-target double polarization analyzing powers, the first vector and the second tensor. The expressions for the analyzing powers are given by[10]

$$A_e = \frac{c}{S_o}\rho_{LT}^{'} f_{LT}^{'} \sin\phi_{pn} \quad , \tag{1.35}$$

$$\begin{aligned} A_d^V = \frac{c}{S_o}\sum_{M=0}^{1}\Bigg[&\Big(\rho_L f_L^{1M} + \rho_T f_T^{1M} \\ &+ \rho_{LT} f_{LT}^{1M+} \cos\phi_{pn} + \rho_{TT} f_{TT}^{1M+} \cos 2\phi_{pn}\Big) \sin M\tilde{\phi} \\ &+ \Big(\rho_{LT} f_{LT}^{1M-} \sin\phi_{pn} + \rho_{TT} f_{TT}^{1M-}\, 2\sin\phi_{pn}\Big) \cos M\tilde{\phi}\Bigg] d_{M0}^1(\theta_d) \quad , \end{aligned} \tag{1.36}$$

$$\begin{aligned} A_d^T = \frac{c}{S_o}\sum_{M=0}^{2}\Bigg[&\Big(\rho_L f_L^{2M} + \rho_T f_T^{2M} \\ &+ \rho_{LT} f_{LT}^{2M+} \cos\phi_{pn} + \rho_{TT} f_{TT}^{2M+} \cos 2\phi_{pn}\Big) \cos M\tilde{\phi} \\ &- \Big(\rho_{LT} f_{LT}^{2M-} \sin\phi_{pn} + \rho_{TT} f_{TT}^{2M-}\, 2\sin\phi_{pn}\Big) \cos M\tilde{\phi}\Bigg] d_{M0}^2(\theta_d) \quad , \end{aligned} \tag{1.37}$$

$$\begin{aligned} A_{ed}^V = \frac{c}{S_o}\sum_{M=0}^{1}\Bigg[&\Big(\rho_T^{'} f_T^{'1M} + \rho_{LT}^{'} f_{LT}^{'1M-} \cos\phi_{pn}\Big) \cos M\tilde{\phi} \\ &- \rho_{LT}^{'} f_{LT}^{'1M+} \sin\phi_{pn} \sin M\tilde{\phi}\Bigg] d_{M0}^1(\theta_d) \quad , \end{aligned} \tag{1.38}$$

$$\begin{aligned} A_{ed}^T = \frac{c}{S_o}\sum_{M=0}^{2}\Bigg[&\Big(\rho_T^{'} f_T^{'2M} + \rho_{LT}^{'} f_{LT}^{'2M-} \cos\phi_{pn}\Big) \sin M\tilde{\phi} \\ &- \rho_{LT}^{'} f_{LT}^{'2M+} \sin\phi_{pn} \cos M\tilde{\phi}\Bigg] d_{M0}^2(\theta_d) \quad . \end{aligned} \tag{1.39}$$

---

[10] The relevant Wigner rotation matrices and the kinematic factors are listed in the Appendix.

The asymmetries are expressed in terms of the spherical components of the virtual photon density matrix $\rho_{ij}^{(')}$. The angle ϕ_{pn} is the neutron-proton azimuthal angle in the center-of-mass frame and $\tilde{\phi} \equiv \phi_{pn} - \phi_d$. The $f_{ij}^{(')(IM)(\pm)}$ are the various nuclear structure functions.

The expression for the inclusive cross section can be derived from that for the corresponding exclusive one by integrating over the solid angle $\Omega_{np}^{c.m.}$ of the recoiling nucleon in the center-of-mass frame[16]. All structure functions $f_{\lambda\mu}^{(')IM}$ with an explicit azimuthal (ϕ) dependence vanish while the remaining ones, denoted $F_{\lambda\mu}^{(')IM}$, are defined as

$$F_{\lambda\mu}^{(')IM} = \frac{1}{6}\int d\Omega\, f_{\lambda\mu}^{(')IM} = \frac{\pi}{3}\delta_{\lambda-\mu,M}\int d(\cos\theta)\, f_{\lambda\mu}^{(')IM}. \tag{1.40}$$

Using the explicit multiple expansion for the t-matrix, one arrives at:

$$\begin{aligned}\frac{d^2\sigma}{dk_2^{lab}\, d\Omega_e^{lab}} &= 6c\Big[\rho_L F_L + \rho_T F_T + P_1^d \rho_{LT} F_{LT}^{1-1}\sin\phi_d d_{-10}^2(\theta_d) \\ &+ P_2^d\Big(\big(\rho_L F_L^{20} + \rho_T F_T^{20}\big)d_{00}^2(\theta_d) + \rho_{LT}F_{LT}^{2-1}\cos\phi_d d_{-10}^2(\theta_d) + \rho_{TT}F_{TT}^{2-2}\cos 2\phi_d d_{-20}^2(\theta_d)\Big) \\ &+ hP_1^d\Big(\rho_T' F_T'^{10} d_{00}^1(\theta_d) + \rho_{LT}' F_{LT}'^{1-1}\cos\phi_d d_{-10}^1(\theta_d)\Big) + hP_2^d \rho_{LT}' F_{LT}'^{2-1}\sin\phi_d d_{-10}^2(\theta_d)\Big] \\ &\equiv \sigma(h, P_1^d, P_2^d)\,.\end{aligned} \tag{1.41}$$

The inclusive cross section above is a function of 10 transition form factors, two of which, F_{LT}^{1-1} and $F_{LT}'^{2-1}$ vanish below the pion threshold.

Alternatively, one can express the cross section in terms of various asymmetry terms, which are functions of the angles defining the target's angular orientation, as

$$\sigma(h, P_1^d, P_2^d) = \sigma_o\Big[1 + P_1^d \alpha_d^V + P_2^d \alpha_d^T + h\big(P_1^d \alpha_{ed}^V + P_2^d \alpha_{ed}^T\big)\Big], \tag{1.42}$$

where the unpolarized cross section σ_o depends on only two form factors

$$\sigma_o = 6c\big(\rho_L F_L + \rho_T F_T\big). \tag{1.43}$$

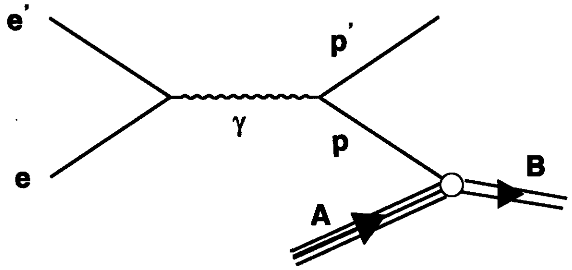

Figure 1-6: Quasi-elastic breakup of a nucleus A. In this special case of the electrodisintegration reaction, the exchanged virtual photon interacts with only a single nucleon within A, with initial momentum p and final momentum p'.

The relevance of the asymmetry term α_{ed}^{V} for the present work is discussed in subsequent chapters.

1.3 NN Interaction Potentials

Potential models aiming to describe the NN interaction have to predict the interaction's fundamental properties. The NN interaction is characterized by a short-range repulsive core, an intermediate-range attraction and a long-range part dominated by one-pion exchange [17].

The Bonn Potential:

The final version of the full Bonn Model was published in 1987 [18]. It provides a field-theoretical model for the NN interaction based on meson exchange below the pion production threshold. In this framework, the primary meson term contributing to the interaction is the one-boson exchange diagram (OBE). In addition, a number of irreducible multi-meson exchanges also contribute. The 2π exchange gives rise to an intermediate range attractive term while the $\pi\rho$ exchange is included to account for cancellations between the two channels. The model also incorporates higher order exchanges (3π, 4π etc) which are comparatively less important in the calculations. Only the Bonn Potential is discussed herein as it is the basis of the calculations by H.

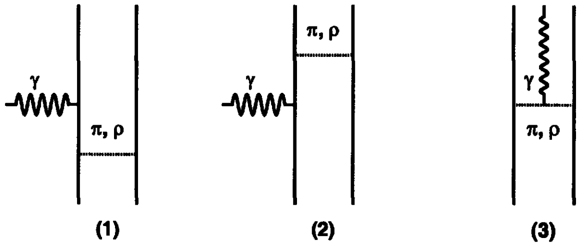

Figure 1-7: Typical examples of meson exchange currents. In (3), the virtual photon couples directly to the virtual meson.

Arenhövel et al. used exclusively in this work. Calculations of the differences between the Bonn and other potentials can be found in [19].

1.3.1 The Deuteron Model by Arenhövel

The calculations by Arenhövel are based on a Plane Wave Born Approximation (PWBA) using the Bonn potential. Different nucleon electromagnetic form factors (such as the dipole parametrization) can be chosen as input. In addition to this, *Final State Interactions* (FSI) and various reaction mechanisms are added. The FSI are the most significant of these corrections, in terms of the size of the effects. *Meson Exchange Currents* (MEC), *Isobar Configurations* (IC) and *Relativistic Corrections* (RC) are also incorporated.

MEC result due to coupling of the hadrons to the electromagnetic field. Their inclusion is most tractable in the case of NN potential models explicitly derived from the meson-exchange model [18]. In the case of potentials with a phenomenologically parametrized medium-range, the underlying physics is obscured and certain techniques need to be developed to account for MEC.

Isobar currents are the result of intermediate excitations of nucleon resonances and as such describe phenomenological, internal nucleon degrees of freedom [20]. They can be accounted for either by effective non-local two-body operators which parametrize certain excitations, or as explicit corrections to the wave-functions. The latter, termed Isobar Configurations, consist of one-to-one replacement of nucleons by isobars, with the corresponding change in the operators. Reference [21] employs the latter procedure[11]. Finally, three distinct sources of Relativistic Corrections may be identified as (1) the dynamics of the rest frame of the nucleus, (2) the Lorentz boost from the laboratory frame to the center-of-mass frame and (3) the explicit form of the current operators. An investigation of all three sources is carried out to leading order in [21], specifically for the p-space Bonn potentials.

Calculations of observables using the full calculation by Arenhövel et al. will be presented in subsequent sections.

1.4 Survey of Experimental Data on Proton Form Factors

1.4.1 Unpolarized Targets

For an unpolarized hydrogen target, eq. (1.14) is exactly valid in one photon exchange and may be used in a *Rosenbluth separation* analysis. The differential cross section can be re-expressed as eq. (1.16). Measuring the cross section at varying kinematics (scattered electron angle and beam energy) and fixed Q^2 and plotting the data versus a function of the $\tan^2(\theta/2)$ as derived from the scattered electron angle, information on both G_E^p and G_M^p can be extracted separately. However, Rosenbluth separation is sensitive to the relative size of the two terms in eq. (1.16). The magnetic term dominates at higher Q^2 rendering the extraction of G_E^p problematic in that region, while the contrary is true at the low Q^2 range.

1.4.2 Polarized Targets

Polarization experiments can be used mainly to extract the ratio of the proton form factors and investigate possible variations with Q^2. The advantage of the double-

---

[11] In fact, only the dominant $N\Delta(1232)$ is used, while the $NN(1440)$ and $\Delta\Delta$ are omitted. Static, regularized $\pi-$, $\rho-$exchange $NN - N\Delta$ transition potentials are used for the calculation of the $N\Delta$.

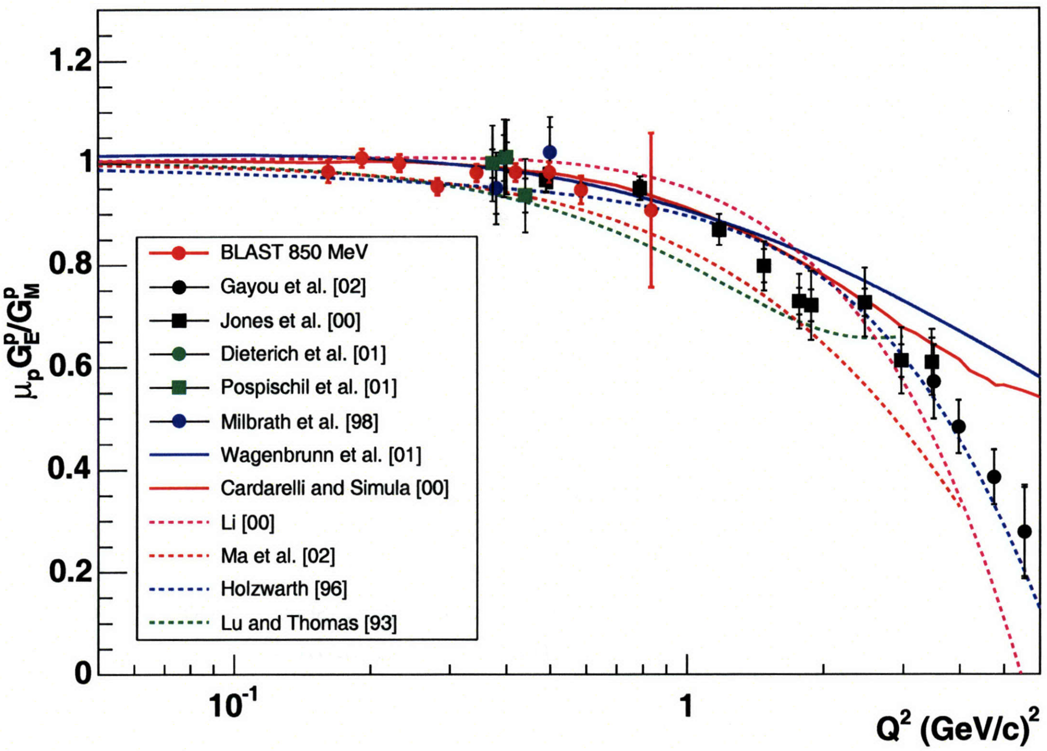

Figure 1-8: Data for the proton electromagnetic form factor ratio. Recent data obtained with the BLAST spectrometer are shown along with a collection of world data [22]. The BLAST experiment will be discussed in detail in Chapter 3.

polarization method stems from the fact that the spin degrees of freedom allow the extraction of the interference terms between the form factors without changing the beam energy. Two different methods have been employed in recent years: polarization transfer and beam-target asymmetry measurements.

In polarization transfer experiments, the form factor ratio can be extracted by detecting the recoil proton from the scattering reaction and measuring the ratio of its transverse over its longitudinal polarization

$$\frac{G_E^p}{G_M^p} = \frac{P_t}{P_l}\left(\frac{\epsilon + \epsilon^{'}}{2M_p}\tan\left(\frac{\theta}{2}\right)\right), \tag{1.44}$$

where P_l and P_t denote the longitudinal and transerse polarization, respectively and M_p denotes the mass of the proton. While low Q^2 data agreed with the unpolarized results, higher Q^2 experiments revealed a significant deviation of the form factor ratio from unity. This deviation is consistent with a faster decrease of G_E^p versus

G_M^p with increasing Q^2. Figure 1-8 shows a sample of the polarized data.

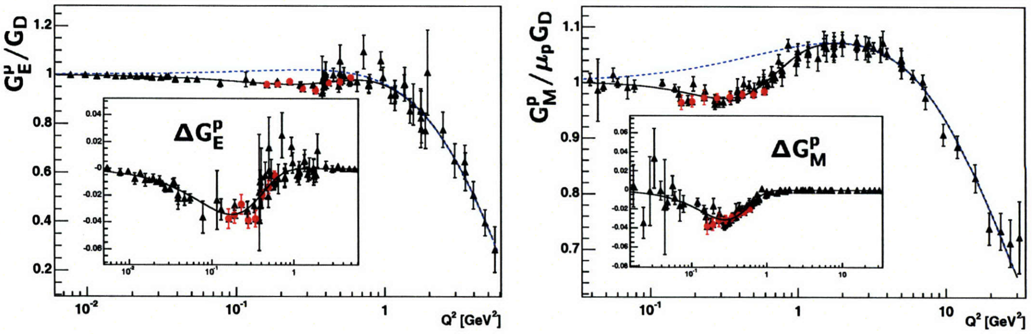

Figure 1-9: Data for the proton electromagnetic form factors [23]: (1) Left Panel: The data on the electric form factor normalized to the dipole form factor G_D. (2) Right Panel: The data for the proton magnetic form factor normalized to the dipole. BLAST data are shown in red on both panels. The inserts in both panels show the difference from the smooth part of the parametrization by Friedrich and Walcher [24] discussed later in this chapter.

A longitudinally polarized electron beam and a polarized hydrogen target allow for an alternative measurement of the ratio. A simultaneous measurement of the asymmetry in eq. (1.19) in two different target spin orientations with respect to $\vec{q}$, allows for a measurement of the form factor ratio independent of the product of the beam and target polarization and thus reduces systematic errors. This can be achieved by taking the super-ratio $\Re$ of the asymmetries measured at the two kinematics yet at the same Q^2 value

$$\Re = \frac{A_L}{A_R} = \frac{4\sqrt{2\tau}\rho'_{LT} G_E G_M \sin\theta_L^* \cos\phi_L^* + \rho'_T G_M^2 \cos\theta_L^*}{4\sqrt{2\tau}\rho'_{LT} G_E G_M \sin\theta_R^* \cos\phi_R^* + \rho'_T G_M^2 \cos\theta_R^*} \quad . \tag{1.45}$$

The asymmetry indeces L and R stand for the two kinematic settings. The BLAST experiment at the Bates Linear Accelerator Center takes advantage of the left-right symmetry of the BLAST detector to measure both the left and right asymmetries at the wide Q^2 range allowed by the spectrometer's large acceptance. The results of the BLAST experiment are shown in figure 1-8 alongside a sample of the world's data from polarization experiments. More details on the BLAST experiment and on how the analysis discussed in this thesis exploits the super-ratio technique can be found in subsequent chapters.

1.5 Survey of Experimental Data on Neutron Form Factors

The absence of free neutron targets in nature renders the extraction of the neutron form factors more difficult and more prone to theoretical uncertainties, depending on the experimental technique used. In addition, as a consequence of the charge neutrality of the neutron, the magnetic form factor dominates over the electric.

1.5.1 Extraction of $\mathbf{G_E^n}$

The $A(Q^2)$ structure function (eq. (1.28)) as measured from unpolarized elastic electron deuteron scattering allows the determination of G_E^n. However, the extraction depends on the theoretical model used for the deuteron structure and the accuracy of the data for $A(Q^2)$.

Quasi-elastic scattering of longitudinally polarized electrons from vector polarized deuterium provides another means to determine G_E^n. Both an asymmetry measurement from the ${}^2\vec{H}(\vec{e},e'n)$ reaction and the recoil polarization method with the ${}^2H(\vec{e},e'\vec{n})$ reaction have been used.

The advantage of the ${}^2H(\vec{e},e'\vec{n})$ reaction lies in the fact that close to the quasi-elastic ridge the FSI, MEC and IC reaction mechanisms are least significant, thus limiting the dependence of the analysis on the deuteron structure. Recoil polarimetry with a longitudinally polarized electron beam and a liquid deuteron target was pioneered at the Bates Linear Accelerator Center [25] to obtain the ratio G_E^n/G_M^n by measuring the ratio of the transverse over the longitudinal polarization component of the recoiling neutron

$$\frac{P_x^n}{P_z^n} = \frac{-\sqrt{2f}}{\sqrt{\tau(1+\epsilon)}}\frac{G_E^n}{G_M^n} \tag{1.46}$$

at $Q^2 = 0.255$ (GeV/c)^2. Ostrick et al. [112] performed the same measurement using the Mainz Microtron MAMI at $Q^2 = 0.34$ (GeV/c)^2. All double polarization experiments are limited to measuring the ratio of the neutron form factors. Knowledge of G_M^n is therefore essential in the final determination of G_E^n.

The asymmetry technique involves measuring the beam-target vector asymmetry A_{ed}^V by detecting scattered neutrons in coincidence with scattered electrons. The sensitivity to G_E^n is maximized at $\theta^* = 90°$ and $\phi^* = 0°$ which occurs when the momentum transfer vector $\vec{q}$ is perpendicular to the target spin angle. In the case of quasi-elastic scattering off the neutron, the A_{ed}^V is given by [26]

$$A_{ed}^V = -\frac{2\sqrt{2\tau}\rho_{LT}^{'} G_E^n G_M^n}{\rho_L G_E^{n\,2} + 2\tau\rho_T G_M^{n\,2}}, \tag{1.47}$$

which indicates how the form factor ratio can be extracted. This extraction was first performed at NIKHEF [27] and most recently at the Bates Linear Accelerator Center with the BLAST detector (more details can be found in reference [26]). Both experiments used an atomic beam source as an internal target. Finally, Zhu et al. [28] extracted G_E^n using the same technique yet from a polarized deuterated ammonia ($^{15}ND_3$) external target. The world data on G_E^n is shown in figure 1-21. In addition to deuterium targets, polarized ^3He has also been used as an effective polarized neutron target [29, 30] to extract G_E^n.

1.5.2 $\mathbf{G_M^n}$ Extraction with Unpolarized Targets

In addressing the absence of free neutron targets, Hofstadter [31] first suggested the possibility of using deuterium targets to extract information on the structure of the neutron. In a survey of the potential applications of electron scattering in exploring nuclear structure, the author pointed out that due to the weak binding of the deuteron, the proton and neutron therein may be considered as effective free particles. Inelastically scattered electrons off of deuterium can then be compared with scattering off hydrogen to extract the neutron's scattering cross section and therefore its size. Such experiments were first performed in the early 1960s, utilizing unpolarized electron beams and unpolarized deuterium targets. These measurements involved either an inclusive cross section of the quasi-elastic reaction or a ratio of cross sections.

Inclusive measurements:

Beginning in the 1960s, several experiments were performed in order to measure G_M^n. One such method was a cross section measurement of ${}^2H(e, e')$, which relied on the PWIA approximation in quasi-elastic kinematics. The resulting cross section was then interpreted as an incoherent sum of the individual electron-nucleon contributions from the proton and the neutron

$$\sigma_{d(e,e')} = \sigma_{ep} + \sigma_{en}. \tag{1.48}$$

However, this analysis is plagued by theoretical uncertainties associated with the limitations of the PWIA. While in principle the approximation is sufficient for the quasi-elastic peak, additional corrections due to MEC, IC and FSI are needed away from the peak. In fact, Fermi smearing inside the deuteron ambiguates the event selection, rendering the corrections significant. In addition, a model-dependent subtraction of the proton contributions from the cross section further adds to the theoretical uncertainties. Finally, cross section measurements require absolute knowledge of detection efficiencies for the relevant scattered particles, in this case the inclusive electrons.

Albrecht et al. [32] measured the ratio of quasi-elastic ${}^2H(e, e')$ to elastic $H(e, e')$, which required good knowledge of the cross sections. Rock et al. [33] used an electron beam incident on deuterium and hydrogen targets at SLAC. They measured both the electron-deuteron and electron-proton cross sections in elastic, quasi-elastic and inelastic kinematics. They assumed that in order to extract the quasi-elastic scattering cross section off the neutron, the quasi-elastic electron-proton part had to be subtracted. In addition, smeared inelastic electron-proton and electron-neutron contributions diluted the quasi-elastic data and had to be accounted as well. The proton cross sections were established using a hydrogen target and the measured deuterium spectrum was expressed as

$$\sigma(\Omega, E') = R_{el}\,(\sigma_{p,el})_{sm} + R_{in}(\sigma_{p,in})_{sm}\ , \tag{1.49}$$

where the proportionality constants $R = \sigma_d/\sigma_p = (\sigma_n + \sigma_n)/\sigma_p$ took into account the Fermi smearing and the width of the inelastic region and were determined by least-squares fits to the data. G_M^n was finally extracted by subtracting all other contributions to the quasi-elastic peak and assuming $G_E^n = 0$.

Arnold et al. [34] used the Nuclear Physics Injector at SLAC with electron beams at four different energy settings and liquid deuterium targets. Scattered electrons at 180° were detected in multi-wire proportion chambers and used to establish the inclusive ${}^2H\,(e, e')$ cross section which was in good agreement with non-relativistic theoretical models, which incorporated FSI and MEC corrections to PWIA. They extracted G_M^n using a procedure similar to that described by Rock et al. [33].

Lung et al. [35] used a similar method to measure the inclusive quasi-elastic cross section ${}^2H\,(e, e')$ at various kinematics. The reduced cross section (eq. 1.16), can be expressed as

$$\sigma_R \equiv R_T + f R_L, \tag{1.50}$$

in terms of the transverse (R_T) and the longitudinal (R_L) nuclear response functions, was used. Rosenbluth separation using linear fits to σ_R were then used to obtain the response functions. A non-relativistic PWIA model with the Paris wavefunction was used to fit R_T and R_L and then subtract the proton form factors from the fit constants.

Exclusive measurements:

To avoid the theoretical uncertainties associated with the proton subtraction in inclusive methods, other experiments measured the neutron in coincidence. Stein et al. [37] used the internal electron beam of the Cornell electron synchrotron and a liquid deuterium target to establish the ratio σ_n/σ_p in quasi-elastic kinematics. The efficiency of the plastic scintillation counters used for neutron detection was measured with neutrons from the reaction $\gamma + p \rightarrow \pi^+ + n$. To extract the neutron form factors, they assumed that the ratio of cross sections as measured in their experiment was essentially equal to the ratio from free electron-nucleon scattering.

Hanson et al. [36] used an electron beam from the Cambridge Electron Accelerator and a liquid deuterium target. A scintillation counter telescope was used for electron detection and a proton scintillation counter with 450 msr solid angle was used for proton detection. The ratio of proton-in-coincidence events to those without a proton in coincidence was then related to the ratio σ_n/σ_p. Their analysis also took into account significant FSI corrections. This method requires good knowledge of deuteron structure as well as accurate background subtraction to account for all the non-detected protons.

Another experiment to extract G_M^n from the quasi-elastic $^2H(e,e'n)p$ reaction was performed at the Bates Linear Accelerator Center [38]. Markowitz et al. used the One-Hundred-Inch Proton Spectrometer (OHIPS) to detect electrons scattered off a liquid deuterium target in quasi-elastic kinematics. Mineral oil scintillators were used for neutron detection at a fixed neutron angle of 57°. Absolute calibration of the neutron detection efficiency was again performed with the associated particle technique using $^2H(\gamma,pn)$ in situ. The value of the form factor was extracted by comparing the measured cross section to a theoretical result from Arenhövel [10] which used the Paris potential and included the necessary MEC, IC and FSI. The results of this experiment showed an enhancement of G_M^n with respect to the dipole at low Q^2.

Bruins et al. [39], used quasi-elastic scattering off unpolarized deuterium to measure the ratio of cross sections for the exclusive reactions $^2H\left(e,e^{'}n\right)$ and $^2H\left(e,e^{'}p\right)$ at ELSA. In this measurement, nuclear effects and model uncertainties were minimal. It did, however, require absolute neutron efficiency calibration, performed here with the $^1H(\gamma,\pi^+)n$ reaction in situ. G_M^n was extracted after taking into account proton yield losses due to nuclear reactions, multiple scattering and edge effects. Nuclear effects, the value of G_E^n and finally the known electron-proton cross sections were also accounted for in the analysis. Kubon et al. [40] and Anklin et al. [41, 42] used the same overall method while opting for an external calibration of the neutron detection efficiency. The neutron detection efficiency for Kubon et al. was measured with a tagged high-intensity neutron beam incident on a liquid ^2H-target. Reconstructing the trajectory of the recoil protons, allowed redundant determination of the kinemat-

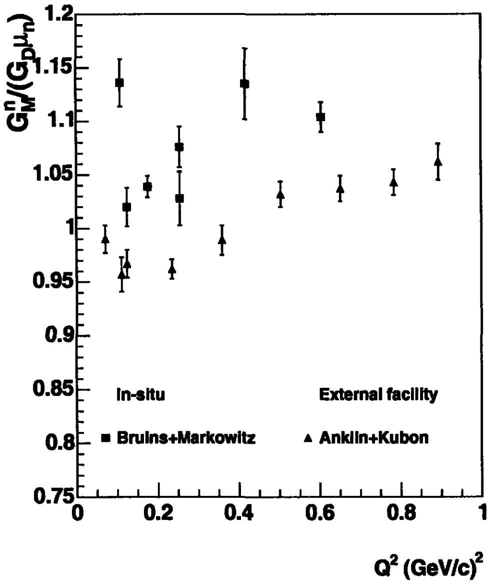

Figure 1-10: Differences in the data between experiments that require absolute neutron detection efficiency calibration. Plotted here are data from [38, 39] for *in-situ* and [41, 42, 40] for external facility calibration. Jourdan et al. [43] identified a source of error in the *in-situ* neutron detection calibration that may have led to an underestimate of the neutron detection efficiency.

ics of the system [40]. Anklin et al. [41, 42] also used the same technique. The external calibrations were all performed at PSI. Jourdan et al [43] identified an uncertainty of the *in-situ* calibration method employed by Bruins et al. [39]. Their argument was that the calibration neglected a significant contribution of electro-produced π^+ which do not lead to a neutron in the direction of the detector. Since an $^1H(\gamma, \pi^+)n$ event was only accepted when the calculated neutron intercepted the central area of the neutron scintillator, this led to an underestimate of the neutron detection efficiency and therefore of an overestimate of the electron-neutron cross section.

1.5.3 $\mathrm{G_M^n}$ Extraction with Polarized Targets

The first experiment to use a polarized target for the extraction of G_M^n was conducted at the Bates Linear Accelerator Center in the mid-1990s [44, 45]. A 370 MeV longitudinally polarized electron beam was used in conjunction with a polarized ^3He target consisting of a glass pumping cell and a copper target cell. Polarization was achieved via the metastability exchange optical pumping technique. The inclusive transverse asymmetry $A_{T'}$ was measured in quasi-elastic kinematics by selecting $\theta^* = 0°$. $A_{T'}$ was averaged over the experimental ω acceptance for a single Q^2 bin of $Q^2 = 0.19$ (GeV/c)^2. The form factor was then extracted by fitting the data to theoretical calculations of ^3He structure. The inherent advantage of this method lies in the fact that in the dominant spatially symmetric S state of ^3He, the spins of the two protons pair off so that the nuclear spin is effectively carried solely by the neutron [49]. The most significant theoretical uncertainy for the extraction was attributed to uncertainties due to the proton form factors[12] as well as model-dependence contributions. Note that a PWIA calculation with spin-dependent spectral function was used without corrections for FSI and MEC. These corrections were shown to be negligible [50].

The same method was used in high-statistics experiments performed at JLab [46, 47]. Six kinematic points were measured in the range $Q^2 = 0.1\text{-}0.6$ (GeV/c)^2. To extract G_M^n at the two lowest Q^2 bins, a full Faddeev calculation including FSI was used. The systematic uncertainties associated with these measurements stem from neglecting MEC and relativistic corrections as well as uncertainties in the proton form factors [46]. The final four kinematic points were compared to a relativistic PWIA calculation while neglecting both MEC and FSI corrections, which were shown to dominate the measurement's theoretical uncertainty.

The world's data on G_M^n are shown in figure 1-22 at the end of this chapter.

1.6 $\mathbf{G_M^n}$ Extraction With $\mathbf{^2\vec{H}(\vec{e}, e)np}$

An inclusive measurement of the electrodisintegration reaction does not allow the separation between struck protons and neutrons. Nevertheless, it is expected that the beam-target vector asymmetry α_{ed}^V in eq. (1.42) will exhibit significant sensitivity to the magnetic form factor G_M^n of the neutron.

As a pedagogical tool in understanding the underlying reasons for this sensitivity,

---

[12] Relative to the proton form factor uncertainty, the knowledge of the neutron electric form factor G_E^n is significantly worse. However, the overall contribution of the latter to the measurement is small due to its much smaller value.

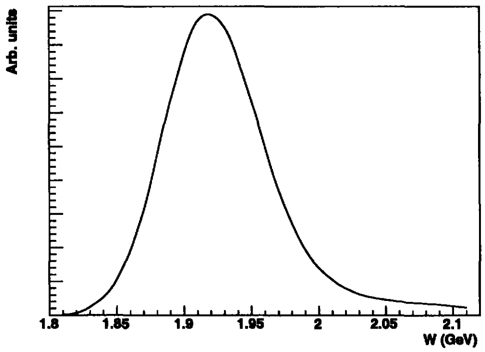

Figure 1-11: Monte Carlo simulation of the invariant mass spectrum for the BLAST acceptance at $Q^2 = 0.135\ (\mathrm{GeV/c})^2$. The spectrum is sharply peaked around the quasi-elastic ridge. The spread of the peak is due to the Fermi momentum of the two nucleons inside the deuteron. The simulation was performed for the ${}^2\vec{H}\,(\vec{e}, e')$ reaction.

the ideal case of the PWIA quasi-free reaction will be considered first. Figure 1-11 shows the invariant mass spectrum for the electrodisintegration reaction with the characteristic quasi-free peak shape. Close to the peak, at missing momentum $p_m = 0$, the MEC, FSI and IC corrections are small and the inclusive asymmetry can be expressed as an incoherent sum of A_n and A_p, the free neutron and free proton asymmetries weighted by their respective cross sections

$$\alpha = \frac{\sigma_n A_n + \sigma_p A_p}{\sigma_n + \sigma_p} \quad , \tag{1.51}$$

where the free nucleon asymmetries are given by eq. (1.19)

$$A_{\vec{e}\vec{N}} = -hP_t \frac{4\sqrt{2\tau}\rho'_{LT} G_E G_M sin\theta^* cos\phi^* + \rho'_T G_M^2 cos\theta^*}{2\sqrt{2\tau}\rho_L G_E^2 + \rho_T G_M^2}. \tag{1.52}$$

In perpendicular kinematics ($\theta^* = 90°$), the second term in equation (1.52) vanishes and the inclusive asymmetry (1.51) can then be approximated by

$$\alpha_\perp \approx \frac{c_1 G_E^p G_M^p + c_2 G_E^n G_M^n}{c_3 {G_E^n}^2 + c_4 {G_E^p}^2 + c_5 {G_M^n}^2 + c_6 {G_M^p}^2} \approx \frac{a}{b + c\left(1 + (G_M^n/G_M^p)^2\right)}, \tag{1.53}$$

where a, b and c are constant terms. Here, the numerator is given by the sum of the

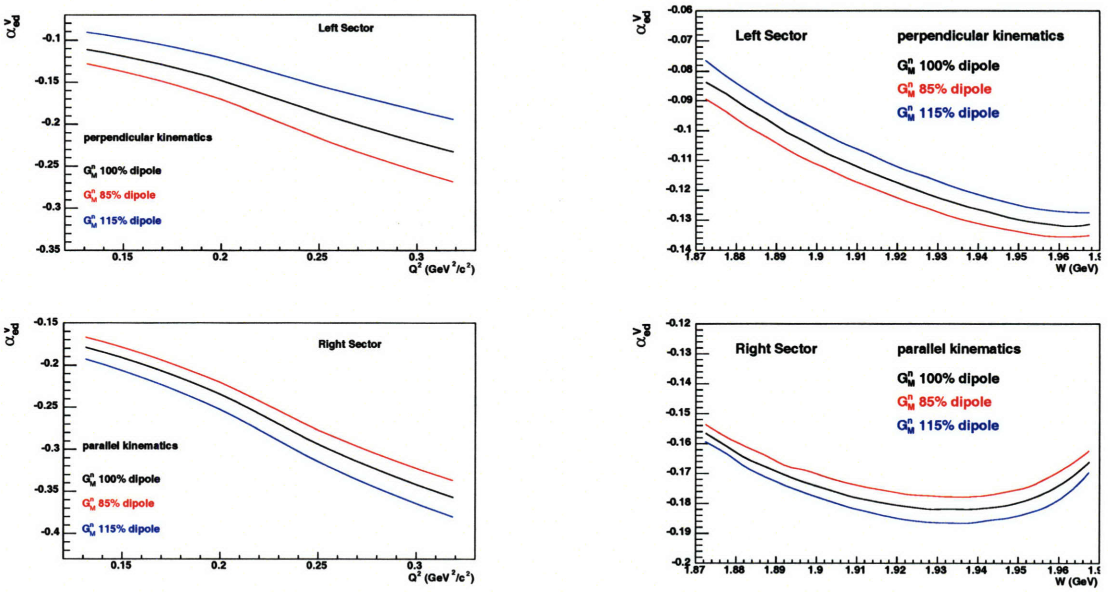

Figure 1-12: The left panels show the sensitivity of the asymmetry to G_M^n in perpendicular (top) and parallel (bottom) kinematics. The asymmetries are plotted here versus Q^2. Alternatively, the right two panels show the variation of the asymmetry in terms of the invariant mass and at a fixed $Q^2 = 0.135$ (GeV/c)^2. The simulations were performed for the BLAST acceptance.

products of electric and magnetic form factors for both the proton and the neutron. However, this can be further approximated by only the proton form factor product due to the small magnitude of G_E^n, which makes the term multiplied by the c2 constant negligible. The denominator can then be expressed as a constant term plus a term proportional to the square of G_M^n. Thus, the dependence of the asymmetry on G_M^n lies solely in the denominator, which indicates that increasing the value of G_M^n reduces the magnitude of the asymmetry itself.

In parallel kinematics, where $\theta^* = 0°$, this picture is slightly different. At $0°$, the sine term vanishes and the asymmetry is given by

$$\alpha_{\parallel} \approx \frac{\left(1 + (G_M^n/G_M^p)^2\right)}{b + c\left(1 + (G_M^n/G_M^p)^2\right)}, \tag{1.54}$$

where b and c are again constants. In this case, due to the relative magnitudes of the constants b and c, the numerator is in fact more sensitive to variations in G_M^n such that the asymmetry increases in magnitude with an increase in the form factor.

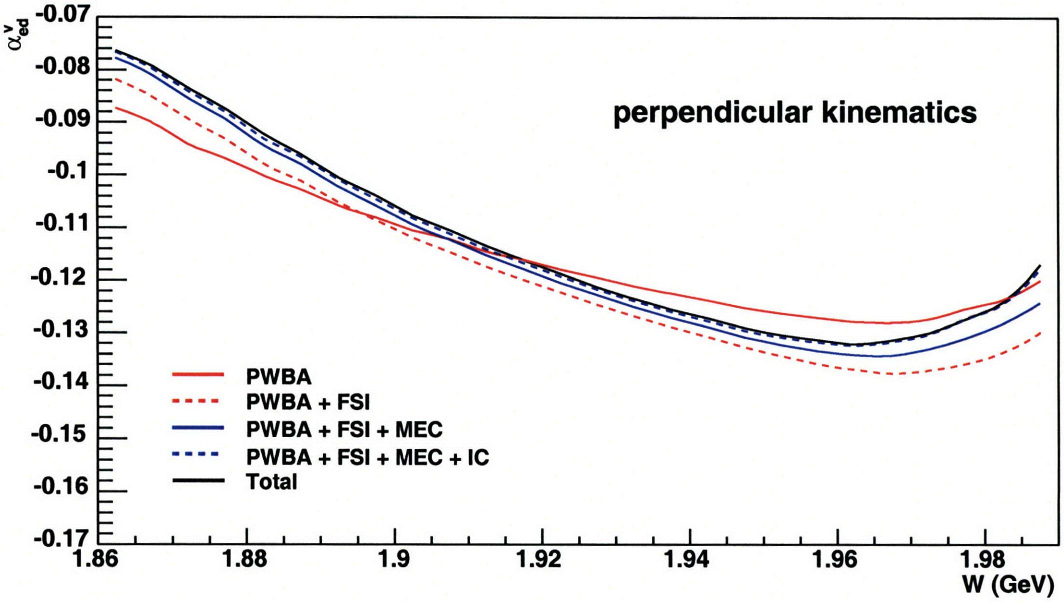

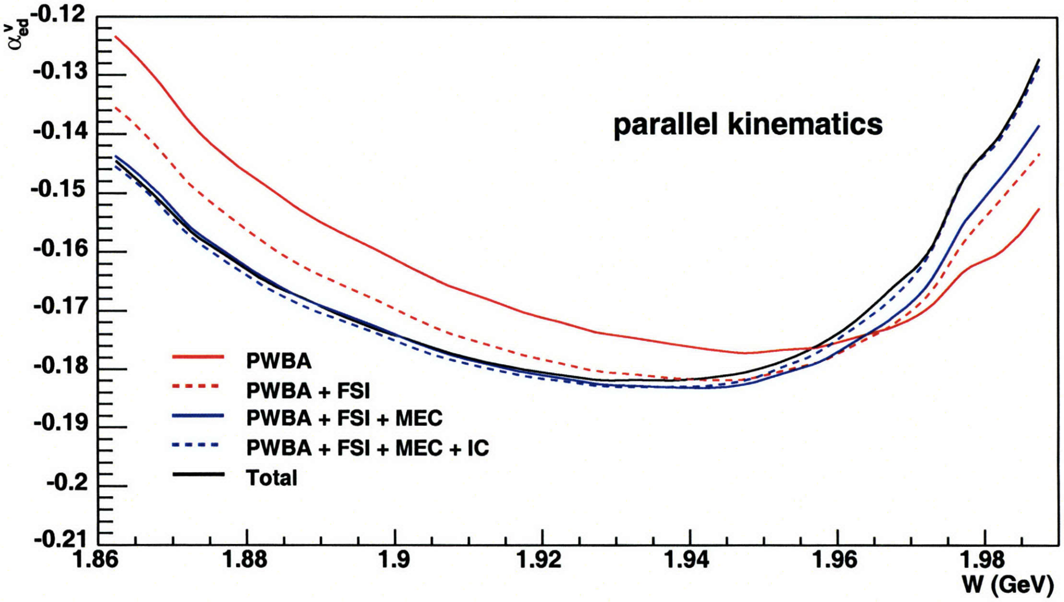

Figure 1-13: Asymmetry in perpendicular (top) and parallel (bottom) kinematics versus the invariant mass. The PWBA represents the simplest calculation of the scattering process (solid red). The solid blue line shows the calculation of PWBA+MEC whereas the dashed blue line adds the IC contributions. The black line is the calculation with the total Arenhövel model. The quasi-elastic ridge is located at approximately 1.91 GeV in invariant mass.

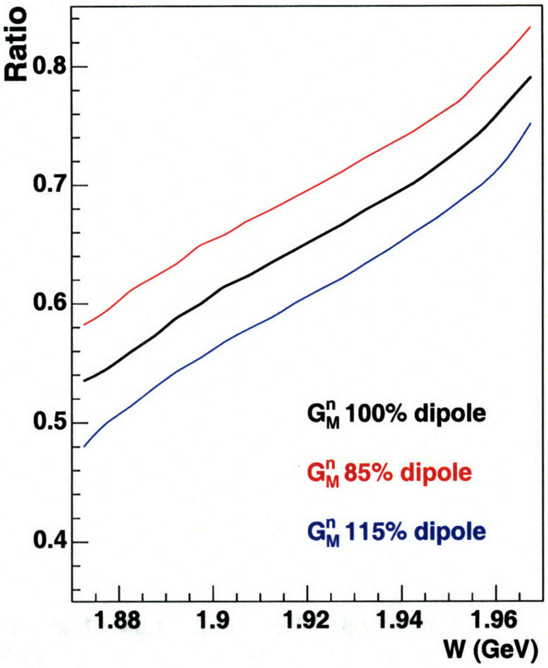

Figure 1-14: The ratio $\Re$ of the asymmetries in perpendicular and transverse kinematics enhances the sensitivity to G_M^n. Shown here is the ratio for three values of G_M^n as a percentage of the standard dipole form factor. Increasing G_M^n decreases the ratio. The top (red) line shows the calculation for 85% dipole, the middle (black) for 100% and the bottom (blue) for 115%.

Calculations performed with the full Arenhövel model verify these considerations. The two left panels of figure 1-12 show the sensitivity of the asymmetry to variations in G_M^n by $\pm 15\%$ with respect to the dipole form factor, versus Q^2. The top panel shows the asymmetry in perpendicular kinematics and the bottom in parallel. A fit of the data to the different curves yields the extracted value of G_M^n, assuming the proton form factors are known with good precision. At θ^* different from 0° and 90°, the asymmetry will combine both terms (eq. (1.53) and (1.54)).

The quasi-elastic selection amounts to a limited range in invariant mass. Alternatively, the entire W spectrum can be used to extract the asymmetries. This method does not only allow more statistics but it is also more robust as it eliminates the dependence on the exact range of the cuts around the peak. The two right panels of figure 1-12 show the asymmetry versus the invariant mass for a fixed $Q^2 = 0.135$ $(\text{GeV/c})^2$. Expanding the range of the invariant mass used in the analysis well beyond the quasi-elastic ridge, renders the ratio of the asymmetries more sensitive to

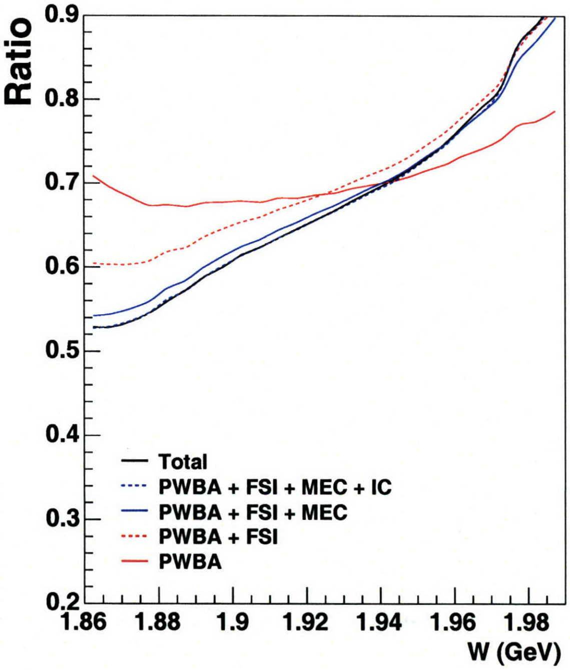

Figure 1-15: The FSI and reaction mechanism corrections for the ratio $\Re$ versus the invariant mass. The PWBA represents the simplest calculation of the scattering process (solid red). The solid blue line shows the calculation of PWBA+MEC whereas the dashed blue line adds the IC contributions. The black line is the calculation with the total Arenhövel model. The quasi-elastic ridge is located at approximately 1.91 GeV in invariant mass.

the various reaction mechanisms. Figure 1-13 shows the effects of the reaction mechanisms as a function of the invariant mass. PWBA (solid red) denotes the Born Approximation, a single-photon exchange reaction with the struck nucleon inside the nucleus. The PWBA should be a valid approximation at the exact location of the quasi-elastic peak. However, the calculations show this to be true only in perpendicular kinematics whereas there are significant deviations from PWBA in parallel. In both cases, FSI corrections appear to be the most important contribution through out the W range.

As eqs. (1.53) and (1.54) indicate, the asymmetry changes have different sign when varying G_M^n in the respective perpendicular and parallel kinematics. In order to take advantage of this fact, the ratio of the two can be used to extract G_M^n instead. Figure 1-14 shows the ratio of perpendicular over parallel asymmetries. The sensitivity to the magnetic form factor is indeed enhanced. The super ratio $\Re$ can be approximated in the PWIA picture by

$$\Re \approx \frac{\alpha_\perp}{\alpha_\parallel} \approx \frac{c\,\frac{G_E^p}{G_M^p}}{1+\left(\frac{G_M^n}{G_M^p}\right)^2}, \tag{1.55}$$

where c is a constant term. Equation (1.55) above shows that the ratio decreases with increasing G_M^n, a result supported by the actual calculations. G_M^n enters here squared, which explains the enhancement in sensitivity.

The ratio measurement necessitates good knowledge of possible left-right differences in the detector. When the left-right equivalence is established, the systematic errors are reduced due to cancellations. For example, the product of the beam and target polarization, which is necessary to compare the raw asymmetries to the calculations, cancels out. In addition, the analysis is less susceptible to experimental backgrounds and possible shifts in the spectra. More details on analysis procedures and systematics can be found in Chapter 4.

1.7 Survey of Theoretical Calculations

The electromagnetic form factors of the nucleons are fundamental quantities that reflect their internal structure and as such can be used as tests of any model or theory which involves sub-nucleonic degrees of freedom. They can also be used to investigate the NN interaction and nuclear structure. The nucleon form factors are important in experiments measuring the nucleon strangeness form factor and the investigations of the nucleon spin problem, namely how the spin is divided among the quarks and gluons.

1.7.1 The Cloudy Bag Model

The MIT bag model [51] was introduced in 1974 as a relativistically invariant description of hadronic structure. A constant, positive energy parameter B was introduced in a space allowing hadronic fields, thus defining a "bag" of finite dimensions. Fol-

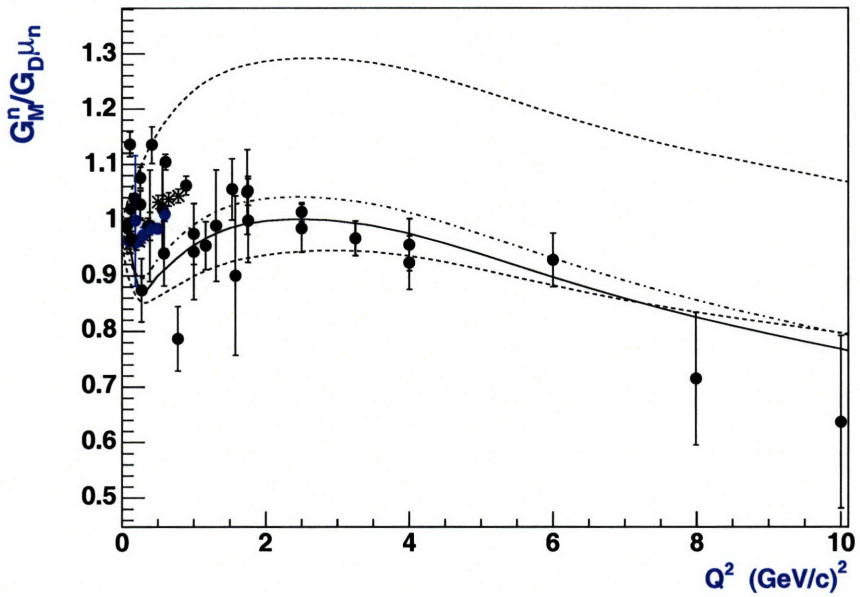

Figure 1-16: Various model calculations by Miller [53] for different fit parameter sets. The pion cloud contributions can be seen in the two dashed curves, one without pions (top) and one with (bottom). At low-Q^2 the model predicts a dip below the dipole for the form factor. Data taken from reference [46, 47, 35, 40, 33, 44].

lowing variational calculus methods on the surface of the bag, the field equations and relevant boundary conditions were derived. Quarks and gluons were identified as the fields contained inside the bag, which in turn enforces their confinement. Despite its early successes in describing the data, the model did not incorporate chiral symmetry. This difficulty was overcome by introducing pionic fields in the bag Lagrangian [52], thus describing the nucleon as a bag including the three constituent quarks and surrounded by a pion cloud.

Miller [53] used a *Cloudy bag model in light-front dynamics (LFCBM)* which incorporated chiral symmetry to calculate the effects of the pion cloud around a bare nucleon on the nucleon electromagnetic form factors. The relevant Feynman diagrams for these processes were calculated using photon-bare nucleon as well as relativistic pion-nucleon form factors. Fit parameters were selected to optimize agreement with the nucleon magnetic moments as well as several measured values of the form factors. The agreement with the data for G_M^n is good over a broad range of Q^2 values, with the exception of the low Q^2 region where the rapid fall-off of the pion cloud contribution leads to an underestimate with respect to the data. Ignoring the pion cloud produces significantly different results and the model ceases to agree with the data (figure 1-16).

1.7.2 The Skyrme / Soliton Model

In Skyrme models, baryons originate from soliton solutions to an effective meson theory characterized by a Lagrangian constructed out of pion fields [54]. Skyrme [55], based on his previous work [56, 57], expressed fundamental field quantities, relevant currents and conservation laws in terms of angular (rather than linear) variables. The periodicity of these variables introduces a multi-value system with different "sheets", the crossing of which produces singularities (sources). The periodicity was also responsible for the conservation of the number of these sources, which was identified with the "baryon number". Traveling waves were identified with pions. A calculation in the early 1980s [58, 59] of certain static properties of the nucleon using the model, encouraged further research in the area in order to expand the original Lagrangian with the addition of new terms designed to improve its predictive power for non-zero momentum transfers. An initial attempt by Braaten et al. [60] arrived at form factors for both proton and neutron that agreed with the dipole parametrizations in shape but differed somewhat in the overall normalization.

Holzwarth [61] used the standard skyrmion as an extended object with the addition of partial coupling to vector mesons and relativistic recoil corrections in the mid 1990s. The results showed agreement with G_M^p for Q^2 up to 30 (GeV/c)^2. However, the same model predicted a zero for G_E^p at Q^2 around 10 (GeV/c)^2 (not supported by the data at the time). In addition, the calculation used a higher neutron charge radius than the experimental measurement, resulting in a G_E^n higher than the Galster parametrization. At a later time, Holzwarth [61], prompted by new data, reexamined the calculation with the inclusion of explicit vector meson contributions in the Lagrangian. Previously, the Sachs form factors were derived from Fourier transformations of the baryon and moment-of-inertia densities with the effect of the vector meson coupling multiplied in later, essentially a factor of

$$\Lambda(t) \;=\; \lambda\,(\frac{m_I^2}{m_I^2 + Q^2}) + (1 - \lambda_I) \quad , \tag{1.56}$$

where I = 0 and I = 1 correspond to isoscalar (T=0) and isovector (T=1) form factors, respectively, and m_0, m_1 to the masses of the ω and the ρ, respectively. The quantities $\lambda_0\,, \lambda_1$ were used as free parameters (Model A). In a new version of the model (versions B1 and B2 which differ only in the fit parameter set used), the vector meson influence was added explicitly to the Lagrangian as

$$L \;=\; L^\pi + L^\omega + L^\rho \quad , \tag{1.57}$$

with L^π the standard Skyrme Lagrangian as in Model A. While both fits of Model B appear to be significantly improved with respect to A in fitting the proton form factors, B1 overestimates G_E^n while B2 results in about the same magnitude but appears to predict a maximum shifted with respect to the Galster parametrization. All models appear to predict G_M^n fairly accurately for $Q^2 < 1.0$ (GeV/c)^2 while significantly overestimating its value at Q^2 above 1.5 (GeV/c)^2. Figure 1-17 shows models B1 and B2 versus the data.

1.7.3 The Quark / Diquark Model

Inspired by the hard scattering model by Brodsky and Lepage [62] and attempting to make the model applicable to moderate Q^2, Kroll et al. [63] implemented the concept of viewing baryons as a combination of quarks and diquarks. The latter were considered as quasi-elementary constituents whose structure is embedded in diquark form factors. The so-constructed baryon thus consisted of only two valence constituents while sea quarks were disregarded. Spin-0 and spin-1 diquarks were considered in order to calculate the electromagnetic form factors of the nucleons. However, this model is only applicable at Q^2 above the range relevant to this thesis due to its perturbative nature. Recent work [64] has claimed some success in describing the proton

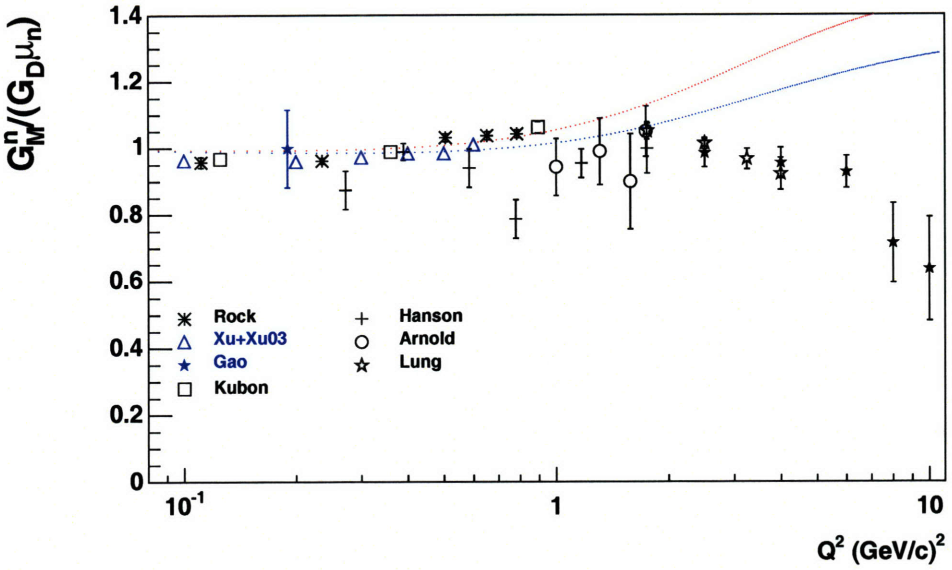

Figure 1-17: Models B1 and B2 from Holzwarth [61]. The data are from [33, 34, 35, 36, 40, 45, 46, 47]. Both models deviate significantly from the data at high Q^2. For the low Q^2 region the models are closer to the data.

charge form factor, in particular at low Q^2, using a quark-diquark model with a direct (Coulomb plus linear) as well as exchange interactions.

More recently, Ma et al. [65], investigated electron-nucleon elastic scattering processes using a relativistic quark / spectator-diquark model in which only the single quark takes part in the interaction. The remaining nucleon constituents are treated as a quasi-particle. The model was formulated in the *light cone frame*[13]. The five parameters of the model (quark mass, scalar and vector diquark masses and harmonic oscillator scale parameters) are fixed by the static properties of protons and neutrons, namely charge and magnetic radii and magnetic moments. The results show significant sensitivity on the relative strength of scalar versus vector diquarks and they describe the data fairly well within the model's claimed validity (Q^2 up to 2 (GeV/c)^2).

---

[13] In 1949, Dirac [66] introduced light-cone quantization while investigating various formulations of relativistic quantum mechanics (in this case the *Poincaré Group*, the set of the ten generators of infinitesimal Lorentz transformations that obey the commutation relations of Poinaré Algebra [67]). The light-cone is the surface defined by the kinematic constraints of special relativity. Defining a system's dynamical variables with respect to this surface, simplifies the relevant Lorentz transformations.

1.7.4 Chiral Perturbation Theory

The difficulties encountered when attempting to solve the full QCD Lagrangian led to the development of the concept of *effective field theories.* The difference between an effective and a fundamental field theory is the issue of renormalization. The underlying principle of the effective theory is the fact that the dynamics of low energies do not depend on those at high energies [68]. Therefore, a description of the low energy regime is possible through an effective Lagrangian which contains only a limited set of degrees of freedom. The theory is then expanded in powers of the energy over the characteristic scale of the problem under investigation. At each energy order, a finite number of coupling constants exist and hence renormalization can be achieved order-by-order. The only caveat of this procedure is the finite accuracy of any resulting computations [68].

As applied to QCD, the theory has to conserve *chiral symmetry*[14]. With this in mind, *Chiral perturbation theory* (ChPT) was formulated. The theory is valid as long as the energy involved is small compared to the chiral scale. Realistically, the theory deals with energy less than 500 MeV. Recently, Faessler et al. [70] used a non-linear, chirally symmetric Lagrangian taken from Baryon ChPT and re-expressed it in terms of external fields and quark and mesonic degrees of freedom. The Lagrangian was then used to dress the constituent quarks by a pseudo-scalar mesonic cloud and derive the relevant transition operators for the interaction of external fields and quarks under the influence of the cloud. Various practical applications were investigated, including the bare constituent quark distributions in the nucleon and the effect of the meson cloud on the nucleon form factors. In particular, in the Breit frame, their calculations predict

$$r_E^p = 0.871 fm \quad , \quad < r^2 >_E^n = -0.1154 fm^2 ,$$

$$r_M^p = 0.870 fm \quad , \quad r_M^n = 0.847 fm \tag{1.58}$$

$$\tag{1.59}$$

---

[14] Chiral symmetry is identified with the invariance of the massless QCD Lagrangian under global left- and right-handed rotations [69].

for the electric and magnetic radii of the proton and the neutron, respectively.

1.7.5 Scaling and Perturbative QCD

High Q^2 Scaling:

Brodsky and Farrar [71] used dimensional scaling laws to link the dynamical behavior of a hadron to the complexity of its structure. Their result [71],

$$\frac{d\sigma}{dt}_{AB \Rightarrow CD} \sim s^{2-n} f(\frac{t}{s}), \tag{1.60}$$

demonstrates the asymptotic ($s \Rightarrow \infty$) behavior of the cross section for fixed angle scattering (t/s fixed). In the above, s and t are the usual Mandelstam variables whereas n represents the total number of lepton, photon and elementary quark fields which carry a finite fraction of the system's momentum. Using dimensional counting and simple assumptions, it can be shown that the leading contribution to the proton Dirac form factor for a three-quark model scales as $(Q^2)^{-2}$ and that the proton Pauli form factor follows

$$F_2(Q^2) \sim F_1(Q^2)/Q^2, \tag{1.61}$$

from which it follows that

$$\frac{G_E^p}{G_M^p} \propto \frac{F_1(Q^2) + kF_2(Q^2)}{F_1(Q^2) + kF_2(Q^2)} \Longrightarrow const \tag{1.62}$$

at large Q^2.

Perturbative QCD:

The success of QED led to the generalization of the formalism used in order to describe QCD. However, despite the formal similarity of their respective Lagrangians, QED and QCD are sufficiently different to forbid treating them as equivalent. The coupling constant for QCD is large with respect to the corresponding one for QED so that the same perturbative treatment does not hold. In addition, the gauge bosons for

QCD carry color-charge whereas those for QED (photons) are neutral. This gives rise to multi-gluon vertices which render the calculations far more complex. Nevertheless, useful results from QCD using a perturbative approach for high Q^2 can be derived by taking advantage of the *asymptotic freedom* of the theory. Such results have little validity in the low-Q^2 regime.

Lepage and Brodsky [62] used such an approach to derive the asymptotic behavior of the form factors rigorously, as they had done previously using a heuristic framework. They found that to leading order in α_s and m^2/Q^2, the dominant term for G_M at high Q^2 is given by

$$G_M(Q^2) \Longrightarrow \frac{32\pi^2}{9} C^2 \frac{\alpha_s^2(Q^2)}{Q^4} \left(ln\frac{Q^2}{\Lambda^2} \right)^{-4/3\beta} (e_{\|} - e_{-\|}), \tag{1.63}$$

where the terms $e_{\|}$, $e_{-\|}$[15] denote the mean total charge of quarks with helicity parallel and anti-parallel to the nucleon's helicity, respectively. The quantity C is a constant and $\beta = 11 - (\frac{2}{3}) n_{flavor}$. As can be seen from the above, the calculation predicts a ratio

$$G_M^n / G_M^p \longrightarrow -2/3 \qquad (Q^2 \to \infty), \tag{1.64}$$

in agreement with data.

1.7.6 Vector Meson Dominance

Vector Meson Dominance (VMD) models consider the coupling of the virtual photon to the nucleon as a process mediated through vector mesons ρ, ω and ϕ. Gari and Krümpelmann [72] extended this concept through form factors which explicitly accounted for the scaling results of PQCD at high Q^2. These additional factors were in effect hadronic form factors. Lomon [73] further extended the model by adding an analytic approximation to the dispersion integral for the ρ meson contributions as well as a pole term for the isovector-vector meson $\rho'(1450)$ and later the isoscalar $\omega'(1450)$. Lomon's hybrid models (DR-GK) yielded significantly better fits to the

---

[15] $e_{\|}^p = 1$, $e_{-\|}^p = 0$, $e_{\|}^n = e_{-\|}^n = -\frac{1}{3}$

data for the individual form factors and the form factor ratios $R_p = G_E^p/G_M^p$ and $R_n = G_E^n/G_M^n$. While the model excludes the widths of the ρ and ω mesons, these contributions are expected to be small as the widths are relatively narrow. However, in the $Q^2 <$ 0.4 (GeV/c)^2 region, the multi-meson continuum and in particular the two-pion contributions may be needed.

1.7.7 The Constituent Quark Model (CQM)

The goal of *Constituent Quark Models (CQM)* is an effective approach to QCD, with constituent quarks, viewed as quasi-particles[16] generated by the spontaneous symmetry breaking of chiral symmetry (SBχS), acting as effective degrees of freedom. This approach provides a convenient framework for calculations of a number of hadronic and reaction observables. Relativistic covariance and necessary QCD properties have been incorporated in various models, mainly using a one-gluon-exchange approach (more details in reference [74] and references therein).

Capstick and Isgur proposed a relativistic *one-gluon-exchange model (OGE)* [75] based on the valence - gluon dominance concept. Using a variational technique, they derived the baryon wavefunctions from a Hamiltonian given by

$$H = \sum_{i=1}^{3} \sqrt{\vec{p}_i^{\,2} + m_i^2} + V_{oge} + V_{conf}. \qquad (1.65)$$

Adapting previously established methods for mesons to the baryon case, a quark smearing function ρ_{ij} is introduced to account for the finite size and off-shell nature of the quarks. All relevant potentials are then smeared following

$$\tilde{V_{ij}} = \int d^3r' \, \rho_{ij}(\vec{r} - \vec{r'}) \, V_{ij}(\vec{r'}). \qquad (1.66)$$

In the Hamiltonian of eq. (1.65), the second term is divided into Coulombic, hyperfine and spin-orbit contributions. The confinement term is in turn given by spin-orbit and

---

[16] In the absence of a rigorous QCD calculation of nucleonic structure, constituent quarks (CQ) are considered to be a consequence of valence quarks coupled ("dressed") with gluons and $q\bar{q}$-pairs.

string potential[17] effects. The results of this model were mostly qualitative and the need for improvements was emphasized.

Glozman et al. [76], attributed the inadequacies of the OGE model to improper accounting for the implications of SBχS. They proposed instead a flavor-dependent Goldstone-boson-exchange model (GBE), in which the Goldstone bosons appear as a natural consequence of SBχS and couple directly to the constituent quarks. Enforcing confinement as well, the authors proposed a three-quark Hamiltonian of the form

$$H = \sum_{i=1}^{3} \sqrt{\vec{p}_i^2 + m_i^2} + \sum_{i<j=1}^{3} V_{ij}, \tag{1.67}$$

using the relativistic form of the kinetic-energy operator (required on account of the large kinetic energy of the quarks) with m_i, p_i the mass and momentum of the i^{th} quark, respectively. The second term denotes the dynamical parts of the (pairwise) quark-quark interaction. These consist of (i) a confinement term of linear form in the inter-quark distance, modulated by a strength parameter (stemming from a string potential) and (ii) a spin-spin component. The model was subsequently tested against data for electroweak [76] and electromagnetic [77] form factors with good results.

Cardarelli and Simula revisited the OGE model by adding both kinematic and dynamic SU(6) breaking and investigating its effects [78, 79] on the nucleon form factors. In [79], the authors compare their calculations using wavefunctions derived from both the OGE and GBE frameworks which seem to predict similar results.

1.7.8 Lattice QCD Calculations

Lattice QCD (LQCD) attempts to solve the nonlinear partial differential equations of QCD exactly, based on numerical algorithms. It has been used for the energy regime where perturbative treatments of QCD fail. In this approach, a space-time lattice with lattice spacing α is used to express the path integral of the action S. This allows for calculations to be approximated through numerical solutions using well-established

---

[17] The concept behind the string potential for confinement as well as the relevant formalism are explained in [75].

statistical mechanics methods. Several results of Lattice QCD calculations of the form factors have been published over the years beginning in the early 90s ([80] and references therein). Some recent calculations can be found in [81, 82].

1.8 Friedrich and Walcher Parametrization

Before ending this chapter, a recent parametrization of the world's form factor data is briefly discussed. Inspired by measurements of G_E^n which suggest the possible interpretation of the shape of the neutron's charge form factor as a smooth broad distribution superimposed with a "bump" at Q^2 around 0.1-0.2 (GeV/c)^2, Friedrich and Walcher [24] (FW) reexamined existing data using an alternative form to the Galster parametrization. This form,

$$G_E^n = \frac{a\,Q^2}{(1 + b\,Q^2 + c\,Q^2)^5} + \frac{d\,Q^2}{(1 + e\,Q^2)\,(1 + f\,Q^2)^2} \tag{1.68}$$

and appropriate boundary conditions, enabled them to describe the additional peak. Extending this approach to all nucleon form factors, a phenomenological ansatz was used for the smooth part

$$G_s(Q^2) = \frac{\alpha_{10}}{(1 + Q^2/\alpha_{11})^2} + \frac{\alpha_{20}}{(1 + Q^2/\alpha_{21})^2} \tag{1.69}$$

(using two dipole forms for additional flexibility) and

$$G_b(Q^2) = e^{-\frac{1}{2}(\frac{Q-Q_b}{\sigma_b})^2} + e^{-\frac{1}{2}(\frac{Q+Q_b}{\sigma_b})^2} \tag{1.70}$$

for the "bump". In terms of the "smooth" and the "bump" parts, the form factors were expressed as

$$G(Q^2) = G_s(Q^2) + a_b\,Q^2 G_b(Q^2), \tag{1.71}$$

where a_b is a free-parameter amplitude for the "bump".

The success of this parametrization in describing the data, led to a physically motivated ansatz in which the nucleons are taken as a sum of a bare nucleon plus a

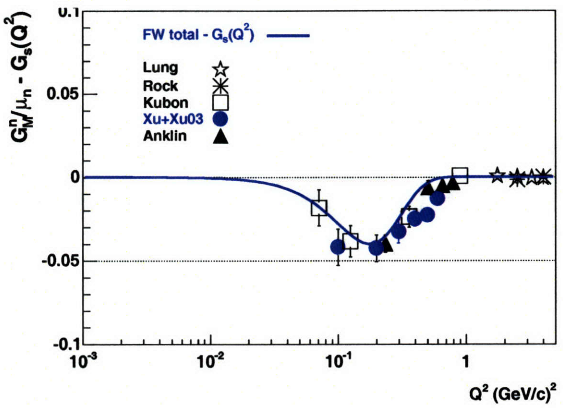

Figure 1-18: Plotted here is the bump of the FW parametrization as seen in eq. (1.70). The dip in the low-Q^2 region indicates the difference of the FW form factors from the smooth part of the parametrization.

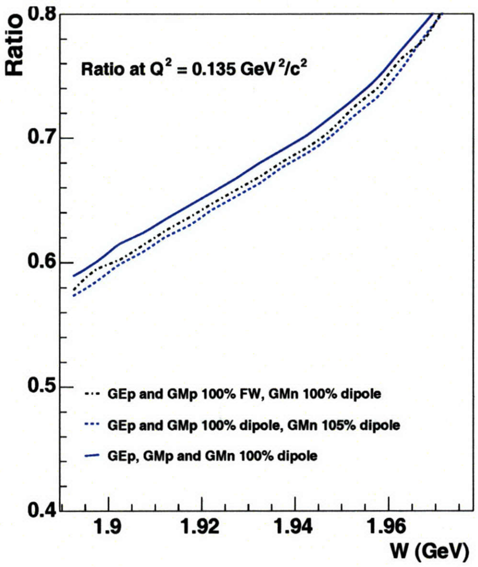

Figure 1-19: The super ratio $\Re$ plotted using the full Arenhövel model with 100% (solid blue) and 105% (dashed blue) dipole for G_M^n and dipole form factors for the proton. The dashed-dotted black line is the result of a calculation with the Arenhövel model but with FW form factors for the proton. The calculations were performed for a fixed $Q^2 = 0.135\,(GeV/c)^2$ which is very close to the maximum difference between dipole and FW parametrizations. The difference is of the order of 3% at its maximum. This simulation was performed for the BLAST acceptance.

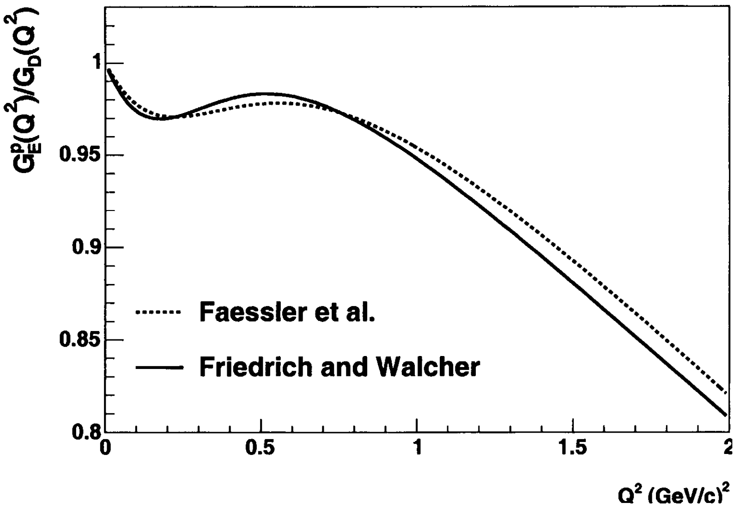

Figure 1-20: A comparison of the FW parametrization and the calculation of Faessler et al. [70] for the proton electric form factor G_E^p normalized to the dipole form factor.

polarization part. The latter consists of contributions from the proton (neutron), its counterpart (neutrons if considering protons and vice versa) and a positively (negatively) charged pion, respectively. The bare nucleon form factor incorporates all the relevant constituent quark form factors, accounted for by using a dipole form. In addition, the pionic term is taken to have a harmonic oscillator form. As shown in [24], the common feature of the form factors at low Q^2 translates into some form of structure at approximately 2 fm in r-space, which the authors interpret as the effect of a pion cloud around a bare nucleon.

The parametrization of Friedrich and Walcher appears to agree well with the calculations of Faessler et al. [70]. Figure 1-20 shows a comparison of the Friedrich and Walcher fit with the calculation of Faessler et al. for the electric form factor of the proton in the low-Q^2 region whereas figure 1-18 shows the deviation of the FW parametrization from the dipole form factor for G_M^n in the low-Q^2 region. Finally, figure 1-19 shows a Monte Carlo calculation of the ratio of the asymmetries in perpendicular over parallel kinematics using the Arenhövel model at a fixed $Q^2 = 0.135\,(GeV/c)^2$ where the deviation of the FW parametrization from the dipole form factors is close to its maximum. The solid blue line shows the calculation using the dipole form for the proton form factors as well as G_M^n, whereas the dashed-dotted black line shows the result using the FW parametrization for the proton and 100%

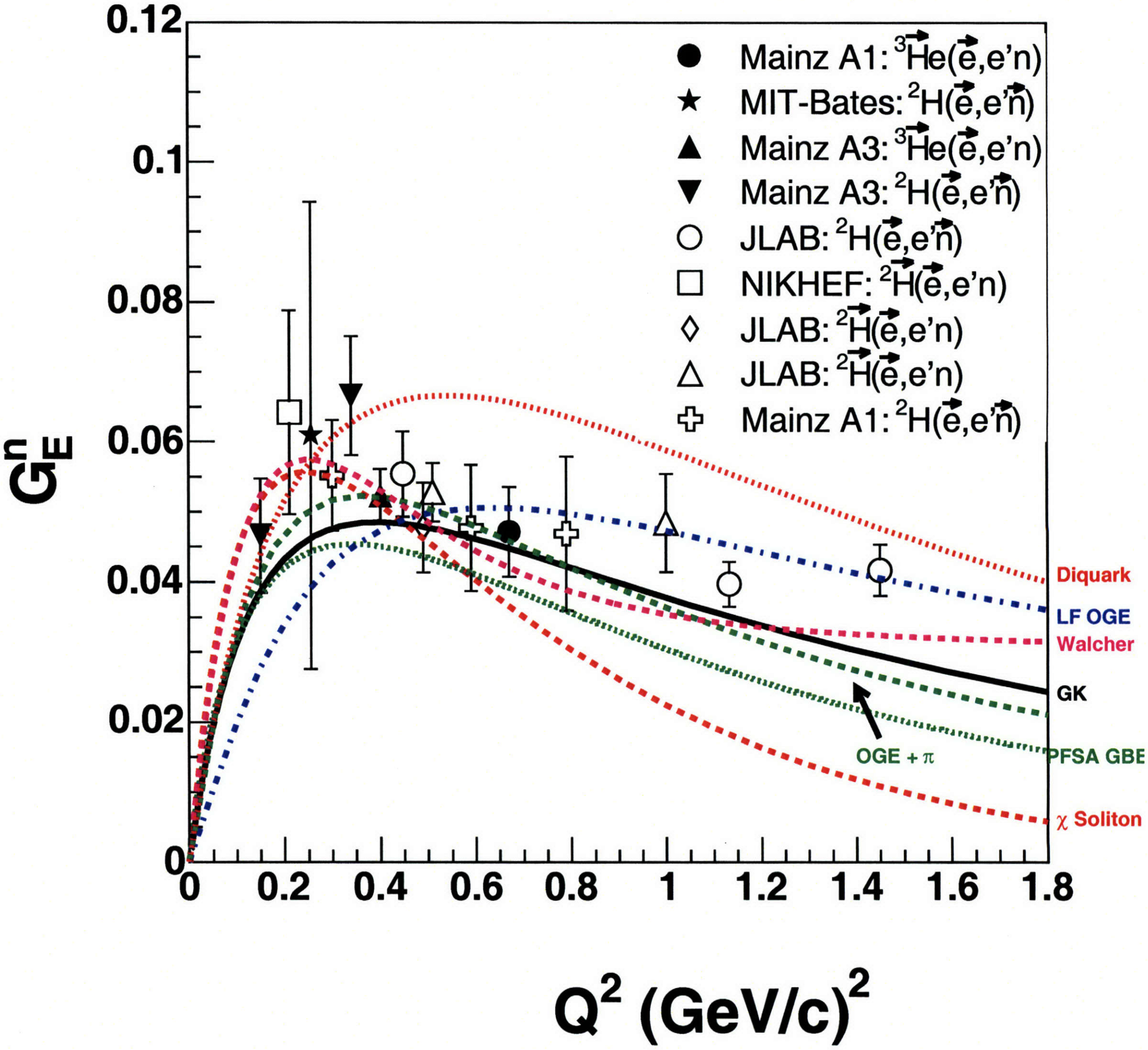

Figure 1-21: The world's data for the neutron electric form factor G_E^n along with theoretical model calculations of the form factor discussed earlier in the text.

dipole for G_M^n. The dashed blue line is a calculation performed using the dipole form for the proton form factors and G_M^n, but with the latter increased by 5% to show the sensitivity of the ratio to changing to the FW parametrization from the dipole.

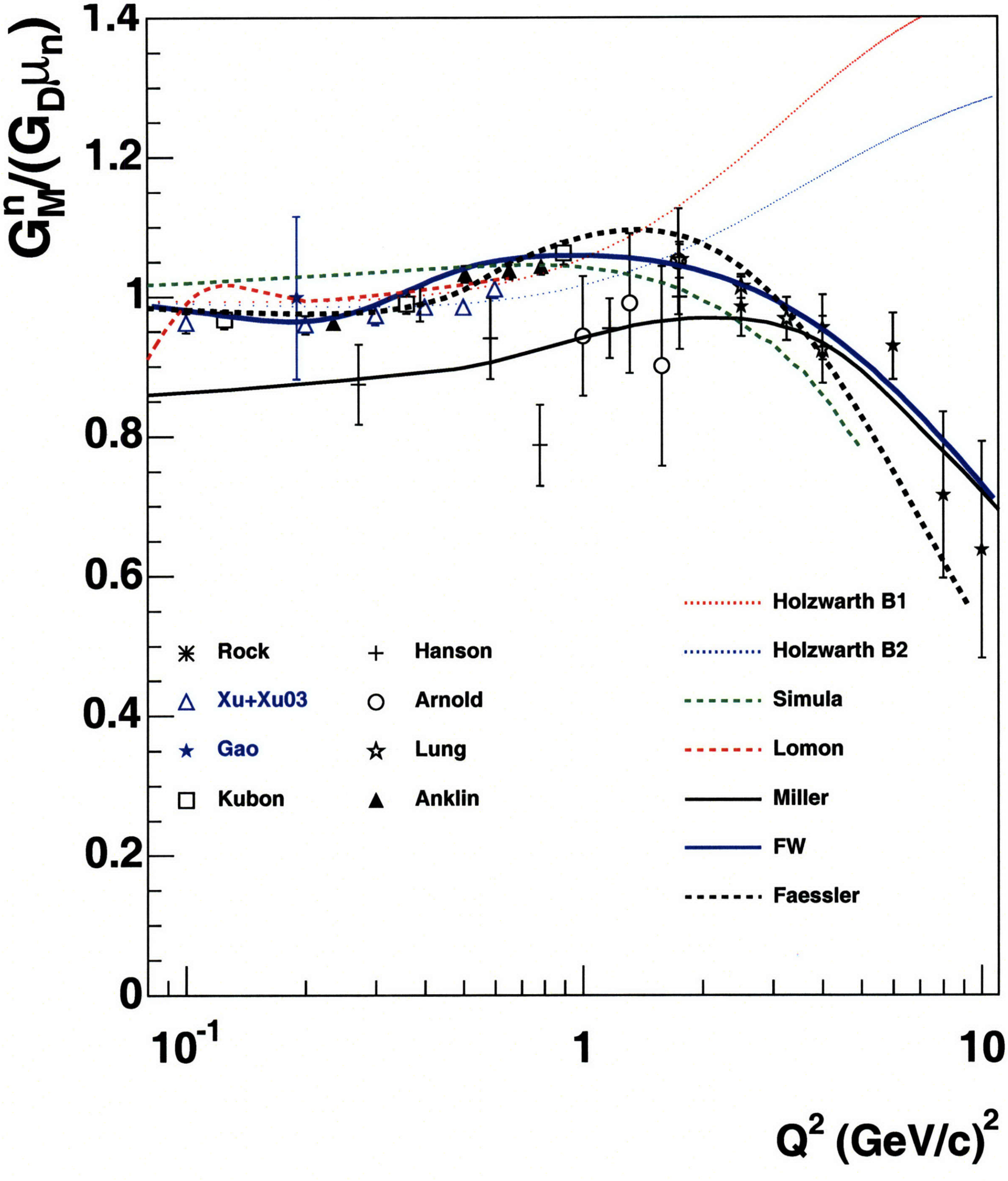

Figure 1-22: The world's data on G_M^n along with theoretical calculations. Holzwarth B1 and B2 are solition model calculations [61], Simula [79] is a CQM model. Lomon [73] is an extension to the Gari-Krümpelmann VMD model and Miller [53] is a cloudy bag model. Faessler is a Chiral Perturbation theory calculation and FW is the Friedrich and Walcher parametrization [24]. The data are taken from references [33, 34, 35, 36, 40, 42, 44, 46, 47].

Chapter 2

Atomic Beam Source

In order to achieve a highly polarized internal target, an Atomic Beam Source (ABS) apparatus was assembled and installed in the South Experimental Hall at the Bates Linear Accelerator Center. An overview of the experimental apparatus, the relevant theoretical facets of the principles invlolved as well as performance results are presented in this chapter.

The BLAST target was based on the NIKHEF ABS [83] and used many of the same components. In this chapter, characteristics and operation principles of the major components of the target system are discussed. Emphasis is also given to modifications of the apparatus necessitated by the constraints of the BLAST detectors. Following a brief overview, the dissociation and atomic beam formation mechanisms are discussed, followed by discussion of the optics of the system, the sextupole magnets and the transition units. The chapter concludes with sections on the storage cell and the Breit-Rabi polarimeter, as well as relevant polarization and performance comments.

2.1 Introduction

Since its development in recent years, internal target technology has been used extensively owing to its inherent advantages. The technology allows the use of highly pure, gaseous targets to limit experimental backgrounds and yield high, undiluted polarization. In addition, the technology facilitates flexible orientation of the target spin to optimize running conditions as well as fast and simple change of target gas to limit downtime between experiments. These advantages more than make up for the lower target density and therefore lower luminosity compared to external, solid targets. While the external targets allow significantly higher luminosity because of their thickness, they cannot be used with a stored beam and the impurities in the material give rise to diluting backgrounds in the data. Such backgrounds have to be subtracted, a procedure that can be complicated.

Molecular hydrogen or deuterium gas is fed into the dissociator tube where the gas is subjected to strong electromagnetic RF fields which dissociate the molecules into atoms. A series of apertures forms an atomic beam which then travels through a system of sextupole magnets and RF transition units. The sextupole magnets de-focus atomic electrons with positive spin while they focus the rest. As such, the intensity of an unpolarized beam will be reduced by half in passing through the magnet system. Furthermore, the transition units are tuned to obtain the desired hyperfine states by the time the beam enters the target storage cell. Therein, the gas diffuses slowly and interacts with the stored electron beam circulating in the ring before being pumped out. A small outlet tube at the bottom of the cell allows for monitoring the relative populations of the hyperfine states in the cell using a Breit-Rabi polarimeter.

2.2 Software Controls and Interlocks

The Experimental Physics Industrial Controls System (EPICS) was used for remote control and software interlock of the various ABS components. EPICS is a distributed software architecture with a convenient set of tools. The system was initiated at the Argonne National Lab in the 1980s and developed through a collaboration of various laboratories and research institutions [84]. The main components of the system consist of:

1. The Operator Interface (OPI).
2. The Input - Output Controller (IOC), a VME-based system containing a pro-

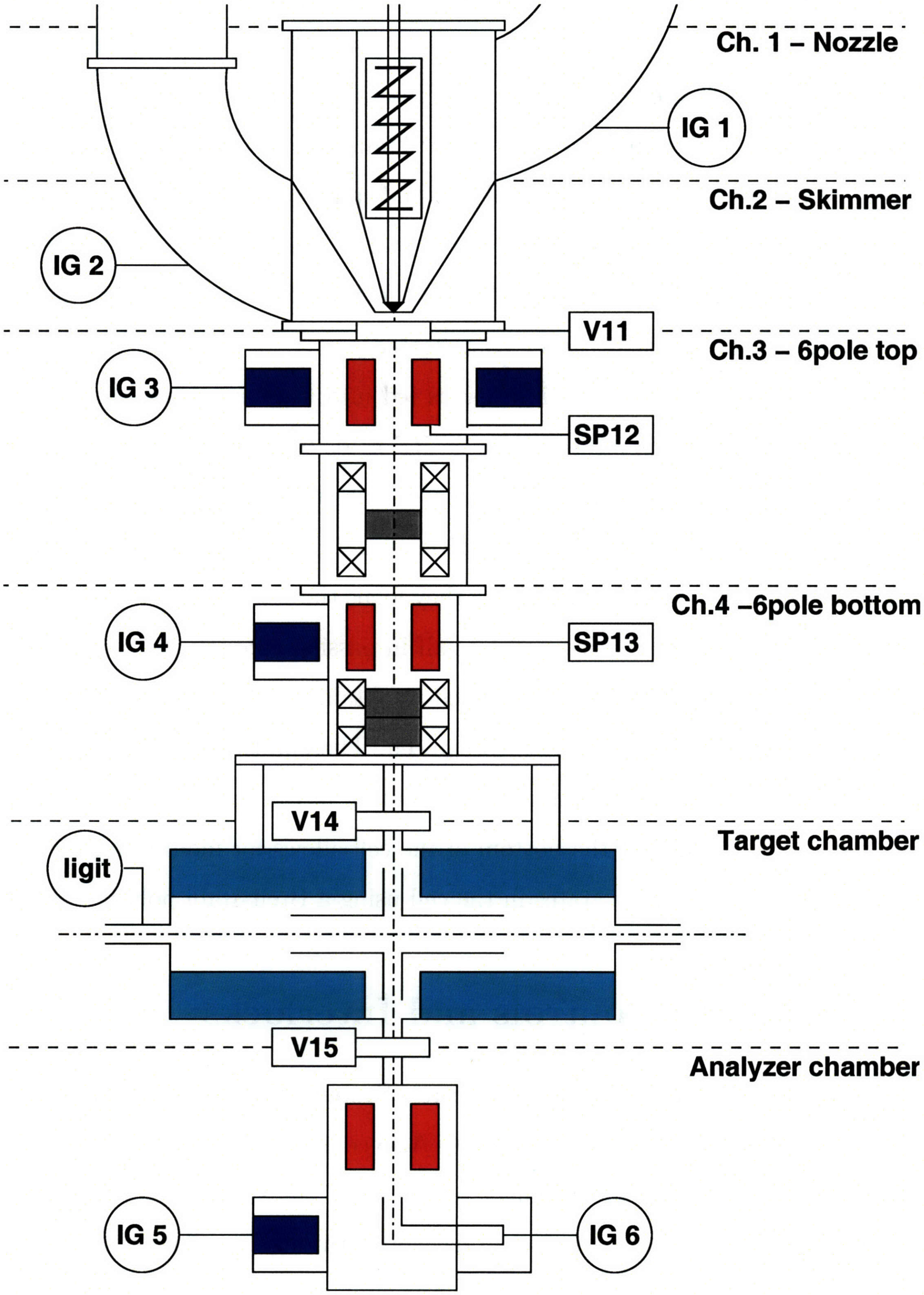

Figure 2-1: A schematic layout of the vacuum system of the ABS.

cessor, I/O modules etc.

3. A Local Area Network (LAN) which allows communication of the user with the controller through Channel Access, a software component (based on the client-server principle) called by the graphical interface.

Several types of VME modules were used to control and interlock the devices of the ABS apparatus. The modules were installed in two separate VME crates in two racks, in a tunnel adjacent to the experimental hall (referred to as the D-tunnel). The signals from the target were collected in patch-panels and sent to the D-tunnel through RG-58 cables.

VME processor	Collects signals from the individual modules and transmits over ethernet connection to software control interfaces.
VMIC 4514	Analog-to-Digital Converter (ADC)
VMIC 2232	Relay Board
XYCOM 2240	Binary I/O board
GPIB	General Purpose Interface Bus

Table 2.1: Main components of the control-interlock system used for the ABS. More information on the above components can be found in [84].

2.3 Gas Feed Systems

2.3.1 Polarized Gas Feed System

Work on the Polarized Gas Feed System (PGFS) began at the end of 2001. Assembly was completed in early 2002 and the system was leak-checked before installation on the mezzanine, a large ramp above the BLAST detector built to facilitate access to the target. By February 2002, connecting pipe-lines were in place and the PGFS was finally integrated with the ABS vacuum.

The PGFS pumped gas directly into the dissociator. Four separate lines connected the system to bottles of Hydrogen, Deuterium, Oxygen and Nitrogen located on the South Hall floor. Through remote controls, the operator of the ABS was able to select the desired gas mixture and flow. The mixture was then channeled into the

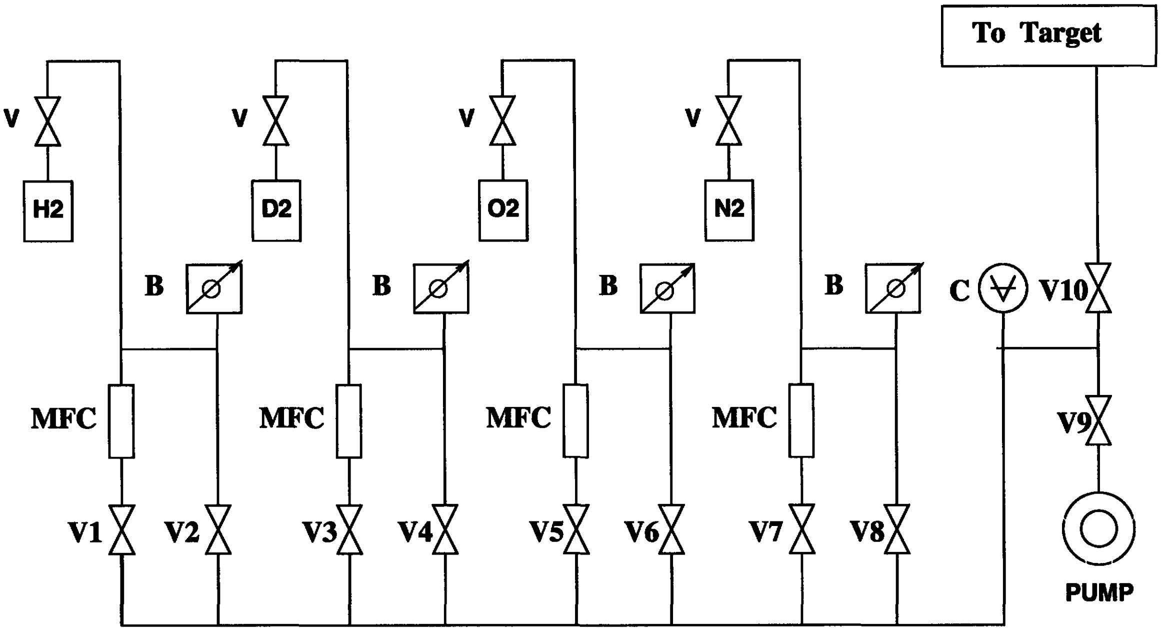

Figure 2-2: Schematic of the Polarized Gas Feed System. The Convectron gauge C was used to determine nozzle clogging during operation.

dissociator through valves V10 and V11 (see figures 2-1 and 2-2).

The PGFS station consisted of 4 separate gas sections. Each section was connected to a single bottle and was equipped with a Baratron gauge to monitor the pressure in the line. A calibrated Mass Flow Controller (MFC) MKS 1479A allowed accurate control of the gas flow from the individual lines into a common section. The accuracy of the MFC was of the order of a few percent, which in the case of the PGFS was not critical. Additional valves on the system allowed for bypassing the MFC (valves V2, V4, V6, V8). Valve V9 connected the common section with a roughing pump through a short bellows.

2.3.2 Unpolarized Gas Feed System

In order to conduct studies necessary to the experiment, an Unpolarized Gas Feed System (UGFS) was assembled and installed on the mezzanine. Pipe-lines connected the UGFS directly to the target cell. The system was equipped with an array of inlets to channel the selected gas into the target. The same type of Mass Flow Controllers used for the PGFS were also used on the UGFS. Since the latter was intended for the

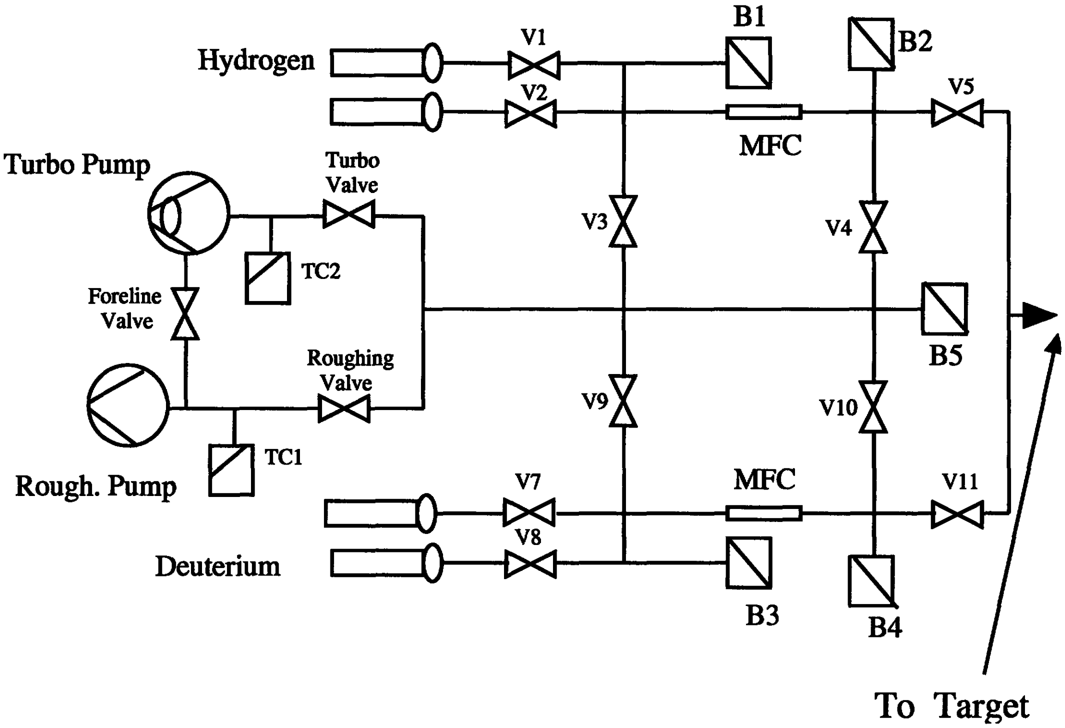

Figure 2-3: Schematic of the Unpolarized Gas Feed System for BLAST. The pressure in the lines and various sections of the system was monitored with Baratron and Convectron gauges. The vacuum was maintained by a Roughing pump and a Turbo pump.

luminosity calibration, it was essential to know the flow through the MFC accurately. Since this was not possible, a buffer system was used instead for that purpose. Figure 2-3 shows the UGFS used at BLAST.

A schematic of the buffer system can be seen in figure 2-4. The buffer system was assembled and adjoined to the UGFS to provide a more accurate calibration of the ABS flows as well as reproduce the polarized gas thickness in the cell for experimental background studies. The system consists of two 4.5 litter vessels, a reservoir and a buffer, connected through a needle-valve. The reservoir is filled to capacity to act as a supply for the buffer. The pressure in both vessels is monitored with Baratron gauges. The buffer system is connected directly to the target cell. The flux $\Phi(P)$ can be expressed as a function of the rate of change of the buffer pressure P_{buf} as

$$\Phi(P) = -\frac{dn}{dt} = -\frac{V}{k_B T}\frac{dP_{buf}}{dt}, \tag{2.1}$$

where V is the volume of the buffer container and T is the temperature of the gas. An accurate measurement of the pressure time-dependence yields a measurement of the flux. The system was automated to limit variation of the pressure in the buffer system to about ±10%, in order to maintain a stable flux into the cell.

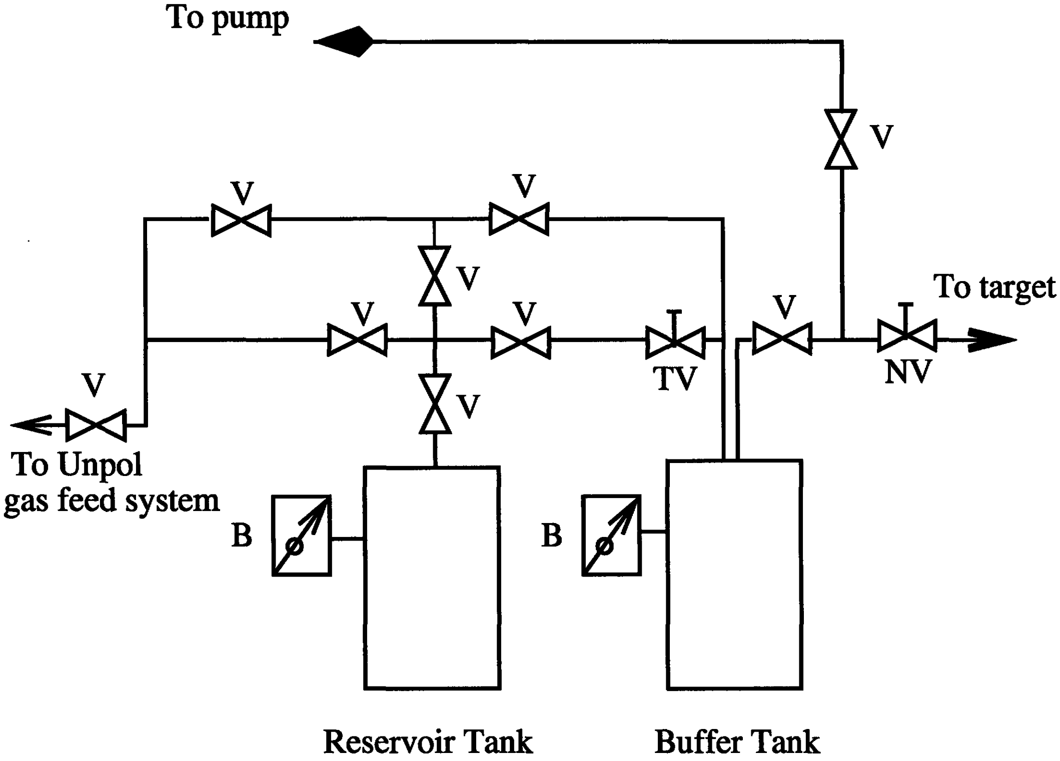

Figure 2-4: A schematic layout of the buffer system.

2.4 System Interlocks

Using EPICS components, a number of interlocks were implemented to ensure safe and reliable operation of the hardware. Different modes of operation were established, based on the type of gas and the number of changes allowed during operation. The HYDROGEN (DEUTERIUM) mode prevented the user from accidentally flowing Deuterium (Hydrogen) gas by disabling operation of the PGFS valve connecting to the Deuterium (Hydrogen) gas-line. If the pressure in the storage cell (monitored with an Ion-gauge referred to as Ligit) exceeded 10^{-6} torr, valves V14 and V15 (see figure 2-1) shut in both modes to prevent possible contamination of the ABS, in case the vacuum in the target chamber had been compromised. Additionally, this interlock protected the ring vacuum from ABS malfunctions or operation errors. The EXPERT mode on the other hand was designed without any interlocks, in order to allow tuning and technical work on the target.

2.5 RF Dissociator

The dissociator was essentially the most critical component of the ABS. In a nutshell, the operation proceeded as follows: gas was injected into the dissociator from the Polarized Gas Feed System with a rate controlled by Mass Flow Controllers. Therein, a field applicator, which consisted of a resonant circuit, produced electromagnetic waves in the radio frequency range (27.1 MHz). The waves were applied to the gas confined in a cylindrical discharge tube. Free electrons, ionized via the discharge, accelerated in the field and dissociated gas molecules through collisions. The resulting atomic population was formed into a beam through a series of apertures at the edge of the dissociator, optimized to maximize intensity. The apertures consisted of a nozzle, a skimmer and a collimator.

Apparatus:

The major components of the dissociator include the discharge tube and the RF coil, the RF generator and the impedance matching circuit, and finally the aforementioned apertures for atomic beam formation.

The RF coil was used to create the plasma through RF power from the generator. It was made of solid Cu bars, 0.1875 inches in diameter, helically wound to fit inside the RF tank with inner diameter approximately 3.5 inches. It had a 2 inch outer diameter, an 8 inch length and consisted of 16 turns. The discharge tube, located inside the coil as seen in figure 2.5, consisted of two concentric tubes with 9 mm and 16 mm inner diameter, respectively. Two different tube materials were tested for performance and durability. GE-214 fuzed quartz and Schott Duran Pyrex were used, the latter yielding better performance and chosen for exclusive use in the experiment. In between the two tubes flowed de-ionized water for cooling, cooled by a 600 W

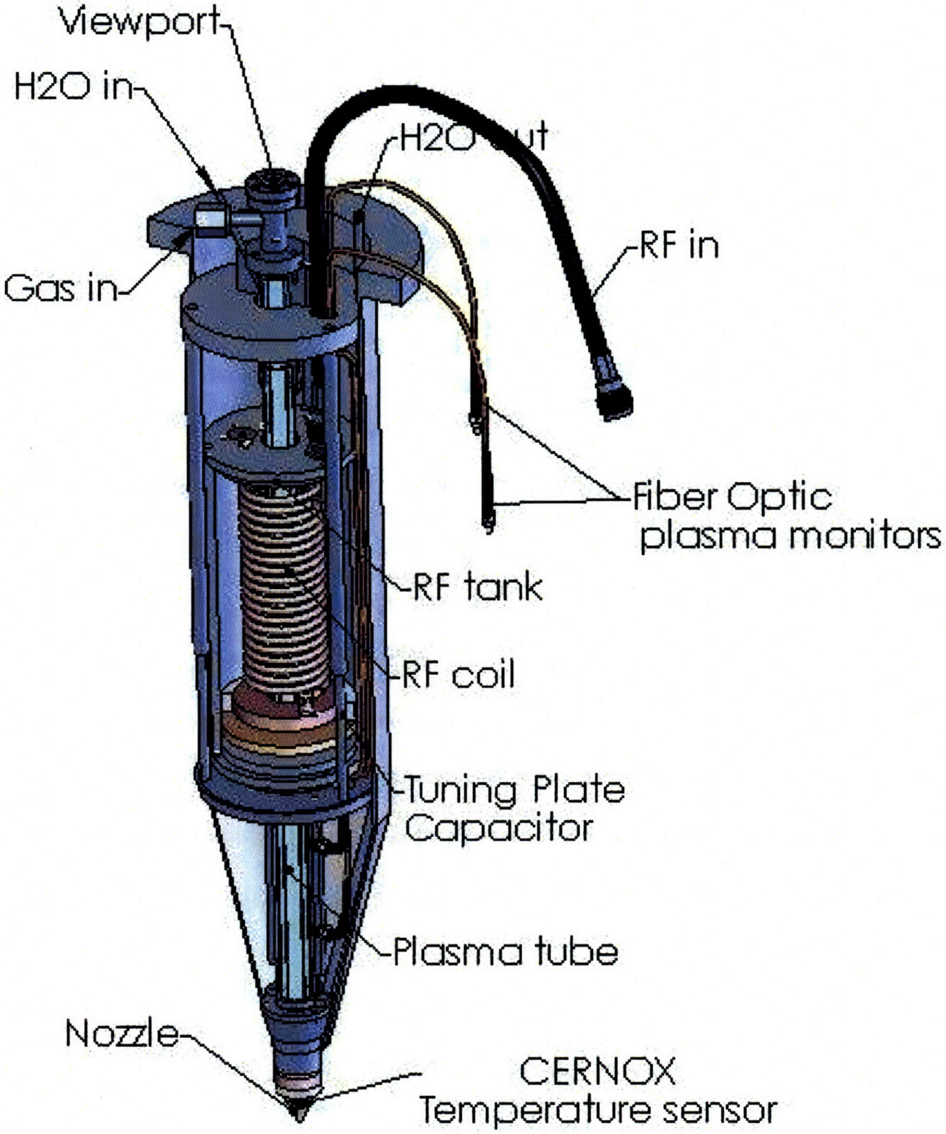

Figure 2-5: The dissociator system of the ABS.

Neslab CFT-25 chiller. The glass discharge tube was connected to the nozzle through a Cu adjuster, bolted to the Al nozzle to prevent the tube from shifting. Originally, the connection of adjuster and tube allowed for excessive thermal contact between them which, given the cooling of the nozzle to 70 K would often lead to freezing of the water and breaking of the tube. To prevent this, ethylene glycol was added to the water to form a 30% ethylene glycol, 70% water mixture. While the addition of the glycol in the water prevented further freezing-related incidents, the RF interaction altered the chemical structure of glycol producing a thick, dark-colored residue. The effect was shown to lower dissociation rates which led to limited performance. Consequently, the glycol was removed from the cooling water and efforts were focused on improving thermal insulation between nozzle and tube instead. A teflon washer was inserted to hold the edge of the tube and provide insulation from the nozzle. In addition, metal spring fingers were installed on the Cu adjuster to limit thermal contact between tube and adjuster as well as to allow the tube to suspend without shifting [85].

The ABS nozzle was the first component of the aperture array that led to beam formation. It was made of aluminum and the aperture had an opening of 2.1 mm in diameter. The temperature of the nozzle and its vertical and horizontal positions had to be optimized for maximum flux. In order to tune the location of the nozzle, the latter was mounted on a flange to allow for three-dimensional offsets every time the nozzle had to be replaced. A rough positioning was done optically at installation while finer adjustments were performed by optimizing the intensity of the ABS at the beginning of operation. The intensity was deduced by a pressure reading of the Ligit ion-gauge.

The low temperature of the nozzle was critical in reducing the kinetic energy of the atoms passing through it. This created a more uniform beam of slower atoms and since the spread of the velocity distribution was thus limited, the effect increased the system's collective focusing efficiency by maximizing transmission probability through the magnets. Additionally, atoms colliding with the nozzle were subjected to surface recombination effects[1]. A temperature of about 70 K was found to be optimal for operation and a Cryomech AL-60 cold-head was used for cooling. Cernox CX-1070-CU carbon-glass temperature sensors were installed to monitor and control the cooling power delivered by the cold-head via an automated feedback loop. A heater was used in addition to the cooling to raise or lower the temperature. The cold-head was connected to a Cu bar through a layer of Indium, which has the property of attaching to the surface it is applied to in such a way as to maximize the area of contact. The advantage of good contact more than makes up for Indium's poor conductivity. The

---

[1] The recombination effects on the nozzle were essentially of the same nature as those in the cell, discussed in the relevant section in this chapter.

Cu bar connected to a Cu braid which in turn was bolted to a clamp connected with the nozzle. The braid connection had to be flexible to allow for shifts in position due to thermal expansion, since the pressure applied to the nozzle through the braid was too strong and the nozzle could have been dislocated from the O-ring between the inner stainless steel part of the dissociator and the outer jacket, thus venting the dissociator. The entire length of the Cu bar as well as part of the braid were covered with Aluminized Mylar layers to prevent heat losses due to thermal radiation. The mylar layers covering the Cu bar and the braid could get damaged due to the flux of atoms through the nozzle and then pulled into the pumps of this ABS section. While this did not affect short-term operation, the mylar had to be replaced periodically. Another maintenance operation necessary was the periodic cleaning of the nozzle. The plasma in the dissociator shredded the inner surface of the pyrex discharge tube even though the tube was not visibly affected. Tiny shreds of glass following the path of the beam could get caught on the nozzle, affecting performance. During deuterium operation, the nozzle had to be cleaned and replaced with an average of three weeks [86].

Dissociator tuning:

The RF discharge in the dissociator was obtained with an ENI Genesis GHWE-25 RF generator which could deliver a maximum 2.5 kW power at 27.12 MHz. The RF input was nominally set at 250 W with about 70% efficiency due to power loss in the cabling. The output RF impedance of the power supply and cable was monitored with an ENI VI probe one meter away from the dissociator coil. The probe provided a graphical measurement of voltage, current and phase angle on a Smith Chart. An impedance matching network was installed just before the dissociator to match the RF coil impedence to 50 Ω . The matching network consisted of a Dressler Variomatch network for automated remote control through EPICS.

Figure 2.5 shows a circuit diagram for the system. The plasma couples to the input RF power through capacitive coupling and the tap point of the inductor coil in the dissociator LC circuit can be used to tune for the amount of RF power coupling with the plasma. The resonant frequency of the LC circuit was set before operation at

27.12 MHz to match the frequency of the power supply. Tuning was performed with an Advantest R3162 spectrum analyzer while the cooling water was flowing through the discharge tube[2]. Using the matching network, dissociation was achieved through the entire length of the dissociator discharge tube [88].

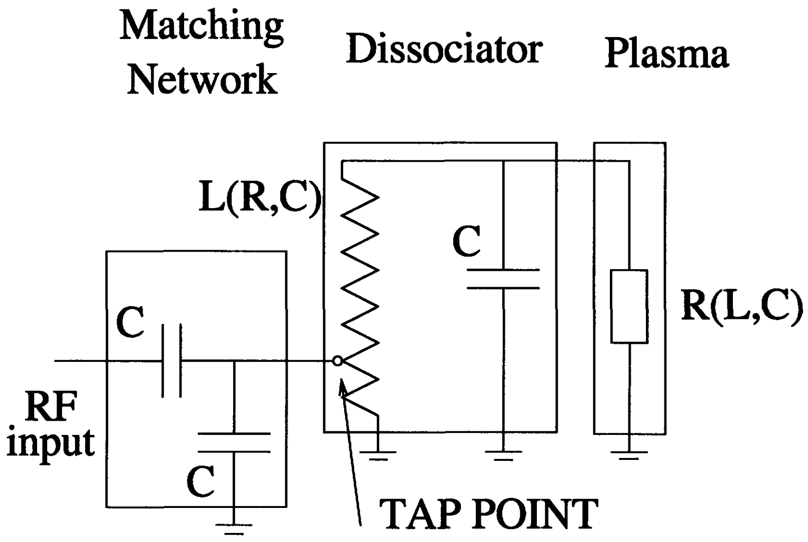

Figure 2-6: Schematic of the dissociator circuit.

Dissociation results:

The degree of dissociation, defined as the fraction of atoms in the beam, was the result of competing atom production and recombination mechanisms. At sufficiently high fields, valence electrons can be stripped from molecules in the gas to create a discharge with a characteristic pink glow for hydrogen and deuterium. The degree of ionization is rather low, but given the high-temperature of the free electrons (referred to as primaries) versus the molecular ions, the dissociation process is dominated by the electron kinematics [89]. In gas discharges with internal electrodes, the primary electrons are accelerated in the cathode to a few hundred electron-volts whereas in the case of electrode-less discharges, the acceleration takes place inside the plasma. For each ionizing collision, the electron participates in a large number of inelastic collisions with neutral molecules, dissipating most of its energy. Therefore, the energy

---

[2] The resonant frequency of the configuration is known to decrease when water is inserted in the discharge tube [87].

needed to create an ion-electron pair far exceeds the relevant threshold ionization energy. Furthermore, free-electrons are also created through metastable state excitations of atoms during collisions. These atoms may transfer their excess energy to other atoms causing ionization. Finally, dissociation is achieved through inelastic collisions between ionized electrons and molecules in the gas. Generally, the high mean electron energy and high electron density in the plasma are necessary for high degree of dissociation.

In order to maximize dissociation, loss mechanisms for both electrons and atoms have to be understood. The main electron loss mechanism is diffusion towards the walls of the container due to a density gradient created by the vanishing densities there. Thus, surface recombination effects become particularly important. Similar loss mechanisms apply to the atomic population. Diffusion-driven surface recombination is still the dominant factor, whereas volume recombination and flow-induced atomic fraction losses, due to the constant loss in atoms through the nozzle and their replacement with molecules, are less significant.

To limit surface recombination, a small admixture of molecular O_2 is added to both hydrogen and deuterium flow to produce water. Water formation, H_2O and D_2O for hydrogen and deuterium, respectively, reduces the number of available adsorption sites on the surface of the nozzle, thereby reducing recombination. In addition, catalytic dissociation on the surface may result through interactions of OH or OD radicals with molecules [90]. During the process of water formation, the number of atoms is reduced. The water layer takes several hours to build, but the loss of operating time is more than compensated by the improved performance. One side-effect of the oxygen admixture is the formation of a water layer on the cooled nozzle. The thickness of the layer increases over time, reducing the size of the aperture and blocking the beam. This obstruction to the flow results in reduced ABS intensity and target thickness, as well as increased pressure in the supply lines of the PGFS. EPICS-monitored alarm signals were interlocked with a Convectron pressure-gauge in the PGFS to alert the experimenters to the onset of nozzle clogging, at which point operation stopped and the nozzle was warmed up to room temperature in order to melt the ice layer. This procedure was necessary approximately once weekly.

The skimmer and collimator are two additional apertures installed after the nozzle to shape the beam and match the opening of the first set of sextupole magnets. The size of their respective apertures as well as their distance from the nozzle were determined by particle flow simulations through the ABS in order to maximize intensity. Coated nozzles were tested at other facilities in an effort to study recombination effects [90]. Specifically, uncoated copper, quartz-coated aluminum and silicone-coated aluminum and copper nozzles were tested at various temperatures. The results indicate that the material-specific recombination properties of the nozzle are suppressed by the formation of the water layer on the surface. All nozzles used at BLAST were uncoated aluminum.

In order to study the performance of the dissociator for different throughput, nozzle temperature and oxygen admixture, a Quadrupole Mass Analyzer Pfeiffer QMA 200 was used. Ideally, the QMA would have been installed in such location as to provide a real-time measurement of dissociation inside the cell. However, installing the QMA underneath the cell proved unfeasible because the signal in the device was swamped by background due to the large distance from the nozzle. Therefore, dissociation studies were performed during commissioning of the ABS by placing the QMA in a vacuum chamber right underneath the nozzle. The obtained optimization parameters were used during operation with periodic checks.

The QMA is based on the principle of a quadrupole filter. The latter consists of a quadrupole field created by four parallel metal rods. The rods are placed at the four directions of an orthogonal coordinate system around the path of incoming particles and are equidistant from the center. AC voltage riding a DC offset is applied to the rods such that the trajectories of the particles are impacted. One pair of opposite rods has negative DC offset and the other positive. Depending on the settings for operation, only ions with specific mass-to-charge ratio are allowed through to a Faraday detector whereas the rest strike either the positive or negative DC rods. A chopper was used for chopping the beam and separating signal and noise, and a lock-in amplifier was used to amplify the AC component of the QMA signal.

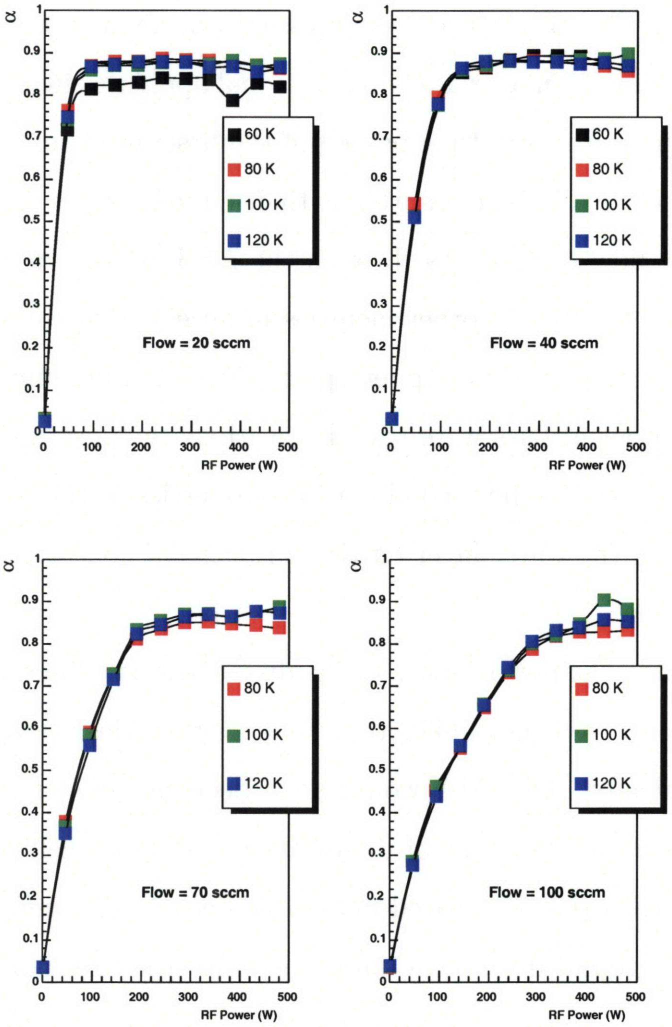

Figure 2-7: Dissociation results for deuterium. The study aimed to map the nozzle temperature-dependence of the degree of dissociation for different deuterium throughputs. Optimal values of 60 sccm and 70 K were used in operation.

The degree of dissociation for both hydrogen and deuterium is defined as

$$\alpha = \frac{n_a}{n_a + n_m}, \tag{2.2}$$

where n_a and n_m are the respective atomic and molecular partial densities in the atomic beam. In order to extract these from the signals of the QMA, two correction factors had to be applied. The ratio of atomic over molecular signals has to be corrected for the amount of time each population spends in the volume of the QMA. Assuming the same temperature and kinetic energy for both atoms and molecules, the

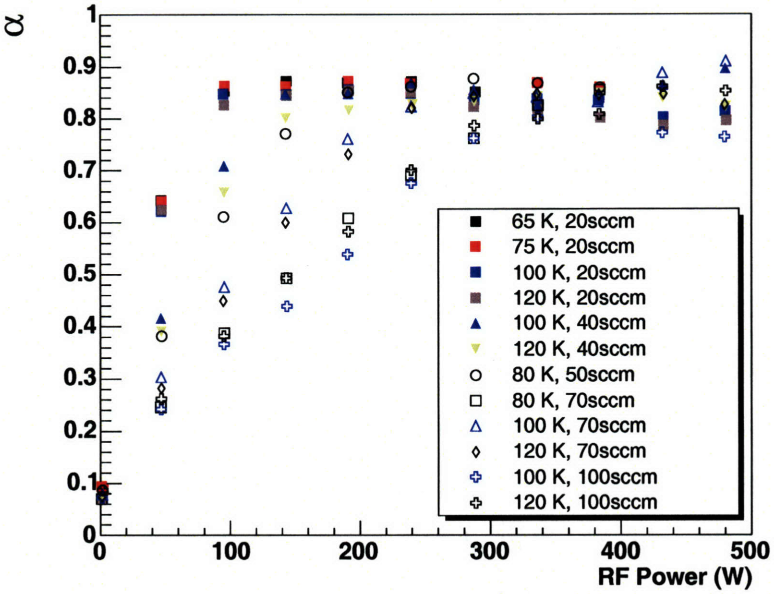

Figure 2-8: Dissociation results for hydrogen for various nozzle temperatures and gas flow rates.

average velocity ratio can be determined. Since the kinetic energy depends linearly on mass and quadratically on velocity, the correction factor, denoted here as k_v, is approximately $1/\sqrt{2}$. Two other correction factors are k_{ion} for the ionization and k_{det} for the detection probabilities, the latter being specific to the QMA device. In terms of the output signals from the device, the degree of dissociation can be expressed as

$$\alpha = \frac{S^a}{S^a + 2k_{det}k_{ion}k_v S^m}, \tag{2.3}$$

where S^a and S^m are the respective atomic and molecular signals from the QMA.

Figure 2-7 shows sample results of the dissociator studies for deuterium. Gas throughput and nozzle temperature were identified as the most critical parameters. Performance was not particularly sensitive to oxygen admixture above some threshold value estimated at 0.1% of deuterium flow. The actual value used in the running was 0.1% and this amount was found to saturate the discharge tube surface. The only drawback of excessive oxygen admixture was the faster formation of ice on the nozzle, which led to somewhat increased frequency for the periodic nozzle regenerations. The degree of dissociation approached 90% and was best for lower gas flow. The top two panels of figure 2-7 show that dissociation peaked at low RF power and then saturated.

Higher flows required higher RF. Optimal values of 70 K nozzle temperature and 60 sccm flow were established.

2.6 Target Storage Cell

In order to enhance luminosity as well as target polarization, a gas storage cell was embedded into the beamline. The cell was vertically aligned with the entire ABS apparatus as well as the Compression Tube array that sampled the atomic beam. A feed tube made of aluminum, connected the final chamber of the ABS to the cell. A similar outlet tube, also made of aluminum, sampled the beam at the bottom of the cell. Polarized gas from the ABS was injected into the cell through the feed tube. The gas density peaked close to the center of the cell, thus vastly increasing the target density per unit area.

The operating principle of the storage cell was based on the physics of diffusive molecular flow in the geometric confines of thin, long tubes[3]. For pressures relevant to the BLAST cell, a gas with large mean free paths and no interparticle interactions may be considered when discussing the flow. In this context, the *diffusion equation* can be written for a tube along the z-axis as

$$\dot{\rho} = D\frac{\partial^2 \rho}{\partial z^2} + Q, \qquad (2.4)$$

where ρ is the gas density and Q any gas source within the region. The solution to this equation for no sources (Q = 0) and steady flow can be expressed as

$$\rho(z) = \rho_o(1 - \frac{|z|}{L}), \qquad (2.5)$$

with L the length of the cell and ρ_o the density at the center of the cell. This

---

[3] Flow can be turbulent, laminar, intermediate and molecular. Turbulent and laminar are categorizations of viscous flow and they are distinguished by the velocity of the gas, or more conveniently the Reynold number, a dimensionless quantity which depends on the velocity and density of the gas, the viscosity and the diameter of the tube. Intermediate flow is the flow in which both viscous and molecular effects coexist. The Knudsen number is often used to separate molecular, viscous and intermediate flows [91].

represents a triangular distribution centered around the input point as shown in figure 2-9.

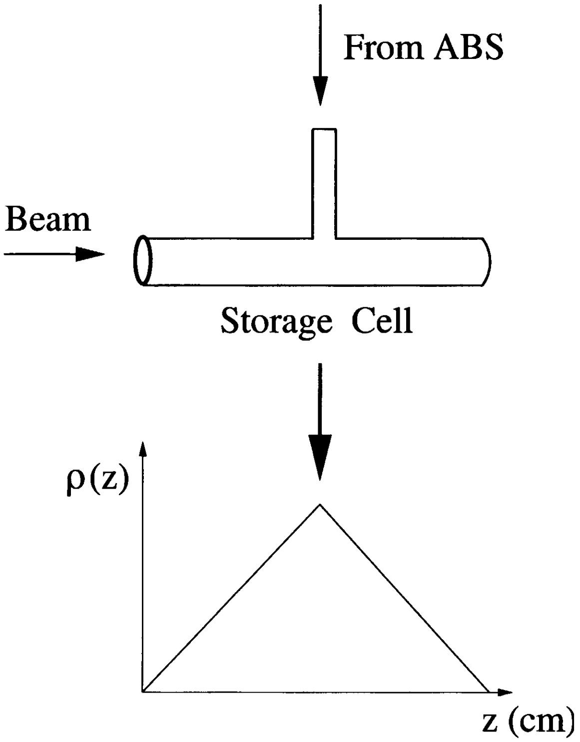

Figure 2-9: Gas entering the storage cell from the ABS diffuses creating a triangular distribution.

In the context of gas flow, the *throughput* Q is defined as the quantity of gas flowing through a volume and has units of [pressure × volume]. The proportionality constant which relates throughput and pressure is defined as the *conductance* C of the system as in

$$Q = C\Delta p, \tag{2.6}$$

where ΔP is the pressure differential between two sections. The simple geometry of the ABS target cell allows for an analytic calculation of the conductance of the system. The ABS input flux traverses the inlet tube and then diffuses in the cell. Knudsen [92] first derived the conductance for molecular flow through thin, long tubes of constant cross sectional area. Knudsen's model describes molecules or atoms impinging on a surface with drift velocity in the direction of the flow as well as an average velocity from a random Maxwell-Boltzmann distribution. On impact with the wall, the particles are stopped and re-emitted at random with velocity v_{av}. The re-emission is isotropic and therefore obeys a $cos\theta$ distribution, where θ is the angle of the trajectory of the escaping particle. Using the assumption that the drift velocity of the particles is proportional to their random velocity, the conductance is then given by

$$C = \frac{3.44 \times 10^4}{\sqrt{\pi}} \left(\frac{T}{M}\right)^{1/2} \left(\frac{A^2}{BL}\right), \tag{2.7}$$

where T is the temperature of the tube, M the particle mass, B the circumference of the cross section and A the cross sectional Area. Therefore, for $A = \pi D^2/4$ and $B = \pi D$. the conductance is given by

$$C = c_0(T/M)^{1/2}(D^3/L), \tag{2.8}$$

where $c_0 = 3.81 cm^3/s$.

While the flow through the inlet tube is ballistic, flow inside the cell is diffusive. In order to calculate the total conductance of the system, the three major openings of the cell have to be considered as parallel pipes with their respective dimensions. The two halves of the cell can be considered equivalent so that

$$C_t = C_{in} + 2C_{c/2} = c_0\Big((D_{in}^3/L_{in})\sqrt{T_{in}/M} + 2(D_c^3/L_{c/2})\sqrt{T_c/M}\Big) \tag{2.9}$$

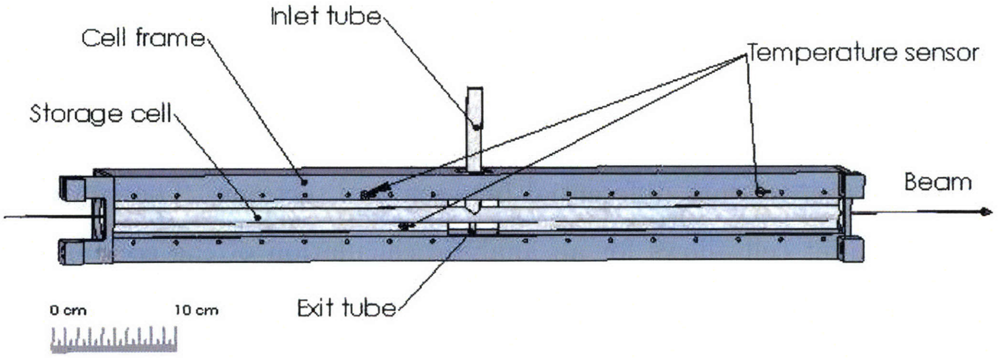

Figure 2-10: The storage cell used at BLAST, shown here within its mounting frame. The inlet tube allows gas from the ABS to enter the target area. The exit tube allows monitoring of the transitions by the Breit-Rabi polarimeter. Several temperature sensors were mounted on the cell and monitored remotely through EPICS.

The cell was conductively cooled through a cryo-pump system installed on the mezzanine. The temperature was monitored with temperature sensors attached on the frame holding the cell within the target region. Studies showed that cooling the cell to around 100 K enhanced polarization by limiting surface de-polarization and intra-beam scattering effects. Moreover, the inside of the cell was coated in *Dryfilm*[4]. Dryfilm is a hydrophobe substance and when a uniform layer of it coats a surface, it prevents water from forming on it. In addition, even when atoms may still stick to the surface, Dryfilm prevents spin exchanges that lead to de-polarization.

The low value of measured polarization led to suspicions about possible damage to the coating of the cell (damaged Dryfilm coating allows water formation on the surface). Such damage is possible through direct interaction with the electron beam, over-heating, radiation etc. The cell was then removed from the target and a water bead test was performed. For the test, a drop of de-ionized water was placed on the inner and outer surfaces of the cell, respectively. The sphericity of the bead, judged by eye, provided a clear indication as to the extent of the damage. Allowing the bead to flow through the cell from end to end and looking closely at the resulting watermark, revealed that the cell coating was indeed damaged. The cell was then replaced with a new coated cell. In order to prevent reoccurrence of the problem, a collimator was installed upstream of the target. Monte Carlo simulations were performed to determine both the size and the location of the collimator.

One 60 cm long cell was physically damaged during installation. The welding junction between the cell and the feed tube that connects to the ABS was not sufficiently strong and broke due to tension caused by thermal shrinking. Several target cells were used over the course of running. For the 2004 data, two 60 cm long and one 40 cm long cells were used. The two 60 cm long cells differed in the length and operating temperature of the inlet tube [26]. For the 2005 data, an attempt was

---

[4] Atoms with single valence electrons are more likely to be involved in strong interactions with the walls of a cavity, leading to spin relaxation. Chemically non-reactive compounds with small polarizability (and therefore lower dielectric constants) are used as surface coating to reduce the van der Waals interaction and as a result limit the time atoms remain physisorbed on the surface. Fedchak et al. [93] investigated the coating performance of several compounds from the organosilicon class known as Dryfilm. During the coating process, the compound undergoes hydrolysis and the molecules join together to form even larger compounds without any available OH sites.

made to switch to a cell of smaller diameter for higher density. Whereas the increase in density was achieved, the target polarization was significantly lower for this cell compared to the 2004 data and yielded overall lower figure-of-merit. In addition, the smaller diameter cell made running the electron beam through it more difficult and on average increased beam losses and experimental background. Since time constraints did not allow further investigation of the polarization issue, the final cell from the 2004 running period was used instead [87].

2.6.1 De-polarization Effects in the Storage Cell

The effects responsible for polarization loss within the storage cell can be separated into two broad categories: *recombination* and *spin relaxation.* Recombination can occur both on a surface and within a volume. However, at the pressures relevant to this experiment, only surface recombination is considered. Spin relaxation on the other hand may occur both on the surface through wall collisions as well as inter-particle spin exchanges within the gas volume.

Recombination effects:

In the presence of a solid, a gas loses particles through absorption (gas particles enter the solid volume) and adsorption (gas particles stick to the surface, referred to as the *adsorbate*). While it is often difficult to differentiate between the two, only adsorption is really relevant here[5]. Adsorption depends on the number of available sites on the surface, or equivalently, the fractional coverage of the surface θ_S. The value of θ_S at equilibrium is obtained when the chemical potentials of the free gas particles and the adsorbate on the surface become equal to each other. Thus at any given temperature, the coverage is a function of the pressure experienced by the adsorbate and can be modelled in terms of isotherms. One such isotherm is the *Langmuir isotherm* [94]. This is based on the assumption that the process will not proceed past the formation of a monolayer on the surface. In addition, site equivalence as well as the independence of adsorption and desorption rates on local coverage are assumed. While the Langmuir

---

[5] Particles with thermal energies cannot penetrate the mololayer at the surface of the solid.

isotherm is a good approximation at low pressures, other models, such as the BET isotherm, describe higher pressure conditions more accurately. For more details on a statistical-mechanical derivation of the coverage in terms of partition functions for the rotational and vibrational degrees of freedom of the absorbate atoms, the reader is referred to [94].

Adsorption onto a surface for both molecules and atoms can occur by two processes: *physisorption* and *chemisorption.* In physisorption, the gas is subjected to a weak yet long-range *van der Waals attraction* as well as a short-range *Pauli repulsion* between the gas electrons and electrons in the solid surface. Additionally, in some cases, induced dipole interactions can originate from a coupling of the Coulomb field of the surface ions and the atomic electron cloud [95]. The interaction can be represented by a Lennard-Jones [95, 96] type potential

$$U(r) = Ar^{-12} - Br^{-6}, \tag{2.10}$$

where the constants A and B depend on the particles involved in the interaction. Chemisorption, prevalent at higher temperatures, results from the capture of a surface electron by the adsorbate and the formation of a chemical bond. Both kinds of adsorption are present at the temperature regime relevant to this experiment, with physisorption dominating at lower temperatures and chemisorption at higher.

Recombination can in turn occur in two ways [92], either through a reaction between two adsorbed atoms or through gas particles reacting with previously adsorbed atoms. Consequently, the process depends on the amount of time an atom will spend on the surface, given by

$$\tau_s = \frac{h}{\Delta E} e^{E_s/kT}, \tag{2.11}$$

where ΔE is the energy difference between possible states for the adsorbed atom and E_s is the adsorption energy.

In an effort to determine the optimal cell temperature for minimum recombination probability at HERMES [92], the recombination probability per wall bounce was plotted versus cell temperature using Hydrogen gas. A fit to the data was performed with the ansatz

$$\Gamma_{Rec}(T) \;=\; k_1 e^{T_1/T} + k_2 e^{-T_2/T} \tag{2.12}$$

for the recombination probability. The two terms describe separate processes. The first describes reactions with already physisorbed atoms and follows an Arrhenius law exponential. As the temperature decreases, this term dominates and the recombination increases. The second term can be understood as reactions with chemisorbed atoms. As the temperature increases, the chemical reactions dominate recombination. The optimal temperature to minimize recombination was found to be around 100-120 K.

Recombination is also affected by water injected ballistically into the cell from the ABS dissociator, where it is created due to the admixture of Oxygen with the intended target gas[6]. For temperatures lower than 140 K, the water sticks to the surface of the cell and the resulting ice coverage limits the amount of chemisorption possible. The water layer in the cell may take up to several hours to build up from activation of the ABS [97].

Spin Relaxation effects:

Spin relaxation effects can change the relative occupancies of the hyperfine states of the gas target. These effects can be separated into two distinct categories: effects of wall collisions and spin exchange collisions.

De-polarization through wall collisions:

The study of wall-collision de-polarization owes its beginning to the pioneering work of Bouchiat and Brossel who established the first simple model for the alkali spin-polarization surface relaxation process [98]. Their experiments investigated the behavior of Rb atoms on paraffin-coated surfaces. Upon impinging on the surface of the enclosure, in this case the storage cell, an atom does not rebound immediately but has a finite probability of being adsorbed by the surface for some time. During this time, the magnetic moment of the adsorbed atom interacts with the local magnetic field and induces transitions between available Zeeman substates. Bouchiat and Brossel also

---

[6] Further details can be found in the dissociator section of this chapter.

introduced another type of interaction which was thought to be spin-orbit coupling between the adsorbed atom and the relative motion of carbon atoms on the surface. Both interactions yielded a time-dependent perturbation with characteristic correlation times. These describe the time it takes for a perturbation to lose information on its past history and the longer the correlation times are the higher the probability of relaxation becomes [99]. In essence, spin relaxation depends on adsorption time, the strength of external or residual magnetic fields acting as perturbations as well as the relevant correlation times.

Following [98, 99], the surface relaxation rate for the model introduced above may be expressed as

$$\gamma_s^A = \left(\frac{2\gamma^2}{3}\right)\left(\frac{\tau_a}{\tau_a + \tau_v}\right)\left(\frac{h_1^2\tau_{c1}}{1 + (\tau_{c1}W_A)^2} + \frac{h_2^2\tau_{c2}}{1 + (\tau_{c2}W_A)^2}\right), \tag{2.13}$$

where τ_{c1} , τ_{c2} are the correlation times of the two distinct relaxation processes, h_1 and h_2 are their respective rms magnetic field amplitudes and W_A is the ground state hyperfine splitting for the relevant atomic species. Since τ_v is defined as the mean time-of-flight between wall bounces and τ_a is the adsorption time, the time ratio in eq. (2.13) is essentially the fraction of time spent by the atom in an adsorbed state. While Bouchiat and Brossel's model is not considered to be definitive, results by Camparo [99], Levy et al. [100] and others have shown general agreement with it[7]. Dry-film coated cells showed the best results because of the weak field in the vicinity of the cell walls which allows for a large number of bounces before de-polarization. Overall, wall de-polarization is believed to be independent of the gas density in the cell and depends mainly on surface properties, such that the coating material and temperature, as well as the static magnetic fields in the region [101].

De-polarization through spin exchange collisions:

Gas particles can also interact with other particles in the gas phase around them. Therefore the interactions are hydrogen-hydrogen or deuterium-deuterium depending

---

[7] Camparo [99] used Pyrex cells coated with dichlorodimethilsilane to study relaxation rates of Rb. Levy et al. [100] used sodium atoms at high magnetic fields in Dry-film coated, uncoated stainless-steel and uncoated copper cells.

on the target gas. Through spin-spin coupling of the respective electrons of the atoms involved in the interactions, the electron spin may be exchanged whereas the nuclear spin remains largely unaffected. Spin exchange collisions have been shown to be density dependent with a weak $1/\sqrt{T}$ temperature depedence due to the time the gas particles spend diffusing in the storage cell.

2.7 Target Holding Field

An electromagnet was used to provide the holding field for both hydrogen and deuterium targets. The main considerations in designing the magnet were the geometry of the target area, the strength and uniformity of the field over the entire cell region as well as the ease of target polarization orientation. Two water-cooled copper coils were installed, one parallel to the beam for the transverse field and one perpendicular to it for the longitudinal. The current applied during operation, and thereby the magnetic field strength of the longitudinal and transverse fields, determined the orientation of the target polarization. Several Hall-probes were mounted in the target chamber to monitor the magnetic field. The magnet used at BLAST was taken from the NIKHEF target and it could provide a magnetic field only in the horizontal plane. It was designed to accomodate the geometry of the storage cell. Both the holding field magnet and the storage cell were housed within the target chamber which also arrived from NIKHEF.

2.8 Sextupole Magnets

The sextupole magnet system takes advantage of the Stern-Gerlach technique to focus the trajectories of atoms with $m_S = +\frac{1}{2}$ and de-focus those with $m_S = -\frac{1}{2}$, where m_S is the projection of the electron spin. In conjunction with the appropriate adiabatic hyperfine transitions, the magnet system selects only the required hyperfine states.

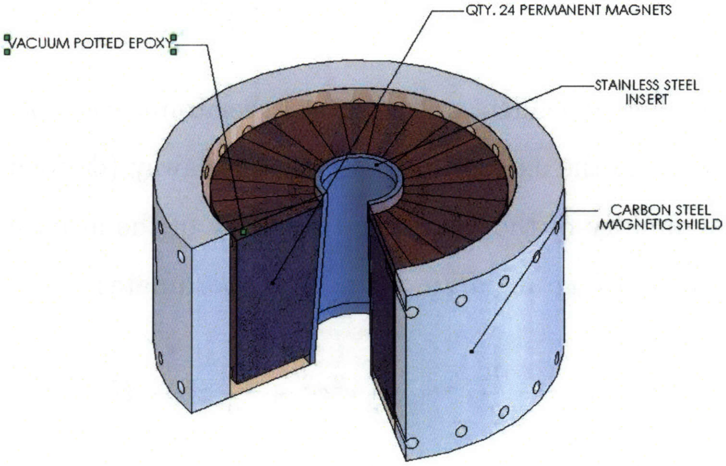

Figure 2-11: The inside of an individual sextupole magnet.

2.8.1 Principles of Operation

The magnetic field inside a sextupole magnet is rotationally symmetric and thus it exhibits no angular dependence. Significantly, the field strength varies quadratically with the radial distance from the magnetic axis as described by

$$B(r) = \frac{3}{2}M\left(\frac{r}{r_{in}}\right)^2\left[1-\left(\frac{r_{in}}{r_{out}}\right)^2\right]\frac{\sin(4\pi\epsilon/N)}{4\pi/N} = B_o(z)\left(\frac{r}{r_o}\right)^2, \tag{2.14}$$

where M is the magnetization, r_{in} and r_{out} the internal and external radii of the magnet, respectively, N the number of magnet segments and ϵ an empirical factor determined by the fraction of magnetized material within the magnet. For simplicity, $B_o(z)$ is used in the calculations by absorbing the non-radiallly dependent factors. The z-axis is defined along beam. The z dependence of the magnetic field is due to the variations of the inner diameter along the length of the magnet system.

The quadratic dependence of the field distribution on the radius gives a gradient which depends on the radius linearly. The force exerted on an atom with electron magnetic moment μ can be calculated by means of the potential V as in

$$F = -\nabla V = -\mu \frac{\partial B}{\partial r} \hat{r}. \tag{2.15}$$

The radial force is then dependent on the spin of the atomic electron, forcing the atom to either orbit closer to the axis (focusing) or further away (de-focusing). Because of the cylindrical symmetry of the force, the trajectory of the atom in the field is best described in terms of a Lagrangian in cylindrical coordinates

$$L = \frac{m}{2} \dot{r}^2 + \frac{m}{2} r^2 \dot{\phi}^2 + \frac{m}{2} \dot{z}^2 - U, \tag{2.16}$$

with the usual kinetic terms and radial potential. The equations of motion are derived using Lagrange's equation of motion [102]

$$\frac{\partial L}{\partial x_i} - \frac{d}{dt} \frac{\partial L}{\partial \dot{x}} = 0 \quad \Rightarrow \quad \ddot{r} = \frac{r \dot{\phi}^2}{2} - \frac{\partial U}{\partial r}. \tag{2.17}$$

Equation (2.17) can be rewritten using conservation of angular momentum in a central-force field and noting the explicit radial dependence of the potential term as

$$\ddot{r} = \frac{L^2}{m^2 r^3} - Ar, \tag{2.18}$$

where L is the angular momentum and A is a constant dependent on the magnetic field. This equation can be integrated analytically to obtain the velocity

$$\dot{r} = \pm \sqrt{const - \frac{L^2}{m^2 r^2} - Ar^2}, \tag{2.19}$$

which is only dependent on the radius.

However, a complication arises if U is non-radial. Considering the same La-

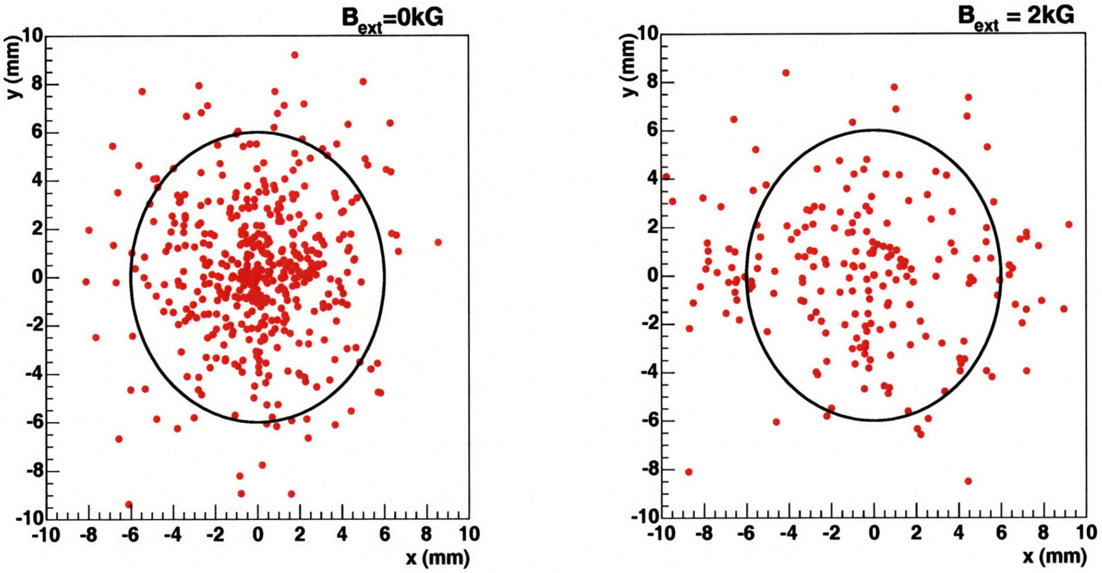

Figure 2-12: Effects of the external field. Shown in both panels is the ABS cross section in overhead view. The left panel shows the expected intensity (particles within the ABS apertures as defined diagrammatically by the circle) for no external field and the right panel for a field of 2 kG. The effect was removed by shielding the sextupoles.

grangian but with $U(r,\, \phi)$, an additional equation of motion has to be obeyed:

$$\ddot{\phi} \;=\; \frac{1}{mr^2}\frac{\partial U}{\partial \phi}, \tag{2.20}$$

which results in a non-zero azimuthal acceleration. This is consistent with a non-radial external magnetic field superimposed to the sextupole field. The effect of the external field is stronger near the z-axis and diminishes as $1/r^2$. Therefore, the presence of an external field will disrupt the focusing capability of the sextupole system.

Such effect was actually observed during operation of the ABS. The intensity of the atomic beam was significantly reduced when the BLAST toroidal field was turned on[8]. While misalignments produced by the field's magnetic strength may have contributed somewhat to the intensity drop, simulations showed that the effect described above was the dominant source. Figure 2-12 shows a simulation of the

---

[8] See Chapter 3 for a description of the toroidal field used at BLAST.

effects of the BLAST toroidal field. Gas particle trajectories are simulated in the ABS geometry for $B_{ext} = 0\,kG$ (left panel) and $B_{ext} = 2\,kG$ (right panel). The presence of the external field reduced the beam intensity by a factor of two [97]. The effect was removed for the most part by adding magnetic shielding to the sextupole magnets, which restored the anticipated intensity.

2.8.2 The Sextupole System at BLAST

The original NIKHEF sextupole magnets were used at BLAST in the beginning. These were Halbach-style permanent magnets and consisted of 24 segments individually fabricated from an NdFeB compound and glued together. The low initial intensity of the ABS led to suspicions that the magnets from NIKHEF were not at full strength. The suspicions were supported by RAYTRACE simulations by varying the magnet strength in the input to the code. To investigate this, the magnets were mounted on a test stand and the magnetic field was mapped with a Gauss probe. The test verified that the top three magnets had lost part of their strength [85, 86] due to exposure to excessive heat ($> 100°C$) during activation of the NEG pumps used to sustain the vacuum in the top sextupole chamber.

New magnets were ordered from Aster Enterprises according to a new design. The material used for the Bates magnets was VAC Vacomax 225HR 2:17 samarium cobalt with improved thermal tolerance. The top three of these magnets had tapered inner diameter, with their inside edges designed to follow the trajectory of the gas particles for optimal focusing. The rest had constant inner diameter. The magnets were assembled at Bates. Each magnet was mounted in a vacuum chamber and a liquid epoxy was spread to cover most of the surface area. The chamber was then sealed and pumped down to allow the air trapped inside the epoxy to escape, thus providing a better vacuum seal. The epoxy used was Masterbond EP39MHT chosen for its low outgassing and good sealing performance. In order to prevent over-heating the magnets in the future, the magnets were mounted in a 0.3 mm stainless steel inner wall. In addition, an 8 mm nickel plated carbon-steel layer was used for magnetic shielding. Finally, the NEG pumps were removed from the sextupole chamber and replaced by SHI APD cryo-pumps [87].

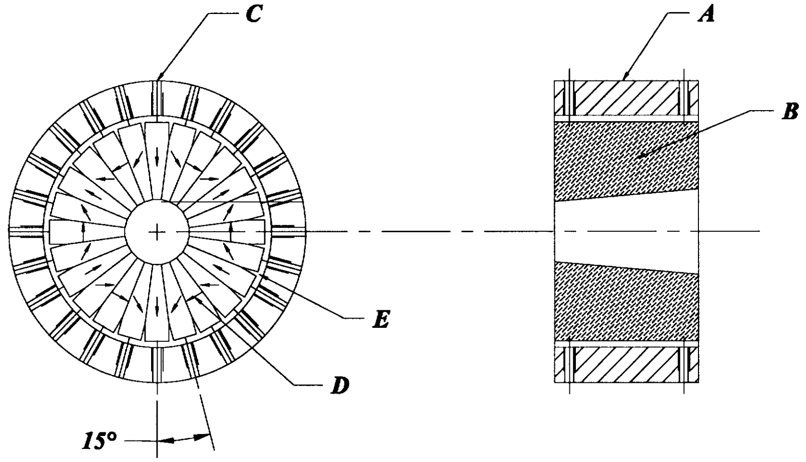

Figure 2-13: The figure on the left shows an overhead view of a sextupole magnet. The figure on the right shows a side cross section from entry point (left) to exit (right). The inner diameter of the magnet increases from left to right (tapering).

2.8.3 The Breit-Rabi Polarimeter

In order to accurately establish the degree of dissociation as well as investigate the relevant hyperfine transitions, a Breit-Rabi Polarimeter (BRP) is typically used. In the current experiment, this proved difficult. Placing a Quadrupole Mass Analyzer (QMA) underneath the target cell was not feasible due to interference from the BLAST magnetic field. Subsequent efforts to shift the position of the QMA downwards towards the floor and away from the region where the toroidal field was strong also proved difficult. The distance to the QMA was too large, thus rendering the signal to noise ratio in the device too small.

In place of the traditional BRP, a dipole electromagnet along with an array of three compression tubes equipped with ion-gauges were placed at the bottom exit of the target cell. The system could provide information on background in the vacuum, degree of dissociation and the hyperfine transitions by separating atoms with positive electronic polarization from those with negative. The compression tubes were used

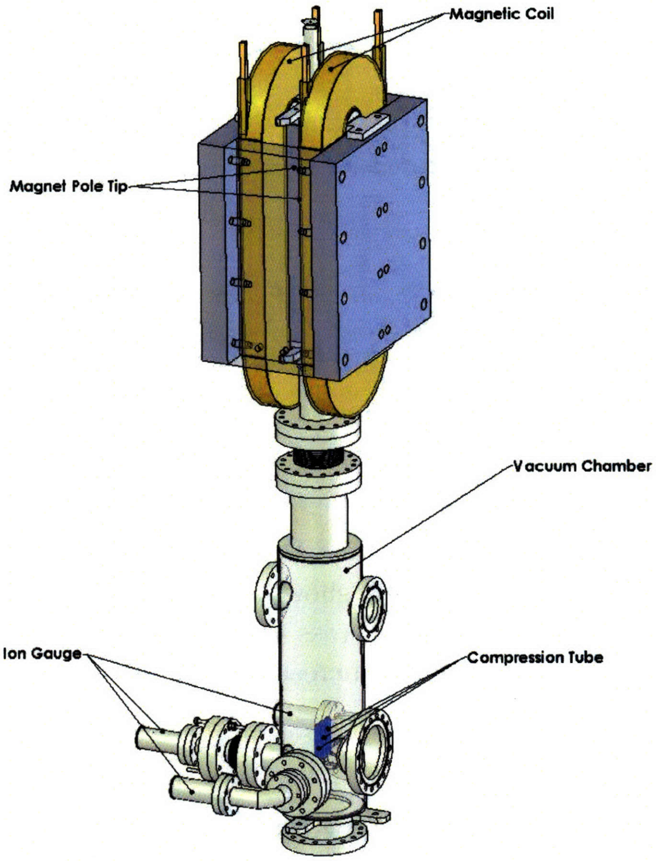

Figure 2-14: Schematic representation of the Breit-Rabi Polarimeter (BRP).

to study the hyperfine transitions for both hydrogen and deuterium.

2.8.4 The Pumping System

The pumps for the ABS were selected for good performance in the BLAST magnetic field and for satisfying the pumping speed requirements of each chamber. NEG pumps originally used for the top-sextupole chamber were replaced due to instablities and the need for regeneration which influenced the sextupole performance. The cryo pumps of the system had to be regenerated with the same frequency as the nozzle (see the Dissociator section). Since cryo-pumps are trap devices and have finite capacity, turbo pumps are used to clean them when turned off. A comprehensive list of the pumps used for the ABS is shown in table 2.2.

Model / Type	Location	Number	Pumping Speed
SHI APD Cryo-pump	Top/Bottom 6pole	1	3000 l/s
OSAKA TG-1120M Turbo-pump	Skimmer	2	2000 l/s
Leybold Vac.Inc. Turbo-pump	Nozzle	2	1800 l/s
Varian Scroll-pump	PGFS	1	250 l/min
Varian V250 Turbo-pump	UGFS	1	250 l/s
Varian PTS300 Scroll-pump	UGFS	1	250 l/min

Table 2.2: Vacuum pumps used for the various chambers of the target and the gas feed systems.

Typical pressures achieved in the various sections of the apparatus during atomic beam operation are listed in table 2.3.

Chamber	Gauge	Pressure (torr)
PGFS	Convectron	9.2
Nozzle	Ion gauge	1.2×10^{-4}
Skimmer	Ion gauge	2.6×10^{-5}
Top sextupole	Ion gauge	2.1×10^{-7}
Bottom sextupole	Ion gauge	9×10^{-8}
Ligit	Ion gauge	1×10^{-7}

Table 2.3: The vacuum for the various chambers of the ABS during Deuterium running.

2.9 Beam Formation

The intensity of the ABS is a function of several variables and can be modeled by

$$I(Q) = Q\times 2D\times P\times\Omega\times T = I_o Q A(Q), \tag{2.21}$$

where I is the intensity of the beam, Q is the flow into the dissociator, D is the degree of dissociation, Ω a solid-angle geometrical factor and T the transmission probability through the sextupole magnet systems. Finally, P denotes the peaking factor of the intensity distribution after beam formation at the nozzle [88]. A(Q) denotes the *beam*

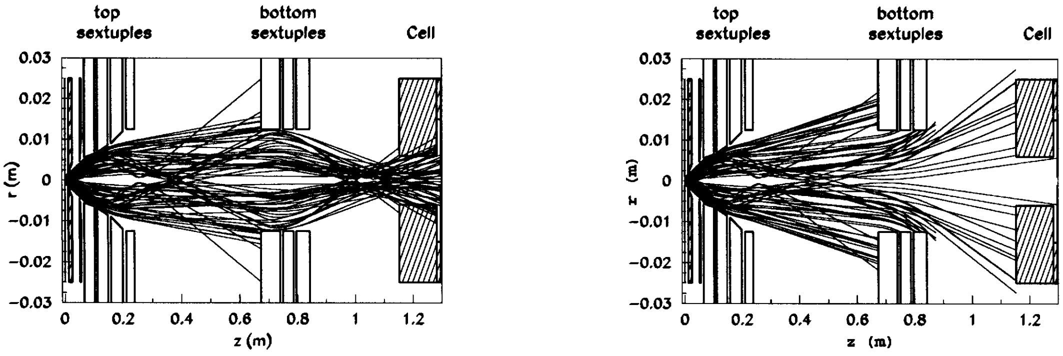

Figure 2-15: Raytrace simulations of beam focusing through the ABS optics and the sextupole system. The sextupoles focus atoms with positive electron polarization into the cell. The simulations were used to optimize the optics during commissioning of the target. They had also been used prior to that to determine the ideal shape and positions for all the magnets of the sextupole systems.

attenuation and can be expressed as a function of the throughput Q and the position along the beam-axis z

$$A(Q) \;=\; e^{-\int \rho(Q,z)\,\sigma(Q,z)dz}. \tag{2.22}$$

The beam attenuation is essentially a measure of the resistivity the beam encounters due to rest gas in the chambers. The presence of rest gas is mainly due to inefficient pumping in the sextupole chambers. Gas particles de-focused by the sextupoles have to be pumped out of the system, otherwise they may remain in the beam-flow area as background of density $\rho(Q,z)$. This background causes interactions with the beam particles with cross section $\sigma(Q,z)$ which attenuate the beam. The effects of the residual gas have to be considered to determine the necessary pumping speed for each chamber. For this purpose, specially made inlets were installed in the chambers to study beam attenuation as a function of the pressure. The effect was also investigated with RAYTRACE simulations. The results showed losses in intensity because of low pumping speed in the first two chambers as well as high-density background in the sextupole chambers [88], where sufficient pumping was most critical. Both problems were addressed by re-designing the pumping system or adding pumps as needed to improve the density in the sextupole chambers by a factor of 2 to 4.

The size of the apertures as well as their relative distances were largely unaltered with respect to the NIKHEF configuration. These can be studied using RAYTRACE simulations as well. By varying all aspects of the geometry invlolved, the intensity output can be maximized. Figure 2-15 shows a typical result of the simulation. Shown here is the path of the beam through the nozzle-skimmer-collimator configuration and the sextupole system. The x axis represents the vertical distance through the ABS and the y axis the perpendicular distance from the central axis. Note the tapering of the magnets which helps guide the beam for optimal results.

2.10 Hyperfine Structure

2.10.1 Theoretical Description

The hyperfine structure of an atom is associated with the magnetic interaction between the dipole moments of its nucleus and the electrons surrounding it. The case of Hydrogen follows the description of the quantum-mechanical two spin-1/2 particle system. Here, the coupling occurs between the nuclear proton and the shell electron and produces a total of four distinct states. Three of these are degenerate in energy (triplet), whereas the fourth state is non-degenerate (singlet). Using the notation $|F\,m_F>$, where $\vec{F} = \vec{I} + \vec{S}$ is the total angular momentum, I and S being the angular momenta of the nucleus and the electron, respectively, one can express the states as

$$\text{triplet (F = 1)} = \begin{cases} |1\,1> = \uparrow\uparrow \\ |1\,0> = \frac{1}{\sqrt{2}}(\uparrow\downarrow \; + \; \downarrow\uparrow), \\ |1\,1> = \downarrow\downarrow \end{cases} \tag{2.23}$$

which are symmetric in spin-space and

$$\text{singlet (F = 0)} = \left\{ |0\,0> = \frac{1}{\sqrt{2}}(\uparrow\downarrow \; - \; \downarrow\uparrow), \right. \tag{2.24}$$

which is anti-symmetric.

In the case of deuterium, the coupling follows the quantum mechanics of a spin-1 - spin-1/2 coupling. As a result, the splitting in this case results in 6 distinct states,

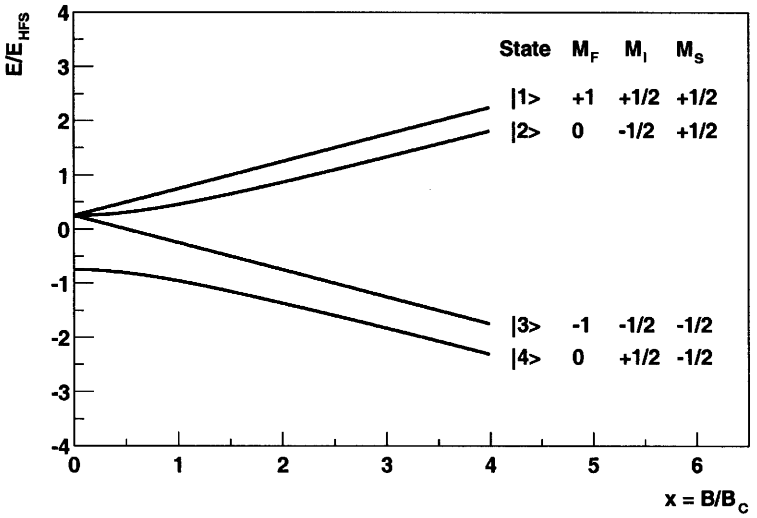

Figure 2-16: The hyperfine structure of Hydrogen. The plot shows the energy separation between the different states as a function of the magnetic field.

a doublet and a quadruplet. In fact, the degeneracy of each level in a system is 2F+1. The coupling of a general system is governed similarly by the laws of addition of angular momenta. The coefficients that determine the states are called Clebsch-Gordan coefficients and can be found in convenient tables [103].

In the presence of an external magnetic field $\vec{B}$, the degeneracy is broken. The Hamiltonian of the system can then be written as

$$H_{\vec{B}} = \frac{2h\nu_o}{3}\vec{I} \bullet \vec{S} + \mu_B(g_S\vec{S} + g_I\vec{I}) \bullet \vec{B}, \tag{2.25}$$

where g_S and g_I are the gyromagnetic ratios of the electron and the nucleus, respectively, and μ_B is the Bohr magneton. Here, the first term describes the spin-spin interaction between the nucleus and the electron whereas the second term describes their respective coupling to the magnetic field. In the limit of $B \longrightarrow 0$, the energy separation is defined as

$$E^H_{HFS} = \alpha_H \hbar^2 \quad \text{(for hydrogen) and } E^D_{HFS} = \alpha_D \hbar^2 \text{ (for deuterium).} \tag{2.26}$$

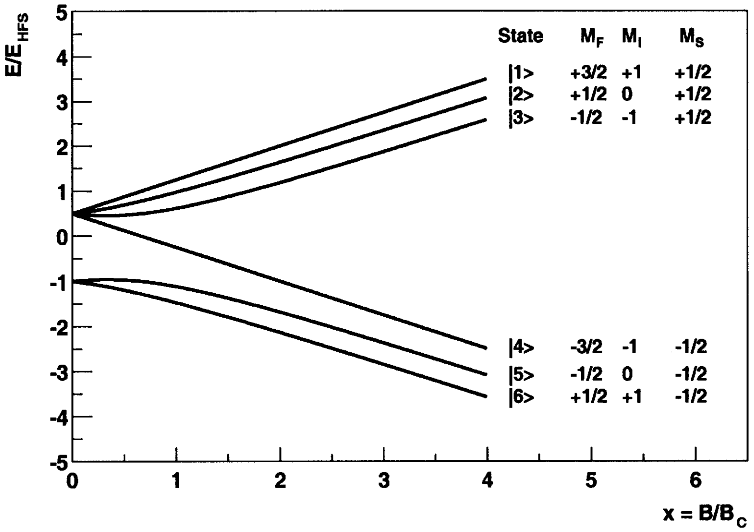

Figure 2-17: The hyperfine structure of Deuterium.

The definition of nuclear vector polarization is shown in eq. (2.27) for hydrogen:

$$P_{nuc} = \frac{N_{I=1/2} - N_{I=-1/2}}{N_{I=1/2} + N_{I=-1/2}}. \tag{2.27}$$

Using the analytic equations for the occupation numbers as derived in the Appendix, the nuclear vector polarization is given by

$$P_z = n_1 - n_3 - (n_2 - n_4) \cos 2\theta \tag{2.28}$$

as a function of the mixing angle θ, which depends on the external magnetic field. Similarly, the atomic electron polarization for hydrogen is given by

$$P_e = n_1 - n_3 - (n_4 - n_2) \cos 2\theta. \tag{2.29}$$

For deuterium, the two polarizations can be expressed in terms of the occupation numbers and two mixing angles as shown in eq. (6.16) of the appendix. Nuclear vector and atomic electron polarizations are then expressed as

$$P_e = n_1 - n_4 + (n_2 - n_6) \cos 2\theta_+ + (n_3 - n_5) \cos 2\theta_- \tag{2.30}$$

$$P_z = n_1 + n_6 - n_3 - n_4 + (n_2 - n_6)\sin^2\theta_+ + (n_3 - n_5)\sin^2\theta_-. \qquad (2.31)$$

The polarizations for both hydrogen and deuterium are shown in figures 2-18 and 2-19 as functions of the external magnetic field. For the hydrogen target at BLAST, the decision was made to run only a single-state sequence, selecting the two pure hydrogen states 1 and 3 for injection into the target cell. While this limited intensity, the polarization dependence of states 2 and 4 on the external magnetic field would dilute the overall polarization, thus decreasing the overall figure of merit. This was a limitation associated with the holding field magnet which can produce a maximum field of the order of 450 Gauss. Therefore, the non-pure states would be incompletely polarized (P_z less than unity).

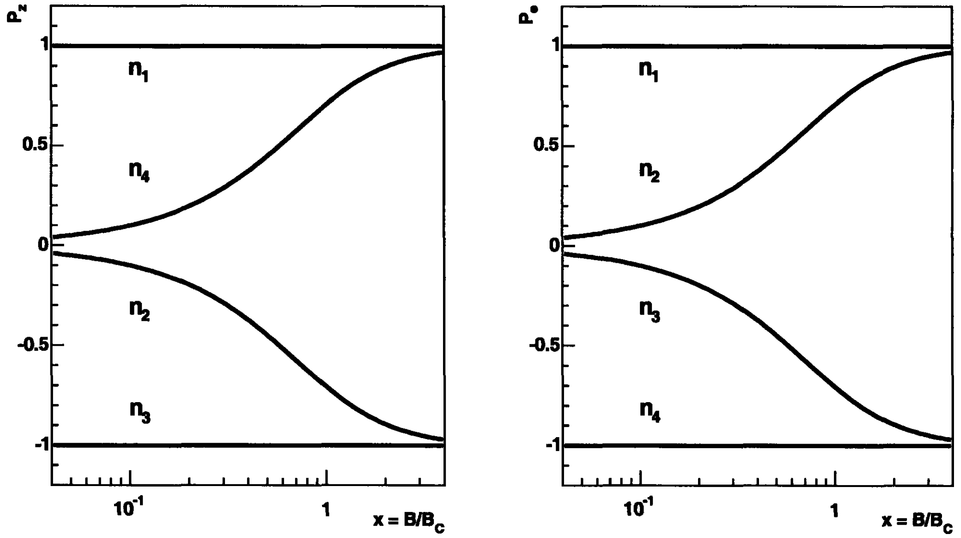

Figure 2-18: The left panel shows the nuclear vector polarization for each of the four hydrogen hyperfine states as a function of the magnetic field. The right panel shows the atomic electron polarization. States 1 and 3 are pure states for which the polarization is independent of the field.

2.11 RF Transitions

Radio-frequency transitions were initially developed at Saclay for an atomic beam which was ionized in a cyclotron magnetic field [104]. Their success in delivering highly polarized beams with easily changeable states helped spread their use. The

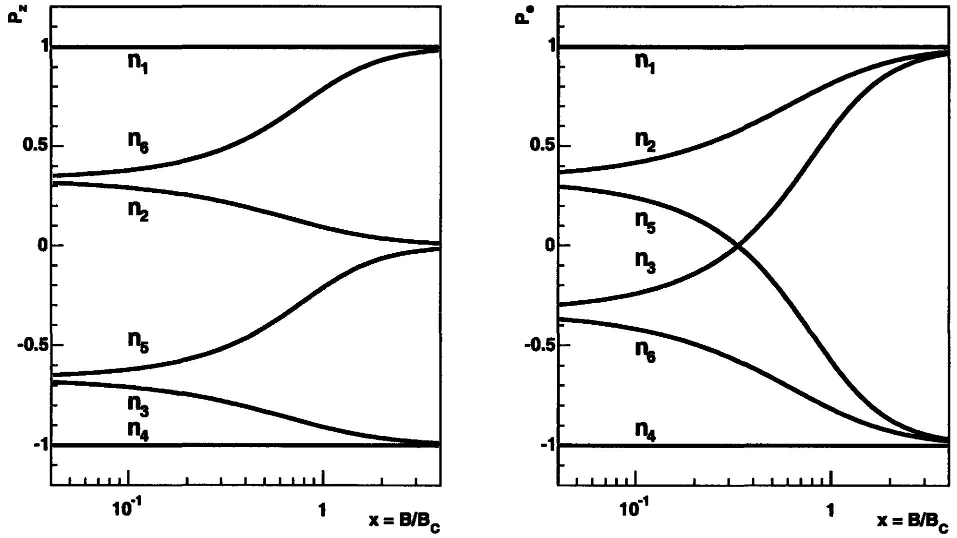

Figure 2-19: The left panel shows the nuclear vector polarization for each of the six deuterium hyperfine states as a function of the magnetic field. The right panel shows the atomic electron polarization. States 1 and 4 are pure states.

transitions are based on the *adiabatic passage method* as first proposed by Abragam and Winter [105].

The adiabatic passage is based on the physics of a magnetic moment precessing in a magnetic field [104, 106]. Three fields are needed for an efficient transition: the static and gradient field and an oscillating RF field. Classicaly, in a stationary frame (henceforth referred to as "lab frame"), a magnetic moment $\vec{M}$ with angular momentum $\gamma\vec{J}$ as shown in figure 2-20, will experience a torque in the presence of a static magnetic field B_{st} in the $\hat{z}$-axis, given by

$$\vec{T} = \frac{d\vec{J}}{dt} = \vec{M} \times \vec{B}_z, \tag{2.32}$$

and will therefore precess around the $\hat{z}$-axis with angular velocity $\omega_z = -\gamma B_z$[9]. In a frame rotating with ω_z with respect to the stationary frame (referred to here as "Larmor frame"), $\vec{M}$ is stationary at a fixed angle with respect to the $\hat{z}$-axis and the static magnetic field is zero. In the lab frame, an oscillating field B_{RF} is applied in a direction perpendicular to $\hat{z}$, in addition to B_{st}. If the frequency of oscillation is matched with the Larmor frequency ω_z, the effect of the oscillating field is equivalent

---

[9] The phenomenon is frequently referred to as *Larmor precession* and ω_z as the Larmor frequency.

to that of a rotating field around the $\hat{z}$-axis with frequency ω_z and magnitude $B_{RF}/2$ [107]. Consequenty, this field is stationary in the Larmor frame, causing precession of $\vec{M}$ in the same manner as before. The total angle of precession is manifestly time-dependent.

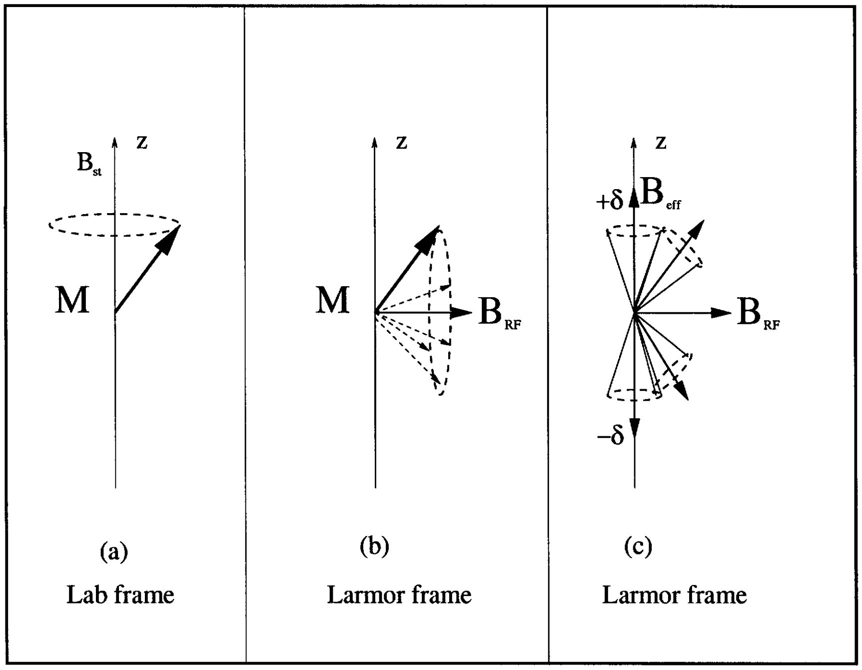

Figure 2-20: The figure above displays the principles of an adiabatic transition. In (a), the magnetic moment M precesses in the presence of a static field in the z-axis of the lab frame. In (b), an RF field oscillating with ω_z in the lab frame manifests itself as a fixed field in the Larmor frame. The magnetic moment will precess around it. In (c), the gradient field is added. The magnetic moment will follow the B_{eff} vector until fully reversed. The transition is complete and velocity independent.

In the ABS configuration, an atom travels through both B_{st} and B_{RF} and its atomic electron spin precesses, thus switching to a different hyperfine state. As the angle of precession is time-dependent, the final hyperfine state essentially depends on the velocity of the atom. Since the velocity distribution of the ABS beam obeys Maxwell-Boltzmann statistics, the transition will be inefficient. This can be remedied with the addition in the lab frame of a gradient field B_{gr} in the direction of the B_{st}, so that the total field in the $\hat{z}$ direction decreases from $B_{st} + \delta$ to $B_{st} - \delta$ in the lab frame and along the direction of travel of the beam. In the Larmor frame, the total field along the axis changes from δ to $-\delta$. Thus, the effective field overall in this frame, will turn 180° and the magnetic moment $\vec{M}$ will be reversed. Certain conditions have to be obeyed for the transition to be complete. First, the magnitude of the RF field has to be much less than that of the gradient field. Moreover, for the transition to remain adiabatic even at the point when the B_{eff} consists entirely of the RF component, the condition

$$\frac{d(B_{st} + B_{gr})}{dt} << \gamma B_{RF}^2 \quad , \tag{2.33}$$

known as the *adiabatic condition*, has to be valid [104].

The quantum-mechanical treatment of the same problem is based on perturbation theory. The high-frequency field is thereby considered as a perturbation to the original Hamiltonian. For a spin 1/2 particle, the eigenstates of the new Hamiltonian are linear combinations of the eigenstates of the original system

$$\begin{aligned} |+> &= \sin\theta\,|a> + \cos\theta\,|b> \\ |-> &= \cos\theta\,|a> - \sin\theta\,|b>, \end{aligned} \tag{2.34}$$

where the mixing angle θ depends on the magnitudes of the magnetic fields used. The mixing angle approaches 0° or 90° at the two extrema of the $\hat{z}$-axis magnetic field. The new Hamiltonian states will be identical to those of the unperturbed Hamiltonian, while a complete reversal of states has also occurred (an atom initially in state $|a>$ has transitioned to state $|b>$ after traversing the region where the magnetic fields are applied and vice versa). In order for the transition to be efficient, the change in the mixing angle, or equivalently, the change in the $\hat{z}$-axis field, has to be slow enough so that the adiabatic condition (eq. (2.33)) still applies.

Strong Field Transitions:

Strong Field Transitions, henceforth referred to as SFT, are transitions between different Zeeman multiplets (see the Breit-Rabi diagrams in figures 2-16 and 2-17). Therefore, the total angular momentum of the system changes by $\Delta F = \pm 1$. In hydrogen for example, such transitions will exchange the occupation numbers of state

$|4>$ of the singlet to one of the three states of the multiplet. The change in the projection of the total angular momentum further separates the SFT into $\pi-$transitions $(\Delta m_F = \pm 1)$ and $\sigma-$transitions $(\Delta m_F = 0)$. Hence there is only one σ and two π transitions in hydrogen while there can be two σ and four π in deuterium.

For the hydrogen target at BLAST, no SFT is necessary. For deuterium, the SFT35 and SFT26 are both used in conjunction with Medium Field Transitions to provide the required polarization modes. In this notation, SFT35 refers to a strong field transition between hyperfine states 3 and 5. The SFT transitions used for deuterium are displayed in the bottom panel of figure 2-22, where the energy separation is plotted versus the static magnetic field.

Medium and Weak Field Transitions:

In contrast to the SFT, Medium Field Transitions (MFT) and Weak Field Transitions (WFT) do not change the total angular momentum of the system $(\Delta F = 0)$. Since there are no two states with the same m_F in a single Zeeman multiplet, only π-transitions may occur.

For the hydrogen target at BLAST, the relevant transitions are MFT23 and MFT12 as shown in figure 2-21. The resulting occupation exchange between the hyperfine states depends on the gradient field. For positive gradient, the MFT23 is traversed first, whereas the opposite is true for negative gradient. In order to achieve an effective MFT13 transition in two stages, the change in the gradient field has to be large enough so that both resonance conditions are traversed. A cascade WFT13 transition is also used. For the deuterium target modes, the effective transition required is an MFT14, which may be obtained through the sequence MFT34, MFT23, MFT12. This corresponds to a positive gradient (see top panel of figure 2-22). A cascade transition WFT14 is also implemented.

Transition sequences at BLAST

Occupation multiplet sequence eq. (2.35) shows the procedure followed to obtain *Vector minus* polarization for hydrogen.

Transition	RF amplitude	Gradient (G/cm)	Total Field(G)	Freq (MHz)
MFT34	-5db	-2	-20	30
MFT14	-5db	-5	45	30
SFT26	-5db	-5	63	420
SFT35	4V	-5	141	420
WFT14	-15db	-4	20	8

Table 2.4: The deuterium transitions used with the BLAST ABS.

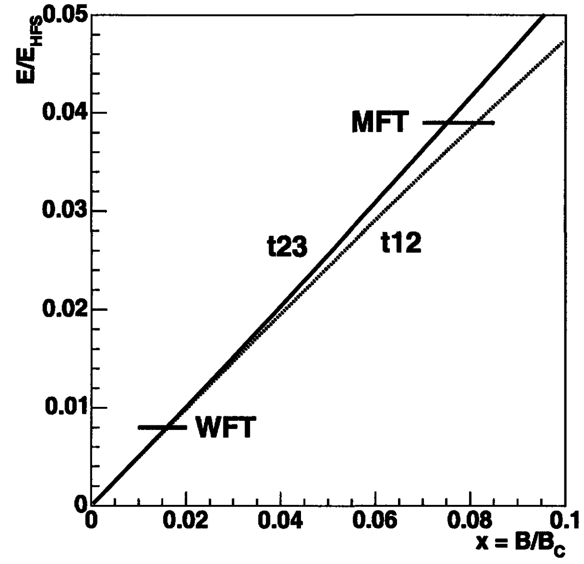

Figure 2-21: The transitions used to create the polarization modes for hydrogen.

$$\begin{pmatrix} n_1 \\ n_2 \\ n_3 \\ n_4 \end{pmatrix} \xrightarrow{\text{sixpole}} \begin{pmatrix} n_1 \\ n_2 \\ 0 \\ 0 \end{pmatrix} \xrightarrow{\text{MFT23}} \begin{pmatrix} n_1 \\ 0 \\ n_2 \\ 0 \end{pmatrix} \xrightarrow{\text{sixpole}} \begin{pmatrix} n_1 \\ 0 \\ 0 \\ 0 \end{pmatrix} \xrightarrow{\text{WFT13}} \begin{pmatrix} 0 \\ 0 \\ n_1 \\ 0 \end{pmatrix} \qquad (2.35)$$

Initially, all hyperfine states were equally populated. In the multiplet, the occupation numbers are denoted by n_1, n_2, n_3 and n_4. The states with negative atomic electron spin, n_3 and n_4, were rejected in the first sextupole system. Subsequently, the MFT23 transition exchanged the populations of states 2 and 3. Since 3 was empty

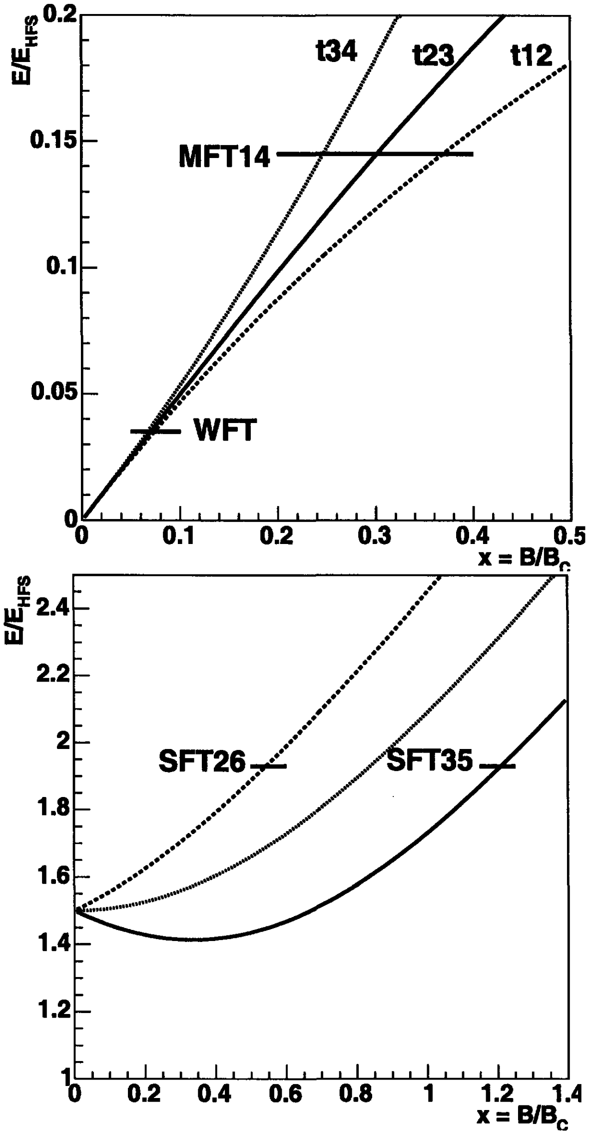

Figure 2-22: The RF transitions used to create the three polarization modes for Deuterium.

when the beam entered the MFT transition area, state 2 was emptied due to the exchange. The second sextupole system discarded state 3 and the final transition, the cascade WFT, transfered all atoms from state 2 to 3. According to the Breit-Rabi diagram (fig. 2-16), state 3 is a pure state with negative polarization. The same principles applied to the sequence for *Vector plus*,

$$\begin{pmatrix} n_1 \\ n_2 \\ n_3 \\ n_4 \end{pmatrix} \xRightarrow{\text{sixpole}} \begin{pmatrix} n_1 \\ n_2 \\ 0 \\ 0 \end{pmatrix} \xRightarrow{\text{MFT23}} \begin{pmatrix} n_1 \\ 0 \\ n_2 \\ 0 \end{pmatrix} \xRightarrow{\text{sixpole}} \begin{pmatrix} n_1 \\ 0 \\ 0 \\ 0 \end{pmatrix} . \tag{2.36}$$

For this mode, the WFT unit was turned off so that the final state was state 1, a pure state with positive electron and nuclear polarization. The two sequences above were selected at random with a 5 minute period.

The principles behind the deuterium sequences are very similar. For the polarized deuterium target, the *Vector minus, Vector plus* and *Tensor minus* polarization modes were used. For Vector minus, the procedure is shown in eq. 2.37

$$\begin{pmatrix} n_1 \\ n_2 \\ n_3 \\ n_4 \\ n_5 \\ n_6 \end{pmatrix} \xRightarrow{\text{sixpole}} \begin{pmatrix} n_1 \\ n_2 \\ n_3 \\ 0 \\ 0 \\ 0 \end{pmatrix} \xRightarrow{\text{MFT(34)}} \begin{pmatrix} n_1 \\ n_2 \\ 0 \\ n_3 \\ 0 \\ 0 \end{pmatrix} \xRightarrow{\text{sixpole}} \begin{pmatrix} n_1 \\ n_2 \\ 0 \\ 0 \\ 0 \\ 0 \end{pmatrix} \xRightarrow{\text{WFT}} \begin{pmatrix} 0 \\ 0 \\ n_2 \\ n_1 \\ 0 \\ 0 \end{pmatrix} . \tag{2.37}$$

Equations (2.38) and (2.39) show the sequences for Vector plus and Tensor minus, respectively.

$$\begin{pmatrix} n_1 \\ n_2 \\ n_3 \\ n_4 \\ n_5 \\ n_6 \end{pmatrix} \xRightarrow{\text{sixpole}} \begin{pmatrix} n_1 \\ n_2 \\ n_3 \\ 0 \\ 0 \\ 0 \end{pmatrix} \xRightarrow{\text{MFT(34)}} \begin{pmatrix} n_1 \\ n_2 \\ 0 \\ n_3 \\ 0 \\ 0 \end{pmatrix} \xRightarrow{\text{sixpole}} \begin{pmatrix} n_1 \\ n_2 \\ 0 \\ 0 \\ 0 \\ 0 \end{pmatrix} \xRightarrow{\text{SFT(26)}} \begin{pmatrix} n_1 \\ 0 \\ 0 \\ 0 \\ 0 \\ n_6 \end{pmatrix} \tag{2.38}$$

$$\begin{pmatrix} n_1 \\ n_2 \\ n_3 \\ n_4 \\ n_5 \\ n_6 \end{pmatrix} \overset{\text{sixpole}}{\Longrightarrow} \begin{pmatrix} n_1 \\ n_2 \\ n_3 \\ 0 \\ 0 \\ 0 \end{pmatrix} \overset{\text{MFT(14)}}{\Longrightarrow} \begin{pmatrix} 0 \\ n_2 \\ n_3 \\ n_1 \\ 0 \\ 0 \end{pmatrix} \overset{\text{sixpole}}{\Longrightarrow} \begin{pmatrix} 0 \\ n_2 \\ 0 \\ 0 \\ n_3 \\ 0 \end{pmatrix} \overset{\text{SFT(35)}}{\Longrightarrow} \begin{pmatrix} 0 \\ 0 \\ n_3 \\ 0 \\ 0 \\ n_6 \end{pmatrix} \tag{2.39}$$

MODE	Vector plus	Vector minus	Tensor minus
MFT	3-4	3-4	1-4
WFT	Off	1-4 and 2-3	Off
SFT	2-6	Off	3-5
P_e	0	0	0
P_z	+1	-1	0
P_{zz}	+1	+1	-2
B_{hold}	350G	350G	350G
n_{target}	1+6	3+4	2 +5

Table 2.5: A summary of the transitions used for the three polarization modes of the deuterium target. Listed are the different transitions required per transition unit and per mode, the target holding field, the remaining states in the storage cell and the electron, vector and tensor polarizations.

Figure 2-23 shows scans of the MFT transition with SFT and WFT off. The left panel shows the MFT14 and the right panel the MFT34 transition. While the MFT34 is well saturated and unambiguous, the transition MFT14 cannot be separated from the MFT34 and MFT24 that also take place. To separate the MFT transitions, an additional transition has to take place. This can be achieved by using the SFT26 transition in the case of Deuterium, as explained in the discussion that follows.

By tuning the magnitude of the static field, one of three transitions, MFT34, MFT24, and MFT14 may be selected. The respective energy difference of the corresponding states in each of these transitions grows from left to right and thus a higher

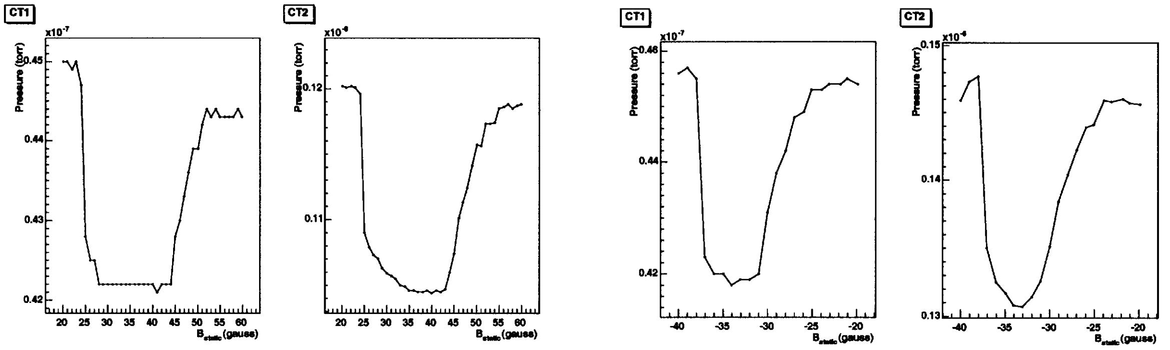

Figure 2-23: The MFT14 (left) and MFT34 (right) transitions.

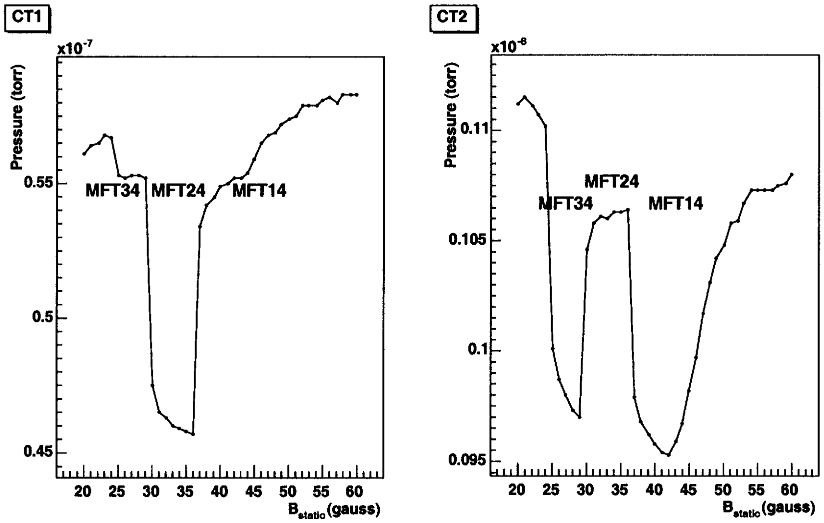

Figure 2-24: A scan of the static field of the MFT unit with the SFT26 transition turned on. The three transitions MFT34, MFT24 and MFT14 are well separated.

magnetic field is required for higher energy exchanges. The left panel in figure 2-24 shows the response of the upstream compression tube (which collects the positively polarized atoms) when the static field of the MFT unit is scanned and the SFT26 transition is turned on. The right panel shows the response of the downstream tube (negative polarization)[10]. The structure here can be explained by writing out the actual sequences in multiplet format.

---

[10] The scale of the background vacuum for each tube depends on the calibration of the ion-gauges. Both backgrounds are presented here not normalized to each other.

2.11.1 Transition Units

Three separate RF transition units were installed in the ABS. The MFT was located in a dedicated chamber in between the two sextupole chambers, whereas the WFT and SFT shared the same chamber located right after the second sextupole set (figure 2-1).

MFT:

The MFT unit consisted of an RF coil inside a water-cooled coil to provide the static field and another set of coils for the gradient field. The unit was located between the two sextupole chambers, in a region where the BLAST toroidal magnetic field was significant, necessitating additional magnetic shielding. The RF-coil, as shown in figure 2-25, was 6 cm in length, 3 cm in diameter, had a total of 6 turns and was located inside the shielding and the static field magnet. The amplitude of the field was monitored with a small pick-up coil while the RF frequency was fixed at 30 MHz for deuterium and 60 MHz for hydrogen operation. In order to eliminate possible transitions induced by external RF fields, end-cups were used on both ends of the beam path through the MFT unit to act as RF-terminators to eliminate RF field leakage into other components.

WFT:

The WFT unit was located right after the second sextupole magnet system and in the same vacuum chamber. The unit consisted of an RF coil inside of an electromagnet. The coil provided RF of 8MHz for deuterium and 12 MHz for hydrogen whereas the electromagnet provided the static field. Finally, the gradient field was produced by coils attached to the inside surface of the static field magnet. The primary RF coil was coupled to a smaller magnetic pick-up coil to produce feedback. The induced current through the pick-up coil was monitored through EPICS. Standard feedthroughs were used for input current and for readout while a Hall-probe was used to monitor the field strength. A matching network was designed and used for both MFT and WFT coil-tuning. An autotuner was used to maximize the RF current delivered to the coils for the intended frequency [108]. Figure 2-26 shows a schematic of the WFT coil.

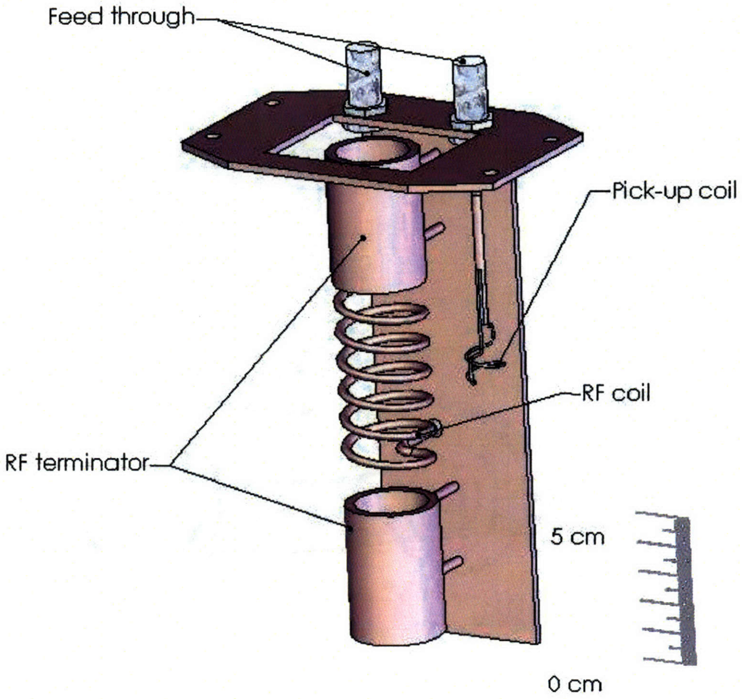

Figure 2-25: The MFT unit consisted of an RF-coil to produce a time-varying field along the path of the atomic beam. Since the unit was located in high magnetic field from the BLAST toroid, it had to be shielded for optimal operation.

SFT:

The SFT unit consisted of a rectangular resonance cavity with two adjustable capacitors for impedance matching. Adjustments of the tap point of the capacitors had to be performed before installation of the unit in the ABS. The SFT used the same electromagnet as the WFT. Since the two units were not used concurrently for any polarization mode, their joint use of the magnet was operationally possible. A small pick-up coil provided real-time feedback on the field inside the cavity, the inside surfaces of which were silver-plated to reduce thermal heating effects. The SFT unit was used exclusively for the deuterium target at 420 MHz with around 10 W forward power. Figure 2-26 shows a schematic of the SFT cavity.

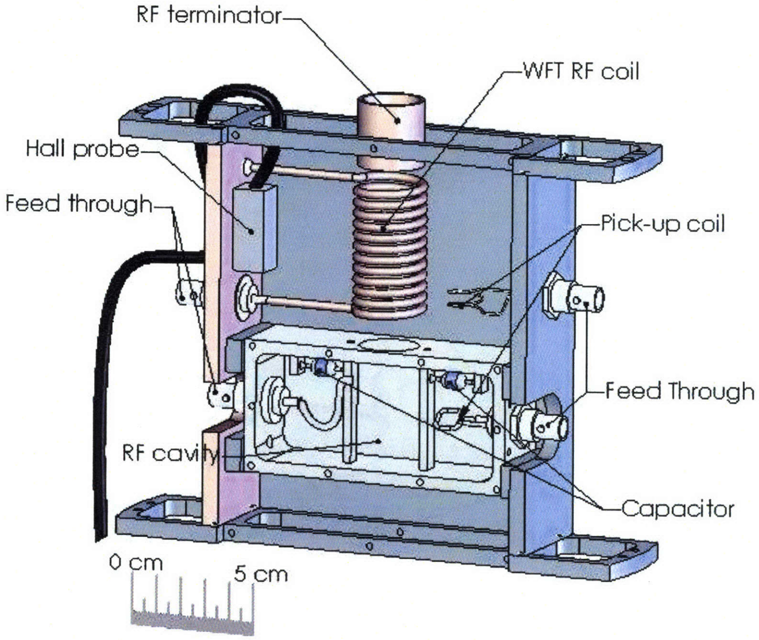

Figure 2-26: The WFT coil and the SFT cavity shared the same electromagnet and gradient field.

2.12 Performance of the BLAST ABS

An evaluation of the performance of the BLAST target system can be attempted in terms of quantifiable and non-quantifiable terms. The latter include opearional efficiency, functionality and ease of use whereas the former consist mainly of polarization and intensity results.

2.12.1 Polarization Results at BLAST

The vector polarization for the Deuterium target was derived from an ${}^{2}\vec{H}\,(\vec{e}, e'p)$ analysis around the quasi-elastic peak and at low missing momentum (less than 100 MeV/c). The value of the product of beam and target polarizations is derived by fitting the vector asymmetry to Monte Carlo in which the product was set to unity. The values for the beam polarization from an analysis of Compton polarimeter data allows extraction of the target vector polarization in itself. Results for the 2004 and

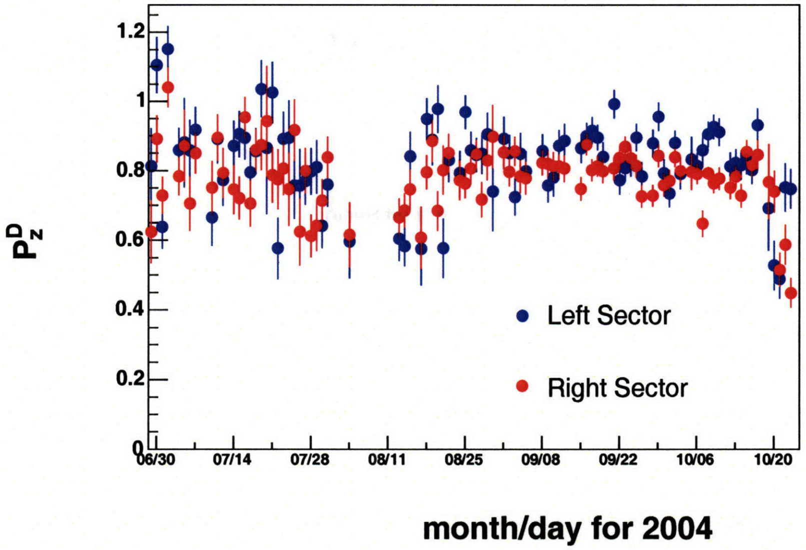

Figure 2-27: Deuterium target Vector polarization P_z^D for the data taken during the 2004 running period. The polarization value is plotted here versus the date the data were collected. Left and right polarizations mostly agree within error bars and were constant during the running period. Blue is used to denote the results from left sector electrons and red from right sector electrons. The errors shown here are only statistical.

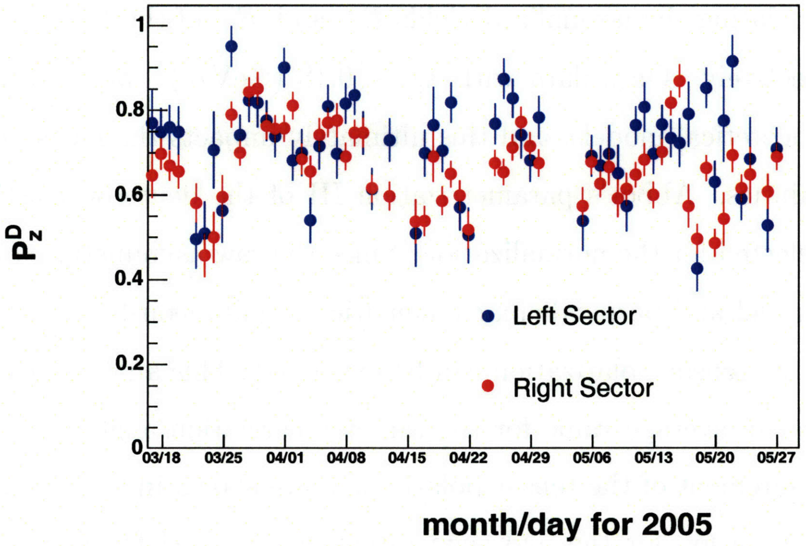

Figure 2-28: Same as figure 2-27 for the 2005 data.

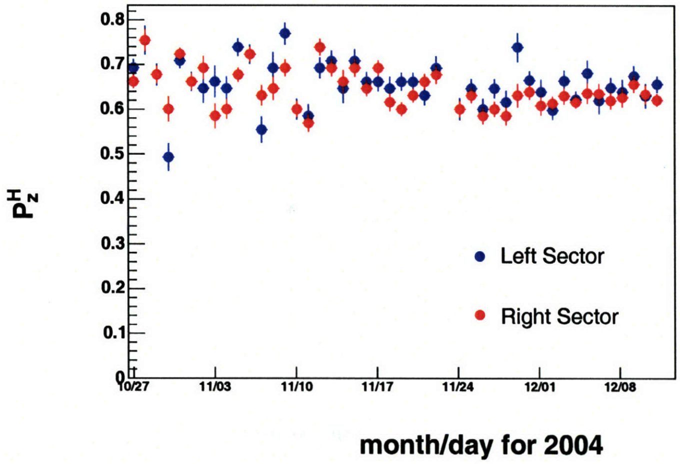

Figure 2-29: Hydrogen target polarization P_z^H for left and right sectors for data taken at the end of 2004.

2005 data sets are shown in figures 2-27 and 2-28, respectively. The target yielded consistently high polarization throughout the production data-taking.

The value of the tensor polarization was extracted from an electron-deuteron elastic scattering analysis. The raw asymmetry

$$A = \sqrt{2}\frac{R^+ - R^-}{R^+ + 2R^-} = P_{zz} \times A_{exp} \tag{2.40}$$

is measured by calculating the normalized yields R^+ and R^- of the tensor plus and minus states, respectively. Only data with $Q^2 < 0.18$ (GeV/c)^2 were used in the normalization to theoretical models, and this ultimately impacts the measurement's systematic uncertainties. Abbot's parametrization III of the deuteron elastic form factors [109] was selected for the normalization. Since the raw asymmetry can be extracted in both parallel and perpendicular kinematics simultaneously, an additional parameter besides the tensor polarization can be extracted. This analysis was therefore used to extract an average value for the target polarization angle [14]. Partial results for the measurement of the tensor polarization are shown in figure 2-29.

Finally, the polarization for the hydrogen target was derived from an electron-proton elastic scattering analysis. Coincidence and timing cuts were used to select

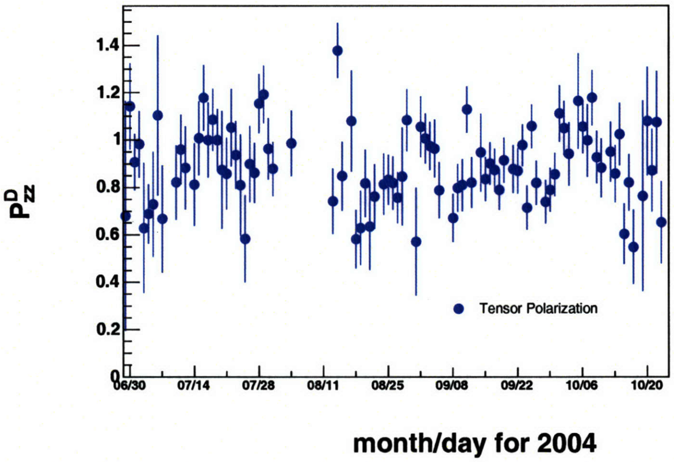

Figure 2-30: Deuterium target tensor polarization P_{zz}^D derived from an electron-deuteron elastic scattering analysis. Only a part of the data is plotted here. A brief description of the method can be found in the text.

good events and the relevant asymmetry was compared to a Monte-Carlo result. The measured polarization for the data collected at the end of 2004 is shown in figure 2-30 for the entire running period.

2.12.2 Intensity Results at BLAST

Since the efficiencies of the BLAST detector components were not established accurately, the target density had to be deduced from an analysis of the electron-deuteron elastic scattering reaction and double-checked with the buffer system. Thus, a thickness of approximately 4.5×10^{13} atoms/cm^2 for both hydrogen and deuterium targets was measured, the former checked with electron-proton elastic scattering off hydrogen. This value corresponds to roughly 2.6×10^{16} atoms/sec intensity into the target cell.

Several steps were taken during commissioning and operation to improve the intensity.

1. The pumping system for all chambers was significantly improved.
2. A systematic method to optimize alignment was used when necessary.

3. Magnetic shielding was added to several components of the ABS.
4. The optics were fine-tuned for optimum beam formation.

More details about the above can be found in the preceding sections.

The results for both intensity and polarization with the BLAST ABS were outstanding, both in consistency as well as actual magnitudes. The BLAST ABS figure-of-merit, defined as the product of the luminosity and the target polarization squared, far exceeded the one at NIKHEF [83] for both hydrogen and deuterium targets.

Chapter 3

The BLAST Detector

3.1 Introduction

The experiment took place at the MIT-Bates Linear Accelerator Center in Middleton, Massachusetts. The BLAST detector was located in the South Experimental Hall to take advantage of the facility's storage ring. In this chapter, a brief description of the experimental apparatus is provided. The BLAST detector components, data acquisition and trigger systems, the Compton polarimeter and the Monte Carlo software are presented.

3.2 Polarized Source and South Hall Ring

A high-gradient-doped GaAs photo-cathode was used for photo-emission at the polarized source. The 5% Phosphate doping was selected to shift the wavelength of peak polarization of the emitted beam to 810 nm, in order to couple to a diode laser system capable of producing up to 150 W unpolarized beam (60 W polarized). The laser beam interacted with the photocathode through a transport system which included aperture focusing lenses for optimum performance, a polarizing filter, and a remotely controlled half-wave plate to determine the helicity of the beam. The electron pulses were then injected into the accelerator and reached 850 MeV in the Linac and recirculator.

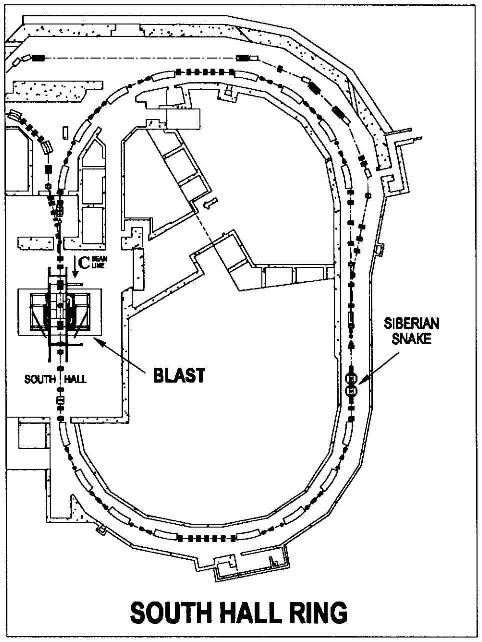

Figure 3-1: The South Hall Ring has a racetrack shape and a circumference of 190 m. Shown here also is the BLAST detector.

The MIT-Bates Linac facility provides intense polarized electron beams for both fixed and internal target experiments. In the former case, the beam is accelerated from the polarized source by a 500 MeV Linac and energies of up to 1 GeV can be achieved with recirculation. In the latter case, high duty cycle beams can be produced by injecting electron pulses into the South Hall Ring (SHR). The SHR was built with two elongated linear sections and a circumference of 190 m. It is equipped with 16 dipole magnets for beam steering and an RF cavity operated at 2.865 GHz. For the BLAST experiment, the SHR was operated in its storage mode, in which a long-lifetime, continuous wave beam was achieved through gradual stacking of electron pulses from the accelerator. Injected pulses had a peak current of 2 mA and were injected at a frequency of 20-30 Hz for about 20-30 seconds depending on the desired peak current. The beam then circulated in the ring for a period of time until the current fell below a threshold set to maximize the total beam current delivered to the experiment. Average lifetimes of about 30 min for beam current of over 200 mA were typically delivered to the experiment.

Total Length	160 m
Number of Klystrons	12
Number of transmitters	6
RF Pulse Length	0-25 μs
Accelerator frequency	2.865 GHz
Recirculated Beam Energy MAX	1.06 GeV
Max Beam Duty Cycle	1%
Max Pulse Repetition Rate	1 kHz

Table 3.1: Characteristics of the MIT-Bates Linear Accelerator.

Operation of the SHR in storage mode was adjusted to satisfy the constraints imposed by the characteristics of the BLAST experiments. Sensitive high-voltage detectors as well as a coated target cell necessitated good understanding and control of beam halos and background rates. Beam Halo Monitors were installed around the beam pipe to monitor the size and offset of the beam continuously. In addition, a collimator was installed upstream of the target cell to reduce background rates and prevent beam scraping off the target cell walls. The location and design of the collimator were determined by Monte Carlo simulation. In order to prevent depolarization of the longitudinally polarized beam due to electron spin precession after injection in the ring, a *Siberian Snake* system was used. The latter is a series of superconducting solenoid magnets assembled around a section of the ring's beam pipe opposite the BLAST detector as shown in figure 1.1. Through Larmor spin precession, an electron traveling in the ring will deviate from longitudinal polarization over time. The system is designed to rotate the spin of each electron traversing it by 180 degrees around the snake axis, thus reversing any perturbations due to precession or other processes. By the time each individual electron circles back to the target, spin precession will shift the polarization vector back to being exactly parallel. The polarization of the beam was reversed by an RF dipole located downstream of the target. Finally, continuous monitoring of the beam polarization in the SHR was established using a *Compton Polarimeter.*

Four blocks made of 1 cm thick Tungsten material were installed upstream of the target in order to limit the amount of stray electrons hitting the detectors due to multiple scattering and Coulomb scattering in the beam-pipe. The position of the slits depended on the tune of the injection and was established empirically during operation. The slits were connected to the endpoints of remotely controled, motorized bellows and they were fully retracted during injection. Once the electron beam was stored, they were moved in slowly, until they began to impact the beam lifetime, at which point they were withdrawn by 1 mm, essentially cutting away electrons outside of a 6σ beam distribution. The slits were located a few betatron $\lambda/2$ upstream of the target in order to image the cell. In addition to the target slits, an additional septum slit was also used for halo reduction.

Four Beam Quality Monitors (BQMs) were installed to monitor the beam halo. The BQMs were plastic scintillators previously used as beam halo monitors for the SAMPLE experiment. They were mounted to the beam pipe upstream of the target, nominally gain-matched with a standard source, and connected to readout electronics through RG-58 cables [120].

The beam current was determined using a *Lattice Direct Current Current Transformer* (LDCCT), a parametric current transformer designed to measure electron beam currents without interference with the beam. A standard PCT unit consists of three components: a sensor head in the form of a circular aperture wrapped around the beam-pipe, a front-end electronics box and an output chassis. Having a frequency response from DC to 100 kHz and resolution of 0.5 μA, the calibrated output signal of the device was digitized by a 16 bit ADC and sent to EPICS [108]. Integration of the LDCCT measurement over time determined the amount of charge delivered to the experiment. The absolute accuracy of the measurement was better than 0.05%.

3.3 The Compton Polarimeter

The well understood process of photon scattering off electrons, also known as the *Compton effect*, was used to monitor the polarization of the beam during data taking, without interfering with the experimental results. Within the framework of QED,

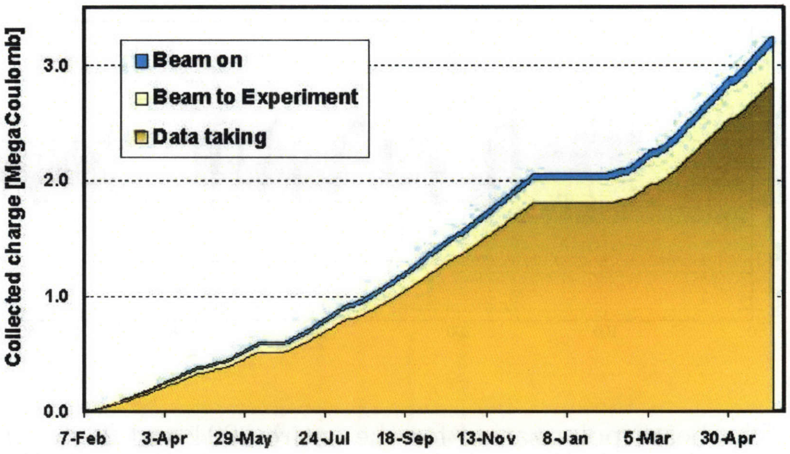

Figure 3-2: The integrated charge delivered to the BLAST experiment over the course of 2004 - 2005 running period. The blue line indicates indicates the distribution of charge for beam in the South Hall Ring, the light yellow the distribution of charge delivered to the experiment and the dark yellow the charge used for data taking. The plot includes charge delivered to both hydrogen and deuterium experiments.

the cross section for scattering of polarized photons off polarized electrons can be calculated exactly as a function of energy and scattering angle. The resulting electron helicity asymmetry may be used to extract the product of the circular photon polarization and the electron beam polarization. In order to implement this principle, a Compton polarimeter was located upstream of the BLAST target area in order to minimize background due to bremsstrahlung radiation. The location demanded a small correction factor for spin procession as a function of the distance from the target. The system consisted of a 5 Watt solid state laser of 532 nm wavelength, an optical transport system, adjustable mirrors and a CsI calorimeter. The laser beam intercepted the electron beam and the backscattered photons were detected by a calibrated calorimeter. A dedicated data acquisition system collected the data and integrated the results with the BLAST data stream [120].

The uncertainties in the beam polarization measurement were dominated by systematic uncertainties of the polarimeter apparatus. Main sources include an uncertainty in the analyzing power calculation, alignment issues as well as knowledge of the photon beam circular polarization. The total uncertainties in the measurement amounted to around 4%. For the running period in 2004, the average polarization

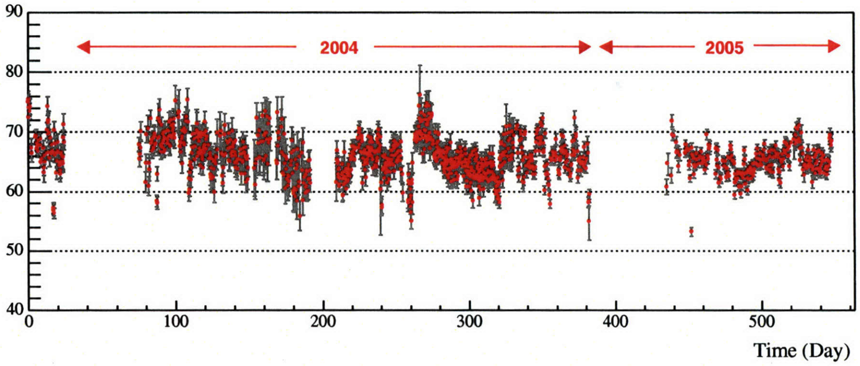

Figure 3-3: The beam polarization for the entire 2004 and 2005 running periods as measured by the Compton polarimeter. The polarization was constant at around 66%. The graph includes both Deuterium and Hydrogen target experiments, with Hydrogen running limited to approximately the last 100 days of 2004. The gap around day 400 was due to a two-month winter shutdown.

was 0.66[1]. The beam polarization was approximately the same for the 2005 running period.

3.4 The Data Acquisition System

The software framework CODA (CEBAF Online Data Acquisition) was used to collect, manipulate and archive detector information at BLAST. CODA allowed various data acquisition systems to be built, depending on the individual needs of an experiment. In a typical system, signals from different components of a detector are routed to embedded readout controllers (ROCs) where the data is collected in a buffer to reduce protocol overhead before being sent over the network. The various data streams are collected and merged, and then formatted by the Event Builder (EB). The EB passes the data to the Event Transport System (ET) which allows for other data streams to be added to the original detector data. An event recorder (ER) function can then store the data in the required format and location.

The BLAST CODA system used information stored in an msql database. A

---

[1] The maximum polarization the polarized source can achieve is correlated with the photocathode material structure as well as the properties of the laser used to induce photoemission. The laser used at Bates was chosen for higher quantum efficiency and thus shorter wavelength and lower polarization.

single Motorola MV162 computer per crate was used as the ROC using the VxWorks operating system. Phototube signals from the detector were collected by LeCroy 1881M ADC and LeCroy 1875A TDC modules whereas information for the drift chambers was collected by LeCroy 1877 TDCs.

3.5 The BLAST Trigger System

3.5.1 Hardware

The trigger system can be segmented into three distinct functions. First, analog signals from the various components of the detector are digitized indicating the exact element where the signals originated. Second, the logic signals in each sector are inputed into memory look-up units (MLU) where they are correlated. Finally, the outputs of both sector MLU are processed by the cross-sector MLU (XMLU) which is responsible for sending gates and start signals to the electronics as well as tagging each event with a trigger type. The signal from the XMLU is then sent to a Trigger Supervisor module where appropriate prescaling is performed depending on the trigger type, before the data are sent to the data acquisition system.

3.5.2 Trigger types

Since the BLAST experimental program was developed to collect data in various channels simultaneously, the trigger was designed to facilitate collection and analysis. Depending on the combination of detectors that fire, every event is assigned a trigger type. Despite the low rate of physical processes at the BLAST beam energy, high background rates in some trigger types caused the data acquisition rate to exceed the maximum handled by the system, resulting in significant *deadtime.* Deadtime is the period of time the data acquisition cannot respond to incoming events which are consequently lost. To limit the computer deadtime, less important triggers with high background were prescaled. A potential source of bias in the data collection process is the possibility that deadtime may be trigger dependent. Since different trigger types

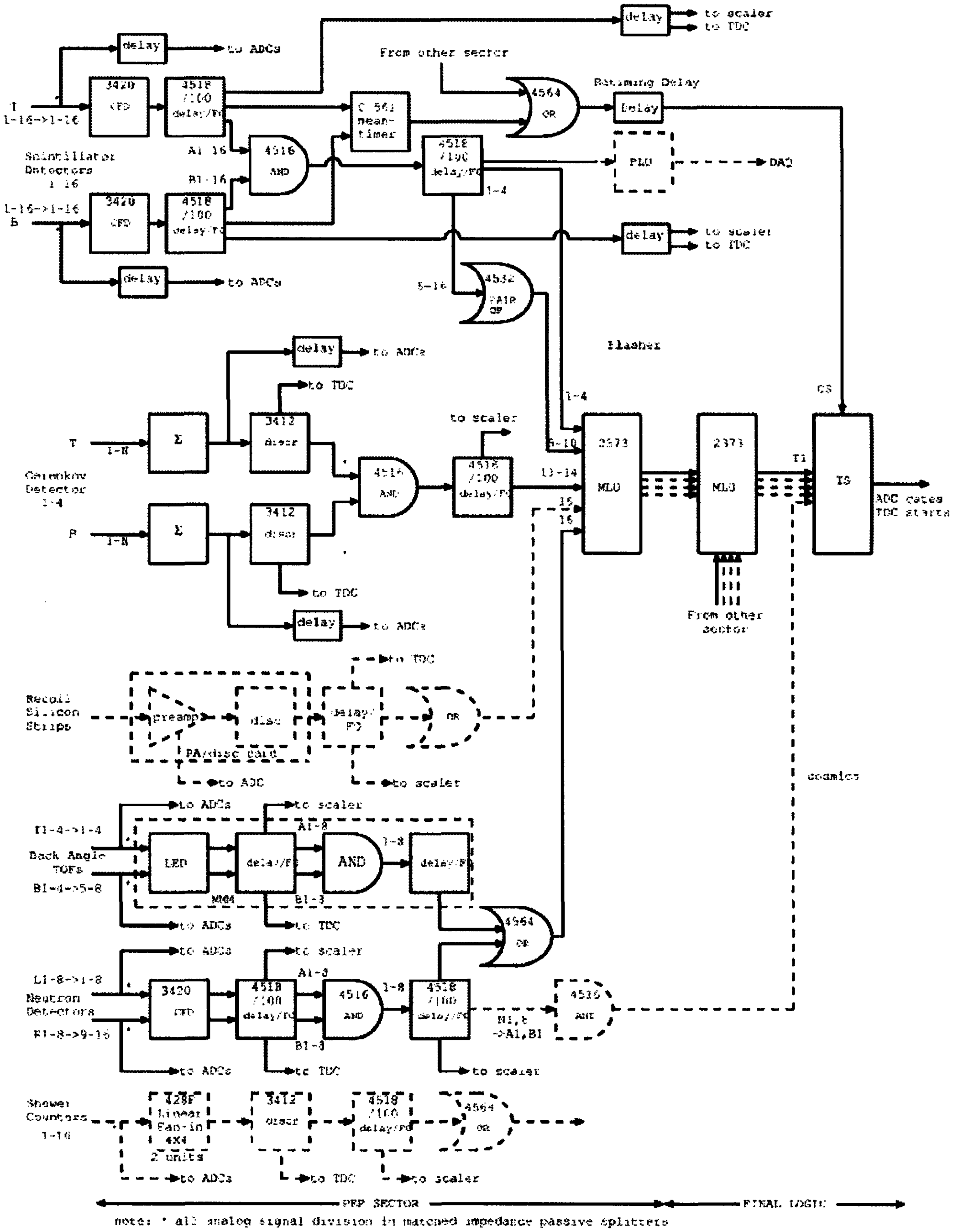

Figure 3-4: The Trigger system used for the BLAST data acquisition.

essentially store different physics channels, trigger dependence in deadtime may bias the count rates recorded. In order to investigate this, scaler information per trigger type can be compared to what is actually recorded in the datastream. At BLAST, there seems to be no significant deadtime variation with trigger type. Thus, all relevant trigger types may be combined by correcting only for the prescaling.

trigger	prescale	configuration
1	1	At least one TOF in each sector
2	1	At least one TOF in each sector, Neutron Counter in the other
3	10	At least two TOF in single sector, with Čerenkov
4	100	At least two TOF in single sector
5	1	At least one TOF in one sector, BATS in the other
6	1000	At least one backward TOF in single sector
7	3	At least one TOF in single sector, with Čerenkov
8	1	Flasher trigger

Table 3.2: The trigger supervisor at BLAST allows tagging the data with different trigger types depending on the detector pattern they obey. The requisite patterns can be configured and saved according to the demands of the experiment.

3.5.3 Software

The trigger control system for the experiment was intended to implement the selected logical flow diagram using the corresponding hardware, while allowing the user to configure, save and download a number of settings through its graphical interfaces. The trigger map was the actual link between hardware and software. This file, a part of the configuration file, converts the logic into actual hardware locations and needs to be updated whenever a change is made in the trigger. During periods of large-scale changes in the detector (such as during commissioning of the apparatus), this was an iterative process with the changes decreasing as production running commenced.

3.6 The BLAST Detector

The BLAST detector was specifically designed to suit the needs of the planned scientific program and in this respect, it offered several advantages. The large acceptance of the detector allows the measurement of observables over a broad kinematic range and additionally offsets the low luminosity of the internal gaseous target. The azimuthal symmetry and two-opposite-sector (left and right) information allow for coincidence and super-ratio experiments. The entire detector package consists of individual detector arrays designed and instrumented according to the intended measurements. More specifically, the design was driven by the experiment's requirements of timing resolution, momentum and tracking resolutions as well as particle identification.

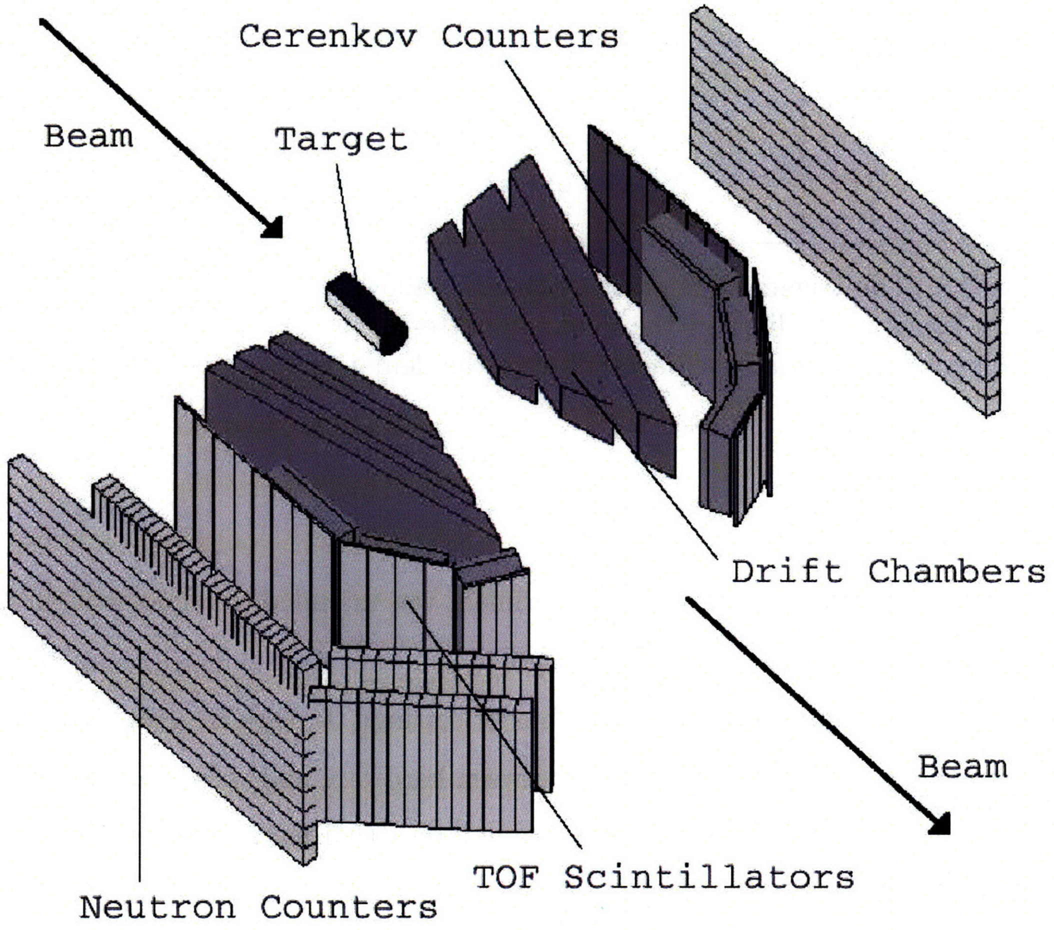

Figure 3-5: Front-overhead view of the BLAST assembly. From left to right shown are the Neutron counters, TOFs, Čerenkov detectors, drift-chambers installed within the toroidal magnet and the beam-line down the middle of the coils.

BLAST is centered around the beam-pipe in the South Hall. The target chamber is embedded into the ring and the gas from the ABS flows in from above, with the ABS itself attached to a mezzanine over the detector. The magnetic coils are symmetrically attached to a sub-frame, allowing space for the dift chambers. The rest of the detector consists of the Čerenkov counters, the Time-of-flight scintillators and the Neutron counters. The detector is shown in figure 1.5.

3.6.1 Wire Chambers

In order to extract information for a detected particle (such as momentum, scattering vertex position, particle identification etc.), drift chambers were used. Operation of the chambers is based on the principles of charged particles traveling through a gas volume. By ionizing the gas, the particles generate a path of ionized electrons along their trajectory. The ionized electrons are then subjected to an electric field and drift towards the readout wires. The origin of the ionized electron can be deduced by measuring the drift time.

The aluminum chassis for the chambers were manufactured by Allied Electronics and delivered to the MIT campus in 2000 where the individual pieces were assembled and the chambers strung. When stringing finished, the chambers were transported to MIT-Bates for installation in the South Hall. The required electronics were connected to the chamber wires after installation, including High Voltage supplies for operation, TDC modules for readout and amplifiers. After calibration, the intrinsic resolution of the chambers was obtained by calculating the hit position deviation from a straight line fit for each event and histogramming the results. The BLAST wire chamber resolution was of the order of 130 μm [19]. The resolution is affected by time-to-distance conversion uncertainties, electron diffusion and energy loss as well as knowledge of the geometry.

A dedicated gas flow system was built for operating the BLAST drift chambers. The gas mixture used was 82.3% Helium and 17.7% isobutane. An ideal gas such as Helium is usually used as the *ionization gas*, which is essentially the main mechanism for tracking. In addition, a gas consisting of large hydrocarbon molecules (such as isobutane) is used as a *quenching gas* to absorb photons created by electron recombination. This is more prominent in the avalanche region, where the electrons accelerated by the strong electric field can ionize the gas. The number of electrons created can thus increase exponentially and lead to exceeding background. Careful

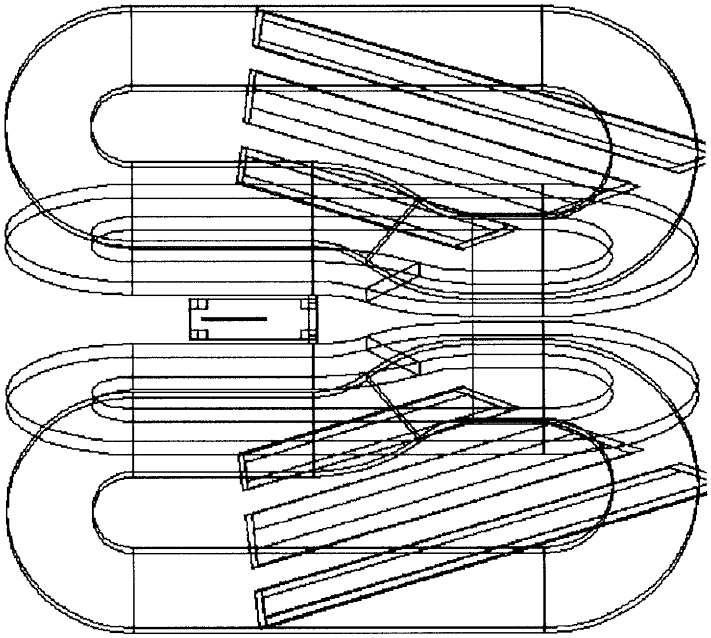

Figure 3-6: The drift chambers for BLAST are shown here in overhead view. For display purposes, non-visible lines are shown. In reality, most of the surface area of the chambers is obscured by the coils.

consideration has to be given to the mixture of ionization and quenching gas used in the chambers. Exceeding absorption by the quenching gas of the electrons ionized by the original charged particle may lead to a reduction of the tracking efficiency. Therefore, an equilibrium mixture has to be established. The exits of the chambers were covered with mylar to maintain the gas pressure in the volume.

BLAST used six chambers, arranged in groups of three per sector with the smaller chamber closer to the beamline to form a trapezoidal shape as shown in figure 3-6. The geometry was largely determined by space restrictions of the BLAST design. The acceptance was measured to be $20^\circ - 80^\circ$ in θ while the azimuthal acceptance varied from -15° to $+15^\circ$ at the downstream end to about -22° to $+22^\circ$ upstream. Each chamber consisted of individual cells, rectangular arrays of 39 wires with transverse dimensions 4 cm×7.8 cm [19]. The wires used for the cells were of three kinds. Sense wires, made of tungsten, were connected to amplifier-discriminator cards and were used for readout. Guard wires, made of copper, were used for gain-matching of the sense wires and finally field wires, also made of copper, used to shape the electric field in the region.

Reconstruction:

Details on the drift chamber reconstruction can be found in [19]. Hits in close cells are identified to form a *cluster*. The distance is then calculated for each hit and a plane, referred to as *stub*, is defined. Fits to the stubs determine the *segments*, one for each chamber, used in the final track reconstrution to establish the initial kinematics. The latter are finalized through an iterative process by accounting for the flight path from the vertex to the drift chambers etc.

The resolution of the reconstruction was determined by studying electron-proton elastic scattering events from hydrogen, a process well understood in principle. Since elastic scattering kinematics are over-determined, the electron polar angle θ_e can be used to calculate the electron momentum and the proton polar angle. The calculated values can then be compared to the measured ones and the difference histogrammed. With a perfect resolution, the difference histogram would be a δ-function whereas finite resolutions smear the distribution. Figure 1.7 shows typical results for elastic electron-proton scattering off Hydrogen.

3.6.2 Time of Flight Scintillators

The time-of-flight scintillators (TOF) were used to obtain timing for the trigger, position information as well as particle identification from timing differences in coincidence events. In the case of singles, the TOFs provide only a self-timing peak.

The scintillator is based on the principle of charged particles moving at high speeds through the material. Via the energy deposited by the moving particles, the free valence electrons of the scintillator molecules undergo transitions through excitations of rotational and vibrational modes to higher states. Relaxation of the molecules back to their original states leads to light emission, which is collected at the top and bottom of the scintillators by photomultiplier tubes (PMT).

The scintillating material of the TOFS was Bicron BC-408 plastic, selected for its fast time response, long attenuation length and structural properties [121]. The plastic was fully covered with Kapton sheaths to prevent light leakage. The forward TOFs ($\theta < 40^\circ$) had 119.38 cm length, 15.24 cm width and 2.54 cm thickness whereas the backwards ones were larger with 180.0 cm length, 26.2 cm width and the same thickness. At both ends of the plastic, lightguides were attached in order to direct the light to the PMTs. The PMTs were covered tightly with μ-metal sheets to cancel the effects of the BLAST field. Signal readouts routed TDC and ADC information to the D-tunnel electronics. There are 16 TOFs on each sector of the detector with the same θ acceptance ($\theta \sim 20^\circ - 80^\circ$) as the drift chambers. In addition, Backward-Angle TOFs (BATs) provide additional coverage ($\theta \sim 90^\circ - 120^\circ$) without drift chamber tracking.

3.6.3 Čerenkov Detectors

In order to distinguish between electrons and negatively charged pions, Čerenkov counters were assembled and installed. The curvature of the trajectory in the magnetic field is similar for an electron and a π^-, thus wire chamber tracking is not sufficient. Additionally, timing resolution effects make electron pion separation difficult in some kinematic regimes. Therefore, Cerenkov detectors, based on the principle of *Čerenkov radiation*, were used.

Čerenkov radiation resembles the shock wave emitted by a wave traversing a medium. In the case of a charged particle traveling in a medium with speed larger than the speed of light in that medium, atomic excitation of the medium itself causes light emission in the form of a coherent wavefront at a specific angle with respect to the charged particle's direction of travel, forming a cone whose half-angle θ is given

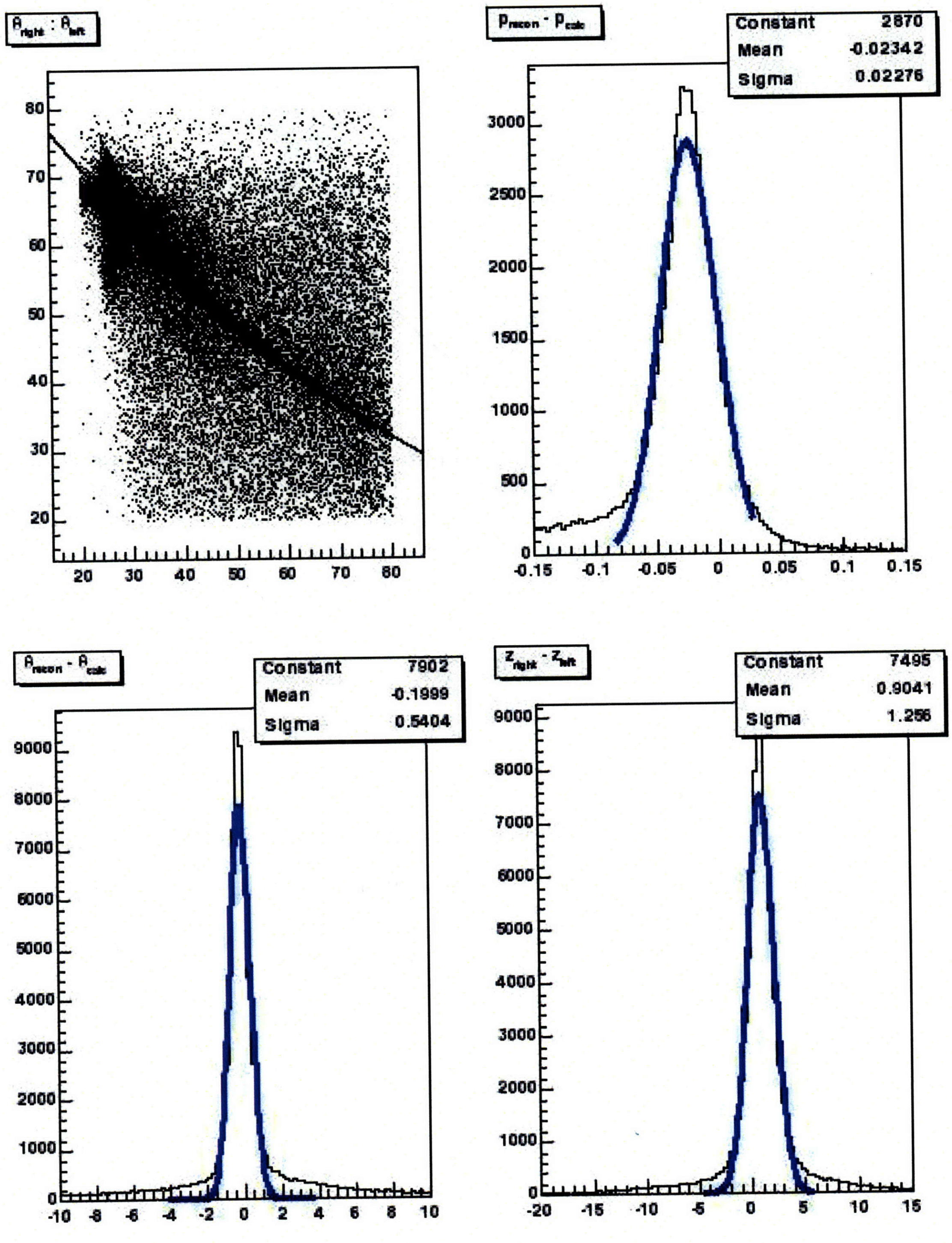

Figure 3-7: The analysis of elastic electron-proton scattering was used to determine the resolutions of the reconstructed momentum and angles. Shown here are plots of momentum, polar angle and vertex position for a representative sample chosen at random from the hydrogen running data.

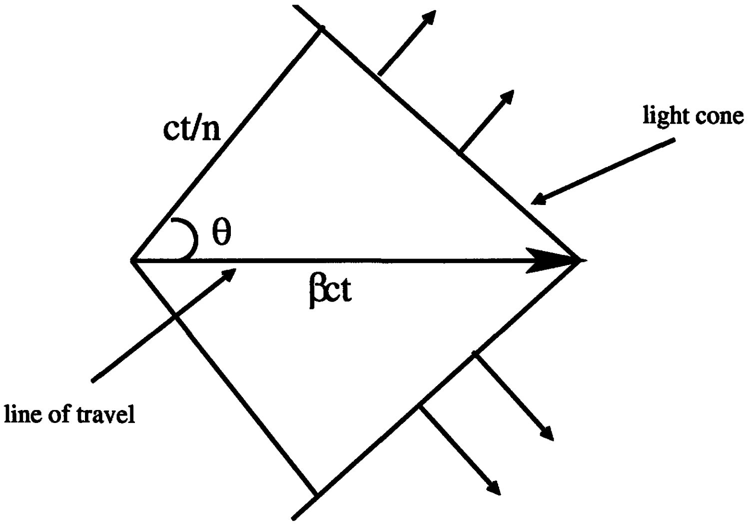

Figure 3-8: Shown here is the light cone emitted by excitation of medium atoms when the speed of a charged particle exceeds that of light in the medium. The angle θ is given by eq. (3.1).

by

$$\theta = \tan^{-1}\left(\sqrt{n^2\frac{v^2}{c^2} - 1}\right). \tag{3.1}$$

The design of the Čerenkov counters took into account the BLAST detector's space limitations, operation in high magnetic fields, high efficiency and minimization of energy loss [122]. Four counters were installed on each side of the beamline. Each counter consists of a light box with interior surfaces coated with diffusively reflective material, a layer of silica aerogel used as radiator, and PMTs at the top and bottom of the light box. Low carbon steel was added to cancel the magnetic field from the toroid. Some of the design characteristics of the counters are listed on table 1.3.

	Box 1	Box 2	Box 3	Box 4
Number of PMT	6	8	12	12
Angle subtending	20° – 35°	35° – 50°	50° – 70°	75° – 115°
Aerogel thickness	7 cm	5 cm	5 cm	5 cm
Refraction Index	1.02	1.03	1.03	1.03

Table 3.3: Čerenkov counter specifications. The aerogel radiator used was manufactured by Matsushida Electronic Works.

The relative efficiency of the counters was obtained by using elastic scattering

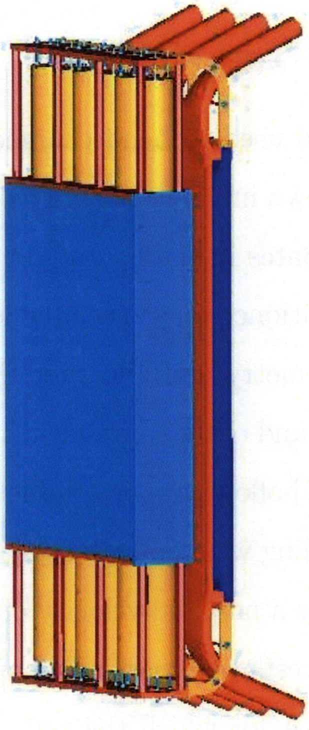

Figure 3-9: Side view of one of the individual Čerenkov counters used at BLAST within its mounting frame. Note the light box (blue) and the PMTs (yellow). Additional shielding installed to encase the PMTs is not shown here.

of electrons off Hydrogen. The event selection used kinematic cuts from the timing and position information given by the TOFs. These events were then checked for Čerenkov firing. This analysis also revealed edge effects due to gaps in the TOF coverage by their respective counters (particularly 4 and 8).

3.6.4 Neutron Counters

With the target spin oriented in the left sector of the detector, neutron detection is more important in the right sector (perpendicular kinematics), for the extraction of the neutron electric form factor G_E^n from a coincidence measurement. Neutron detection in the left sector allows the measurement of an asymmetry dependent only on kinematic factors and is thus only important as a cross-check. The neutron counters consist of 2 OHIO walls, one in each sector, plus an additional four LADS walls, all placed in the right sector.

3.6.5 The BLAST Toroidal Field

The toroidal magnetic field used to bend charged particle tracks was obtained with the 8-coil configuration shown in figure 1.10. The coils were manufactured by Everson Electric and delivered to Bates in the Fall of 1998. For integration with the BLAST detector, the coils were positioned on a specially designed aluminum subframe in order to preserve azimuthal symmetry and allow for the installation of the Atomic Beam Source, the drift chambers and other components. All eight coils consisted of 26 turns of cable wrapped around a hollow copper conductor filled with water coolant. As the water flow required for cooling was too high for a single water passage, a dual-passage system was used instead for a nominal velocity of 7.7 ft/sec [123]. Electrical, leakage, insulation and acceptance tests were performed prior to operation. Operating current was calculated to be 6730 A for which the coils provided 0.38 Tesla maximum field strength. Power to the coils was provided by a BTSPS MON 1 250/7000 C5 power supply from BRUKER, which was installed on the South Hall floor adjacent to the BLAST detector and shielded from direct radiation with large cement blocks. The supply was capable of delivering a maximum current of 7000 A at 250 V.

Before the beginning of the running, the toroidal field was mapped with an EPICS controlled coordinate table with resolution of 0.5 mm and two 3-dimensional Hall probes. The location of the table was determined by surveying at each new measurement position. The results of the mapping were in good agreement with analytic Biot-Savart calculations as well as TOSCA simulations. A critical test of the stability of the coil configuration and the reproducibility of the field was performed by powering the coils to full power. The test revealed that while the subframe remains fixed, the coils move radially inwards by approximately 7-10 mm. At various instances during running, additional magnetic shielding of other BLAST components became necessary. In order to establish the effect on the field, the field mapping was repeated in June 2005 at the end of the final running period. The final mapping revealed no considerable misalignments or shifts and agreed well with the original results [124].

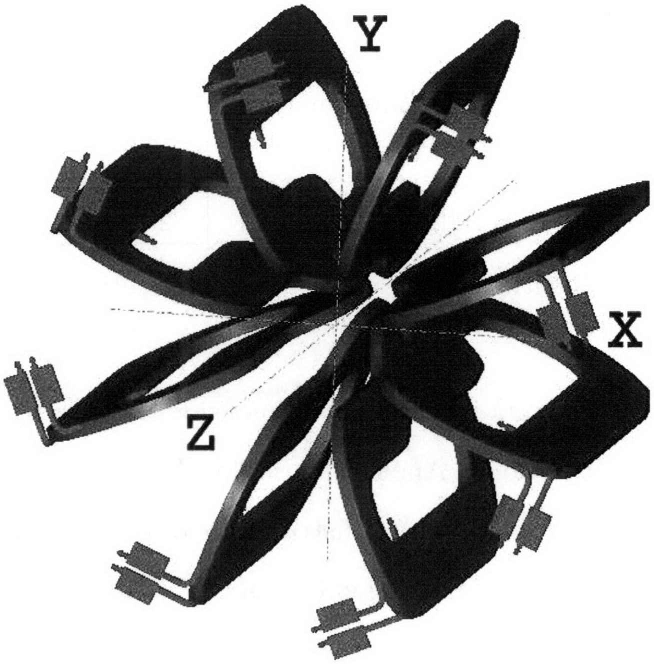

Figure 3-10: The eight copper coils used to produce the toroidal field for BLAST are shown here oriented in the relevant coordinate system.

In order to account for walk effects in the individual timing spectra of the detectors, a flasher system was used. A pulse from an LSI ultraviolet nitrogen laser was coupled to the center of the relevant detectors through fiber optic cables. A photodiode detector was then used to trigger the data acquisition system to record the flasher offset for each channel and correct the corresponding TDC spectrum.

3.7 The BLAST Monte Carlo

GEANT-based Monte Carlo simulations were used to model the experiment as well as to compare the obtained experimental results to theory. Detailed information on the geometry of the detector was used as input to form the experimental acceptance. A specially written, C++ object-oriented library was used for event generation. The generator was based on structure function calculations by H. Arenhövel for various channels (elastic, electrodisintegration, inclusive etc). In the case of electrodisintegration, the structure functions were computed on a 5-dimensional grid

Number of turns	26
Current per conductor	6730.77 A
Area of conductor	1.742 in^2
Mean turn length	357.6 in
Current Density	3864 A/in^2
Water velocity	7.7 ft/sec
Weight of single coil	2380 Kg

Table 3.4: Coil specifications. The coils were manufactured by Everson Electric and delivered to Bates in 1998

(ϕ_e, θ_e, ϕ_{cms}, θ_{cms} and ω) whereas a 3-dimensional grid (ϕ_e, θ_e and ω) was used for the inclusive calculations. Another variable, the vertex position for the event, is added to the list using a triangular distribution (see ABS chapter). With the variables used for the grid spanning the entire range of the detector's acceptance, cubic spline and other interpolations were performed to obtain the relevant cross section at each kinematic point. The event generator was initially designed to handle only the Deuterium channels from Arenhövel's calculations but in subsequent years it was modified to incorporate Hydrogen and MAID pion-production calculations as well.

Two different techniques were used to obtain the relevant Monte-Carlo calculations. In the first, events were generated according to cross section and then propagated through the GEANT code which simulated the components and the acceptance of the BLAST detector. This code had the additional capacity of simulating a number of physical processes (such as energy loss and multiple scattering) which may impact the final kinematics. Events that did not enter the experimental acceptance were discarded, whereas the remaining events were reconstructed using the same software used for data reconstruction. The output of the reconstruction codes allowed direct comparisons of the kinematics of the generated events to the data. The second technique involved "WHITE" generation. The term refers to the generation of uniformly distributed events in the six electro-disintegration variables. The spin-dependent cross section was then calculated event-by-event and used as a weight. The events were finally filtered according to the desired reaction (i.e. electron singles).

Chapter 4

Data Analysis

4.1 Introduction

The two data sets analyzed herein were collected during four months of running in 2004 and four months of running in 2005. The data represent a total beam charge of 320 kC for the 2004 set and 550 kC for the 2005 set. The ABS provided the polarized deuterium target. The target polarization states were selected at random from the set of vector plus, vector minus and tensor minus configurations (see ABS chapter) in order to reduce systematics associated with the beam. During transition from one spin state to another, data acquisition was inhibited. The change was performed every five minutes and took around 30 seconds to complete. The entire process was fully automated and did not significantly impact running efficiency.

The data were collected on 60 cm storage cells only, predominantly on the same cell, which yielded stable, high polarization during operation. The maximum current of the beam increased steadily over the course of running, from about 100 mA in 2004 to over 200 mA by the end of the 2005 running period. The beam energy was 850 MeV for both running periods and the beam polarization was constant at approximately 65% (more details in the chapter on the BLAST detector).

	2004 set	2005 set
Running Period	June - October 2004	March - June 2005
Total Charge	320 kC	550 kC
Target Polarization Angle	32°	47°
Average beam current	100 mA	180 mA
Cell length	60 cm	60 cm
Target Thickness	6×10^{31} cm^{-2}	6×10^{31} cm^{-2}
Luminosity	4×10^{31} cm^{-2} sec^{-1}	4×10^{31} cm^{-2} sec^{-1}
Average Vector Polarization	$\approx 80\%$	$\approx 75\%$

Table 4.1: Synopsis of parameters pertinent to the two running periods.

4.2 Event Selection

4.2.1 Electron Identification

To identify electrons, events with a negatively charged Wire Chamber track that also fired a TOF and a corresponding Čerenkov were selected. Negative charge was assigned to particles that followed an in-bending path (towards the beam pipe) in the wire chambers. The Čerenkov detectors were used to eliminate negatively charged particles which do not emit Čerenkov radiation. These were mainly negatively charged pions which are more massive and thus slower than electrons. Knowledge of the efficiency of the Čerenkov counters is important in comparing observed and expected yields but has little effect in studying asymmetries because the inefficiency is not expected to have a spin-dependence. On the other hand, any misidentification of pions as electrons may alter the final asymmetry results. For the BLAST detector, the misidentification rate is considered to be negligible. In addition, to reduce accidental coincidence of Čerenkov and TOF detectors, the correlation pattern shown in table 4.2 was imposed, based on the physical overlap in acceptance.

Cerenkov Box	TOF
0	0, 1, 2, 3
1	3, 4, 5, 6
2	6, 7, 8, 9

Table 4.2: The TOF - Čerenkov correlation scheme used in the analysis to eliminate accidental firing by the Čerenkov boxes.

4.2.2 Vertex Cut

To ensure the origin of the scattered electron is inside the target cell, a vertex cut was applied to the data. Tracking of the detected particle allowed reconstruction of the exact location in $\hat{z}$ (along the beam) where the interaction took place[1]. Even though the target density distribution extended all the way to the edges of the cell (±30 cm from the origin), the holding field was limited to ±20 cm due to the physical size of the target magnets. Therefore only this region of the storage cell was selected for data analysis to avoid scattering from unpolarized target particles. This did not limit statistics significantly. Over 60% of the events in the current data set originated from the central 20 cm (-10 cm to 10 cm) of the cell.

In the case of a coincidence event, information on the vertex position could be obtained through tracking of both left and right detected particles independently. The two values for z should agree within reconstruction uncertainties and their difference could be used to exclude badly reconstructed events. In the case of inclusive events, information on a single sector only was available and this safeguard could not be used. An additional complication for vertex reconstruction arose from energy loss and multiple scattering. The dominant contribution to this energy loss occured before the electrons exited the material in the target area and entered the region of the wire chambers. Unless this was taken into account, the reconstruction was likely to misidentify the origin of the electron by a small amount. The energy loss was accounted for in the Monte Carlo simulations (see section 4.8.5).

4.2.3 Invariant Mass Spectrum

The invariant mass W is defined as

$$W = \sqrt{M_d^2 + 2\omega M_d - Q^2}, \tag{4.1}$$

---

[1] Reconstructing the $\hat{x}$ and $\hat{y}$ coordinates for each event is more complicated. This information would have been useful in eliminating events that originate from the target cell region but not from the target gas itself. The majority of such events originate from interactions of beam electrons with the cell walls.

where M_d is the deuteron mass. The invariant mass can be constructed solely from electron information, has an almost gaussian shape and the location of the peak is determined by quasi-elastic kinematics. The width of the W distribution is determined by the Fermi momentum of the nucleons inside the nucleus which results in a smearing. Experimentally, the Fermi smearing is convoluted with the electron momentum and scattering angle resolutions. Quasi-elastic electrons could be selected by cutting around the W distribution peak. The spectra of the invariant mass for all relevant Q^2 bins are shown in figures 4-11 and 4-15. The four Q^2 bins used in the analysis are shown in table 4.3.

Q^2 bin	Q^2 Range $((GeV/c)^2)$	$< Q^2 >$ $((GeV/c)^2)$
1	0.100 - 0.163	0.135
2	0.163 - 0.225	0.189
3	0.225 - 0.288	0.252
4	0.288 - 0.350	0.316

Table 4.3: The range and average Q^2 values used for the G_M^n extraction.

While explicit quasi-elastic cuts were not used, the data used in the analysis were in fact dominated by scattered electrons originating from that reaction. This was ensured loosely with invariant mass cuts. The definition of quasi-elastic scattering off one of the nucleons is given by

$$X_{qfree} \equiv \sqrt{M_N^2 + 2\omega M_N - Q^2} - M_N = 0, \tag{4.2}$$

where M_N is the mass of the nucleon. However, the Fermi momentum due to the internal motion of the nucleons within the nucleus smears the distribution of events around zero. Figure 4-1 shows the X_{qfree} distribution for $Q^2 = 0.135\,(GeV/c)^2$. The solid line histogram shows the spectrum before cuts in invariant mass are applied and the dashed histogram shows the spectrum after the cuts. The spectra are shown both in perpendicular (left panel) and parallel (right panel) kinematics[2]. The invariant mass cuts used in the analysis limited contamination due to backgrounds from electromagnetic shower and inelastic reactions. Strict selection of quasi-elastic kinematics

---

[2] These kinematic regimes were defined in Chapter 1. Also, see section 4.2.4.

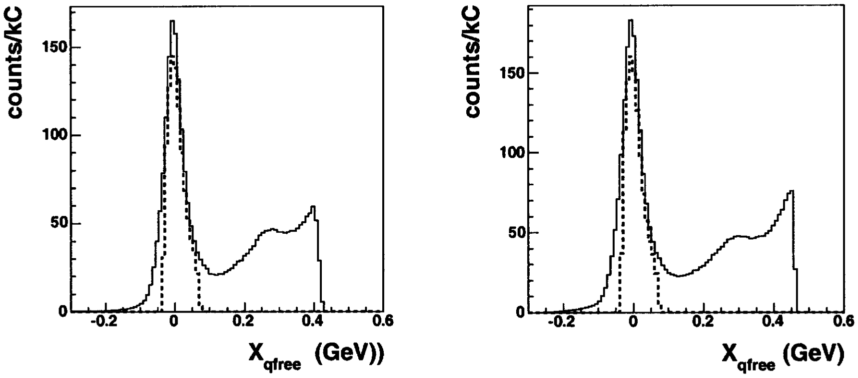

Figure 4-1: The spectrum in terms of the quasifree kinematic condition X_{qfree} for $Q^2 = 0.135\,(GeV/c)^2$. The left panel shows perpendicular and the right panel parallel kinematics. The dashed histogram shows the spectrum after the invariant mass cuts were applied.

was not critical for this analysis. While FSI and reaction mechanism corrections become increasingly important away from this regime, they are in fact included in the theoretical calculations by H. Arenhövel used in the final G_M^n extraction.

4.2.4 Perpendicular and Parallel Kinematics

Perpendicular and parallel kinematics are defined as $\theta_d^* = 90°$ and $\theta_d^* = 0°$, respectively, where θ_d^* is the target polarization angle with respect to the momentum transfer vector (see figure 1-5). However, since this angle varies within the detector's acceptance, the data deviates from exactly perpendicular and parallel kinematics. Figure 4-2 shows a contour plot of the θ_d^* spectrum versus the invariant mass with an upper bound of W = 1.98 GeV and for the entire Q^2 range. The left panel shows the perpendicular and the right panel shows the parallel kinematics for the 2004 data set. The angle of the momentum transfer vector was approximately 60° degrees for both sides of the detector for quasi-elastic kinematics. Since the target polarization vector was set at 32° to the left of the electron beam, θ_d^* for the quasi-elastic peak was approximately 98° for perpendicular and 35° for parallel kinematics, averaged

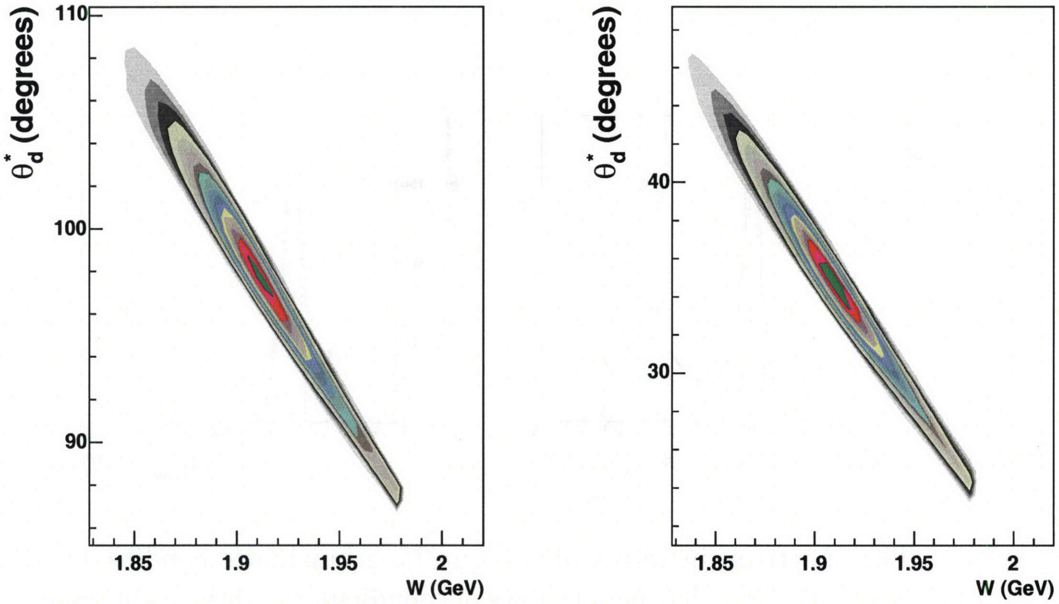

Figure 4-2: Plot of the θ_d^* spectrum versus the invariant mass with an upper bound of W = 1.98 GeV and for all Q^2 bins. The left panel shows the perpendicular and the right the parallel kinematics for the 2004 data set.

over the entire Q^2 range. Figure 4-3 shows θ_d^* for the same data set. The left panel shows the perpendicular and the right the parallel kinematics. The solid line histograms show the data for $Q^2 = 0.135\,(GeV/c)^2$ and the dashed line ones show the data for $Q^2 = 0.252\,(GeV/c)^2$. Finally, figure 4-4 shows θ_d^* for the 2005 data set. The spectra shown here were also verified with Monte Carlo simulations.

While the deviation from perpendicular and parallel kinematics does not contribute to any uncertainty in the analysis, the exact knowledge of θ_d^* for all events is important. For this, precise knowledge of the target polarization angle was required (see section 4.8.1).

4.2.5 Yields

The data were collected into three sets representing different triggers[3]. The first (trigger 1) was dominated by events from the $^2\vec{H}\,(\vec{e}, e'p)$ reaction while the second (trigger 2) was configured to collect events from the $^2\vec{H}\,(\vec{e}, e'n)$ reaction. Trigger

---

[3] See Chapter 3 for more details on the trigger system at BLAST and the definitions of each trigger.

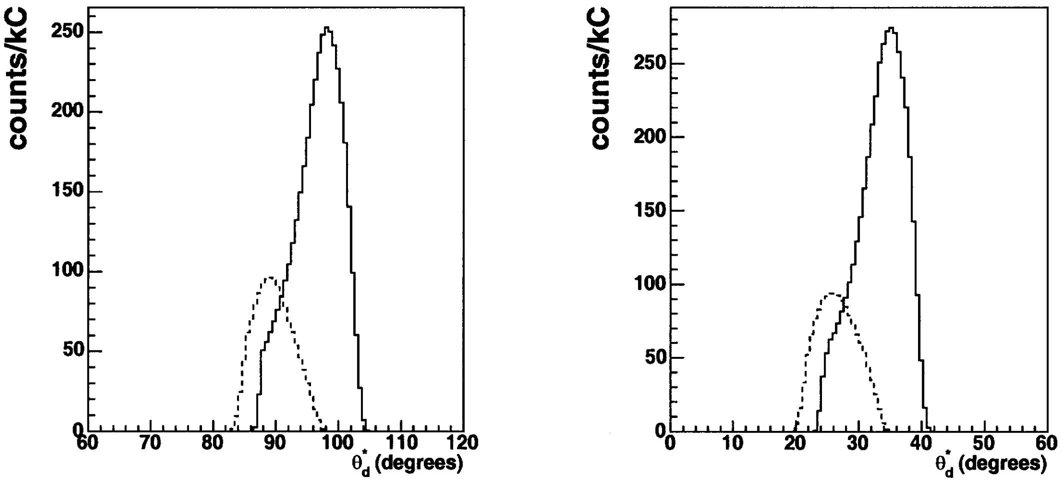

Figure 4-3: θ_d^* spectra for the 2004 data set with inclusive electron cuts applied. The left panel shows the perpendicular and the right the parallel kinematics. The solid line histograms show the data for $Q^2 = 0.135\,(GeV/c)^2$ and the dashed line ones show the data for $Q^2 = 0.252\,(GeV/c)^2$. The data are shown after invariant mass cuts were imposed.

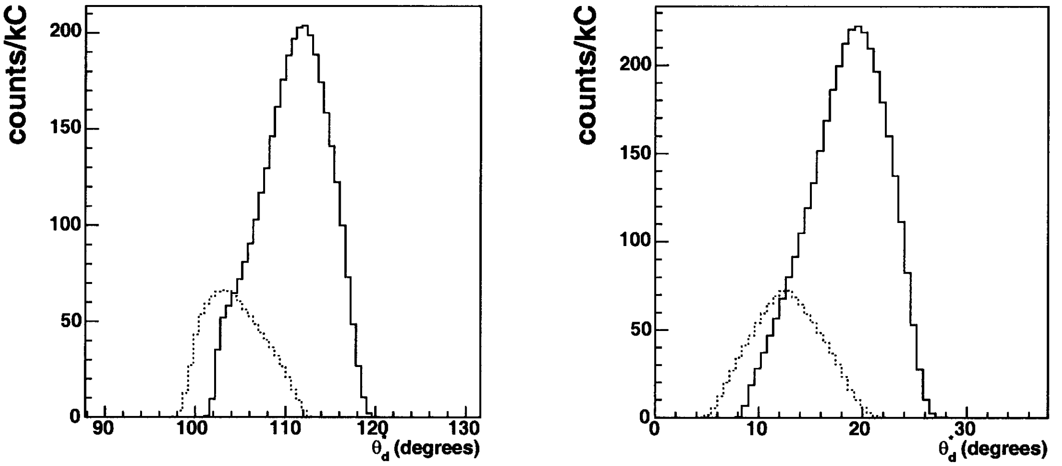

Figure 4-4: θ_d^* spectra for the 2005 data set with inclusive electron cuts applied. The left panel shows the perpendicular and the right the parallel kinematics. The solid line histograms show the data for $Q^2 = 0.135\,(GeV/c)^2$ and the dashed line ones show the data for $Q^2 = 0.252\,(GeV/c)^2$.The data are shown after invariant mass cuts were imposed.

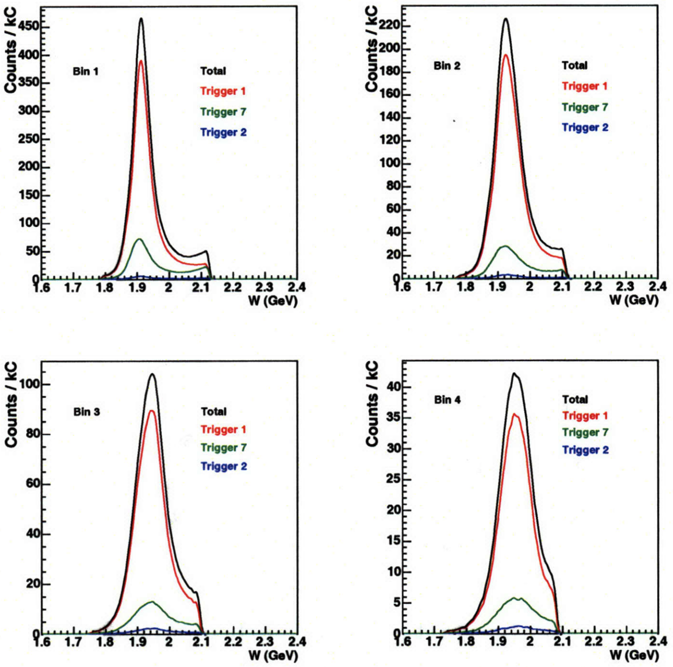

Figure 4-5: Invariant mass spectra per trigger per Q^2 bin for parallel kinematics and the 2005 data set. The "true-counts" yield of trigger 7 is displayed here (without the pre-scaling adjustment). The Q^2 bins used here are shown in table 4.3.

1 also collected events from the ${}^2\vec{H}\,(\vec{e}, e'\,{}^2H)$ elastic scattering reaction. The final trigger (trigger 7) was configured to collect singles ${}^2\vec{H}\,(\vec{e}, e')$ trigger events, for which only an electron was detected. This trigger was characterized by high backgrounds during data taking, mostly from electron positron pairs created by interactions of beam electrons with material in the vicinity of the target cell. While these could be easily eliminated in the final analysis, they overwhelmed the data acquisition system and created significant deadtime. Therefore, a pre-scale factor of 3 was imposed on this trigger. The pre-scaling had no effect on the resulting normalized inclusive yield, which could be constructed by adding triggers 1 and 2 with 3 times the events in trigger 7. The pre-scaling did, however, limit statistics. Figure 4-5 shows the invariant mass spectra per trigger for the 2004 data set and parallel kinematics. The coincidence trigger 1 accounted for almost 80% of the data. The contribution from trigger 2 was the smallest of the three. The difference in trigger 2 counts between parallel and perpendicular kinematics was due to the asymmetric configuration of the neutron detectors, most of which were placed to the right side of the electron

beam-line. The event sample, cross sections and asymmetries discussed herein were constructed by summing the three triggers while taking into account the pre-scale for trigger 7.

Parallel kinematics				
	trig 1	trig 2	trig 7	total
bin 1	1.6×10^{6}	0.82×10^{5}	0.36×10^{6}	2.1×10^{6}
bin 2	1.1×10^{6}	3.2×10^{4}	1.7×10^{5}	1.2×10^{6}
bin 3	5.9×10^{5}	1.6×10^{4}	9.0×10^{5}	7.0×10^{5}
bin 4	2.7×10^{5}	7.2×10^{3}	4.2×10^{4}	3.2×10^{5}
Perpendicular kinematics				
	trig 1	trig 2	trig 7	total
bin 1	1.4×10^{6}	1.5×10^{5}	2.7×10^{5}	1.8×10^{6}
bin 2	1.1×10^{6}	8.8×10^{4}	1.5×10^{5}	1.3×10^{6}
bin 3	4.9×10^{5}	3.8×10^{4}	6.3×10^{4}	5.9×10^{5}
bin 4	2.6×10^{5}	2.2×10^{4}	3.4×10^{4}	3.2×10^{5}

Table 4.4: Per trigger yield for inclusive electrons for the entire 2004 data set. The "true counts" yield for trigger 7 is shown without the pre-scale adjustment. During data taking, trigger 7 was pre-scaled by a factor of 3. The yields are shown divided into the four Q^2 bins as shown in table 4.3.

Parallel kinematics				
	trig 1	trig 2	trig 7	total
bin 1	2.2×10^{6}	3.9×10^{4}	5.5×10^{5}	2.8×10^{6}
bin 2	1.4×10^{6}	2.7×10^{4}	2.5×10^{5}	1.7×10^{6}
bin 3	7.5×10^{5}	1.9×10^{4}	1.3×10^{5}	8.9×10^{5}
bin 4	3.2×10^{5}	1.0×10^{4}	5.9×10^{4}	3.9×10^{5}
Perpendicular kinematics				
	trig 1	trig 2	trig 7	total
bin 1	1.9×10^{6}	2.2×10^{5}	4.0×10^{5}	2.5×10^{6}
bin 2	1.4×10^{6}	1.3×10^{5}	2.2×10^{5}	1.8×10^{6}
bin 3	6.0×10^{5}	5.1×10^{4}	8.5×10^{4}	7.4×10^{5}
bin 4	2.0×10^{5}	1.8×10^{4}	2.8×10^{4}	2.5×10^{5}

Table 4.5: Per trigger yield for inclusive electrons for the entire 2005 data set. The "true counts" yield for trigger 7 is shown without the pre-scale adjustment.

The normalized yield per Coulomb versus run number for the 2004 data set is shown in figure 4-6. The red histogram indicates the yield in parallel kinematics and blue in perpendicular. The fluctuations in the yield are due to variations in the target

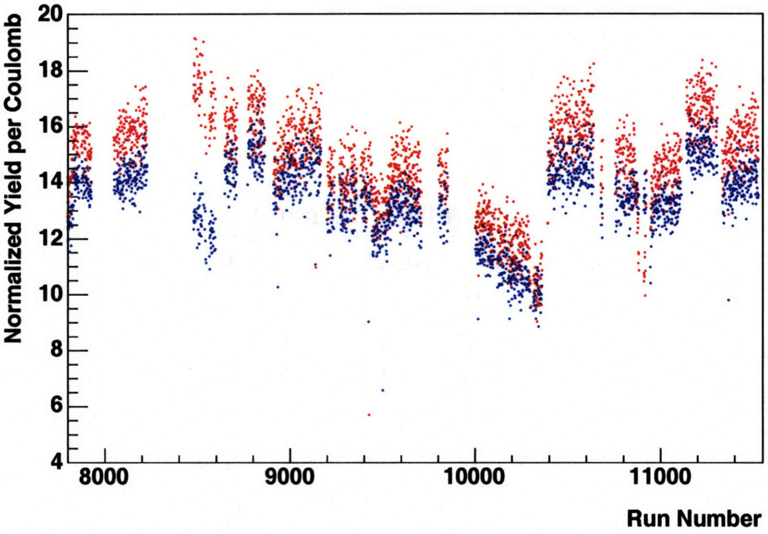

Figure 4-6: Electron yields for perpendicular (blue) and parallel (red) kinematics versus the run number for the 2004 running period.

thickness. The left-right difference in rate is attributed to differences in the Čerenkov detector efficiency as well as the asymmetric configuration of the neutron detectors. Tables 4.4 and 4.5 show the total event set per trigger for the 2004 and 2005 data sets respectively. It is important to note that the total counts listed here belong to all 6 spin states, divided approximately equally among them.

The spectra for both data sets are shown in figures 4-8 through 4-15. Figure 4-8 (4-12) shows the electron scattering angle for the 2004 (2005) data set. The top four panels show the data in perpendicular kinematics, in increasing Q^2 bin order from top left to bottom right. The bottom four panels show the corresponding spectra for parallel kinematics. Figures 4-9 (4-13) shows the electron azimuthal angle, 4-10 (4-14) shows the energy transfer ω and 4-11 (4-15) shows the invariant mass W. All figures follow the same Q^2 bin order. Data and Monte Carlo are normalized to the same maximum count.

4.3 Q^2 Determination

The value of Q^2 for each event was determined from the scattering angle and momentum of the reconstructed electron. As such, it was sensitive to the reconstruction

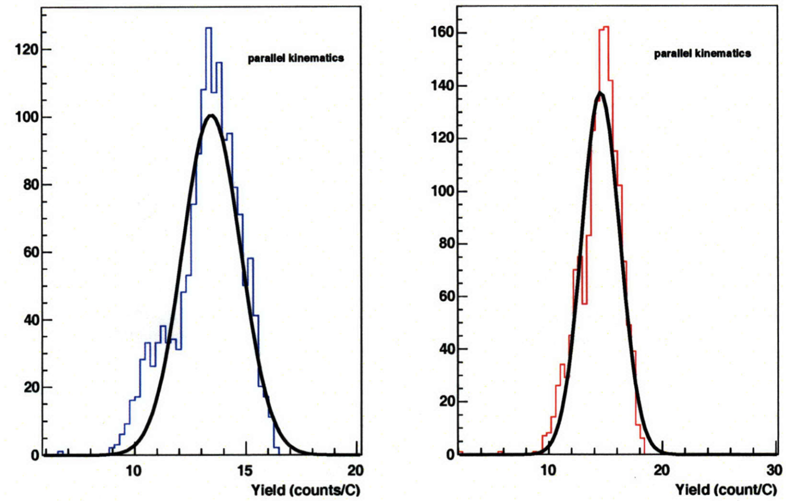

Figure 4-7: Histograms of the normalized electron yields for perpendicular (blue) and parallel (red) kinematics for the 2004 running period. The σ of the gaussian fit is 1.3 for the left (mean is 13.5 counts per Coulomb) and 1.7 for the right (mean is 14.6 counts per Coulomb). A 4σ cut was applied to establish a good data set.

uncertainties of both. This is a disadvantage compared to the elastic $^{2}\vec{H}\,(\vec{e}, e'\,^{2}H)$ and $\vec{H}\,(\vec{e}, e'p)$ scattering reactions, where the kinematics is overdetermined and only one of the two variables is needed for Q^2 determination. These analyses used only the scattering angle which had better resolution [14, 23].

The range of Q^2 considered in this analysis was determined by the BLAST Čerenkov counter coverage which spanned from $Q^2 = 0.1\,(GeV/c)^2$ to $Q^2 = 0.35\,(GeV/c)^2$ approximately. The acceptance is divided into four Q^2 bins of equal width and the extracted value of G_M^n within each bin corresponds to the average Q^2 determined from the data.

The four Q^2 bins used in the analysis are shown on table 4.3.

4.4 Momentum Corrections

Corrections to the electron momentum were imposed to account for errors in the reconstruction which led to systematic shifts in the data. Efforts are currently under way to identify the exact cause of the shifts seen in the data. While physical effects, such as internal radiation which is not currently implemented in the Monte Carlo simulations, may account for a fraction of the shift seen in the $^{2}\vec{H}\,(\vec{e}, e'p)$ corrections,

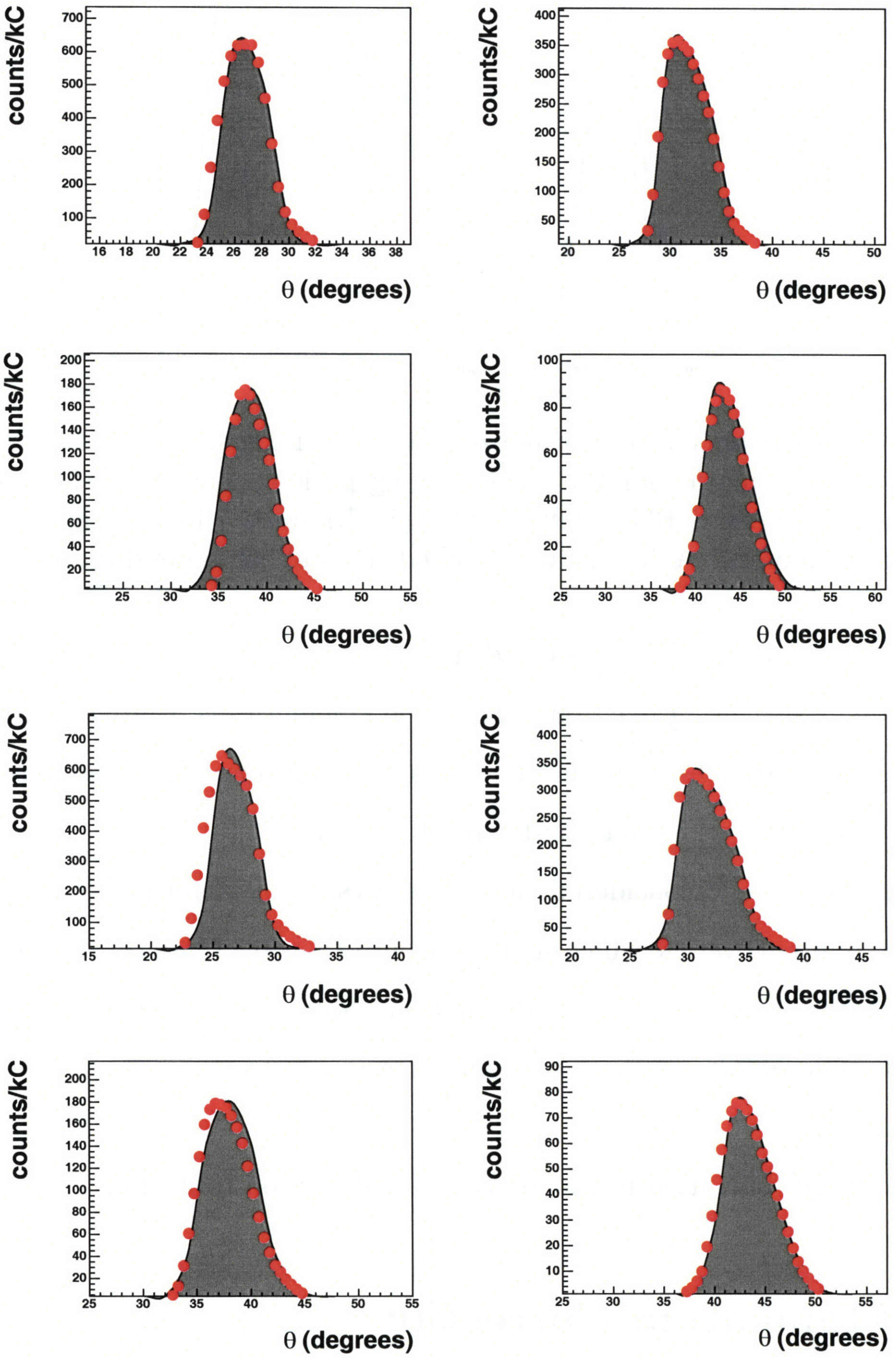

Figure 4-8: Histograms of the electron scattering angle θ for the data (red dots) and the Monte Carlo simulation (filled histograms). The top four panels show the data for the 2004 data set in perpendicular kinematics and the bottom four in parallel. Each set of four panels shows the four Q^2 bins in increasing order from top left to bottom right.

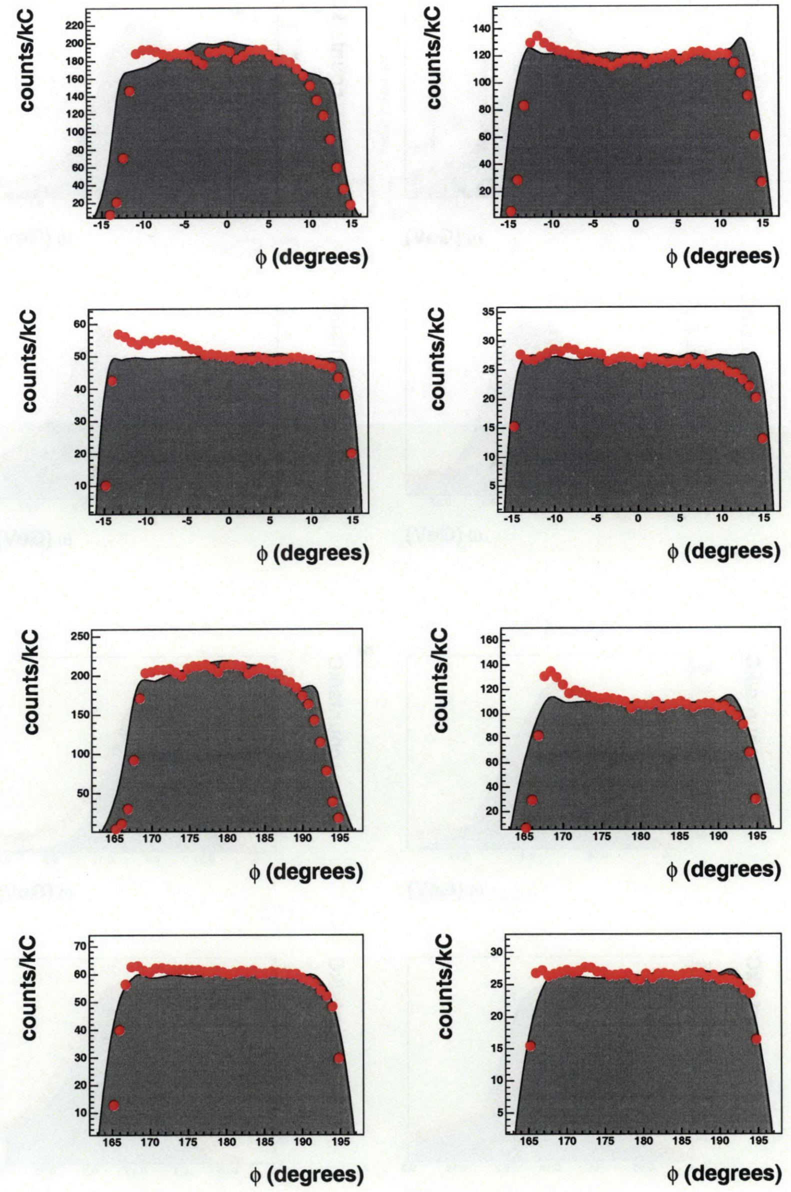

Figure 4-9: Histograms of the electron azimuthal scattering angle ϕ for the data (red dots) and the Monte Carlo simulation (filled histograms). The top four panels show the data for the 2004 data set in perpendicular kinematics and the bottom four in parallel. Each set of four panels shows the four Q^2 bins in increasing order from top left to bottom right.

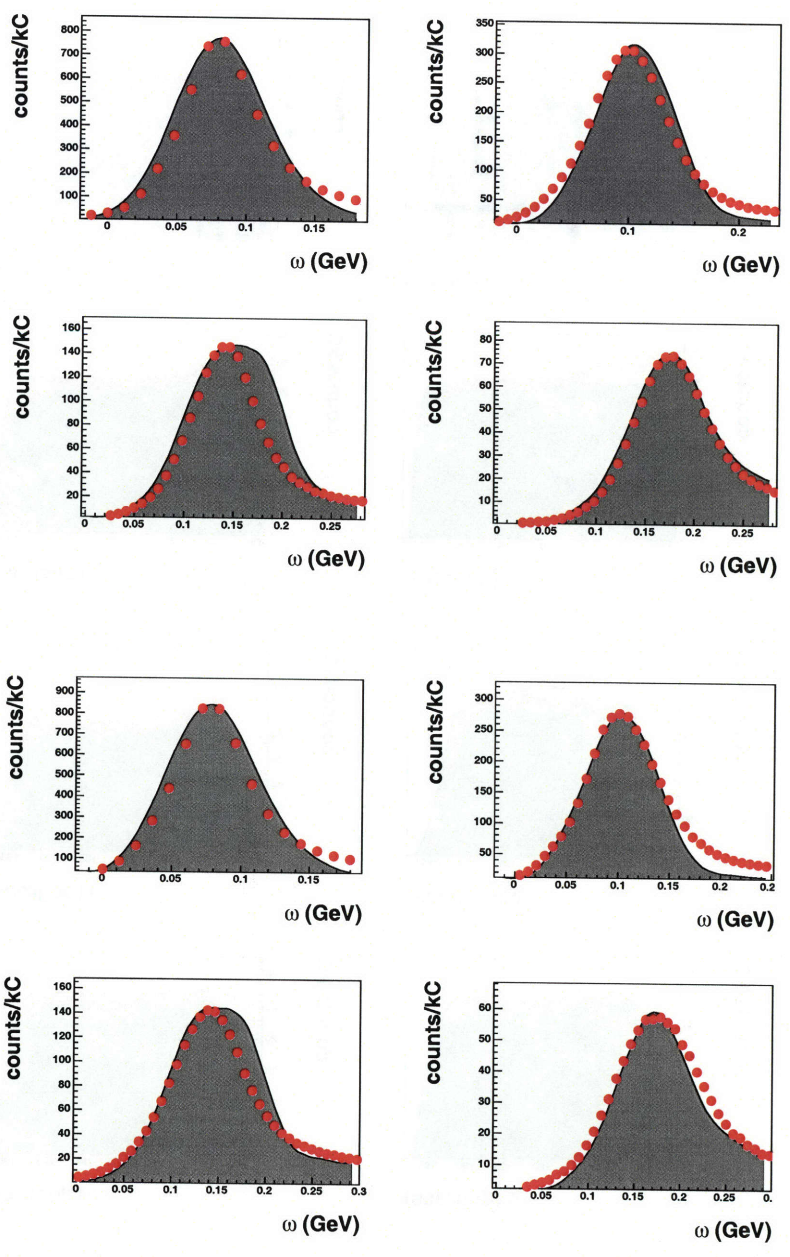

Figure 4-10: Histograms of the energy transfer ω for the data (red dots) and the Monte Carlo simulation (filled histograms). The top four panels show the data for the 2004 data set in perpendicular kinematics and the bottom four in parallel. Each set of four panels shows the four Q^2 bins in increasing order from top left to bottom right.

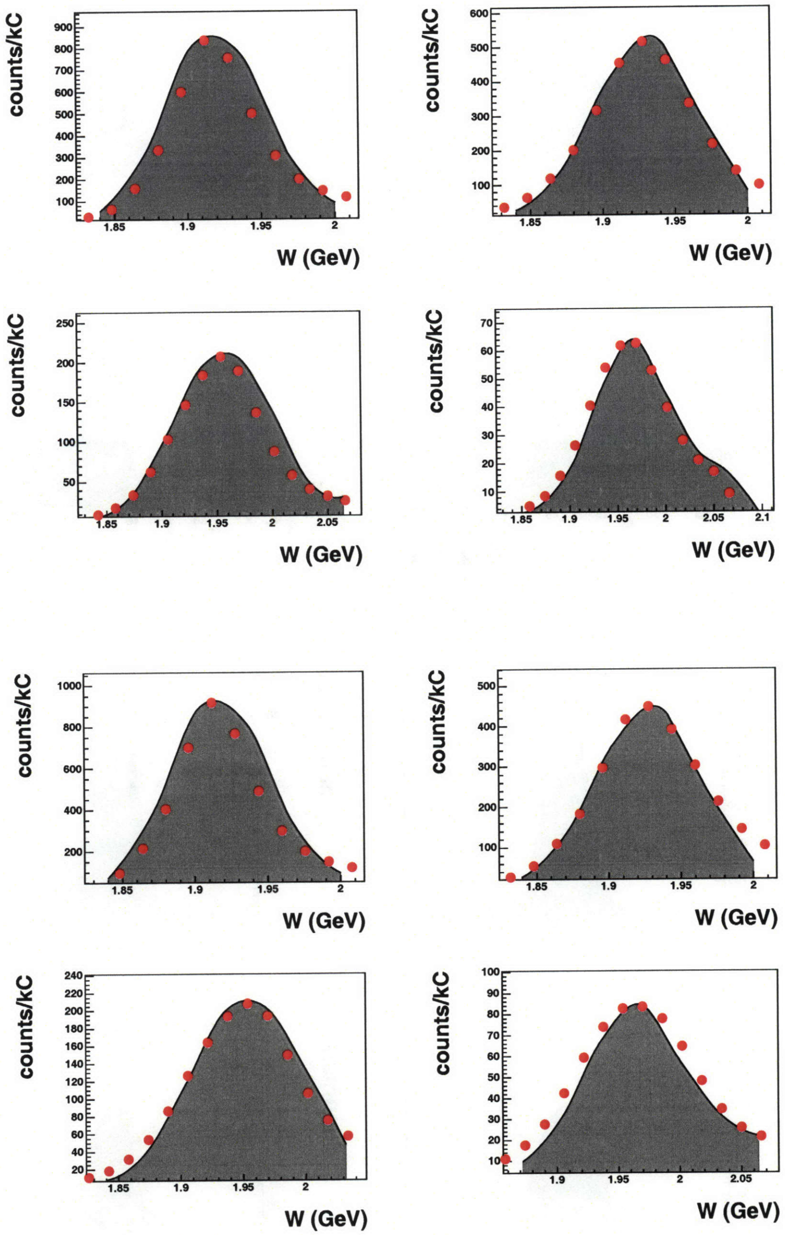

Figure 4-11: Histograms of the invariant mass W for the data (red dots) and the Monte Carlo simulation (filled histograms). The top four panels show the data for the 2005 data set in perpendicular kinematics and the bottom four in parallel. Each set of four panels shows the four Q^2 bins in increasing order from top left to bottom right.

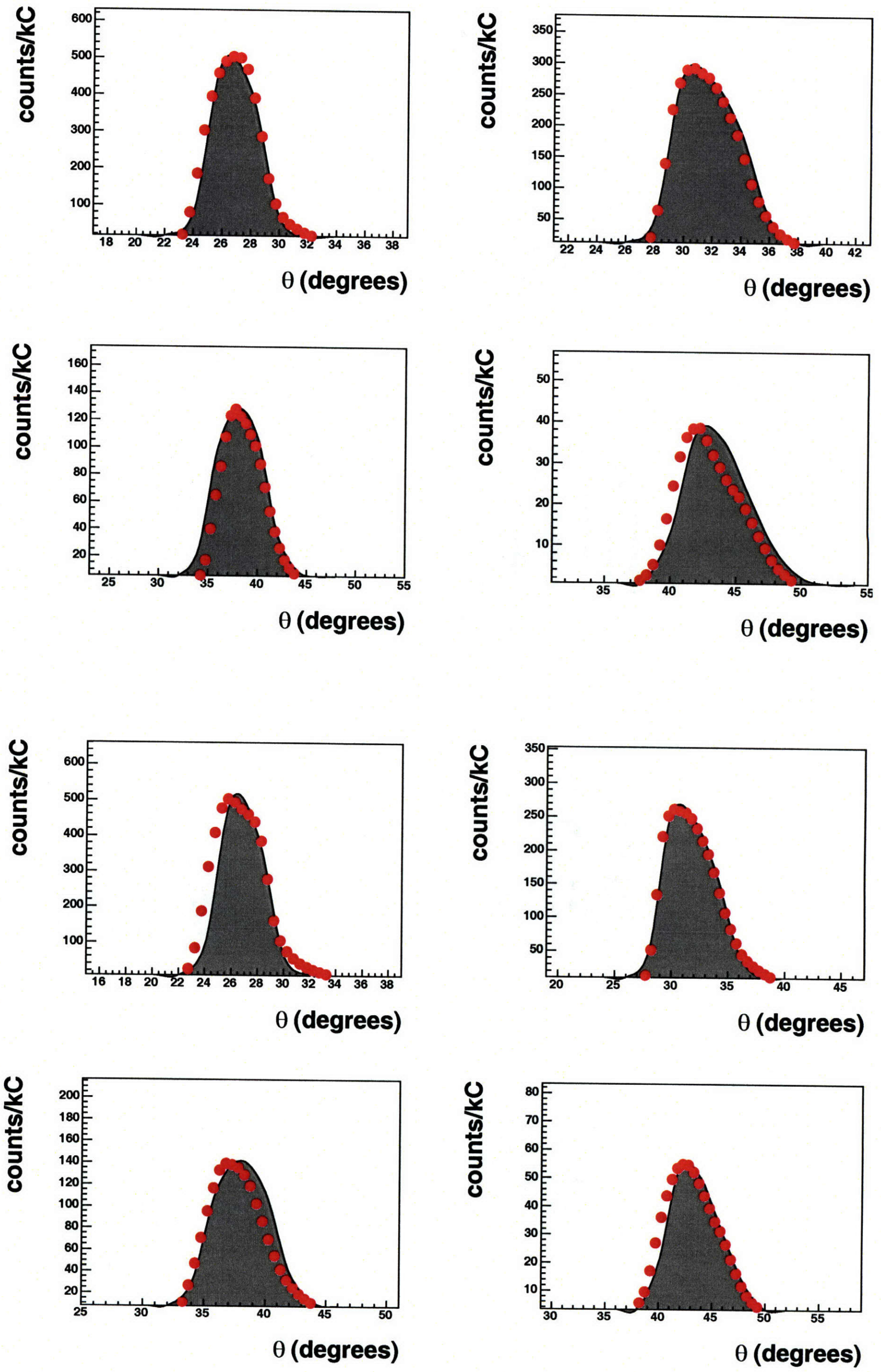

Figure 4-12: Histograms of the electron scattering angle θ for the data (red dots) and the Monte Carlo simulation (filled histograms). The top four panels show the data for the 2005 data set in perpendicular kinematics and the bottom four in parallel. Each set of four panels shows the four Q^2 bins in increasing order from top left to bottom right.

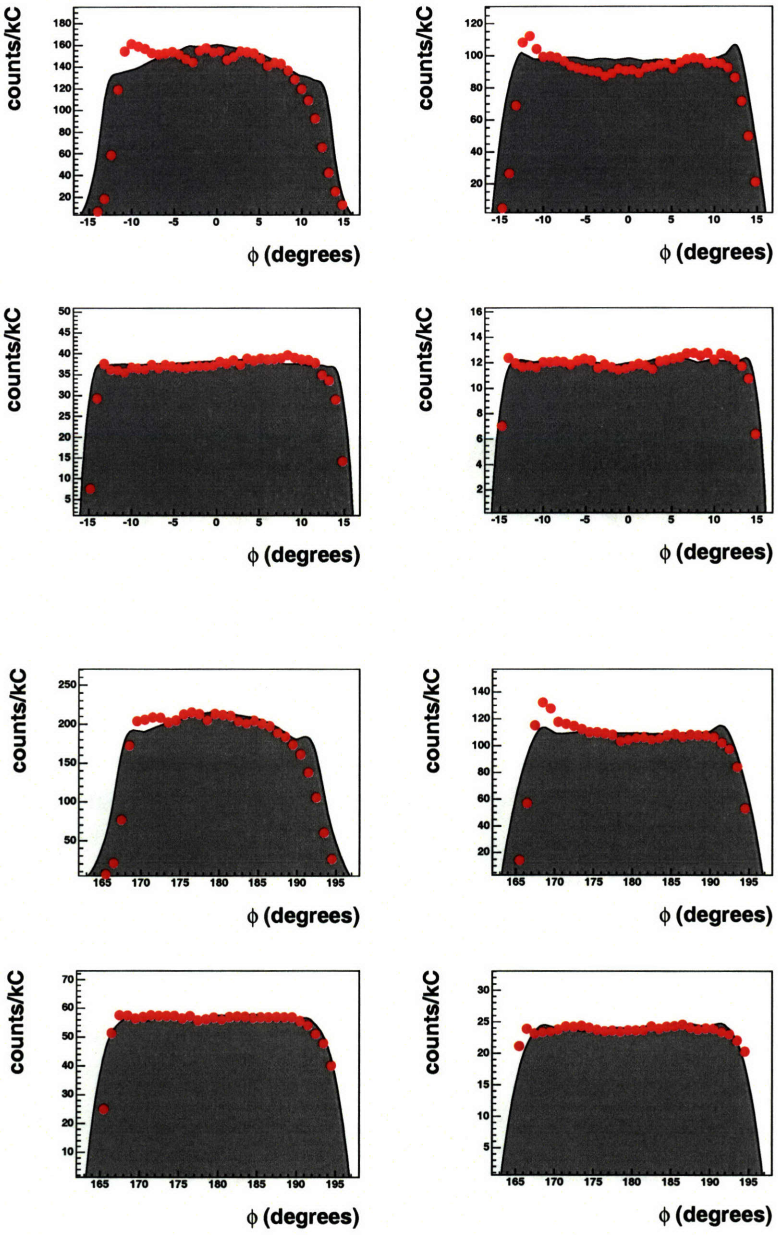

Figure 4-13: Histograms of the electron azimuthal scattering angle ϕ for the data (red dots) and the Monte Carlo simulation (filled histograms). The top four panels show the data for the 2005 data set in perpendicular kinematics and the bottom four in parallel. Each set of four panels shows the four Q^2 bins in increasing order from top left to bottom right.

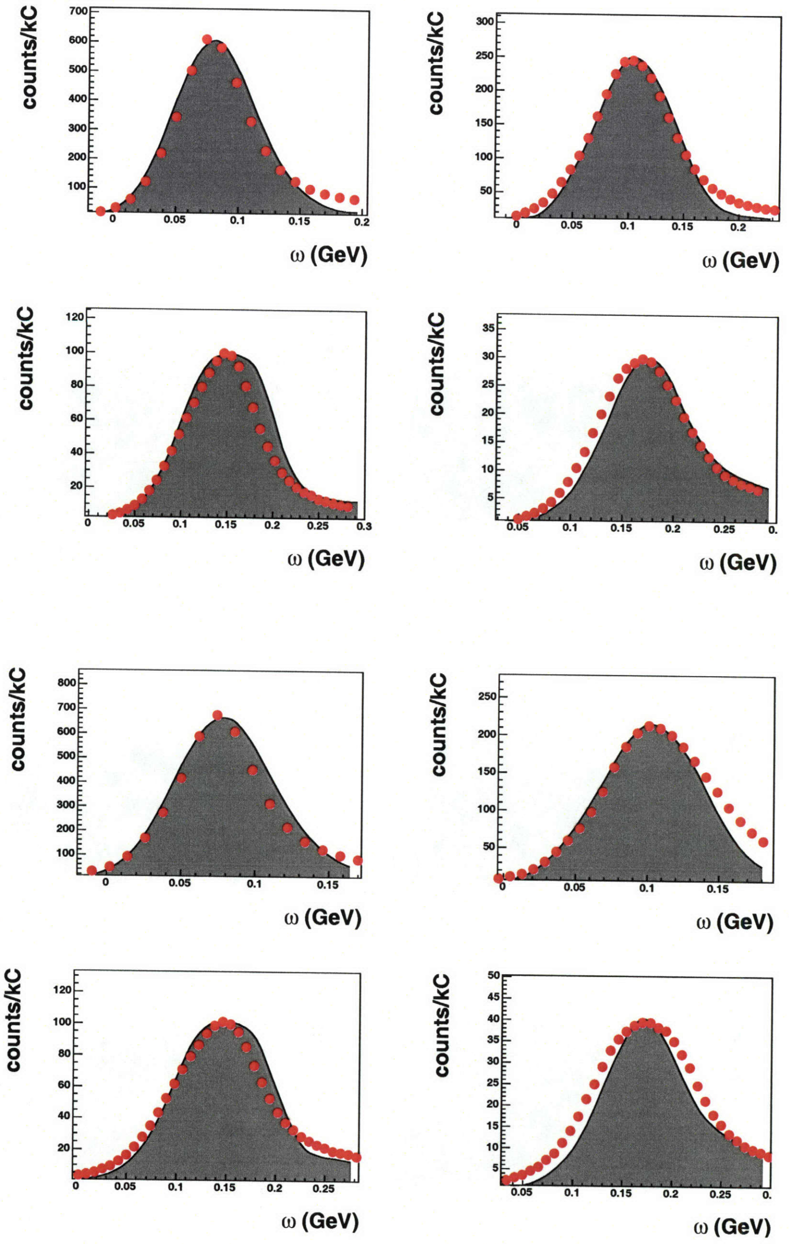

Figure 4-14: Histograms of the energy transfer ω for the data (red dots) and the Monte Carlo simulation (filled histograms). The top four panels show the data for the 2005 data set in perpendicular kinematics and the bottom four in parallel. Each set of four panels shows the four Q^2 bins in increasing order from top left to bottom right.

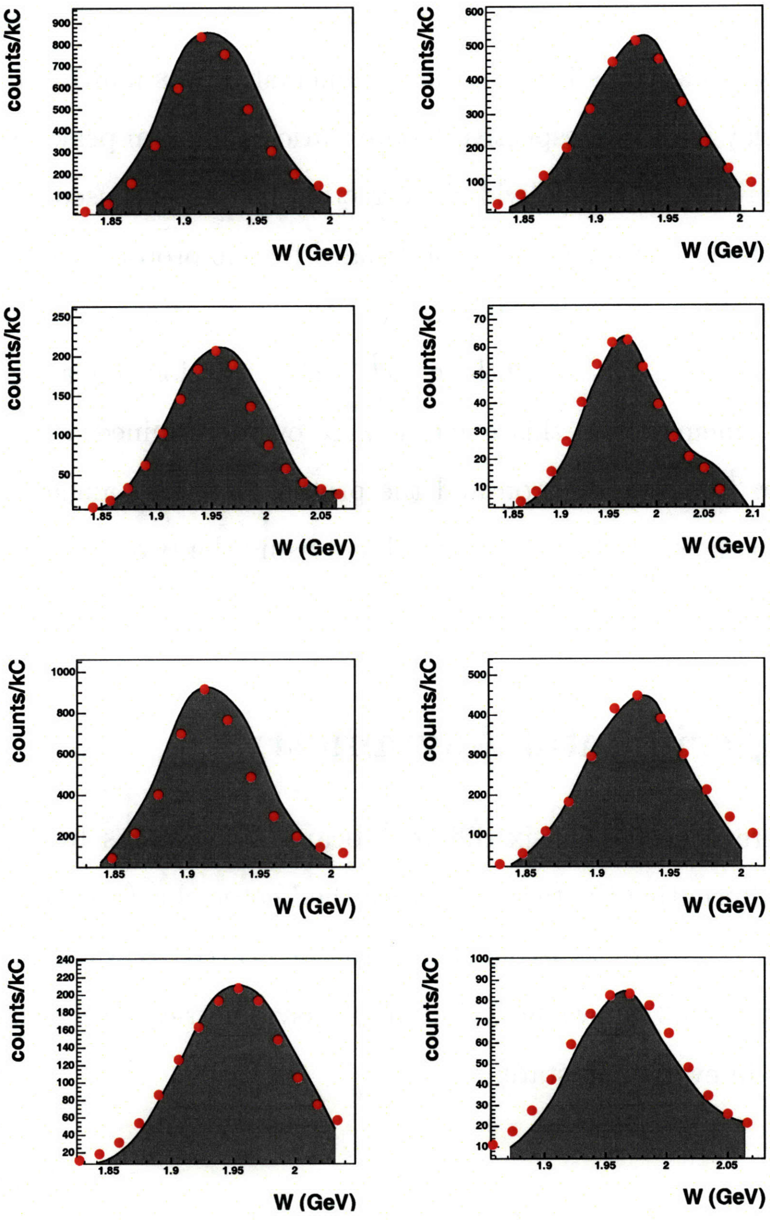

Figure 4-15: Histograms of the invariant mass W for the data (red dots) and the Monte Carlo simulation (filled histograms). The top four panels show the data for the 2005 data set in perpendicular kinematics and the bottom four in parallel. Each set of four panels shows the four Q^2 bins in increasing order from top left to bottom right.

inaccuracies in the geometry of the detector are seen as the most likely candidate.

Several methods were used to determine the magnitude of the corrections. One method used the ${}^2\vec{H}\,(\vec{e}, e'p)$ reaction to compare the data with the respective Monte Carlo simulation spectra bin-by-bin for the entire Q^2 range [19]. Bin-by-bin, the momentum peak of electrons in quasi-elastic kinematics was multiplied by a correction factor to overlay with the respective Monte Carlo simulation peak. A polynomial was then constructed from the individual correction factors and used in the data. Using the same method, corrections were established for the proton and neutron (from the ${}^2\vec{H}\,(\vec{e}, e'n)$ reaction) as well. Alternatively, the momentum corrections for electrons and protons were determined with the $\vec{H}\,(\vec{e}, e'p)$ reaction in elastic scattering kinematics. The kinematics in this reaction were overdetermined, and a comparison of Q^2 calculated from the electron and the proton scattering angles respectively gave an estimate of the corrections. The results of using the two correction sets discussed above agree fairly well.

4.5 Experimental Asymmetry

The data were collected in six different beam-target states by flipping the beam helicity and alternating the target between the Vector plus (+), Vector minus (-) and Tensor minus (t) states as explained in the dedicated ABS chapter earlier in this thesis. Equation (4.3) shows how the various asymmetries can be expressed in terms of the counts in every spin state:

$$\begin{pmatrix} P_z\,\alpha_d^V \\ P_{zz}\,\alpha_d^T \\ h\,P_z\,\alpha_{ed}^V \\ h\,P_{zz}\,\alpha_{ed}^T \end{pmatrix} = \frac{1}{N} \begin{pmatrix} \sqrt{\frac{3}{2}} & -\sqrt{\frac{3}{2}} & 0 & \sqrt{\frac{3}{2}} & -\sqrt{\frac{3}{2}} & 0 \\ \sqrt{\frac{1}{2}} & \sqrt{\frac{1}{2}} & -\sqrt{2} & \sqrt{\frac{1}{2}} & \sqrt{\frac{1}{2}} & -\sqrt{2} \\ \sqrt{\frac{3}{2}} & -\sqrt{\frac{3}{2}} & 0 & -\sqrt{\frac{3}{2}} & \sqrt{\frac{3}{2}} & 0 \\ \sqrt{\frac{1}{2}} & \sqrt{\frac{1}{2}} & -\sqrt{2} & -\sqrt{\frac{1}{2}} & -\sqrt{\frac{1}{2}} & \sqrt{2} \end{pmatrix} \begin{pmatrix} N^{++} \\ N^{+-} \\ N^{+t} \\ N^{-+} \\ N^{--} \\ N^{-t} \end{pmatrix} . \quad (4.3)$$

Here, h is the helicity of the beam, P_z the target vector polarization, P_{zz} is the target tensor polarization and N is the total number of events in the 6 spin states. The final column uses the notation $N^{beam,\, target}$ to denote the yields in the 6 beam-target states. The first superscript in the notation used above refers to the beam helicity, whereas the second to the target polarization state.

The symmetry of the detector allows the measurement of α_{ed}^V in both perpendicular and parallel kinematics. The explicit form of the polarization observable used in the extraction of G_M^n is the double-polarization vector asymmetry α_{ed}^V, expressed in terms of raw counts as

$$\alpha_{ed}^V = \frac{1}{hP_z}\sqrt{\frac{3}{2}}\,\frac{N^{++} + N^{--} - N^{-+} - N^{+-}}{N^{++} + N^{--} + N^{-+} + N^{+-} + N^{+t} + N^{-t}}. \tag{4.4}$$

The factor hP_z is the beam-target polarization product and it is necessary when the asymmetries are compared to Monte Carlo calculations. The size of the asymmetry varies between perpendicular and parallel kinematics, while it also depends on the target spin angle. Figure 4-16 show the results in both kinematics. As discussed earlier in this work, taking the super-ratio of the asymmetries enhances the sensitivity to G_M^n. In addition, the hP_z factor cancels out, reducing the systematic uncertainty of the extracted measurement.

The uncertainty for each asymmetry was calculated assuming that all spin states are independent random variables. It was given by

$$\sigma_\alpha = \frac{1}{hP_z}\sqrt{\frac{3}{2}}\sqrt{\frac{4N^+N^- + N^t(N^+ + N^-)}{(N^+ + N^- + N^t)^3}}, \tag{4.5}$$

where $N^+ = N^{++} + N^{--}$, $N^- = N^{+-} + N^{+-}$ and $N^t = N^{+t} + N^{-t}$. The error for the ratio was then calculated by assuming the asymmetries themselves are independent random variables. It was calculated using

$$\sigma_\Re = \sqrt{(\sigma_{\alpha_R})^2\left(\frac{\alpha_L}{\alpha_R^2}\right)^2 + (\sigma_{\alpha_L})^2\left(\frac{1}{\alpha_R}\right)^2}, \tag{4.6}$$

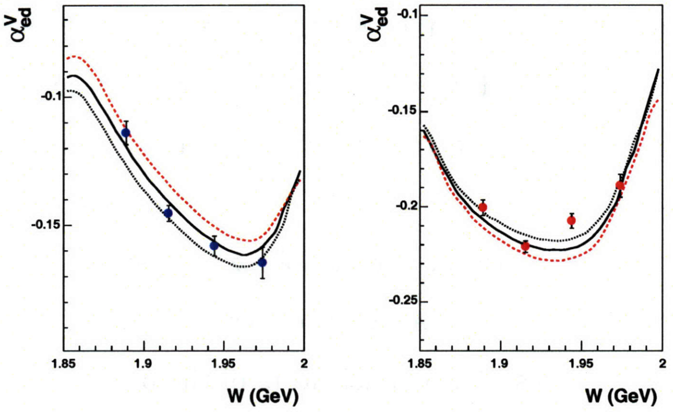

Figure 4-16: The experimental asymmetries in perpendicular (left panel) and parallel (right panel) kinematics and $Q^2 = 0.135\,(GeV/c)^2$. The red dashed curve shows the calculated asymmetry for $G_M^n = 115\%$ of the dipole form factor, the solid line for $G_M^n = 100\%$ and the black dotted line for $G_M^n = 85\%$. The FW parametrization for the proton form factors was used [24]. The data were normalized using an hP_z value of 0.491, determined from a ${}^2\vec{H}(\vec{e}, e')$ analysis for the 2004 data set.

where $\sigma_{\Re}$ is the uncertainty of the ratio and σ_{α_L} and σ_{α_R} the uncertainties of the left and right asymmetries.

4.6 Experimental Background

4.6.1 Empty Target Background

The electron identification cuts were not suited to eliminate cell wall background. The majority of these events resulted through quasi-elastic scattering of beam electrons on metallic surfaces in the vicinity of the cell and the cell walls which were made of Aluminum. In addition, shower events from the collimator upstream of the target area were another source of background. To accumulate enough statistics to study the spectrum of cell-wall scattering, gas flow into the target was halted for a period of several hours weekly and data were collected on an empty target. The weekly regeneration of the ABS nozzle provided a natural time slot for empty target operation.

Cell-wall background is not expected to be polarization-dependent. However, even a small unpolarized background rate can dilute the measured asymmetries and needs to be accounted for. The raw asymmetry is then given by

$$\alpha_{raw} = \frac{N^{+} + N^{+,empty} - (N^{-} + N^{-,empty})}{N^{+} + N^{+,empty} + N^{-} + N^{-,empty} + N^{tensor} + N^{t,empty}}, \tag{4.7}$$

where the superscript *empty* refers to the empty background in each state. Since the background exhibits no dependence on the state spin, the raw asymmetry can be expressed as:

$$\alpha_{raw} = \frac{N^{+} - N^{-}}{N^{+} + N^{-} + N^{t} + N^{empty}}. \tag{4.8}$$

This can be re-expressed as

$$\alpha_{raw} = \frac{N^{+} - N^{-}}{N^{total}} \left(\frac{1}{1 + f^{empty}} \right) \tag{4.9}$$

where N^{total} is the total number of counts in all six states with background subtracted and $f^{empty} = N^{empty}/N^{total}$. The N^{empty} was determined by summing the empty target counts in triggers 1, 2 and 7 and all spin states, and then scaling by the integrated charge ratio of polarized deuterium and empty target. Table 4.6 shows the measured backgrounds for both perpendicular and parallel kinematics as a percentage of the counts from the $^{2}\vec{H}(\vec{e}, e')$ reaction.

While the effect of the empty target background on the asymmetries can be of the order of $2-3\%$, the ratio of the asymmetries can only be affected by the difference in background of perpendicular versus parallel kinematics, since the ratio itself is diluted by the ratio of the backgrounds. The effect of the empty target background is taken into account in the analysis.

4.6.2 Beam Blow-up Factor

A measurement of the empty target background is not sufficient to establish the actual background during running. Background rates are likely to change when gas is inserted in the storage cell due to the transverse emittance blow-up of the beam, caused by interactions of the beam electrons with the target gas.

In order to investigate any possible beam blow-up, the $^{2}\vec{H}(\vec{e}, e'n)p$ rate was

Perpendicular kinematics				
Q^2 bins	W bin1	W bin2	W bin 3	W bin4
bin1	1.0%	1.4%	2.9%	5.5%
bin2	3.0%	1.6%	1.3%	2.2%
bin3	1.9%	1.5%	1.6%	2.3%
bin4	2.0%	1.9%	1.7%	1.4%

Perpendicular kinematics				
Q^2 bins	W bin1	W bin2	W bin 3	W bin4
bin1	1.0%	1.3%	2.5%	4.5%
bin2	2.8%	1.4%	1.2%	2.0%
bin3	2.5%	1.6%	1.2%	1.6%
bin4	4.0%	1.6%	1.1%	1.3%

Table 4.6: Empty target background as a percentage of the data used in the final G_M^n extraction for the 2004 data set. Similar background was observed in the 2005 data set.

obtained both for empty and polarized hydrogen targets. Since neither the empty nor the hydrogen target should produce any neutrons in quasi-elastic kinematics, only the background is measured in both cases [26]. After taking into account the possibility of misidentified protons, the ratio of the counts in trigger 2 for the hydrogen target and empty targets was shown to be of the order of 1.05. This ratio was associated with the beam blow-up factor. In the case of a ratio measurement, the beam blow-up is not a significant factor since it should be the same for both left and right sector and therefore cancel out in the analysis.

4.6.3 Pion Contamination

While electron event selection guarantees that what is detected is indeed an electron, the reaction channel the electron originated from cannot be determined unambiguously. Quasi-elastic cuts are meant to address exactly this question. For a pion to be produced in the final state, the invariant mass of the system has to be at least equal to the sum of the masses of the pion and the deuteron, slightly over 2 GeV. In practice however, due to the finite electron momentum resolution, the onset of threshold pion electro-production may begin up to 25 MeV lower than in theory. By limiting the upper limit of the invariant mass distribution of the data used in the analysis, the pion-production contamination is expected to be negligible [125].

4.6.4 Electron-Deuteron Elastic Scattering

The inclusive electron data set will inevitably include electrons from electron-deuteron elastic scattering. Most of the elastic events are expected to be registered in the coincidence trigger 1 (because of the elastic scattering kinematics) and could in principle be identified one-by-one and excluded from the analysis. However, the full inclusive cross section requires use of the singles trigger 7 for which no such identification is possible. Since the hadron detection efficiency of the BLAST spectrometer was less than 100%, elastic events that should have registered in trigger 1, may have instead registered in trigger 7 because only the electron was actually detected. Figure 4-17 shows a simulation of the relative yields of electrodisintegration versus elastic in perpendicular kinematics for the four Q^2 bins used in this analysis. In principle, even when the Fermi momentum inside the deuteron is taken into account, the electrodisintegration and elastic peaks should be separated, the latter being a delta function located at the deuteron rest mass. However, reconstruction resolution smears both peaks significantly as shown in figure 4-17, in which data-reconstruction resolution is simulated with the Monte Carlo. Due to the cross section of the elastic reaction, the elastic events are concentrated in the two lowest Q^2 bins whereas bins 3 and 4 show practically negligible elastic contribution. More specifically, the contamination is expected to be of the order of 5% for the first bin, 3.6% for the second and less than 1% for the final two bins in both parallel and perpendicular kinematics.

It is important to quantify the elastic contamination due to the radically different ratio of asymmetries as compared to the electrodisintegration ratio. The combined asymmetry is affected mostly in the lowest edge of the invariant mass distribution of the two first Q^2 bins. Figure 4-18 shows Monte Carlo calculations for ed elastic events only (blue) and electrodisintegration (red) for $Q^2 = 0.135$ (GeV/c)^2. The black line shows the weighted average of the two. In perpendicular kinematics the asymmetries are close and the deviation of the average versus the electrodisintegration asymmetries is rather small. In parallel kinematics the effect is more significant. In

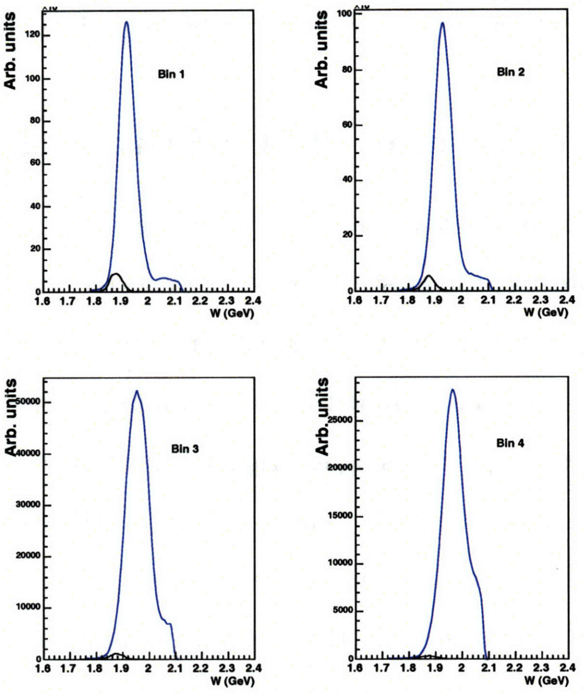

Figure 4-17: A Monte Carlo simulation of the relative yields for electrodisintegration (blue) versus ed elastic (black) for perpendicular kinematics. Reconstruction resolution smears both the electrodisintegration and the elastic peaks. The former is also smeared by the Fermi momentum inside the deuteron. The elastic contamination is more important in the two lowest Q^2 bins whereas it is practically negligible in the higher ones. The full Arenhövel model Monte Carlo calculations used for the present analysis incorporated the elastic yields as well. The relative yields appear identical in parallel kinematics and that picture is therefore omitted. The histograms shown here are in arbitrary units.

both cases, the elastic contributions are limited to the low edge of the invariant mass spectrum. Finally, figure 4-19 shows the ratio for the three cases and the same Q^2.

The Monte Carlo used herein for the extraction of G_M^n incorporates both the electrodisintegration and elastic reactions weighed by their respective cross sections as given by the full Arenhövel model. The simulation assumes the same hadron detection efficiency for both reactions. However, there are reasons to believe that the detection and reconstruction efficiency for deuterons is slightly lower than that for protons. As for detection, for a fixed Q^2 value, deuterons recoil to more backward angles compared to electrodisintegration events. Consequently, they hit closer to the edge of the wire-chamber acceptance which has lower detection and reconstruction efficiency. In addition, energy loss mechanisms and multiple scattering are more

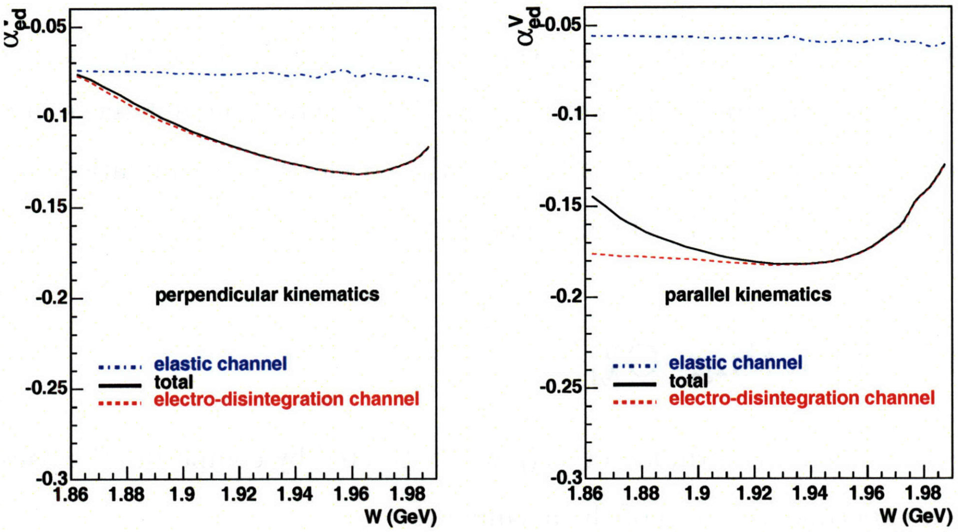

Figure 4-18: Monte Carlo simulations of the asymmetries in perpendicular and parallel kinematics and $Q^2 = 0.135$ (GeV/c)^2. The red line shows the vector asymmetry from electrodisintegration events only, whereas the blue shows the corresponding asymmetry from ed elastic events. The black line shows the weighted average of the two and is essentially what is being measured in the experiment. The contribution of the elastic events is more prominent in parallel kinematics where the relative difference in asymmetry between electrodisintegration and electron-deuteron elastic scattering is larger.

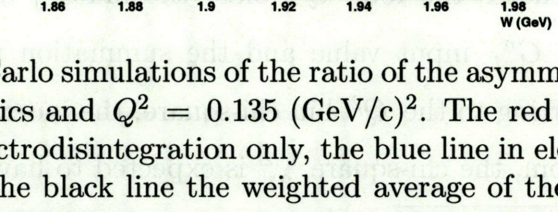

Figure 4-19: Monte Carlo simulations of the ratio of the asymmetries in perpendicular over parallel kinematics and $Q^2 = 0.135$ (GeV/c)^2. The red line is a calculation of the asymmetry in electrodisintegration only, the blue line in electron deuteron elastic scattering only and the black line the weighted average of the two. The ratio in ed elastic is significantly higher than the ratio from electrodisintegration events alone. However, the effect is limited to the lowest edge of the W spectrum because of the cross section (see figure 4-17).

significant for deuterons than either protons or neutrons. Since these effects are not corrected for in the data, deuteron reconstruction is less likely to have a good χ^2 fit, leading to more discarded events on average [14]. Overall, the difference in efficiency is rather small and given the small size of the ed elastic contamination in the data set, the effect was deemed to be insignificant[4].

4.7 Extracting $\mathbf{G_M^n}$

The neutron magnetic form factor G_M^n was extracted by comparing the background-corrected experimental ratio of the asymmetries

$$\Re \equiv \frac{\alpha_{perpendicular}}{\alpha_{parallel}}, \tag{4.10}$$

to the calculation of this observable with the BLAST Monte Carlo using the full Arenhövel model. The Friedrich and Walcher parametrization [24] was used for the proton form factors and the Galster parametrization [9] was used for G_E^n. The extraction was performed in four Q^2 bins independently. Within each bin, four invariant mass bins were used to fit to the theoretical calculations performed by varying the value of G_M^n in units of the dipole form factor. The W average for each bin in shown in table 4.7 for both data sets. A χ_{ij}^2 is calculated for each theoretical calculation. The χ_{ij}^2 is given by

$$\chi_{ij}^2 = \sum_k \frac{\Re_k^{data} - \Re_k^{MC}}{(\sigma_k^{data})^2}, \tag{4.11}$$

where the index i denotes the four Q^2 bins, the index j denotes the theoretical calculations for each G_M^n input value and the summation runs over the W bins (index k). When referring to the Q^2 bin chi-square, the index j will be dropped.

Within each Q^2 bin, the chi-square χ_i^2 is expected to have a parabolic shape in

---

[4] Comparing the relative yields of the electrodisintegration and ed-elastic reactions in the coincidence trigger 1 against the Monte Carlo simulations shows a difference of less than 5% in efficiency.

2004 data set				
Q^2 bin	W bin1	W bin2	W bin3	W bin4
1	1.895	1.919	1.942	—
2	1.893	1.919	1.945	1.972
3	1.888	1.915	1.941	1.967
4	1.891	1.918	1.945	1.971

2005 data set				
Q^2 bin	W bin1	W bin2	W bin3	W bin4
1	1.891	1.914	1.935	1.957
2	1.886	1.913	1.940	1.968
3	1.894	1.921	1.947	1.973
4	1.904	1.927	1.949	1.972

Table 4.7: The average W values within each Q^2 bin. Only three W bins were used for the extraction of G_M^n for the lowest Q^2 bin of the 2004 data set.

the vicinity of its minimum [126]. The parametrization

$$\chi_{ij}^2 = p_1 + \frac{(p2 - y_j)^2}{(p_3 + p_4 y_j)^2} \tag{4.12}$$

was used for the parabola. Here, p_1, p_2, p_3, p_4 are the parameters of the fit. The minimum of χ_i^2 for each bin occurs at the value of the fit variable denoted as y_{min}. The value of G_M^n which best fits the data is equal to y_{min} as a percentage of the dipole form factor. The uncertainty of y_{min} and therefore of the value of G_M^n is defined as the variation in y_{min}, denoted as δy_{min}, which increases the minimum value of χ_i^2 by one

$$\chi_i^2\Big|_{(y_{min} + \delta y_{min})} = \chi_i^2\Big|_{(y_{min})} + 1. \tag{4.13}$$

The procedure described above had to be performed for the two data sets independently since the asymmetries and the ratios are different.

The results for the fit and minimization procedure for each Q^2 bin are shown in figures 4-20 for the 2004 and 4-21 for the 2005 data set. The left panels show the ratio $\Re$ as a function of the invariant mass W. The lines indicate theoretical calculations with 85%, 90%, 100%, 110% and 115%, all with respect to the dipole parametrization. The right panels show the result for the value of the form factor and the corresponding uncertainty, as well as the minimum value of the χ_i^2. Table

4.8 shows a summary of the results for the 2004 and 2005 data sets separately.

2004 data set				
$< Q^2\,((GeV/c)^2) >$	G_M^n	ΔG_M^n (stat)	ΔG_M^n (syst)	χ^2_{min}/ndf
0.135	0.948	0.041	0.028	1.05
0.189	0.929	0.033	0.028	1.41
0.252	0.971	0.038	0.029	1.69
0.316	0.966	0.050	0.029	0.77

2005 data set				
$< Q^2\,((GeV/c)^2) >$	G_M^n	ΔG_M^n (stat)	ΔG_M^n (syst)	χ^2_{min}/ndf
0.135	0.978	0.028	0.022	0.84
0.189	0.958	0.024	0.021	1.10
0.252	0.941	0.028	0.021	0.17
0.316	0.976	0.053	0.022	0.98

Table 4.8: Extracted G_M^n values for the 2004 (top) and 2005 (bottom) data sets.

Ratios				
2004 data set				
$< Q^2\,((GeV/c)^2) >$	$\Re_{Wbin1}$	$\Re_{Wbin2}$	$\Re_{Wbin3}$	$\Re_{Wbin4}$
0.135	0.595	0.658	0.744	—
0.189	0.618	0.627	0.693	0.706
0.252	0.537	0.598	0.622	0.711
0.316	0.657	0.637	0.624	0.677
2005 data set				
$< Q^2\,((GeV/c)^2) >$	$\Re_{Wbin1}$	$\Re_{Wbin2}$	$\Re_{Wbin3}$	$\Re_{Wbin4}$
0.135	0.358	0.463	0.527	0.573
0.189	0.379	0.403	0.476	0.550
0.252	0.347	0.427	0.466	0.524
0.316	0.383	0.506	0.433	0.465

Table 4.9: The values of the ratio $\Re$ for each W and Q^2 bin. The top half shows the results for the 2004 data set and the bottom half for the 2005.

The extracted values were combined weighted by their respective error bars according to [126]

$$(G_M^n)_{ave} = \frac{\frac{v_1}{\sigma_1^2} + \frac{v_2}{\sigma_2^2}}{(\frac{1}{\sigma_1^2} + \frac{1}{\sigma_2^2})}, \tag{4.14}$$

where v_1 and v_2 are the extracted G_M^n values for the two data sets and σ_1 , σ_2 the

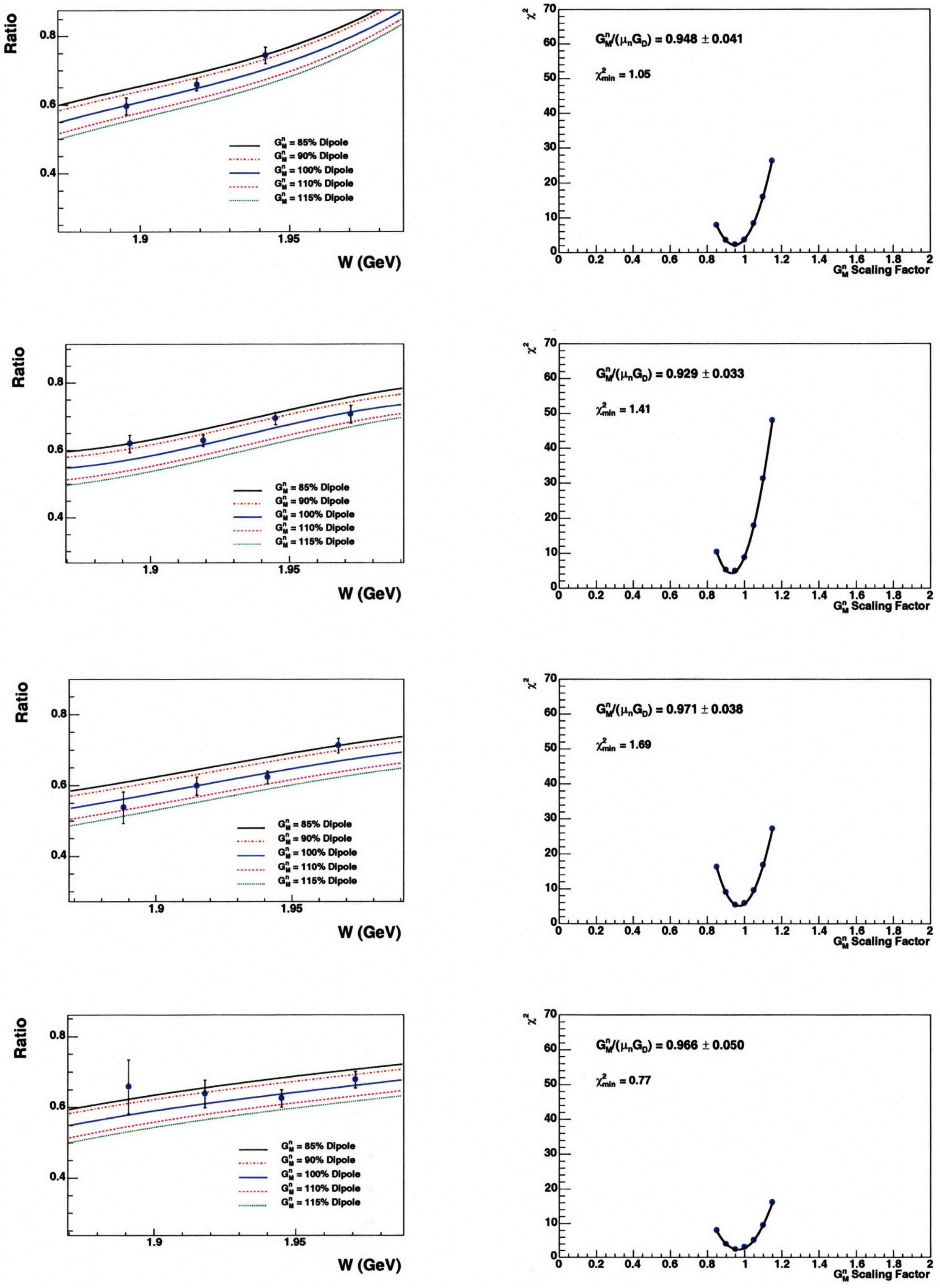

Figure 4-20: The left panels show the ratio versus the invariant mass for the 2004 data set in the four Q^2 bins. The right panels show the χ^2-minimization and the extracted value of G_M^n for each bin as well as the relevant error bar.

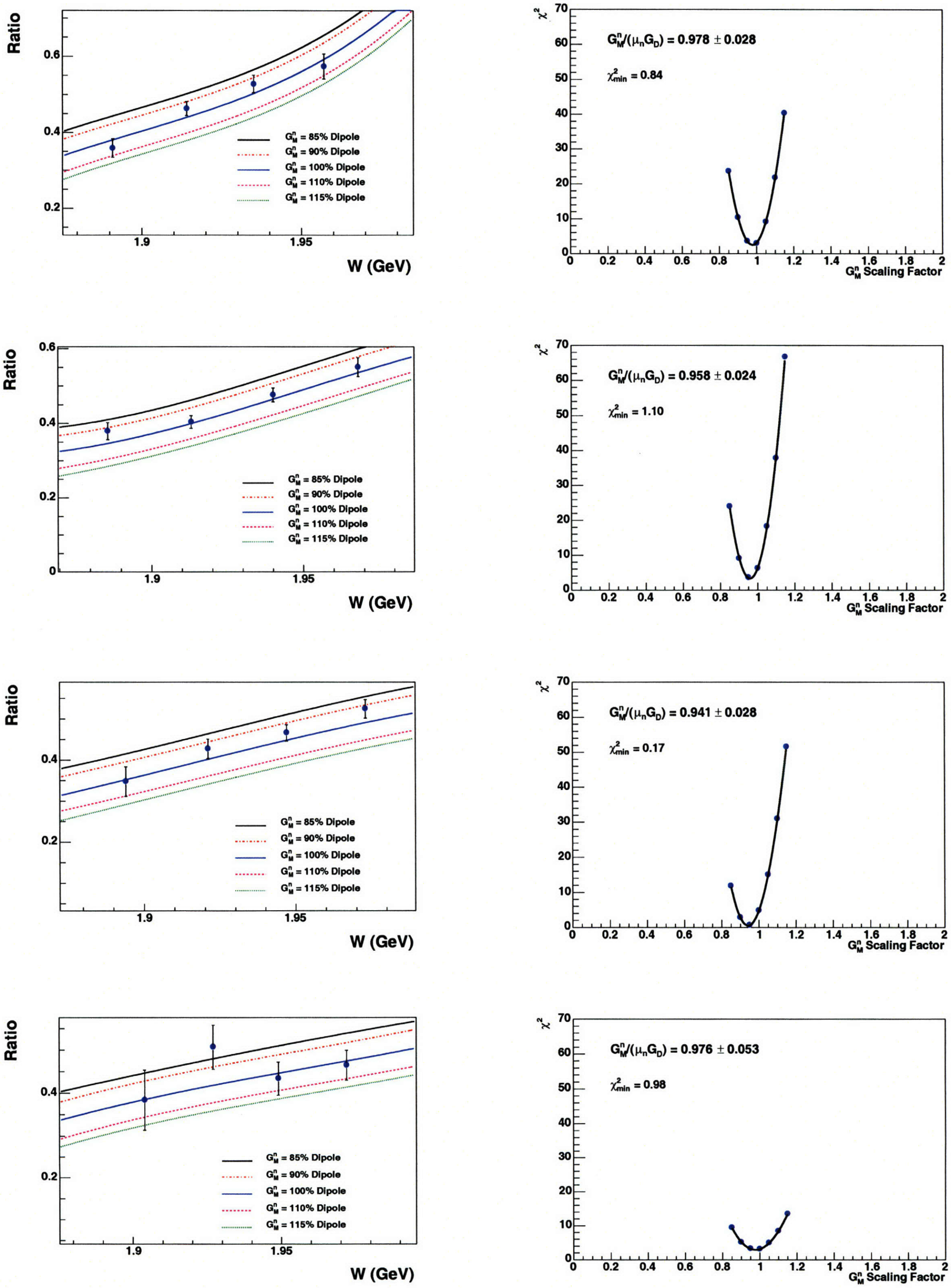

Figure 4-21: The left panels show the ratio versus the invariant mass for the 2005 data set in the four Q^2 bins. The right panels show the χ^2-minimization and the extracted value of G_M^n for each bin as well as the relevant error bar.

respective error bars. The combined error bar was calculated using

$$\frac{1}{\sigma_t^2} = \frac{1}{\sigma_1^2} + \frac{1}{\sigma_2^2}, \tag{4.15}$$

where σ_t is the combined error bar. The combined results are shown in table 4.10.

Combined results			
$< Q^2\,((GeV/c)^2) >$	G_M^n	ΔG_M^n (stat)	ΔG_M^n (syst)
0.135	0.968	0.023	0.025
0.189	0.948	0.019	0.025
0.252	0.951	0.022	0.025
0.316	0.971	0.036	0.025

Table 4.10: Combined extracted G_M^n values.

The systematic errors listed in the tables above are discussed in the next section.

4.8 Systematic Uncertainties

In this section, the different factors contributing to the overall systematic uncertainties listed in tables 4.8 and 4.10 are discussed. Table 4.11 shows a summary of the systematic uncertainties of this measurement.

Source of Error	% error (2004)	% error (2005)
Spin Angle	2.5 %	1.5 %
Cut dependence, Reconstruction and Resolution	1.5 %	1.5 %
G_E^n value	0.5%	0.5%
Radiative effects	0.5%	0.5%
Total	3.0%	2.2%

Table 4.11: Systematic uncertainties for each data set. Each source of systematic error is discussed in detail in the following sections. The individual systematic errors are combined in quadrature.

4.8.1 Target Polarization Angle

Precise knowledge of the target polarization angle was required to generate Monte Carlo simulations of the experiment. The target holding field was mapped in situ and with the BLAST toroidal field turned on for consistency with the actual data. In the present analysis, the results of the June 2005 holding field measurement were used[5]. This measurement had an uncertainty of 0.5° for both spin angles. Figure 4-22 shows the effect of variations in the average polarization angle on the asymmetries. The uncertainty is much higher in perpendicular kinematics (top panel).

Equation (1.19) explains the difference in the uncertainty of the asymmetries with respect to variations in the target polarization angle between perpendicular and parallel kinematics. In perpendicular kinematics, the angle θ_d^* peaks at about 35° and in parallel at about 98°, respectively. In the perpendicular case, the two terms in eq. (1.19) (multiplied by a sine and a cosine, respectively), vary in the same direction with variations in the target polarization angle, while the oppposite is true in the parallel case. Hence the combined effects of the two terms on the asymmetry add in the perpendicular case and subtract in the parallel. Figure 4-23 shows the combined uncertainty of the ratio. Increasing the target polarization angle by one degree increases decreases both asymmetries, albeit by a different percentage. Therefore, the combined systematic uncertainty in the ratio is smaller than that for the individual asymmetries. The uncertainty of the extracted value of G_M^n due to the polarization angle was estimated to be of the order of 2.5% for the 2004 data set and 1.5% for the 2005. Some of the difference is attributed to the difference in the polarization angle itself. While both are known with 0.5° precision, the relative uncertainty is in fact smaller for the 2005 data set. The target polarization angle uncertainty dominates systematics in both data sets.

4.8.2 Cut dependence, Reconstruction and Resolution

The invariant mass range used in the analysis could give rise to systematic biases of certain kinematic regions which could be different between the data and the Monte Carlo. This could result in offsets in the asymmetries and therefore the ratio. In

---

[5] The June 2005 field-map is inconsistent with a determination of the target polarization angle using an ed-elastic analysis of the data. The inconsistency could be due to differences in the geometrical information for the detector used in the reconstruction as opposed to the actual geometry. Investigations into the causes of this are still ongoing.

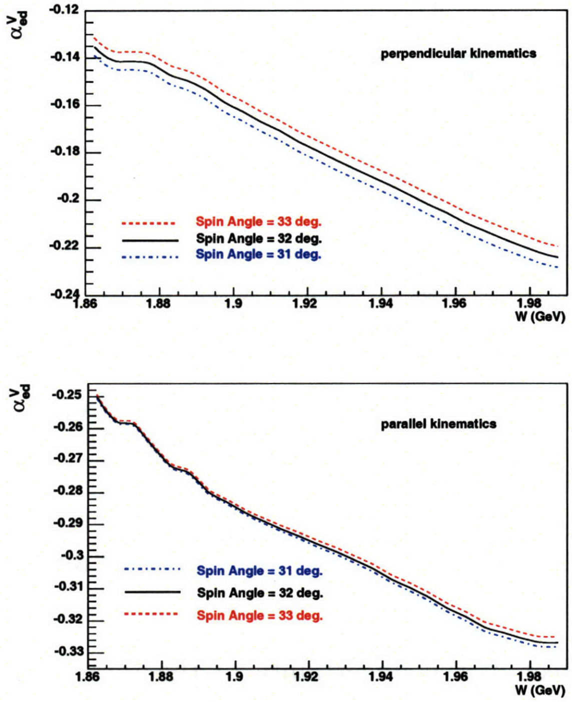

Figure 4-22: The effect of the uncertainty of the target polarization angle on the asymmetries. The top panel shows the effect in perpendicular kinematics whereas the bottom panel shows the effect in parallel. Parallel kinematics shows almost no effect. The asymmetries are plotted here for the third Q^2 bin.

addition, imperfect modeling of the detector resolution in the reconstruction could have a similar effect even though the resolution itself is not critical for an asymmetry measurement (as long as it is matched well to the Monte Carlo). Finally, systematic misreconstruction may introduce shifts in the data. This would be important, since a direct comparison of the data asymmetry at a specific invariant mass to the Monte Carlo has to be performed at exactly the same value of W. While the momentum corrections discussed earlier in this chapter were designed to match data and Monte Carlo and reduce this source of error, the uncertainty is not eliminated completely. Since it is diffcult to deconvolute the aforementioned sources of error, they are all considered together.

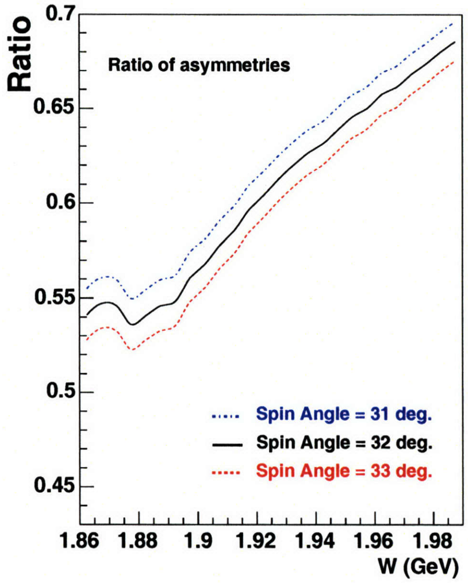

Figure 4-23: The effect of the uncertainty of the target polarization angle on the ratio. The error is almost entirely due to the resulting uncertainty in perpendicular kinematics. The ratio is plotted here for the third Q^2 bin.

Another possible source of error is radiative effects (section 4.8.5). For an electron that radiates, the measured final energy is in fact lower than the true $E^{'}$ by an amount ΔE , therefore

$$E^{'}_{new} = E^{'} - \Delta E. \tag{4.16}$$

The calculated invariant mass for this electron would be

$$W = \sqrt{M_d^2 + 2M_d\,(E - E_{new}) - 4E_{beam}E_{new}\sin^2\left(\frac{\theta}{2}\right)}, \tag{4.17}$$

which deviates from the unradiated W value. While this is a significant correction for a cross section, the asymmetry and ratio measurement are largely unaffected by this uncertainty in W.

Two systematic methods were employed to study the possible dependence on cuts, reconstruction and resolution. First, the cuts were varied both in the data and the

Monte Carlo. The second method involved artificially shifting the mean value of the invariant mass for each bin and comparing the results on the extracted form factor value. The systematic uncertainty due to these shifts was estimated to be of the order of 1.5% for all bins.

4.8.3 False Asymmetries

Equation 4.3 indicates the spin-state composition of the asymmetry terms:

$$\alpha_d^V = \frac{1}{P_z}\sqrt{\frac{3}{2}}\frac{(N^{++} + N^{-+} - N^{+-} - N^{--})}{N}, \tag{4.18}$$

and

$$\alpha_{ed}^T = \frac{1}{hP_{zz}} \frac{\sqrt{\frac{1}{2}}(N^{++} + N^{+-} - N^{-+} - N^{--}) - \sqrt{2}(N^{+t} - N^{-t})}{N}. \tag{4.19}$$

These can be calculated from the individual spin-state yields.

The asymmetries α_d^V and α_{ed}^T are explicit functions of the azimuthal angle ϕ_d between the target-spin vector and the momentum transfer vector $\vec{q}$, given by

$$\alpha_d^V = \frac{6c}{\sigma_o}\rho_{LT} F_{LT}^{1-1} sin\phi_d \, d_{-10}^1(\theta_d) \tag{4.20}$$

and

$$\alpha_{ed}^T = \frac{6c}{\sigma_o}\rho_{LT}^{'} F_{LT}^{'2-1} sin\phi_d \, d_{-10}^2(\theta_d), \tag{4.21}$$

respectively, as well as two form factors, F_{LT}^{1-1} for α_d^V and $F_{LT}^{'2-1}$ for α_{ed}^T. Since these two form factors vanish below pion threshold [16], both asymmetry terms should be identically zero in that region. However, the possibility of these being non-zero in the data cannot be excluded. Likely causes of non-zero α_{ed}^T and α_d^V include erroneous determination of the charge in each spin state and differences between the target polarization and density in its different states. Figure 4-24 shows these asymmetries for a fixed $Q^2 = 0.135\,(GeV/c)^2$ to be consistent with zero. The same result holds true for the rest of the Q^2 range.

Yet another possible asymmetry term is the beam asymmetry, defined here as

$$\alpha_e = \frac{1}{h} \frac{(N^{++} + N^{+-} + N^{+t} - N^{-+} - N^{--} - N^{-t})}{N}, \tag{4.22}$$

similar to the corresponding beam asymmetry in the coincidence cross section. This asymmetry should be proportional to $sin\phi_{pq}^{cms}$, defined as the center-of-mass angle between the scattering and reaction planes (see figure 1-5). Since the inclusive cross section is formed by integrating the coincidence cross section over the entire phase-space, this asymmetry term should be identically zero. However, a small asymmetry may still be found in the data. This may be due to the fact that the BLAST spectrometer is not perfectly inclusive despite the fact that Monte Carlo studies have shown that the expected number of electrons missed by the detector acceptance is negligible. The singles trigger 7 shows no such asymmetry, which indicates that the integration over the phase space is done correctly. The coincidence triggers 1 and 2 however do show a small non-zero behavior, possibly because of the selected kinematics and efficiency fluctuations in ϕ_{pq}^{cms}. The beam asymmetry at $Q^2 = 0.135\,(GeV/c)^2$ is shown in the top panel of figure 4-24 and other bins show similar behavior in size. The possible effects of a beam asymmetry on α_{ed}^V were investigated by introducing artificial discrepancies in the spin-state yields and comparing the result to the asymmetry from the actual counts. The effects on α_{ed}^V were thus shown to be negligible. False asymmetries are therefore not expected to be a source of systematic error for the present analysis.

4.8.4 Dependence on $\mathbf{G_E^n}$

Since the inclusive asymmetries are functions of all four nucleon form factors, any uncertainties in the values of the proton form factors and the neutron electric form factor G_E^n will have an impact on the extraction of G_M^n. This is because a certain value has to be assumed in generating the Monte Carlo used in the extraction. In this case, the values of the proton form factors are known to good precision, but the uncertainty in G_E^n is significant. Figure 4-25 shows the effect of variations in

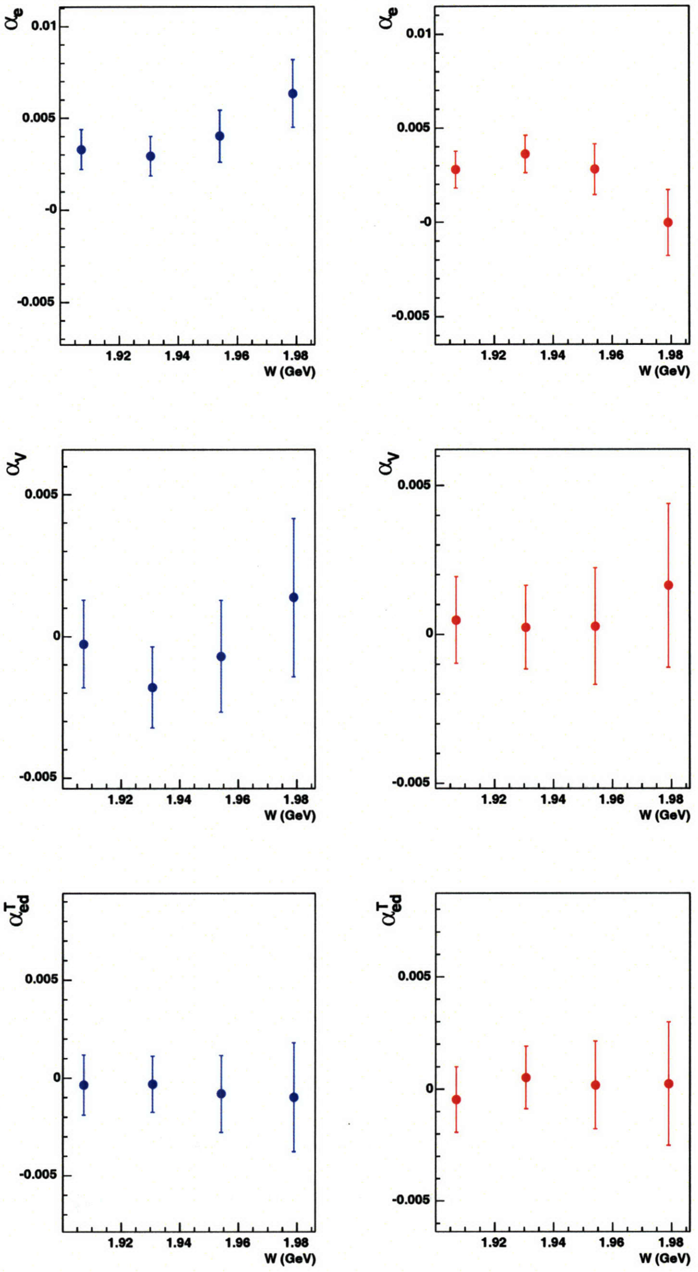

Figure 4-24: False asymmetries α_e (top), α_d^V (middle) and α_{ed}^T (bottom) for the first Q^2 bin at $Q^2 = 0.135\,(GeV/c)^2$. The left panels show the asymmetries in perpendicular (blue) and the right panels in parallel (red) kinematics. The asymmetries α_d^V and α_{ed}^T are consistent with zero whereas the α_e is small and has negligible effect on the ratio.

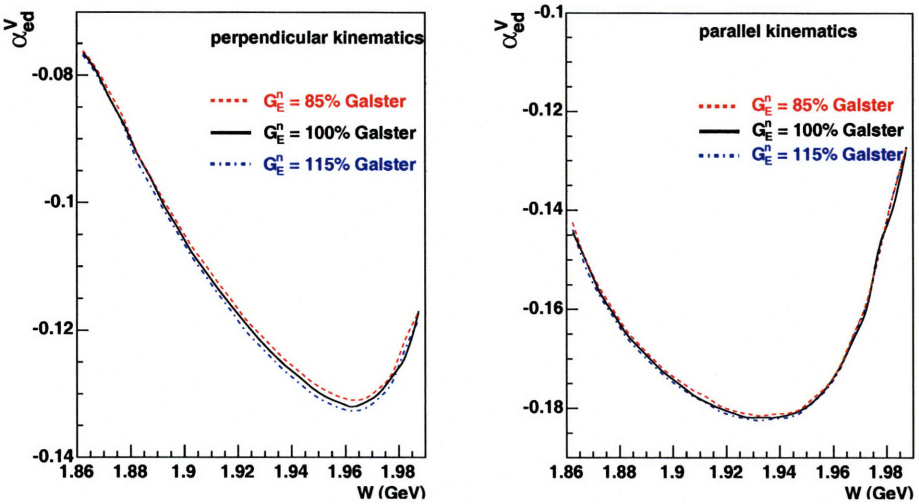

Figure 4-25: Monte Carlo simulations of the inclusive asymmetries in both perpendicular and parallel kinematics. The calculations were performed by varying the effective size of the G^n_E form factor by ±15% with respect to the Galster parametrization. The effects are shown to be small owing to the size of the form factor itself.

G^n_E on the inlusive asymmetries. With G^n_M fixed, G^n_E is varied by $\pm 15\%$ with respect to the Galster parametrization. The effect is more significant in perpendicular kinematics where the two form factors enter as a product in the numerator and as a sum of squares in the denominator (as shown in eq. (1.53)). The double contribution actually decreases the overall contribution, since a decrease in the numerator also occurs in the denominator, albeit with different magnitude. On the other hand, since G^n_E is small compared to the other form factors, the effect in parallel kinematics is almost negligible. Here, G^n_E contributes only in the denominator and its effect is diluted by the presence of the other form factors. Figure 4-26 shows the combined effects of the G^n_E uncertainty on the ratio. Taking into account 20% error in the knowledge of G^n_E in this region, the consequent error on G^n_M was estimated to be of the order of 0.5%.

4.8.5 Radiative Effects

The radiative effects leading to energy loss and kinematic changes for the scattered electrons are often classified into two separate categories. *Internal radiation*, for radiative processes that take place during the interaction process, both before and

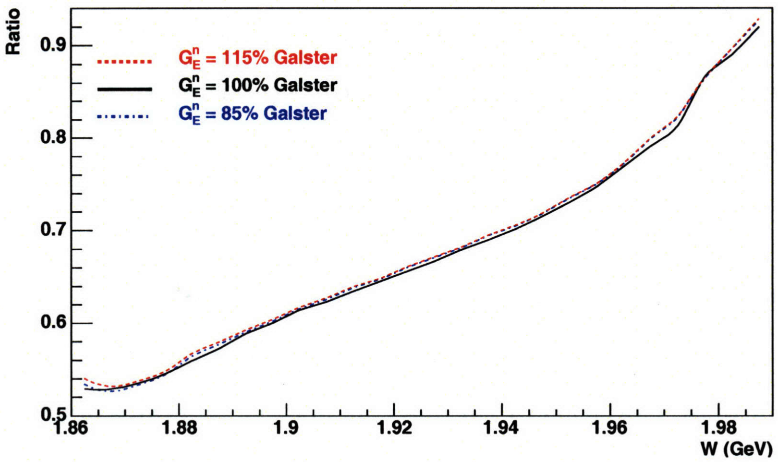

Figure 4-26: Monte Carlo simulation of the ratio of the inclusive asymmetries in perpendicular over parallel kinematics. The systematic uncertainty of the extracted value of G_M^n due to the uncertainty in G_E^n is small.

after, and close to the vertex. And *external radiation*, for all other effects.

External Radiative Corrections

External processes are heavily dependent on the material the electrons have to traverse. *Ionization* is a process which leads to energy loss during collisions of the electrons with atomic electrons in the material. *Multiple scattering* refers to the Coulombic interaction between the traveling electron and the atomic nuclei of the material, which may result in small angle deviations for the trajectory. Finally, *external bremsstrahlung* can lead to additional energy loss due to the emission of real photons by the electrons during interactions with the electromagnetic fields in the material.

Ionization occurs predominantly through interactions with atomic electrons in the medium and results in energy loss and energy spread of a monoenergetic beam.

Multiple scattering is a series of successive scatterings which change the direction of motion and can be considered statistically independent and thus quantum-mechanically incoherent. For charged particles, the effects are treated as a correction and are dominated by electrostatic forces [127]. While strong interaction effects are considered to be small, Coulomb screening and inelastic effects have been discussed in the literature. A modified form of the Rutherford equation is used to calculate the cross section for scattering of fast charged particles by atoms. For density of scattering centers n(t) at time t and a solid angle element χ, the single-scattering probability is given by

$$W(\chi, t) = N(t)\,\sigma_{Ru}(\chi), \tag{4.23}$$

when only small angles are considered and both relativistic and non-relativistic particles are taken into account. Several complications have to be accounted for. Coulomb screening by atomic electrons of the nuclear field is generally dealt with a first order Born approximation and relativistic effects are added for higher order Born approximations. Contributions by direct interaction with the atomic electrons, effects due to nuclear structure or crystalline structure of the medium as well as recoil effects, are higher order corrections and have been discussed at length [127]. Moliere showed that in the small angle approximation, the total angle of deflection is a function of the charge number and thickness of the medium as well as momentum and velocity of the scattering particle and it asymptotically approaches a Gaussian form. Thus defining $\theta_o = (1/\sqrt{2})\theta_{rms}^{space}$, the deflection angle obeys a Gaussian distribution, with a width expressed as [128]

$$\theta_o = \frac{13.6\,MeV}{\beta c p} z \sqrt{\frac{x}{X_o}} \left[1 + 0.038\,ln\left(\frac{x}{X_o}\right)\right]. \tag{4.24}$$

In the above, x/X_o denotes the thickness of the scattering material in radiation lengths whereas p and β represent the scattering particle's kinematics and z its charge number. For larger deflection angles, Rutherford scattering appears to be a closer approximation. In the case that the electron traverses several different types of material, eq. (4.24) has to be applied once only after calculating the combined x and X_o for the system, as opposed to finding the individual widths and adding them in quadrature.

Internal Radiative Corrections

To account for internal radiative corrections to the data, the Fortran code MASCARAD was translated to C/C++ and incorporated in the BLAST Monte Carlo and event generator software.

MASCARAD

Afanasev et al. [129] calculated the radiative corrections in elastic electron proton scattering including the dominant QED processes of radiation of an unobserved real photon, vacuum polarization and lepton-photon vertex correction. The calculation includes the lowest-order model-independent corrections to leptonic radiation while neglecting the much smaller corrections to the hadronic side. While the latter has additional theoretical uncertainties stemming from model-dependence, the leptonic contributions have uncertainties related only to structure functions from fitting the experimental data.

Two methods have been used in the past to calculate the contributions of radiation. The first method [130] separates the radiated photon energy into soft and hard, separated by a cutoff energy Δ, often set to the experimental resolution. The soft part lies below the energy cutoff and was first introduced by Schwinger as a multiplicative factor to the Born cross section

$$\frac{d\sigma}{d\Omega} = (1 + \delta) \left(\frac{d\sigma}{d\Omega}\right)_{Born} . \tag{4.25}$$

It is spin independent but depends on the incoming electron energy, the maximum energy loss of the electron in the scattering process and the relative kinematic factors. Schwinger also noted that as the energy loss goes to zero, δ goes to infinity because the calculation neglected the contributions due to multiple photon emission. It was later shown that taking these higher order corrections into account, the factor $(1+\delta)$ has to be replaced by an exponential e^{δ}. Conversely, the hard part results in an additive factor to the cross section and is responsible for the radiative tail evident in elastic scattering. Mo and Tsai [130] calculated the radiative tail effect in unpolarized electron scattering using the *peaking approximation.* This approximation takes advantage of the fact that both the incoming and scattered electrons tend to radiate in a cone that overwhelmingly favors their direction of travel. Thus, calculating the tail in this limit does not compromise the results, while it simplifies the calculations significantly.

In order to avoid the introduction of the cutoff parameter Δ, Bardin and Shumeiko [131] proposed an alternative in the 1970s. Their approach focused on extracting and cancelling the infrared divergences and allowed them to calculate the model-independent corrections exactly. Afanasev, Akushevich and Merenkov [129] used this framework with both hadronic and leptonic variables. The difference in the two variable sets lies in the possibility for emission of an additional photon in the final state of the system. Since the leptonic variables is the appropriate set to consider for an inclusive analysis with BLAST, the hadronic variable results will not be discussed herein.

The Born cross section can be expressed in terms of the leptonic and hadronic tensors as

$$\frac{d\sigma_o}{d\Omega} = \frac{2\pi\alpha^3}{S^2Q^4}\Sigma_i \theta_B^i F_i, \tag{4.26}$$

where the index i ranges from 1 to 2 for the unpolarized part and 3 to 4 for the polarized. The structure functions are then given by the familiar forms

$$\begin{aligned} F_1 &= 4\tau_p M^2 G_M^2 & F_2 &= 4M^2\frac{G_E^2 + \tau_p G_M^2}{1 + \tau_p} \\ F_3 &= -2M^2 G_E G_M & F_4 &= -M^2 G_M \frac{G_E - G_M}{1 + \tau_p}, \end{aligned} \tag{4.27}$$

while the θ functions denote the contractions of the leptonic and hadronic tensors excluding the F structure functions and can be found in [129].

However, the cross section for the radiation has to be expressed in its own variable phase-space. The reaction process in terms of the particles involved is given by

$$e(k_1) + N(p_1) \Longrightarrow e'(k_2) + \gamma(k) + N(p_2). \tag{4.28}$$

The corresponding cross section is written as

$$d\sigma_r = \frac{M_r^2}{4p_1k_1}d\Gamma_r, \tag{4.29}$$

where the phase-space element $d\Gamma_r$ can be expressed in terms of three variables necessary to parametrize the radiation phase-space. The first is *inelasticity*, defined as the energy radiated by the electron. This can be expressed as $v = \Lambda^2 - M^2$, where Λ is a 4-vector combination of the relevant momenta. The second is the 4-momentum ratio $\tau = \frac{kq}{kp_1}$ and the angle between the planes defined by $(\vec{q}, \vec{k})$ and $(\vec{k_1}, \vec{k_2})$, denoted as ϕ_k. In turn, the phase-space element can be expressed as

$$d\Gamma_r = \frac{dQ^2}{4(2\pi)^4 S} \int_0^{v_m} \frac{dv}{4\sqrt{\lambda_q}} \int_{\tau_{min}}^{\tau_{max}} d\tau \frac{v}{(1+\tau)^2} \int_0^{2\pi} d\phi_k. \tag{4.30}$$

Finally, the squared matrix element of the radiative process is given by

$$M_r^2 = \frac{e^6}{Q^4} L^r_{\mu\nu} W_{\mu\nu}, \tag{4.31}$$

where $L^r_{\mu\nu}$ is the leptonic and $W_{\mu\nu}$ the hadronic tensor, respectively.

Infrared divergence prohibits integration over the entire inelasticity range. The cross section has to be separated into a term that includes all divergent parts σ_{IR} and one without any of them, σ_F. The treatment of σ_{IR} echoes the Mo & Tsai technique of segmenting the space into soft and hard contributions using the cutoff parameter. Therefore, this part is proportional to the sum of soft and hard integrals, denoted by δ_S and δ_H, respectively, and expressed as

$$\begin{aligned} \delta_S &= \frac{-1}{\pi} \int_0^{\Delta} dv \int \frac{d^{n-1}k}{(2\pi\mu)^{n-4} k_o} F_{IR} \delta((\Lambda - k)^2 - M^2) \\ \delta_H &= \frac{-1}{\pi} \int_{\Delta}^{v_m} dv \int \frac{d^3k}{k_o} F_{IR} \delta((\Lambda - k)^2 - M^2), \end{aligned} \tag{4.32}$$

where the cutoff parameter Δ cancels out in the end. Note that so far, only the bremsstrahlung radiation terms have been taken into account. The advantage of this method is that when the vertex correction δ_V is added to the above, the infrared divergences cancel out and the remainder can be expressed in closed form $\delta_S + \delta_H + \delta_V \approx \delta_{inf} + \delta_{VR}$. The δ_{inf} can be exponentiated and the final expression for the observed cross section, including the vacuum polarization term, is given by

$$\sigma_{obs} = \sigma_0 \, e^{\delta_{inf}} \left(1 + \delta_{VR} + \delta_{vac}\right) + \sigma_F. \tag{4.33}$$

The final term, denoted by σ_F, incorporates the remainder of the internal bremsstrahlung radiation terms after subtracting the infrared divergences. It can be calculated exactly as

$$\begin{aligned} \sigma_F &= -\frac{\alpha^3}{2S^2} \int_0^{v_m} dv \int_{\tau_{min}}^{\tau_{max}} \frac{d\tau}{1+\tau} \int_0^{2\pi} d\phi_k \\ &\times \sum_i \left(\sum_{j=1}^{3} AR^{j-2} \theta_{ij} \frac{F_i}{Q_h^4} - 4F_{IR}^0 \theta_i^B \frac{F_i^0}{RQ_l^4} \right), \end{aligned} \tag{4.34}$$

where A is a function of the ϕ acceptance. The internal bremsstrahlung radiative tail can then be considered separately and without any divergences.

The FORTRAN code MASCARAD was based on the calculations above. In order to adapt the package to the BLAST software framework, a C++ based class was written to interface the generated events from DGen with radiative contributions. While the implementation of MASCARAD for electron-proton scattering in hydrogen is straightforward, there are several complications to take into account when used for deuterium.

One such complication for the integral in eq. (4.34) arises from the fact that radiation is sharply peaked in τ−space. This is exactly the reason why the peaking approximation considered by Mo and Tsai was valid. Electrons radiate predominantly in their direction of travel. The challenge here is in randomly generating events in τ-space within the Monte Carlo method. The grid has to be fine enough to ensure neither the incoming nor the scattered electron radiation peak is missed during generation, thus missing the terms that contribute the most to the integral. However, a fine enough grid leads to a prohibitively large number of event samples in τ−space, and consequently to long computing times. The problem can be avoided by evaluating τ around both peaks and then smearing the results with a gaussian distribution.

MASCARAD at BLAST

At the time of this writing, the MASCARAD package is not fully incorporated into the various BLAST analyses. In order to estimate the radiative effects for this work, the FORTRAN code was used instead. As an approximation, the inclusive channel in quasi-elastic kinematics can be considered as an incoherent sum of electron-proton and electron-neutron elastic scattering, weighted by their respective cross sections. The FORTRAN code can give the correction or the asymmetries in both perpendicular and parallel kinematics and for a specified polarization angle. While the original code can produce only electron-proton elastic scattering results, the form factors of the proton can be replaced by those of the neutron to effectively yield electron-neutron elastic scattering asymmetries. The results for both the proton and the neutron were shown to be very similar.

Equation 4.33 can be factorized as

$$\sigma_{obs}^{u,p} = (1 + \delta)\,\sigma_o^{u,p} + \sigma_R^{u,p}, \tag{4.35}$$

Here, σ_o is the cross section without any radiative effects, δ denotes the radiative effects which enter as a multiplicative factor and σ_R the effects which enter as an additional term. The superscripts u and p stand for unpolarized and polarized, respectively. Both the radiated and unradiated asymmetries (α_r and α_o) can be expressed as the ratio of the unpolarized and polarized cross sections. Their difference is given by [129]

$$\Delta\alpha = \alpha_r - \alpha_o = \frac{(1+\delta)\sigma_o^p + \sigma_R^p}{(1+\delta)\sigma_o^u + \sigma_R^u} - \frac{\sigma_o^p}{\sigma_o^u}. \tag{4.36}$$

Figure 4-27 shows MASCARAD calculations for $\Delta\alpha/\alpha_o$ for the inclusive asymmetry versus Q^2. The left panel shows three calculations in parallel kinematics for a target polarization angle of 47°. The solid curve shows the result for an inelasticity range derived from the data, whereas the dotted and dashed curves use a uniform inelasticity of 300 MeV and 500 MeV, respectively. The right panel shows the difference

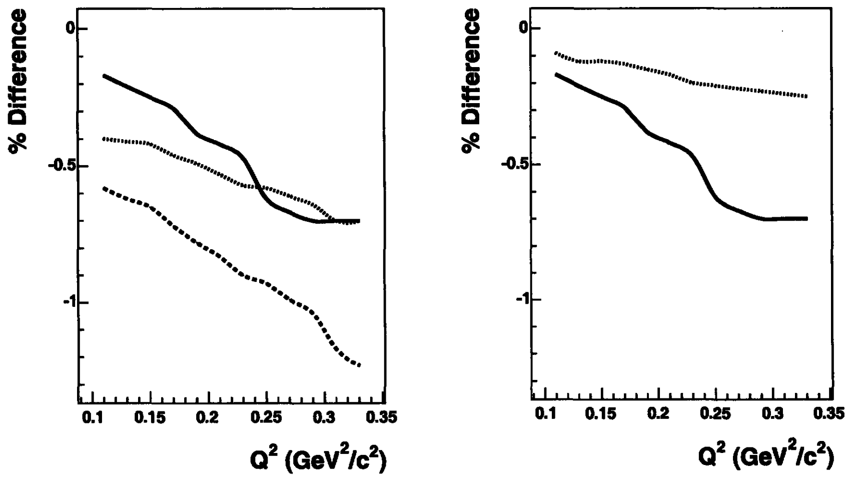

Figure 4-27: Radiative effects on the inclusive asymmetry calculated with the MASCARAD code. The left panel shows the percent difference in parallel kinematics for three different sets of inelasticity values. The dashed curve shows the difference for a uniform inelasticity of 0.5 GeV whereas the dotted curve for inelasticity 0.3 GeV. The solid curve shows the calculation for the inelasticity values that match the data. The right panel shows a comparison of the difference in parallel kinematics (solid curve) and perpendicular (dotted curve). The effect is larger in parallel kinematics.

for parallel (solid curve) and perpendicular (dotted curve). The non-uniform slope of the calculation is due to matching the binning of the data with the MASCARAD input. The radiative effects in the parallel case are slightly larger than those in perpendicular. They are, however, of the same sign, and their combined effect on the ratio is smaller than the effect on the individual asymmetries. Since the procedure above is merely an approximation, the ratio was not corrected for these effects and a systematic uncertainty was estimated to be of the order of 0.5%. The main source of error in these calculations stems from the difference between the actual inclusive asymmetry and the PWIA sum of the neutron and the proton in the deuteron. The latter ignores both FSI and the relevant reaction mechanisms. Since the data are dominated by events in quasi-elastic kinematics where these effects are smallest, the approximation is still valid.

Chapter 5

Conclusion

5.1 Results of $\mathrm{G_M^n}$ Extraction

The neutron magnetic form factor G_M^n has been extracted at $Q^2 = 0.135$, 0.189, 0.252 and 0.316 $(\mathrm{GeV/c})^2$. These results are presented in figure 5-1 along with a selection of the world's data. The BLAST results are in remarkable agreement with the data from the $^3\vec{He}\,(\vec{e}, e')$ analysis of [45, 46, 47], as well as the most recent cross section ratio measurement of [40]. Several calculations for the form factor, discussed in Chapter 1, are shown as well. The blue solid line is the Friedrich and Walcher parametrization (FW) [24]. Friedrich and Walcher expressed the form factors in terms of a smooth part and a bump, as discussed in Chapter 1 (see eq. (1.69) and (1.70)). Denoting the smooth part as $G_s(Q^2)$ and the bump as $G_b(Q^2)$, the form factor is given by

$$G(Q^2) = G_s(Q^2) + a_b Q^2 G_b(Q^2). \tag{5.1}$$

Plotted in figure 5-2 is the difference of $G(Q^2)$ and $G_s(Q^2)$, shown by the solid blue curve. The BLAST data appear to be in good agreement with the FW parametrization. The data from [46, 47] appear to favor a larger and broader deviation from the dipole form factor than the FW parametrization, and therefore a larger $G_b(Q^2)$. Note that the FW parametrization shown here was performed before the data of Xu et al. [47] were published. However, Friedrich and Walcher repeated their fit to the

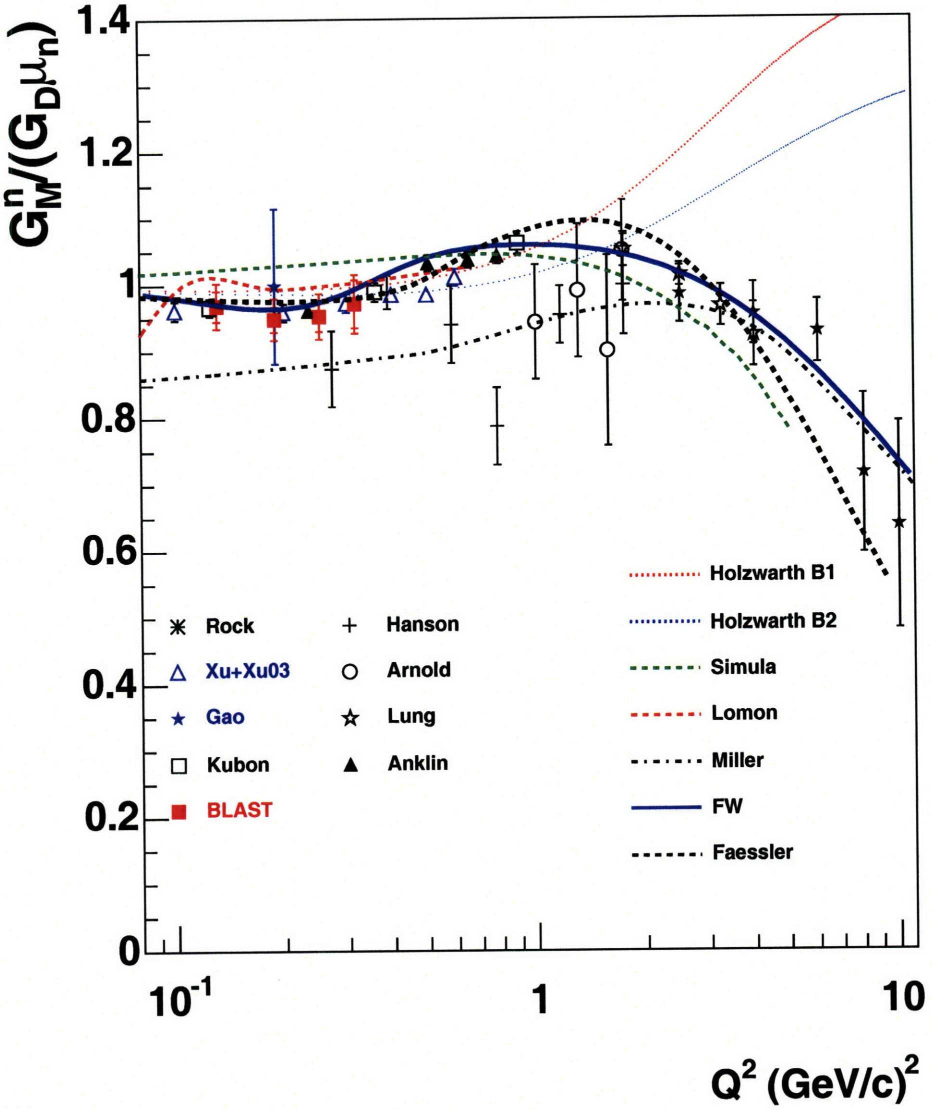

Figure 5-1: The values of G_M^n extracted from this analysis along with a subset of the world's data. The blue and red dotted lines are soliton model calculations by Holzwarth [61], the green dashed line is a CQM model calculation by Simula [78] and the red dashed line a calculation by Lomon [73], an extension to the GK MD model. Also shown are cloudy bag model calculations by Miller [53] (dashed-dotted black line) and a very recent calculation by Faessler et al. [70] using Chiral Perturbation theory (dashed black line). Finally, the blue solid line is a parametrization of the world's data by Friedrich and Walcher [24]. The data shown here are taken from this work and from [33, 34, 35, 36, 40, 42, 45, 46, 47]. The total error presented here for the BLAST data includes both statistical and systematic errors added in quadrature.

data including the data of [47] without any change in the resulting parameters.

It is not immediately obvious what the underlying cause of the "bump" in the form factors is. In the electric form factors, FW argue that it results from an interplay between the pion cloud and the bare nucleon. In the magnetic form factors however, the situation is more complicated beceuse of the vector coupling of the spins and the magnetic moments involved in the picture. While it is clear which component carries the charge for the electric form factor, the total magnetic moment depends on the coupling of the quark spins. In addition, it is unclear what magnetic moment to assign to the quarks, or the pion (because the latter is highly off-shell). The authors then proceed to break the magnetic form factor (eq. (18) in their paper) into inner and outer quark distributions plus a pion part. Their conclusion is that the magnetic moment is dominated by the outer distribution and the inner distribution is -11% and the pion around 20%. However, this result fails normalization of the FF at $Q^2 = 0$ (GeV/c)^2 by 10%. FW conclude without any explicit statements about what the bump is. It appears to be a convolution of the pion cloud with the bare nucleon and they admit that further corrections and higher-order terms need to be added.

5.2 The BLAST $\mathbf{G_M^n}$ Extraction

The characteristics of the detector make the BLAST scientific program as a whole unique. Both neutron form factors, the proton form factor ratio and several other observables could be extracted with the same experimental set-up, thus providing self-consistent results. The large acceptance made these measurements possible over a broad kinematic range. The polarized beam and target allowed the study of difficult to measure physical observables and reduced dependence on detection efficiency knowledge, needed to study cross sections. The internal, isotopically pure target reduced background and theoretical uncertainties frequently associated with background subtraction. The left-right symmetry of the detector enabled super ratio measurements in which accurate knowledge of the target and beam polarizations was not necessary.

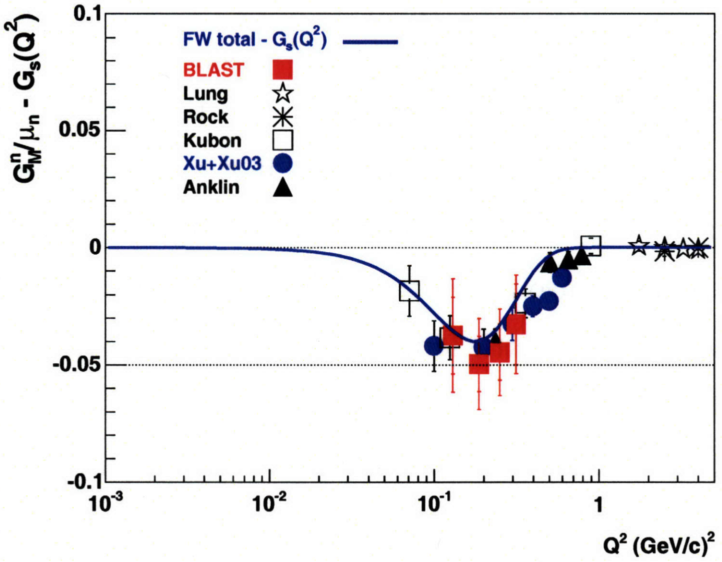

Figure 5-2: The values of G_M^n extracted from this analysis along with a subset of the world's data. The data shown here are taken from this work and from [33, 35, 40, 46, 47]. The BLAST data are in agreement with the rest of the world's data as well as the Friedrich and Walcher parametrization (solid blue curve). The total error presented here for the BLAST data includes both statistical and systematic errors added in quadrature.

5.2.1 The Various Extraction Methods

The G_M^n extraction with the ${}^2\vec{H}\,(\vec{e}, e')$ reaction at BLAST, inherited many of its advantages from the BLAST detector itself. The advantages can be summarized as follows.

1. The deuteron is the simplest nuclear system. As such, it provides the ideal testing ground for any theory describing nucleon-nucleon interactions and nuclear structure. The model by H. Arenhövel used in this analysis incorporates the necessary FSI, reaction mechanisms and relativistic corrections so that any theoretical uncertainty is expected to be small.

2. Asymmetry measurements with respect to spin variables do not require accurate knowledge of all detection and reconstruction efficiencies involved.

3. For the super ratio method, the systematic uncertainty in the beam-target polarization product hP_z cancels out. In addition, background dilution and sys-

tematic shifts in the spectra are also less significant. As shown earlier in this thesis, the ratio method enhances sensitivity to G_M^n with respect to an individual asymmetry extraction.

4. The data had low experimental background due to the isotopically pure target.

5. The measurement required no dedicated detectors or kinematic configurations and ran simultaneously with the other reaction channels.

The difficulties associated with the present measurement stem from the need for precise tracking and resolution as well as for precise knowledge of the target polarization angle. In addition, the relatively low luminosity increased the amount of time needed for the accumulation of the desirable number of events.

In comparison with the extraction from the $^3\vec{He}\,(\vec{e},e')$ reaction by [45, 46, 47], the method used at BLAST has the disadvantage of lower statistical accuracy. It does however have an advantage in the theoretical uncertainty. As discussed in Chapter 1 of this work, the two lowest Q^2 points of Xu et al. [46] were based on Faddeev calculations for the structure of polarized ^3He which neglected relativistic corrections and MEC contributions. Moreover, the four remaining data points were compared to a relativistic PWIA calculation which did not include MEC and FSI.

As compared to the cross section ratio measurements of [38, 39, 40, 41, 42], the BLAST extraction does not require precise knowledge of the detection efficiencies involved. In particular, determining the neutron detection efficiency for these experiments can be time-consuming and complicated.

5.3 Outlook

While our knowledge of the neutron form factors has improved in recent years, more precise data, particularly for G_E^n and certain Q^2 regions for G_M^n, are still needed. In addition, consistency between the various extraction methods and better understanding of the theoretical uncertainties associated with each one are also necessary.

5.3.1 BLAST at ELSA

In recent months, an opportunity to continue and expand the operation of the BLAST detector has been proposed. The proposal calls for the transfer of the spectrometer and ABS target components for operation at the ELSA electron ring at the University of Bonn in Germany. Assuming certain technical issues can be resolved, the higher beam energies (up to 3.5 GeV) at ELSA can potentially extend both the accuracy and the range of the BLAST measurements [132].

The proposed scientific program includes operation of polarized hydrogen, deuterium and ^3He[1]. The proposed deuterium experiments include measurements of the neutron magnetic form factors, the polarization observables A_{ed}^V and A_d^T from coincidence electrodisintegration data, the electron-deuteron elastic scattering polarization observable T_{20} and the elastic deuteron form factors G_M and G_Q. In order to enhance the BLAST detector, certain changes and additions have been suggested [133].

1. Construction and installation of recoil tracking detectors.
2. Implementation of a forward tagging system to investigate pion and kaon photoproduction.
3. Modification of the holding field coils to enable vertical target spin orientation.
4. Enhancement of the tracking resolution through enhancements in the toroidal magnetic field.

Specifically for G_M^n, the program will yield measurements from both deuterium and ^3He through inclusive analyses of the respective breakup channels. Using the same spectrometer for the measurements should yield self-consistent results which differ mostly by their respective theoretical uncertainty. The Q^2 range of 0.4 - 1.5 (GeV/c)^2 is expected to be accessible for both targets. For polarized deuterium, G_M^n can then be extracted using the inclusive super ratio method described herein. For the $^3\vec{He}$

---

[1] Polarized ^3He studies were originally planned at BLAST but did not take place due to time constraints.

measurement, the extraction could be similar to the most recent data from [46, 47]. The BLAST data and the data of [45, 46, 47] are the only measurements to date that used the double-polarization method and only extend to $Q^2 = 0.6$ (GeV/c)^2. In addition, no accurate data exist in the range 1.0 - 1.5 (GeV/c)^2. In this region, BLAST at ELSA is expected to make a significant contribution.

Chapter 6

Appendix

6.1 Hyperfine Structure

In order to express the Hamiltonian of eq. (2.25) in matrix form, one first has to derive the matrix representation for the various terms in the basis of the total angular momentum F of the system. The notation $|S\, m_S>$ and $|I\, m_I>$ for the individual spin bases and $|S\, I\, m_S\, m_I>$ to denote the basis of the combined system will be used here.

The first term,

$$< S\, I\, m_S\, m_I |\, \vec{I}\vec{S}\, | S'\, I'\, m_S'\, m_I' >, \tag{6.1}$$

will be discussed first. This has to be transformed into $< F\, M_F |\, \vec{I}\vec{S}\, | F'\, M_F' >$ by using

$$\vec{F} \;=\; (\vec{I} + \vec{S}) \Longrightarrow \vec{I}\vec{S} \;=\; \frac{1}{2}(\, F^2 \,-\, I^2 \,-\, S^2\,). \tag{6.2}$$

In the above, both $\vec{I}$ and $\vec{S}$ are proportional to the unitary Pauli spin matrices

$$\vec{\mathbf{S}} \;=\; \frac{\hbar}{2}\left(\begin{pmatrix} 0 & 1 \\ 1 & 0 \end{pmatrix}, \begin{pmatrix} 0 & -i \\ i & 0 \end{pmatrix}, \begin{pmatrix} 1 & 0 \\ 0 & -1 \end{pmatrix} \right), \tag{6.3}$$

giving $I^2 \;=\; S^2 \;=\; \frac{3}{4}\hbar^2\, \delta_{F\,F'}\, \delta_{M\,M'}$.

On the other hand, the total angular momentum acts on its own basis giving a factor of $\hbar^2 F(F+1)\,\delta_{F\,F'}\,\delta_{M\,M'}$ so that the operator yields

$$< F\,M_F|\,\vec{I}\,\vec{S}\,|F'\,M_F' > \;=\; \hbar^2\,(\frac{F(F+1)}{2} - \frac{3}{4})\delta_{F\,F'}\,\delta_{M\,M'}\,. \tag{6.4}$$

Using the notation $|\,m_S\,m_I >$, the F states in the absence of an external magnetic field are then expressed as

$$\begin{cases} \psi_{00} \;=\; \frac{1}{\sqrt{2}}\,(\,|\,\frac{1}{2}\,\frac{-1}{2} > -\,|\,\frac{-1}{2}\,\frac{1}{2} >) \\ \psi_{11} \;=\; |\,\frac{1}{2}\,\frac{1}{2} > \\ \psi_{10} \;=\; \frac{1}{\sqrt{2}}\,(\,|\,\frac{1}{2}\,\frac{-1}{2} > +\,|\,\frac{-1}{2}\,\frac{1}{2} >) \\ \psi_{1-1} \;=\; |\,\frac{-1}{2}\,\frac{-1}{2} > . \end{cases} \tag{6.5}$$

Solving for the $|\,m_S\,m_I >$ states, one arrives at

$$\begin{cases} |\,\frac{1}{2}\,\frac{1}{2} > \;=\; \psi_{11} \\ |\,-\frac{1}{2}\;-\frac{1}{2} > \;=\; \psi_{1-1} \\ |\,\frac{1}{2}\;-\frac{1}{2} > \;=\; \frac{1}{\sqrt{2}}\,(\psi_{00} + \psi_{10}) \\ |\,-\frac{1}{2}\,\frac{1}{2} > \;=\; \frac{1}{\sqrt{2}}\,(-\psi_{00} + \psi_{10})\,. \end{cases} \tag{6.6}$$

Similarly, the terms in the Hamiltonian due to the interaction of the individual spins with the external magnetic field can be simplified by considering a static field in the $\hat{z}$ direction. Due to the fact that the gyromagnetic ratio of the electron is far larger than that of the nucleus, the interaction with the external field is mainly due to coupling between the field and the electron. Thus the term that describes the interaction with the nucleus can safely be neglected and

$$< F\, M_F|\, g_S\, \mu_B\, \vec{S}\, \vec{B}\, |F'\, M_F' > \, = \, < F\, M_F|\, g_S\, \mu_B\, S_z\, B_z\, |F'\, M_F' > \,, \tag{6.7}$$

which reduces to

$$F\, M_F|\, g_S\, \mu_B\, S_z\, B_z\, |F'\, M_F' > \, = \; \hbar\, m_S\, g_S\, \mu_B\, Bz\, \delta_{m_S m_S'} . \tag{6.8}$$

Using the basis $\left(|\frac{1}{2}\;\frac{1}{2} > , |\frac{1}{2}\; -\frac{1}{2} > , |-\frac{1}{2}\;\frac{1}{2} > , |-\frac{1}{2}\; -\frac{1}{2} > \right)$, the final Hamiltonian for the static field coupling can be written as

$$\mathbf{H^{st}} \; = \; \begin{pmatrix} 1+2x & 0 & 0 & 0 \\ 0 & -1+2x & 0 & 2 \\ 0 & 0 & 1-2x & 0 \\ 0 & 2 & 0 & -1-2x \end{pmatrix} . \tag{6.9}$$

Note that while the electron-nucleus coupling results in both diagonal and non-diagonal terms, the coupling to the field only gives rise to diagonal ones. In order to derive the basis states for the new Hamiltonian, H^{st} has to be diagonalized. An orthogonal similarity transformation has to be performed [134] to reduce all non-diagonal elements to zero. Since this is a real, symmetric matrix, the diagonalization may be performed through a $H'^{st} \; = \; S^{\dagger}\, H^{st}\, S$ transformation, where S is a matrix that has the normalized eigenvectors of H^{st} as its columns. The secular equation

$$\begin{vmatrix} 1+2x-\lambda & 0 & 0 & 0 \\ 0 & -1+2x-\lambda & 0 & 2 \\ 0 & 0 & 1-2x-\lambda & 0 \\ 0 & 2 & 0 & -1-2x-\lambda \end{vmatrix} \; = \; 0, \tag{6.10}$$

has to be solved to find the characteristic values for H^{st}.

Solving the equation yields the four eigenvalues of the matrix $\lambda \; = \; 1-2x \;, 1+$

$2x$, $-1 + \pm 2\sqrt{1+x^2}$.

The eigenvectors can be calculated from these in order to form the unitary transformation S

$$\mathbf{S} = \begin{pmatrix} 1 & 0 & 0 & 0 \\ 0 & \frac{1}{a}[\frac{x}{\sqrt{1+x^2}} + 1] & 0 & \frac{1}{b}[\frac{x}{\sqrt{1+x^2}} - 1] \\ 0 & 0 & 1 & 0 \\ 0 & \frac{1}{a}\frac{1}{\sqrt{1+x^2}} & 0 & \frac{1}{b}\frac{1}{\sqrt{1+x^2}} \end{pmatrix}, \tag{6.11}$$

where $a = \sqrt{\frac{1}{2}(1 + \frac{x}{\sqrt{1+x^2}})}$ and $b = \sqrt{\frac{1}{2}(1 - \frac{x}{\sqrt{1+x^2}})}$ for normalization. The transpose of S can now be calculated and the diagonalization performed. Since $a^2 + b^2 = 1$, the constants a and b can be set to $a = \sin\theta$ and $b = \cos\theta$, respectively.

The eigenvectors of the new Hamiltonian can be calculated from the old ones using

$$e_j^{'} = \sum_i S_{ij}\, e_i \, . \tag{6.12}$$

The energy levels and new states then are

$$\left\{ \begin{array}{lcl} E_1 & = & \frac{\hbar\nu}{4}(1 + 2x) \\ E_2 & = & \frac{\hbar\nu}{4}(-1 + 2\sqrt{1 + x^2}) \\ E_3 & = & \frac{\hbar\nu}{4}(1 - 2x) \\ E_4 & = & \frac{\hbar\nu}{4}(-1 - 2\sqrt{1 + x^2}) \end{array} \right. \qquad \left\{ \begin{array}{l} |1> = |\frac{1}{2}\,\frac{1}{2}> \\ |2> = \sin\theta\,(|\frac{1}{2}\,\frac{-1}{2}> + \cos\theta\,|\frac{-1}{2}\,\frac{1}{2}>) \\ |3> = |\frac{-1}{2}\,\frac{-1}{2}> \\ |4> = \sin\theta\,(|\frac{1}{2}\,\frac{-1}{2}> - \cos\theta\,|\frac{-1}{2}\,\frac{1}{2}>) \end{array} \right. \tag{6.13}$$

The same process yields the deuterium states. The Hamiltonian for the static field coupling can be expressed as

$$\mathbf{H}^{\mathbf{st}} = \begin{pmatrix} 1+\frac{3}{2}x & 0 & 0 & 0 & 0 & 0 \\ 0 & \frac{3}{2}x & 0 & 0 & 0 & \sqrt{2} \\ 0 & 0 & -1+\frac{3}{2}x & 0 & \sqrt{2} & 0 \\ 0 & 0 & 0 & 1-\frac{3}{2}x & 0 & 0 \\ 0 & 0 & \sqrt{2} & 0 & -\frac{3}{2}x & 0 \\ 0 & \sqrt{2} & 0 & 0 & 0 & -1-\frac{3}{2}x \end{pmatrix}. \tag{6.14}$$

The resulting eigenstates and eigenvalues are given by 6.15

$$\left\{\begin{array}{lll} E_1 & = & \frac{\hbar\nu}{3}(1 + \frac{3}{2}x) \\ E_2 & = & \frac{\hbar\nu}{6}(-1 + \sqrt{(1 + 3x)^2 + 8}) \\ E_3 & = & \frac{\hbar\nu}{6}(-1 + \sqrt{(1 - 3x)^2 + 8}) \\ E_4 & = & \frac{\hbar\nu}{3}(1 - \frac{3}{2}x) \\ E_5 & = & \frac{\hbar\nu}{6}(-1 - \sqrt{(1 - 3x)^2 + 8}) \\ E_6 & = & \frac{\hbar\nu}{6}(-1 - \sqrt{(1 + 3x)^2 + 8}) \end{array}\right. \qquad \left\{\begin{array}{l} |1> = \; |\frac{1}{2} \; +1> \\ |2> = \; \cos\theta_+ \, |\frac{1}{2} \; 0> + \sin\theta_+ \, |\frac{-1}{2} \; +1> \\ |3> = \cos\theta_- \, |\frac{1}{2} \; -1> + \sin\theta_- \, \frac{-1}{2} \; 0> \\ |4> = \; |\frac{-1}{2} \; -1>) \\ |5> = \; -\sin\theta_- \, |\frac{1}{2} \; -1> + \cos\theta_- \, |\frac{-1}{2} \; 0> \\ |6> = \; -\sin\theta_+ \, |\frac{1}{2} \; 0> + \cos\theta_+ \, |\frac{-1}{2} \; +1> \end{array}\right. \tag{6.15}$$

where $\cos\theta_\pm$ and $\sin\theta_\pm$ are given by

$$\cos\theta_\pm \; = \; \sqrt{\frac{1}{2}\left(1 \; + \; \frac{(3x \pm 1)}{\sqrt{(1 \pm 3x)^2 + 8}}\right)} \qquad \sin\theta_\pm \; = \; \sqrt{\frac{1}{2}\left(1 \; - \; \frac{(3x \pm 1)}{\sqrt{(1 \pm 3x)^2 + 8}}\right)}. \tag{6.16}$$

6.2 Miscellanea

6.2.1 Electron-Deuteron Scattering

Listed here are the polarization observables of polarized electron-deuteron elastic scattering.

$$\begin{aligned} T_{20}(Q^2,\theta) &= \frac{-1}{\sqrt{2}R_o}\left(\frac{8}{3}\tau G_C(Q^2)G_Q(Q^2) + \frac{8}{9}\tau^2 G_Q^2(Q^2)\right. \\ &\qquad \left. + \frac{1}{3}\tau\Big[1 + 2(1+\tau)tan^2(\frac{\theta}{2})\Big]G_M^2(Q^2)\right). \end{aligned} \tag{6.17}$$

$$T_{21}(Q^2,\theta) = -\frac{2}{\sqrt{3}R_o}\tau\sqrt{\tau + \tau(1+\tau)\tan^2(\frac{\theta}{2})}G_M(Q^2)G_Q(Q^2). \tag{6.18}$$

$$T_{22}(Q^2,\theta) = -\frac{1}{2\sqrt{3}R_o}\tau G_M^2(Q^2). \tag{6.19}$$

$$T_{10}^e(Q^2,\theta) = -\frac{1}{R_o}\sqrt{\frac{2}{3}}\tau(1+\tau)\tan\left(\frac{\theta}{2}\right)\sqrt{\frac{1}{1+\tau} + \tan^2\left(\frac{\theta}{2}\right)}G_M^2(Q^2). \tag{6.20}$$

$$T_{11}^e(Q^2,\theta) = \frac{2}{\sqrt{3}R_o}\sqrt{\tau+\tau^2}\tan(\frac{\theta}{2})G_M(Q^2)\Big[G_C(Q^2) + \frac{\tau}{3}G_Q(Q^2)\Big], \tag{6.21}$$

where R_o is defined as

$$R_o = A(Q^2) + B(Q^2)\tan^2\left(\frac{\theta}{2}\right). \tag{6.22}$$

6.2.2 Matrix Representation of Rotations

In order to facilitate coordinate transformations, a formal treatment of the properties of angular momentum under rotations is needed. The algular momentum operator J^2 commutes with the rotation operator (is invariant under rotations) and therefore the rotation of its eigenfunctions ψ_{jm} results in a new set of eigenfunctions for the operator. While a rotation around the quantization axis leads to a simple phase difference for the eigenfunctions, a more general rotation has to be treated with the Euler formalism [102]. The rotation operator may be expressed as the product of the individual rotations

$$\lambda \; = \; \lambda_\alpha \, \lambda_\beta \, \lambda_\gamma . \tag{6.23}$$

This amounts to a rotation by angle γ around $\hat{z}$, β around $\hat{y}$ and α around $\hat{z}$. The rotation can be described in terms of a rotation matrix $D^j_{m'm}(\alpha\beta\gamma)$ [118]

$$\lambda \, \psi_{jm} \; = \; \sum_{m'} D^j_{m'm}(\alpha\beta\gamma) \, \psi_{jm'}, \tag{6.24}$$

given in factorized form by

$$D^j_{m'm}(\alpha\beta\gamma) \; = \; e^{-im'\alpha} \, d^j_{m'm}(\beta) \, e^{-im\gamma}. \tag{6.25}$$

The matrix elements $d^j_{m'm}(\beta)$ are expressed as

$$\begin{aligned} d^j_{m'm}(\beta) \; &= \; \sqrt{\Big((j+m)!(j-m)!(j+m')!(j-m')!\Big)} \\ &\times \sum_x \frac{(-)^x}{(j-m'-x)!(j+m-x)!(x+m'-m)!x!} \\ &\times \left(\cos\frac{\beta}{2}\right)^{2j+m-m'-2x} \left(-\sin\frac{\beta}{2}\right)^{m'-m+2x} \end{aligned} \tag{6.26}$$

or, equivalently, by

$$\begin{aligned} d^j_{m'm}(\beta) \; &= \; \sqrt{\frac{(j-m)!(j+m')!}{(j+m)!(j-m')!}} \, \frac{\left(cos\frac{\beta}{2}\right)^{2j+m-m'} \left(-\, sin\frac{\beta}{2}\right)^{m'-m}}{(m'-m)!} \\ &\times {}_2F_1\left(m'-j, -m-j; m'-m+1; -\tan^2\frac{\beta}{2}\right) \end{aligned} \tag{6.27}$$

where $m' > m$, expressed in terms of the hypergeometric function

$${}_2F_1(a,b;c;z) \; = \; 1 + \frac{ab}{c} z + \frac{1}{2!} \frac{a(a+1)b(b+1)}{c(c+1)} z^2 . \tag{6.28}$$

Taking advantage of the symmetry properties of the hypergeometric function, the following useful relations can be derived [118]

$$d^j_{m'm}(\beta) \;=\; (-)^{m'-m}\, d^j_{mm'}(\beta) \qquad \textit{and} \qquad d^j_{m'm}(\beta) \;=\; (-)^{m'-m}\, d^j_{-m'-m}(\beta). \tag{6.29}$$

Using the above relations, the following results for the rotation matrix elements are derived

$$\begin{cases} d_2^{00} \;=\; \cos^2\beta \,-\, \frac{1}{2}\sin^2\beta \\ d_2^{-10} \;=\; -\frac{\sqrt{6}}{4}\sin 2\beta \\ d_2^{-20} \;=\; \frac{\sqrt{6}}{4}\sin^2\beta \\ d_1^{00} \;=\; \cos\beta \\ d_1^{-10} \;=\; \sqrt{2}\sin\frac{\beta}{2}\,\cos\frac{\beta}{2}. \end{cases} \tag{6.30}$$

In the Arenhövel formalism used in this thesis, the angle β corresponds to the polar angle of the target spin vector θ_d.

Bibliography

[1] T.W.Donnelly, Lecture Notes (2002).

[2] L.H.Ryder, Quantum Field Theory, Cambridge University Press (1996).

[3] M.E.Peskin and D.V.Shroeder, An Introduction to Quantum Field Theory, Addisson Wesley Publishing Company (1995).

[4] D.Griffits, Introduction to elementary particles, Wiley and Sons Inc., ISBN 0-471-60386-4 (1987).

[5] T.W.Donnelly and A.S.Raskin, Ann. Phys. 169, 247 (1986).

[6] M.N.Rosenbluth, Phys. Rev. 79, 615 (1950).

[7] F.J.Ernst, R.G.Sachs, K.C.Wali, Phys. Rev. 119, 1105 (1960).

[8] R.G.Sachs, Phys. Rev. 126, 2256 (1962).

[9] S.Galster et al., Nuclear Physics B, 32:221 (1971).

[10] H.Arenhövel, W.Leidemann and E.L.Tomusiak, Z. Phys. A 331, 123 (1988).

[11] M.Garcon and J.W.Van Orden, Adv. Nucl. Phys. 26, 293(2001).

[12] R.Gilman and F.Gross, J. Phys. G 28, R37 (2002).

[13] R.Arnold, C.Carlson and F.Gross, Phys. Rev. C 23, 363 (1981).

[14] C.Zhang, private communication (2005).

[15] H.Arenhövel, W.Leidemann and E.L.Tomusiak, Phys. Rev. C 46, 455 (1992).

[16] W.Leidemann, E.L.Tomusiak and H.Arenhövel, Phys. Rev. C 43, 1022 (1991).

[17] J.Carlson and R.Schiavilla, Rav. Mod. Phys. 70, 743 (1998).

[18] R.Machleidt, K.Holinde and Ch.Elster, Phys. Rep. 149, 1 (1987).

[19] A.J.Maschinot, Ph.D. thesis, MIT (2005), unpublished.

[20] H.Arenhövel, W.Leidemann and E.L.Tomusiak, MKPH-T-04-12 (2004) nucl-th/0407053.

[21] F.Ritz et al., Phys.Rev. C 55, 2214 (1997).

[22] A.Sindile, private communication (2005).

[23] C.Crawford, Precision measurement of proton electric to magnetic form factor ratio from $\vec{p}(\vec{e}, e'p)$ (2005), unpublished.

[24] J.Friedrich and Th.Walcher, Eur. Phys. J. A 17, 607 (2003).

[25] T.Eden et al., Phys.Rev.C 50, R1749 (1994)

[26] V.Ziskin, Ph.D. thesis, MIT (2005), unpublished.

[27] I.Passchier et al., Phys. Rev. Lett. 82, 4988 (1999).

[28] H.Zhu et al., Phys. Rev. Lett. 87, 081801 (2001).

[29] D.Rohe et al., Phys. Rev. Lett. 83, 4257 (1999).

[30] J.Bermuth et al., Phys. Lett. B 564, 199 (2003).

[31] R.Hofstadter, Rev. Mod. Phys. 28, 214 (1956).

[32] W.Albrecht et al., Phys. Lett. B 26, 642 (1968).

[33] S.Rock et al., Phys. Rev. Lett. 49, 1139 (1982).

[34] R.G.Arnold et al., Phys. Rev. Lett. 61, 806 (1988) .

[35] A.Lung et al., Phys. Rev. Lett. 70, 718 (1993).

[36] K.M.Hanson et al., Phys. Rev. D 8, 753 (1973).

[37] P.Stein et al., Phys. Rev. Lett. 16, 592 (1966).

[38] P.Markowitz et al., Phys. Rev. C 48, R5 (1993).

[39] E.E.W.Bruins et al., Phys. Rev. Lett. 75, 21 (1995).

[40] G.Kubon et al., Phys. Lett. B524, 26 (2002).

[41] H.Anklin et al., Phys. Lett. B336, 313 (1994).

[42] H.Anklin et al., Phys. Lett. B428, 248 (1998).

[43] J.Jourdan et al., Phys.Rev.Lett. 79, 5186 (1997).

[44] H.Gao, Measurement of the Neutron magnetic form factor from inclusive quasielastic scttering of polarized electrons from polarized ^3He, Ph.D. thesis, California Institute of Technology (1994), unpublished.

[45] H.Gao et al., Phys. Rev. C 50, R546 (1994).

[46] W.Xu et al., Phys. Rev. Lett. 85, 2900 (2000).

[47] W.Xu et al., Phys. Rev. C 67, R012201 (2003).

[48] W.Xu, A precision measurement of the transverse asymmetry $A_{T'}$ from quasielastic $^3\vec{He}(\vec{e}, e')$ process, and the Neutron magnetic form factor G_M^n at low Q^2, Ph.D. thesis, MIT (2002), unpublished.

[49] J.L.Friar et al., Phys. Rev. C 42, 2310 (1990).

[50] J.M.Laget, Phys.Lett.B 273, 367 (1991).

[51] A.Chodos, R.L.Jaffe, C.B.Thorn and V.F.Weisskopf, Phys.Rev.D 9, 3471 (1974).

[52] A.Chodos and C.B.Thorn, Phys.Rev.D 9, 2733 (1975).

[53] G.A.Miller, Phys.Rev.C 66 (2002) 032201.

[54] J.Schechter and H.Weigel, hep-ph/9907554 .

[55] T.H.R.Skyrme, Proc. Roy. Soc. London, Ser. A 260, 127 (1961).

[56] T.H.R.Skyrme, Proc. Roy. Soc. London, Ser. A 247, 260 (1958).

[57] T.H.R.Skyrme, Proc. Roy. Soc. London, Ser. A 252, 236 (1959).

[58] E.Witten, Nucl.Phys B160, 57 (1979).

[59] G.S.Adkins et al., Nucl. Phys. B228, 552 (1983).

[60] E.Braaten et al., Phys. Rev. Lett. 56, 2008 (1986).

[61] G.Holzwarth, Z. Phys. A356, 339 (1996).

[62] G.P.Lepage and S.J.Brodsky, Phys. Rev. Lett. 43, 545 (1979).

[63] P.Kroll et al., Bad Honnef Workshop 1992:179-191 (QCD161:S902:1992).

[64] E.Santopinto, Phys.Rev.C72:022201 (2005).

[65] B.Ma, D.Qing and I.Schmidt, Phys. Rev. C 65 , 035205 (2002).

[66] P.A.M.Dirac, Rev. Mod. Phys. 21, 392 (1949).

[67] L.Kisslinger, Int. J. Mod. Phys.E 13, 375 (2004).

[68] A.V.Manohar, Lectures given at 35th Internationale Universitatswochen fuer Kern- und Teilchenphysik (1996) , hep-ph/9606222.

[69] B.Holstein, Lectures given at 7th Summer School in Nuclear Physics Symmetries, Seattle (1995), hep-ph/9510344.

[70] A.Faessler et al., hep-ph/0511319.

[71] S.J.Brodsky and G.R.Farrar, Phys.Rev.Lett. 31, 1153 (1973).

[72] M.F.Gari and W.Krümpelmann, Phys. Lett. B 274, 159 (1992); 282, 483(E) (1992).

[73] E.Lomon, Phys. Rev. C 64, (2001) 035204; 66 (2002) 045501.

[74] P.Demetriou, hep-ph/9908241 .

[75] S.Capstick and N.Isgur, Phys. Rev. D 34, 2809 (1986).

[76] L.Ya.Glozman et al., Phys. Rev. D 58 (1998) 094030.

[77] R.F.Wagenbrunn et al., Phys. Lett. B 511, 33 (2001).

[78] F.Cardarelli and S.Simula, Phys. Lett. B 467, 1 (1999) .

[79] F.Cardarelli and S.Simula, Phys. Rev. C 62 (2000) 065201.

[80] D.B.Leinweber et al., Phys. Rev. D 43, 1659 (1991).

[81] H.H.Matevosyan et al., Phys. Rev. C 71, 055204 (2005).

[82] M.Göckeler et al., Phys. Rev. D 71, 034508 (2005).

[83] M.Ferro-Luzzi et al., Phys. Rev. Lett. 77, 2630 (1996).

[84] http://www.aps.anl.gov/epics/docs/index.php, unpublished.

[85] P.Binns, private communication.

[86] B.O'Rourke, private communication.

[87] E.Ihloff, private communication.

[88] H.Kolster et al., Polarized sources and targets, Proceesings of the 9th International Workshop, World Scientific (2001).

[89] O.A.Popov editor, High density plasma sources, Noyes publications (1995).

[90] N.Koch, Phd Thesis, University of Munich (2000), unpublished.

[91] A.Roth, Vacuum Technology, North - Holland, Amsterdam (1982).

[92] C.Baumgarten, Studies of Spin relaxation and Recombination at the HERMES Hydrogen/Deuterium gas target , Ph.D. thesis, University of Munich (2000), unpublished.

[93] J.A.Fedchak et al., NIM S 391 (1997), 405-416.

[94] F.C.Tompkins, Chemisorption of gases on metals, Academic Press Inc. (1978), ISBN 0-12-694650-7.

[95] H.Hoinkes, Rev. Mod. Phys. 52, 933 (1980).

[96] J.E. Lennard-Jones. Trans. Faraday Soc. 28 (1932), p. 333.

[97] E.Tsentalovich, private communication (2005).

[98] M.A.Bouchiat and J.Brossel, Phys. Rev. 147, 41 (1966).

[99] J.C.Camparo, J. Chem. Phys. 86, 1533 (1987).

[100] C.D.P.Levy et al., J. App. Phys. 63 , 4819 (1988).

[101] B.Braun, Spin Relaxation of Hydrogen and Deuterium in Storage Cells, Ph.D. thesis, University of Munich (1995), unpublished.

[102] J.B.Marion and S.T.Thornton, Classical dynamics of particles and systems, Saunders College Publishing, (1995), ISBN 0-03-097302-3.

[103] J.Griffiths, Introduction to Quantum Mechanics, Prentice Hall , New Jersey (1995).

[104] W.Haeberli, An. Rev. Nuc. Sci. 17, 373 (1967).

[105] A.Abragam and J.M.Winter, Phys. Rev. Lett. 1, 374 (1958).

[106] J.Griffiths, Introduction to Electrodynamics, Prentice Hall , New Jersey (1995).

[107] F.Bloch and A.J.Siegert, Phys. Rev. 70, 522 (1940).

[108] D.Cheever, Private communication (2005).

[109] D.Abbot et al., Phys. Rev. Lett., 82:1379 (1999).

[110] N.Isgur, Phys. Rev. Lett. 83, 272 (1999) .

[111] R.Schiavilla and I.Sick, Phys. Rev. C 64, 041002-1 (2001).

[112] M.Ostrick et al., Phys. Rev. Lett. 83, 276 (1999).

[113] T.W.Donnelly and A.S.Raskin, Ann. Phys. 169, 247 (1986).

[114] H.Arenhövel, W.Leidemann and E.L.Tomusiak, archiv:nucl-th/0407053 (2004).

[115] R.Machleidt and I.Slaus, J. Phys. G 27, R69 (2001).

[116] S.Boffi et al., Eur. Phys. J. A 14, 17 (2002).

[117] K. Berger, R. F. Wagenbrunn, and W. Plessas, Phys. Rev. D, 70, (2003) 094027.

[118] M.E.Rose, Elementary theory of algular momentum, Wiley and Sons (1961).

[119] J.Kelsey et al., Blast Coil calculations technical design report.

[120] W.Franklin, Private communication (2005).

[121] P.Karpius, Ph.D. thesis, UNH (1995), unpublished.

[122] B.Tonguk, BLAST internal report (2005).

[123] J.Kelsey, coil report (2000).

[124] D.Hasell, BLAST internal report (2005).

[125] H.Arenhövel, private communication (2005).

[126] P.R.Bevington and D.K.Robinson, Data Reduction and Error Analysis for the Physical Sciences, McGraw-Hill Publications (2003).

[127] W.T.Scott, Rev. Mod. Phys 35, 231 (1963).

[128] Particle Data Book (2000).

[129] A.Afanasev et al., Phys. Rev. D 64, 113009 (2001).

[130] L.W.Mo and Y.Tsai, Rev. Mod. Phys. 41, 205 (1969).

[131] D.Y.Bardin and N.M.Shumeiko, Nucl. Phys. B127, 242 (1977).

[132] M.Kohl, private communication (2005).

[133] The Blast Collaboration, Letter of Intent, "BLAST @ ELSA" (2005).

[134] K.F.Riley, M.P.Hobson and S.J.Bence, Mathematical Methods for Physicists and Engineers, Cambridge University Press (1997).